

# Fuel Analysis and Licensing Code: FALCON MOD01

## Volume 1: Theoretical and Numerical Bases



**WARNING:**  
Please read the Export Control  
and License Agreement on the  
back cover before removing the  
Wrapping Material.

*Technical Report*

Effective December 6, 2006, this report has been made publicly available in accordance with Section 734.3(b)(3) and published in accordance with Section 734.7 of the U.S. Export Administration Regulations. As a result of this publication, this report is subject to only copyright protection and does not require any license agreement from EPRI. This notice supersedes the export control restrictions and any proprietary licensed material notices embedded in the document prior to publication.



# **Fuel Analysis and Licensing Code: FALCON MOD01**

Volume 1: Theoretical and Numerical Bases

**1011307**

Final Report, December 2004

EPRI Project Manager  
S. Yagnik

## **DISCLAIMER OF WARRANTIES AND LIMITATION OF LIABILITIES**

THIS DOCUMENT WAS PREPARED BY THE ORGANIZATION(S) NAMED BELOW AS AN ACCOUNT OF WORK SPONSORED OR COSPONSORED BY THE ELECTRIC POWER RESEARCH INSTITUTE, INC. (EPRI). NEITHER EPRI, ANY MEMBER OF EPRI, ANY COSPONSOR, THE ORGANIZATION(S) BELOW, NOR ANY PERSON ACTING ON BEHALF OF ANY OF THEM:

(A) MAKES ANY WARRANTY OR REPRESENTATION WHATSOEVER, EXPRESS OR IMPLIED, (I) WITH RESPECT TO THE USE OF ANY INFORMATION, APPARATUS, METHOD, PROCESS, OR SIMILAR ITEM DISCLOSED IN THIS DOCUMENT, INCLUDING MERCHANTABILITY AND FITNESS FOR A PARTICULAR PURPOSE, OR (II) THAT SUCH USE DOES NOT INFRINGE ON OR INTERFERE WITH PRIVATELY OWNED RIGHTS, INCLUDING ANY PARTY'S INTELLECTUAL PROPERTY, OR (III) THAT THIS DOCUMENT IS SUITABLE TO ANY PARTICULAR USER'S CIRCUMSTANCE; OR

(B) ASSUMES RESPONSIBILITY FOR ANY DAMAGES OR OTHER LIABILITY WHATSOEVER (INCLUDING ANY CONSEQUENTIAL DAMAGES, EVEN IF EPRI OR ANY EPRI REPRESENTATIVE HAS BEEN ADVISED OF THE POSSIBILITY OF SUCH DAMAGES) RESULTING FROM YOUR SELECTION OR USE OF THIS DOCUMENT OR ANY INFORMATION, APPARATUS, METHOD, PROCESS, OR SIMILAR ITEM DISCLOSED IN THIS DOCUMENT.

ORGANIZATION(S) THAT PREPARED THIS DOCUMENT

**ANATECH Corp**

## **ORDERING INFORMATION**

Requests for copies of this report should be directed to EPRI Orders and Conferences, 1355 Willow Way, Suite 278, Concord, CA 94520, (800) 313-3774, press 2 or internally x5379, (925) 609-9169, (925) 609-1310 (fax).

Electric Power Research Institute and EPRI are registered service marks of the Electric Power Research Institute, Inc. EPRI. ELECTRIFY THE WORLD is a service mark of the Electric Power Research Institute, Inc.

Copyright © 2004 Electric Power Research Institute, Inc. All rights reserved.

# CITATIONS

---

This report was prepared by

ANATECH Corp.  
5435 Oberlin Drive  
San Diego, California 92121

Principal Investigator  
Y. Rashid  
R. Dunham  
R. Montgomery

This report describes research sponsored by EPRI.

The report is a corporate document that should be cited in the literature in the following manner:

*Fuel Analysis and Licensing Code: FALCON MOD01: Volume 1: Theoretical and Numerical Bases*, EPRI, Palo Alto, CA: 2004. 1011307.



# REPORT SUMMARY

---

FALCON Mod01 software and accompanying three-volume documentation are being released as the state-of-the-art light water reactor (LWR) fuel performance analysis and modeling code validated to high burn-up. Based on a robust finite element numerical structure, FALCON is capable of analyzing both steady state and transient fuel behavior with a seamless transition between the two modes. FALCON is the culmination of focused developmental activities since 1996 (with its origins in EPRI's two historic fuel performance codes developed in the 1980s: ESCORE and FREY).

## Background

Historically, EPRI has been supporting two codes to provide fuel analysis capabilities to utilities: ESCORE for steady state reload analysis and FREY for fuel reliability and off-normal transient analysis. In 1996, EPRI initiated development of FALCON (Fuel Analysis and Licensing Code—New) to address the need for more detailed fuel behavioral analysis, which had become necessary for the fuel designs and operational changes of recent years. The traditional separation of fuel analysis methodologies between steady state and transient had constrained the ability to address important fuel behavioral problems that fall into both regimes. Further, many users of ESCORE and FREY had requested program enhancements (for example, validation to higher burn-ups, ability to deal with newer cladding materials, MOX fuel, and burnable absorbers).

## Objectives

To provide a robust and independent code that is validated up to high burn-ups to support fuel performance analyses, reload design, and licensing activities.

## Approach

Using the existing experience base from ESCORE and FREY, FALCON's developers focused their efforts on three major tasks: (1) assimilate a robust numerical scheme with fully coupled thermal and mechanical iterations to perform steady state and transient analyses seamlessly in a single code; (2) incorporate pellet and cladding material and behavior models required for steady state and transient fuel performance analysis, with an emphasis to upgrade these models for high burn-up applications where appropriate; and (3) extensively benchmark, verify, and validate the code using a wide variety of test reactor experiments and commercial reactor fuel rod data. The developers also completed a detailed three-part documentation on the code: (a) Theoretical and Numerical Bases (EPRI report 1011307), (b) User's Manual (1011308), and (c) Verification and Validation (1011309). These reports are an integral part of the FALCON Mod01 release.

## Results

Various interim versions of FALCON have already been used in support of a variety of recent industry demands, including fuel rod design evaluations, analysis of reactivity-initiated accident

(RIA) tests, development of revised RIA acceptance criteria, analytical support for the Argonne National Laboratory - Nuclear Regulatory Commission Loss of Coolant Accident (ANL-NRC LOCA) program, and dry storage of high burn-up spent fuel. As a result, this formal release of FALCON has not only undergone substantial improvements compared to ESCORE and FREY, but has been duly validated up to high burn-up for modern high-duty fuel operations.

### **EPRI Perspective**

Although licensing analyses have traditionally been performed by fuel vendors, and many utilities continue to rely on vendor-supplied services, an increasing number of utilities prefer to acquire the tools necessary to perform licensing analyses or to conduct independent verification of vendor calculations. FALCON is an essential tool for such work.

Fuel behavior during both normal and off-normal operations is a complex interaction of thermal mechanical and chemical processes. Under some abnormal operational conditions, these processes can threaten fuel integrity and increase demands for more detailed fuel licensing analyses. The large economic benefits of increased fuel use have led to many fuel design changes in recent years. However, no comparable improvements in fuel analysis capabilities have been introduced in the last decade. For optimum plant operation, the detailed behavior of fuel rods under anticipated high-burn-up operations needs to be understood and licensed. As new results emerge from various poolside fuel inspections and hot cell post-irradiation examination (PIE) programs, an analytical capability is indispensable to understand and interpret the results. EPRI anticipates that FALCON will be the tool to meet these challenges.

A FALCON Users Group has been formed, and depending on subsequent utility guidance, the code also may be submitted for design review to obtain Appendix B Quality Assurance (QA) status and NRC approval in the future.

### **Keywords**

Fuel performance and modeling  
Finite element methods  
High burn-up fuel behavior  
Steady state fuel operation  
Fuel response to transients  
Fission gas release  
Core reload and licensing  
Operational transients  
Postulated accidents



# NOMENCLATURE

---

This report conforms to typical notation found in the technical literature, but because of the extent of the notation, the use of symbols overlap. However, ambiguities are eliminated by giving appropriate meaning to the symbols where they occur.

Because field continuum and finite element equations are represented in the text, it is convenient to use tensor and matrix notation. Since FALCON is a two-dimensional (2D) code, only Cartesian notation is used; where axisymmetric coordinates are needed, they are given explicitly.

## Tensor Notation

Standard tensor notation is used throughout. For example,  $x_i$  refers to the Cartesian coordinates of a spatial point where the subscript  $i$  ranges over the number of coordinates. Since this report is concerned only with 2D systems,  $i = 1, 2$ . However, the states of stress and strain are triaxial, thus, when referencing the stress ( $\sigma_{ij}$ ) or strain ( $\epsilon_{ij}$ ) tensors, it is necessary to have  $i, j = 1, 2, 3$  because  $\epsilon_{33}$  and  $\sigma_{33}$  are not zero, whereas  $\epsilon_{13} = \epsilon_{23} = 0$  and  $\sigma_{13} = \sigma_{23} = 0$ .

The conventions of indicial notation are employed, repeated indices imply summation

$$q_i n_i = q_1 n_1 + q_2 n_2$$

and the Kronecker delta,  $\delta_{ij}$ , is the identity tensor

$$\delta_{ij} = \begin{cases} 1, & \text{if } i = j \\ 0, & \text{otherwise} \end{cases}$$

Derivatives are sometimes written explicitly as

$$\partial T / \partial t \quad \text{or} \quad \frac{\partial T}{\partial t}$$

and

$$\frac{\partial T}{\partial x_i} \quad \text{or} \quad \partial T / \partial x_i$$

or they are abbreviated as

$$\dot{T} = \partial T / \partial t$$

or

$$T_{,i} = \partial T / \partial x_i$$

Superimposed dots ( $\dot{\phantom{x}}$ ) always represent partial differentiation with respect to time, and commas followed by an indicial subscript ( $_{,i}$ ) always represent partial differential with respect to the indicated spatial coordinate.

Arguments of functions are not always listed explicitly where the meaning is clear, e.g.,

$$T = T(x_i, t)$$

### Matrix Notation

Matrix notation is used throughout the text and it is frequently intermixed with tensor notation without loss of clarity. Matrix notation is used extensively where finite element equations are given.

A single curved underscore on any symbol represents a multidimensional vector of unspecified length, e.g.,

$$\underset{\sim}{\phi} = \begin{bmatrix} \phi_1 \\ \phi_2 \\ \vdots \\ \phi_N \end{bmatrix}$$

Thus,  $\phi$  is an  $N \times 1$  matrix. An  $N \times 1$  “matrix” is called a “column vector” or simply a “vector”. A “T” superscript following either a vector or matrix indicates the transpose, e.g.,

$$\underset{\sim}{\phi}^T = [\phi_1, \phi_2, \dots, \phi_N]$$

The transpose of a  $N \times 1$  column vector is a  $1 \times N$  row vector.

Matrices are represented by a double curved underscore on any symbols, e.g.,

$$\underset{\approx}{\beta} = \begin{bmatrix} \beta_{11} \beta_{12} \cdots \beta_{1M} \\ \beta_{21} \beta_{22} \cdots \beta_{2M} \\ \vdots \\ \beta_{N1} \beta_{N2} \cdots \beta_{NM} \end{bmatrix}$$

Thus,  $\beta$  is an  $N \times M$  matrix. Most of the matrices used in this report are square and symmetric, but this is not implied by the notation. The elements of the matrix are identified as  $\beta_{ij}$  where  $i$  and  $j$  identify the row and column, respectively.

The recurrence of matrix and/or vector quantities in an expression imply matrix multiplication, e.g.,

$$\underset{\sim}{S} = \underset{\sim}{\phi}^T \underset{\sim}{\phi} = \sum_{n=1}^N \phi_n^2$$

or

$$\underset{\sim}{S} = \underset{\sim}{\phi} \underset{\sim}{\phi}^T = \begin{bmatrix} \sigma_1 \sigma_1 & \sigma_1 \sigma_2 & \cdots & \sigma_1 \sigma_N \\ \sigma_2 \sigma_1 & \sigma_2 \sigma_2 & \cdots & \sigma_2 \sigma_N \\ \vdots & & & \\ \sigma_N \sigma_1 & \sigma_N \sigma_2 & \cdots & \sigma_N \sigma_N \end{bmatrix}$$

Matrix and tensor notation are combined, e.g.

$$\underset{\sim}{x}_i = \underset{\sim}{\phi}^T \underset{\sim}{x}_i$$

which implies the scalar inner product of the vectors  $\underset{\sim}{\phi}$  and  $\underset{\sim}{x}_i$  where the subscript  $i$  ( $i = 1, 2$ ) refers to the  $i^{\text{th}}$  Cartesian component of the matrix column vector  $\underset{\sim}{x}$  (which is used to denote spatial coordinates herein). Derivative notation is also combined.

$$\underset{\sim}{\phi}_{,j} = \partial \underset{\sim}{\phi} / \partial x_j$$

and

$$\underset{\sim}{\dot{T}} = \partial \underset{\sim}{T} / \partial t$$

## Symbols

The following is a partial list of the more important symbols used:

$\underset{\sim}{C}$	Convection matrix
$C_p$	Heat capacity
$D$	Damage factor

$D_{hy}$	Hydraulic diameter
$E$	Elastic modulus
$e$	Emissivity
$F_{\sim Q}$	Consistent nodal point heat flux vector
$F(\sigma, \epsilon^p, K)$	Yield function
$G$	Mass flux
$h$	Heat transfer coefficient
$I_{\sim}$	Identity matrix
$[J]$	Jacobian matrix
$J$	Jacobian
$J(\sigma, t)$	Creep compliance function
$K_{\sim}$	Conductivity matrix or stiffness matrix
$k(k_{ij})$	Thermal conductivity (tensor)
$k_L$	Thermal conductivity of liquid phase
$L_{\sim}$	Natural coordinates for element shape functions
$M_{\sim}$	Heat capacity matrix
$n_i$	Outward normal to $\Omega$
$p$	Pressure
$Q$	Volume heat source
$QC_i$	Correction shape functions for quadrilateral elements
$QH_i$	Linear shape functions for quadrilateral elements
$QQ_i$	Quadratic shape functions for quadrilateral elements
$q$	Heat flux
$R, r$	Material (spatial) axisymmetric radial coordinate
$R_{\sim}$	Radiation matrix
$T$	Temperature
$TC_i$	Correction shape functions for triangular elements
$x$	

$TH_i$	Linear shape functions for triangular elements
$TQ_i$	Quadratic shape functions for triangular elements
$T_{sat}$	Saturation temperature of coolant
$T_w$	Wall temperature
$t$	Time
$\Delta t$	Time step
$U_i, \tilde{U}$	Displacements
$dU_i, d\tilde{U}_i$	Increments in displacements in a time step
$\delta U_i, \delta \tilde{U}_i$	Virtual displacements
$V$	Volume
$v_j^n$	The $j^{th}$ component of the displacement at node $n$
$X, x$	Material (spatial) Cartesian coordinate
$X_i$	Cartesian material coordinates
$x_i$	Cartesian spatial coordinates
$Y, y$	Material (spatial) Cartesian coordinate
$Z, z$	Material (spatial) axisymmetric axial coordinate
$\alpha$	Vapor volume fraction
$\beta_{\approx}$	Strain-displacement matrix
$\Gamma$	Boundary of $\Omega$
$\Gamma_Q$	Portion of boundary where $Q$ is specified
$\Gamma_T$	Portion of boundary where $T$ is specified
$\delta_{\sim}$	Identify tensor in vector from $\delta_{\sim}^T = [1, 1, 1, 0]$
$\delta_{ij}$	Identify tensor
$\dot{\epsilon}_{\sim}, \dot{\epsilon}_{\sim ij}$	Strain rate
$\epsilon_{ij}, \epsilon_{\sim}$	Strains

$\delta \varepsilon_{ij}, \delta \varepsilon_{\sim}$	Virtual strains
$\theta, \theta_n$	Nodal point temperature vector
$\mu$	Viscosity
$\mu_L$	Viscosity of liquid phase
$\nu$	Poisson's ration
$\xi, \eta$	Parametric coordinates for quadrilaterals
$\rho$	Material density
$\rho_L$	Density of saturated liquid
$\sigma_{\sim}$	Cauchy stress
$\overset{\nabla}{\sigma}_{\sim}$	Jaumann stress rate
$\sigma'_{ij}$	Deviatoric stresses
$\phi_{\sim}$	Vector of shape functions
$\phi_n$	$n^{\text{th}}$ finite element shape function
$\chi$	Quality
$\Omega$	2D region
$\Omega_{\approx}$	Spin tensor – antisymmetric part of the velocity gradient
$\Omega_e$	2D finite element region or area

# CONTENTS

---

<b>1 INTRODUCTION .....</b>	<b>1-1</b>
1.1 Background .....	1-1
1.2 General Description of FALCON .....	1-2
1.3 Program Capabilities .....	1-5
1.4 Purpose .....	1-13
1.5 References .....	1-14
<b>2 SPATIAL FINITE ELEMENT MODEL .....</b>	<b>2-1</b>
2.1 Background .....	2-1
2.2 Element Shape Functions .....	2-1
2.3 References .....	2-4
<b>3 HEAT TRANSFER.....</b>	<b>3-1</b>
3.1 Heat Conduction.....	3-1
3.1.1 Basic Equations.....	3-1
3.1.2 Finite Element Equations.....	3-3
3.1.3 Boundary Conditions .....	3-5
3.2 Power Generation .....	3-9
3.2.1 Fission Heat Generation.....	3-9
3.2.2 Decay Heat.....	3-10
3.2.3 Heat of Oxidation.....	3-14
3.3 Fuel Rod Voids Heat Transfer.....	3-14
3.3.1 Gap Conductance.....	3-14
3.3.1.1 Open Gap .....	3-15
3.3.1.2 Solid-Solid Contact .....	3-17
3.3.2 Pellet-Pellet Contact Conductance .....	3-19
3.3.3 Plenum Heat Transfer .....	3-20
3.4 Fuel Rod Surface Heat Transfer .....	3-20

3.4.1 Coolant Enthalpy Model .....	3-20
3.4.2 Heat Transfer Correlations .....	3-23
3.4.3 Model Assumption Implications .....	3-25
3.5 References .....	3-26
<b>4 DEFORMATIONS .....</b>	<b>4-1</b>
4.1 Displacement Approximations .....	4-2
4.2 Strain-Displacement Relations .....	4-3
4.3 Stress-Strain Relations .....	4-4
4.3.1 Elastic Relations .....	4-4
4.3.2 Creep Relations .....	4-5
4.3.3 Time-Independent Elastic-Plastic Relations .....	4-5
4.3.4 Pellet-Cladding Mechanical Interaction (PCMI) .....	4-7
4.3.5 Incremental Stress-Strain Relations .....	4-9
4.4 Equilibrium Equations .....	4-9
4.5 References .....	4-10
<b>5 MATERIAL AND PHYSICAL MODELS .....</b>	<b>5-1</b>
5.1 UO <sub>2</sub> Fuel Material Properties & Behavioral Models .....	5-5
5.1.1 Melting Temperature Model .....	5-5
5.1.2 Thermal Conductivity .....	5-7
5.1.2.1 MATPRO Revision 11 Model Modified for Burnup .....	5-7
5.1.2.2 NFIR Thermal Conductivity Model .....	5-9
5.1.3 Swelling Model .....	5-14
5.1.4 Densification .....	5-16
5.1.4.1 ESCORE Model .....	5-17
5.1.4.2 MATPRO Model .....	5-18
5.1.5 Relocation .....	5-19
5.1.5.1 HEDL Model .....	5-19
5.1.5.2 ESCORE Relocation Model .....	5-20
5.1.6 High Burnup Rim Structure .....	5-21
5.2 Internal Void Volume and Gas Pressure .....	5-22
5.3 Clad Material Properties & Behavioral Models .....	5-24
5.3.1 Zircaloy and ZrO <sub>2</sub> Thermal Conductivity .....	5-24
5.3.1.1 Zircaloy Thermal Conductivity .....	5-24



5.3.1.2 Zirconium Oxide (ZrO <sub>2</sub> ) Thermal Conductivity .....	5-24
5.3.2 Elasticity & Plasticity.....	5-25
5.3.3 Thermal/Irradiation Creep.....	5-26
5.3.3.1 ESCORE.....	5-26
5.3.3.2 MATPRO Rev 2 Cladding Creep Model .....	5-28
5.3.3.3 Limbäck and Andersson Cladding Creep Model.....	5-28
5.3.4 Irradiation Growth.....	5-31
5.3.4.1 MATPRO-11 Revision 2 Model.....	5-31
5.3.4.2 ESCORE Model .....	5-32
5.3.4.3 FRANKLIN Model .....	5-32
5.3.5 Oxidation .....	5-33
5.3.5.1 Low Temperature Oxidation.....	5-33
5.3.5.2 High Temperature Oxidation.....	5-35
5.4 Failure .....	5-38
5.4.1 High Temperature Transient Failure Model (Burst) .....	5-39
5.4.2 Low Temperature PCI Failure Model (SCC).....	5-41
5.4.3 Pellet-Cladding Mechanical Interaction (PCMI) Failure Model .....	5-42
5.5 Fission Gas Release .....	5-50
5.5.1 ANS-5.4 Model and ANS-5.4 Modified Model .....	5-51
5.5.2 Forsberg – Massih Model .....	5-53
5.5.3 Athermal Fission Gas Release Model .....	5-57
5.5.4 ESCORE Fission Gas Release Model .....	5-59
5.5.5 EPRI/CE Transient Model .....	5-59
5.6 Radial Power Distribution.....	5-60
5.6.1 BNFL -- RADAR-G Model.....	5-60
5.6.2 TUBRNP Model .....	5-61
5.7 Burnup Calculation.....	5-62
5.8 References.....	5-64
<b>6 NUMERICAL SOLUTION PROCEDURE.....</b>	<b>6-1</b>
6.1 General .....	6-1
6.2 Iteration Procedure Between Thermal and Mechanical Analysis .....	6-1
6.3 Thermal Analysis.....	6-2
6.3.1 Steady State Solution .....	6-3
6.4 Deformation (Mechanical) Analysis.....	6-3

6.5 Time-Step Selection Criteria .....	6-7
6.5.1 Thermal Solution Criteria.....	6-7
6.5.2 Deformation Solution Criteria .....	6-8
6.6 References.....	6-9
<b>A APPENDIX A: FINITE ELEMENT SPATIAL EQUATIONS.....</b>	<b>A-1</b>
A.1 Element Shape Functions and Basic Equations.....	A-1
A.2 Quadrilateral Shape Functions .....	A-5
A.3 Triangular Shape Functions (For Research Purposes Only) .....	A-5
A.4 Shape Function Derivatives/Jacobian.....	A-6
A.5 Isoparametric Interpolation .....	A-7
<b>B APPENDIX B: COOLANT ENTHALPY MODEL .....</b>	<b>B-1</b>
B.1 Steady State Flow Conditions.....	B-1
B.2 Transient Flow Conditions .....	B-3
B.3 Heat Transfer Coefficient and Critical Heat Flux Correlations .....	B-9
B.4 Sodium Heat Transfer Correlation .....	B-13
B.5 Water Heat Transfer Correlations .....	B-13
B.6 Critical Heat Flux Correlations .....	B-16
B.7 Critical Power Ratio Correlations .....	B-21
B.8 References.....	B-25
<b>C APPENDIX C: FIELD AND EQUILIBRIUM EQUATIONS.....</b>	<b>C-1</b>
C.1 Strain Displacement Relations.....	C-1
C.2 Stress-Strain Relations .....	C-4
C.2.1 General Relations .....	C-5
C.2.2 Creep Relations .....	C-6
C.2.3 Time-Independent Elastic-Plastic Relations .....	C-6
C.2.4 Incremental Stress-Strain Relations .....	C-9
C.2.5 Radial Return Correction .....	C-11
C.2.6 Incremental Stress-Strain Relations for Clad Material .....	C-11
C.2.7 Incremental Stress-Strain Relations for Fuel Material .....	C-12
C.2.7.1 Hot Pressing Parameters .....	C-12
C.2.7.2 Pellet Cracking .....	C-13
C.3 Equilibrium Equations .....	C-19

C.4 References .....	C-23
<b>D APPENDIX D: NUMERICAL SCHEME FOR ANS-5.4 (MODIFIED) MODEL .....</b>	<b>D-1</b>
<b>E APPENDIX E: RADIAL POWER AND BURNUP DISTRIBUTION.....</b>	<b>E-1</b>
E.1 RADAR-G Model.....	E-1
E.2 TRANSURANUS Burnup Model (TUBRNP) .....	E-10
E.3 References.....	E-15
<b>F APPENDIX F: EQUATION OF STATE .....</b>	<b>F-1</b>
F.1 Water Properties .....	F-1
F.1.1 Saturated Liquid and Saturated Vapor Enthalpies as Functions of Pressure .....	F-1
F.1.2 Liquid and Vapor Temperature as Functions of Enthalpy and Pressure .....	F-3
F.1.3 Specific Volume of Liquid and Vapor as Functions of Enthalpy and Pressure.....	F-5
F.1.4 Thermal Conductivity as a Function of Temperature and Density .....	F-6
F.1.5 Dynamic Viscosity as a Function of Temperature and Density .....	F-8
F.2 Sodium .....	F-9
F.2.1 Heat Capacity as Function of Temperature.....	F-9
F.2.2 Enthalpy as Function of Temperature .....	F-9
F.2.3 Density as Function of Temperature .....	F-9
F.2.4 Thermal Conductivity as Function of Temperature .....	F-10
F.3 References.....	F-10



## LIST OF FIGURES

Figure 1-1 ESCORE Program Architecture .....	1-7
Figure 1-2 FREY Program Architecture .....	1-8
Figure 1-3 FALCON Program Architecture .....	1-9
Figure 1-4 FALCON Steady State and Transient Numerical Models.....	1-11
Figure 2-1 Natural Coordinates for 9-Node Quadrilateral Elements .....	2-2
Figure 2-2 Element Shapes and Nodal Variables.....	2-3
Figure 3-1 Finite Element Idealization of a Region .....	3-3
Figure 3-2 Finite Element Idealization of a Boundary .....	3-6
Figure 3-3 Example of a Power History Representation Used in the Decay Heat Model .....	3-13
Figure 3-4 Coolant Channel Nodalization .....	3-22
Figure 3-5 Schematic Representation of the Boiling Curve .....	3-23
Figure 5-1 Comparison of Yamanouchi $\text{UO}_2$ Melting Temperature Data to Earlier Measurements by Christensen [5]. References in Figure Are Defined in Reference 5. Yamanouchi Measurements Display No Burnup Dependency out to 30 GWd/MTU. ....	5-6
Figure 5-2 Comparison of Komatsu Data for Mixed Oxide Melting Temperature Data to Earlier Measurements by Krankota and Craig [9]. The Data Show a Slight Burnup Dependency beyond a Burnup of 50 GWd/MTU.....	5-6
Figure 5-3 Comparison of Fuel Centerline Temperature as a Function of Irradiation Time for IFA 515.10, Rod A1 ( $\text{UO}_2$ Rod) for the MATPRO and NFIR Fuel Thermal Conductivity Models .....	5-13
Figure 5-4 Comparison of Fuel Centerline Temperature as a Function of Irradiation Time for IFA 515.10, Rod A2 ( $\text{UO}_2\text{-Gd}_2\text{O}_3$ Rod) for the modified NFIR Fuel Thermal Conductivity Model.....	5-14
Figure 5-5 Comparison of Measured Density to the FALCON Fuel Swelling Model as Function of Burnup for $\text{UO}_2$ fuel. ....	5-15
Figure 5-6 Schematic Diagram of Strain Energy, Force Deflection and Stress-Strain Relationship .....	5-45
Figure 5-7 Strain Energy Density as a Function of Strain for Uniaxial Loading .....	5-49
Figure 5-8 Strain Energy Density as a Function of Strain for Biaxial Strain Ratio of 0.5 ( $\sigma_1/\sigma_2 = 0.5$ ).....	5-49
Figure 5-9 Strain Energy Density as a Function of Strain for Equi-Biaxial Loading ( $\sigma_1/\sigma_2$ $= 1$ ) .....	5-50
Figure 5-10 Comparison of the Forsberg - Massih Fission Gas Release Model to the Vitanza Threshold .....	5-56

Figure 5-11 Fission Gas Release for RISO III AN-2 Calculated by FALCON using the Forsberg-Massih/EPRI-CE models. Experimental data shown for comparison .....	5-57
Figure 5-12 Gas release fractions from FRAMATOME fuels irradiated in EDF reactors [70] .....	5-58
Figure A-1 Linear-Quadratic Quadrilateral Elements .....	A-2
Figure A-2 Linear-Quadratic Triangular Elements .....	A-2
Figure A-3 Symbolic Natural Coordinates for Quadrilateral and Triangular Elements.....	A-3
Figure B-1 Coolant Channel Nodalization.....	B-2
Figure B-2 Adjacent Rod Weighting Patterns for Hench-Gillis J Factor.....	B-24
Figure C-1 Normalized Tension Response Curve for Ceramic Materials .....	C-13
Figure C-2 $UO_2$ Failure/Yield Surface .....	C-15
Figure C-3 Fuel Cracking Pattern .....	C-18
Figure D-1 Gas Release Predictions for Two Numerical Forms of the ANS-5.4 Model.....	D-3

## LIST OF TABLES

---

Table 1-1 Thermal and Mechanical Properties and Behavioral Models Included in FALCON.....	1-4
Table 3-1 Parameters for $^{235}\text{U}$ Thermal Fissions .....	3-12
Table 3-2 Parameters for $^{239}\text{Pu}$ Thermal Fissions.....	3-12
Table 3-3 Parameters for $^{238}\text{U}$ Fast Fissions .....	3-13
Table 3-4 Heat Transfer Modes and Corresponding Correlations for Water .....	3-24
Table 5-1 Thermal Property Models Used in FALCON.....	5-2
Table 5-2 Mechanical Property Models Used in FALCON.....	5-3
Table 5-3 Behavioral Models Used in FALCON .....	5-4
Table 5-4 Model Coefficients for the Modified NFIR $\text{UO}_2$ Thermal Conductivity Model .....	5-12
Table 5-5 High Temperature Oxidation Rate Constants used in FALCON.....	5-36
Table 5-6 Model Parameters Used to Calculate Grain Boundary Saturation Density in Forsberg-Massih Model .....	5-55
Table 6-1 Guidelines for Time Step Size Selection .....	6-9
Table B-1 Symbol Definitions for Appendix B .....	B-9
Table B-2 Data Ranges for Pre-CHF Heat Transfer Correlations.....	B-11
Table B-3 Data Ranges for Post-CHF Heat Transfer Correlations .....	B-11
Table B-4 Data Ranges for Critical Heat Flux Correlations.....	B-12
Table E-1 Spectrum Average Cross-Sections Used in TUBRNP (in Barns).....	E-11
Table F-1 Constants for Saturated Liquid and Vapor Enthalpies as Functions of Pressure .....	F-3
Table F-2 Constants for Temperature as a Function of Pressure and Enthalpy .....	F-4
Table F-3 Constants for Specific Volume as a Function of Pressure and Enthalpy.....	F-6
Table F-4 Coefficients $b_{ij}$ for Dynamic Viscosity.....	F-8





# 1

## INTRODUCTION

---

### 1.1 Background

Utilities need a reliable and easy-to-use computer program to support their fuel performance and cycle-reload design activities. These activities range from complete licensing analyses carried out in-house to independently verify vendor-supplied design and analysis services. While some utilities continue to rely on fuel vendors to provide these services, many prefer to have the capabilities to perform such analyses in-house, and some utilities are already performing these analyses. This may become a matter of necessity because vendors' R&D resources are diminishing, therefore, utilities must inevitably seek alternative analytical support as they continue to strive for higher fuel burnup. Under these circumstances, it is imperative that EPRI provide a fuel performance computer program that is validated for burnup levels of current and future designs.

Historically, EPRI has supported two fuel performance codes, ESCORE and FREY [1, 2]. ESCORE is a finite difference quasi-steady state core reload evaluator which has been licensed by the NRC for batch average burnups to 50 GWd/MTU (lead rod ~60 GWd/MTU). ESCORE is used to support fuel licensing and design basis evaluations. FREY is a finite element transient thermomechanical fuel analysis program that is used to evaluate fuel rod response under operational transients, Safety Analysis Report (SAR) Chapter 15 design basis events, and other operational conditions that might lead to fuel rod failures. Both ESCORE and FREY meet 10CFR50 Appendix B Quality Assurance (QA) requirements. ESCORE was reviewed and approved by the NRC and has been used by many utilities. FREY has not been submitted to NRC for review, but it was qualified in a design review under a 10CFR50-compliant QA program.

The large economic benefits associated with increased fuel utilization have led to many fuel design changes in recent years. However, no comparable improvements in fuel analysis capabilities have been introduced in ESCORE and FREY in the last decade. The fuel design changes include new cladding alloys and heat treatments to reduce cladding corrosion and hydriding and fuel pellet changes to accommodate the enhancement of fission gas release at high burnup. Also, important additions to experimental databases for LWR fuel have been made since ESCORE and FREY were released. Particularly important are new experimental observations at fuel peak nodal burnups above 40 GWd/MTU. More fission gas release data became available at these high burnups, and a new phenomenon called the high burnup structure in the pellet periphery was observed in post-irradiation examinations of the fuel pellet microstructure [3]. These effects and the effects of hydrogen uptake from outer surface corrosion on clad mechanical properties came into focus in the recent Reactivity Initiated Accident (RIA) issues which raised NRC concerns about high burnup operation [4]. The ability

*Introduction*

of the industry to address these concerns depends on the capabilities, veracity and robustness of the fuel analysis codes and the ability these codes to calculate accurately the behavior of high burnup fuel under a variety of normal and off-normal operating conditions.

As operational requirements on fuel performance increase so will the need for more detailed fuel behavioral analysis. The traditional separation of fuel analysis methodologies between steady state and transient places significant constraints on the ability to address important fuel behavioral problems which typically fall into both regimes. Thus, to bring fuel analysis capabilities up to the level required to treat extended fuel utilization and higher duty, to update material property databases, and to prepare for high burnup licensing issues which will inevitably be raised by the NRC, EPRI has undertaken the development of the FALCON computer program as an enhanced and integrated derivative of ESCORE and FREY.

The NRC's audit codes that are equivalent to ESCORE and FREY are FRAPCON and FRAPTRAN, respectively [5, 6]. In addition, NRC has initiated new material behavioral programs on high burnup fuel to support future actions on licensing reviews [7]. In undertaking these activities, the NRC has realized that enhanced fuel analysis capabilities are needed to cope with increased demands on fuel performance in the upper range of currently licensed burnup levels as well as in anticipation of industry applications for burnup extensions.

## **1.2 General Description of FALCON**

The development of FALCON is aimed at producing a state-of-the-art fuel behavior program for licensing and best estimate analyses of LWR fuel rods. Adhering to this objective, the present version of FALCON, MOD01, incorporates advanced thermomechanical capabilities in a both a one-dimensional (1D) and a fully two-dimensional (2D) continuum framework. The 1D capabilities of FALCON were constructed to represent the approach used in the empirically-based ESCORE [1] program. The 1D axial slice model representation was merged with the mechanics-based 2D FREY-01 program [2] to produce a new code FALCON. FALCON has been developed as a general purpose fuel rod evaluation system applicable to the analysis of normal operation, off-normal events and accident conditions. The program's transient analysis capabilities are consistent with the requirements outlined in EPRI Report NP-1022 [8]. With both best estimate and licensing analysis capabilities present, FALCON provides the user with the versatility and convenience of dealing with a single program for multiple applications, thus maintaining consistency between the various types of analysis.

FALCON is a computer program that models best estimate LWR fuel rod thermomechanical performance under steady state and transient conditions. FALCON is an enhancement beyond the combined capabilities of ESCORE and FREY. The integrated software is a general purpose fuel response analysis system that couples the two uncoupled fuel analysis methodologies, namely, steady state fuel performance analysis (ESCORE 1D methodology) and transient fuel rod response analysis (FREY 2D methodology). Note that ESCORE treats steady state fuel rod analysis using an axial series of uncoupled 1D slices. FREY treats transient analysis fuel rod analysis using fully coupled 2D finite element models. FALCON now provides the user a choice of steady state modeling using either the ESCORE 1D or FREY 2D analysis approaches to evaluate fuel rod behavior.

FALCON is based on the finite element computational method and utilizes a single compatible grid for both the thermal solution and the deformation solution. The fuel rod geometric representation can be either axisymmetric (R-Z) or plane (R- $\theta$ ) slice models. Axisymmetric representations can be modeled as a series of 1D slice models without shear stresses or as full 2D axisymmetric continuum models. Plane representations must be 2D continuum models. FALCON's 2D finite element library consists of 4, 8 and 9-node quadrilateral elements which are used to model the fuel and clad. Fuel-clad gap and pellet-pellet contact are modeled by 2-node elements which simulate gap thermal conductance, friction-slip and contact-release properties. The plenum is modeled by 2-node elements with the thermal and mechanical properties representing the plenum spring and the gas mixture. Dished and hollow pellets are considered. The rod-to-coolant heat transfer may be modeled using a closed channel thermal hydraulics enthalpy rise model with heat transfer coefficients and critical heat flux correlations similar to those used in the EPRI RETRAN and VIPRE thermal-hydraulic programs [9, 10]. The coolant flow model is also complemented by an option to input time and space-dependent heat transfer coefficients or specified cladding surface temperature time histories, thus extending the program's utility to a wide range of operating conditions and heat transfer regimes other than those represented by the thermal-hydraulic model.

The temperature and deformation solutions are consistent in the time-stepping and iteration procedures. In each time step, the heat transfer and the deformation solutions are carried out in sequence with provisions for performing multiple iterations within each solution. Furthermore, a thermal-mechanical iteration procedure is performed to insure overall convergence between the temperature and deformation solutions. The material property models used in FALCON were obtained from a variety of sources including the Materials Property (MATPRO) package developed by the US NRC [11], models published in the open literature or developed through industry research activities such as the Nuclear Fuel Industry Research (NFIR) program and ESCORE [1]. Table 1-1 contains a list of thermal and mechanical material properties used in FALCON to model the normal and transient behavior LWR  $\text{UO}_2$  – Zircaloy clad fuel rods. In addition, limited mixed uranium-plutonium (MOX) material properties are also included in FALCON from the MATPRO package. As shown in Table 1-1, the properties models in FALCON can be divided into three categories, thermal properties, mechanical properties, and behavioral models. An important and unique capability of FALCON is the robust constitutive relations used to calculate the mechanical state of the pellet and cladding. These relations include elastic and inelastic behavior of the pellet and cladding, strain-rate dependent plasticity of the cladding, and pellet cracking, relocation, hot-pressing, densification and swelling. The advanced finite element formulation used in FALCON allows for the integration of the different thermal, mechanical, and behavioral effects together to provide an advanced analysis capability for fuel rod behavior under all types of conditions.

## Introduction

**Table 1-1**  
**Thermal and Mechanical Properties and Behavioral Models Included in FALCON**

<i>Material</i>	<b>Thermal Properties</b>	<b>Mechanical Properties</b>	<b>Behavioral Models</b>
Fuel	Specific Heat Capacity Thermal Conductivity Emissivity Melting Temperature	Thermal Expansion Young's and Shear Modulus Compressive Yield Stress Fracture Strength Thermal/Irradiation Creep Densification Swelling Relocation	Steady State Fission Gas Release Transient Fission Gas Release Radial Power Distribution High Burnup Structure
Cladding	Specific Heat Capacity Zircaloy Thermal Conductivity ZrO <sub>2</sub> Thermal Conductivity Zirconium Dioxide Emissivity Melting Temperature	Thermal Expansion Young's Modulus for Isotropic Cladding Shear Modulus for Isotropic Cladding Yield Stress Plastic Strain Hardening Annealing of Cold Work/Irradiation Damage Meyer Hardness Thermal/Irradiation Creep Irradiation Growth	Low Temperature Oxidation (Water) High Temperature Oxidation (Steam) Phase Transformation Stress Corrosion Cracking High Temperature Rupture
Gap	Gas Thermal Conductivity Gas Viscosity Temperature Jump Distance	Friction Coefficient	Open and Solid Gap Conductivity

The governing equations for the heat transfer part of the problem are formulated, using the Galerkin error minimization method and the Crank-Nicholson central differencing technique, as a system of equations relating the heat flow vector to the nodal temperatures of the current and previous time step. The deformation part of the problem, on the other hand, is formulated using the virtual work variational principle and a forward differencing algorithm with a Newton iteration technique. The resulting system of equations relates the nodal forces to the nodal displacements increments at each time step. Principles of continuum thermomechanics are rigorously applied in both formulations, thus maintaining theoretically consistent and continuous behavior for the fuel rod as it undergoes various thermal and deformation regimes from the low temperature, small deformation response, to the high temperature, large deformation response.

Using time-dependent input and previous step information (or initial conditions information for the first time step), the thermal solution is performed first, and the nodal temperatures are calculated using a frontal solver. The incremental displacements are obtained next, using as input the nodal temperatures, the internal and external pressure distributions and the boundary constraints. As in the case of the thermal problem, the same frontal solver is used in the deformation solution except for the modification from a scalar to a vector field. The element strains and stresses are calculated at the integration points of the fuel, clad and gap elements.

Some convergence checks are performed for the thermal and deformation solutions independently. Presently the user specifies the number of thermal, mechanical, and combined thermomechanical iterations. In the near future fully automated convergence will be implemented. Updated feedback variables, such as gap size distribution, fuel-clad contact conditions, gas pressure, etc., are accounted for in the iteration solution. Some automatic time-stepping procedure is provided, which is governed by thermal and mechanical stability criteria.

### 1.3 Program Capabilities

The general capabilities and applications that FALCON supports include:

- Steady state and transient analyses in support of fuel licensing requirements in conformance with Chapter 4 of the Standard Review Plan (SRP) NUREG-0800 [8].
- Accident analyses conforming to Chapter 15 of the SRP; may require coupling with thermal-hydraulic system analysis codes for some of the cases specified in Chapter 15
- Fuel design evaluations
- Technical specifications and setpoint applications
- Comparisons to measured data from fuel rod experiments
- Establish initial fuel rod conditions (stored energy, internal rod pressure, etc.) for input into other accident analysis codes

## *Introduction*

The integrated software merges the relevant modules from ESCORE and FREY, Figures 1-1 and 1-2, respectively, into the new architecture shown in Figure 1-3. The main modules of FALCON include:

- Pre-Processor Module
  - Read/Write/Plot Input Data
  - Consistency Checks of Input Data and Diagnostic Messages
  - Finite Element Grid Generation
- Analysis Module
  - Material Properties and Behavioral Models Subprogram
  - Radial Power and Burnup Distribution
  - TUBRNP
  - PFCC
  - Behavioral Correlations
- Thermal Analysis Module
  - Thermal Hydraulic Calculations
  - Temperature Calculations
- Deformation Analysis Module
  - Displacement Calculations
  - Stress and Strain Calculations
- Post-Processor Module
  - Time History Plots of Input and Output Variables
  - Profile and Contour Plots
  - Printed Output Lists
  - Spreadsheet Formatted Text Files
  - ASCII Files for External Plotting Devices

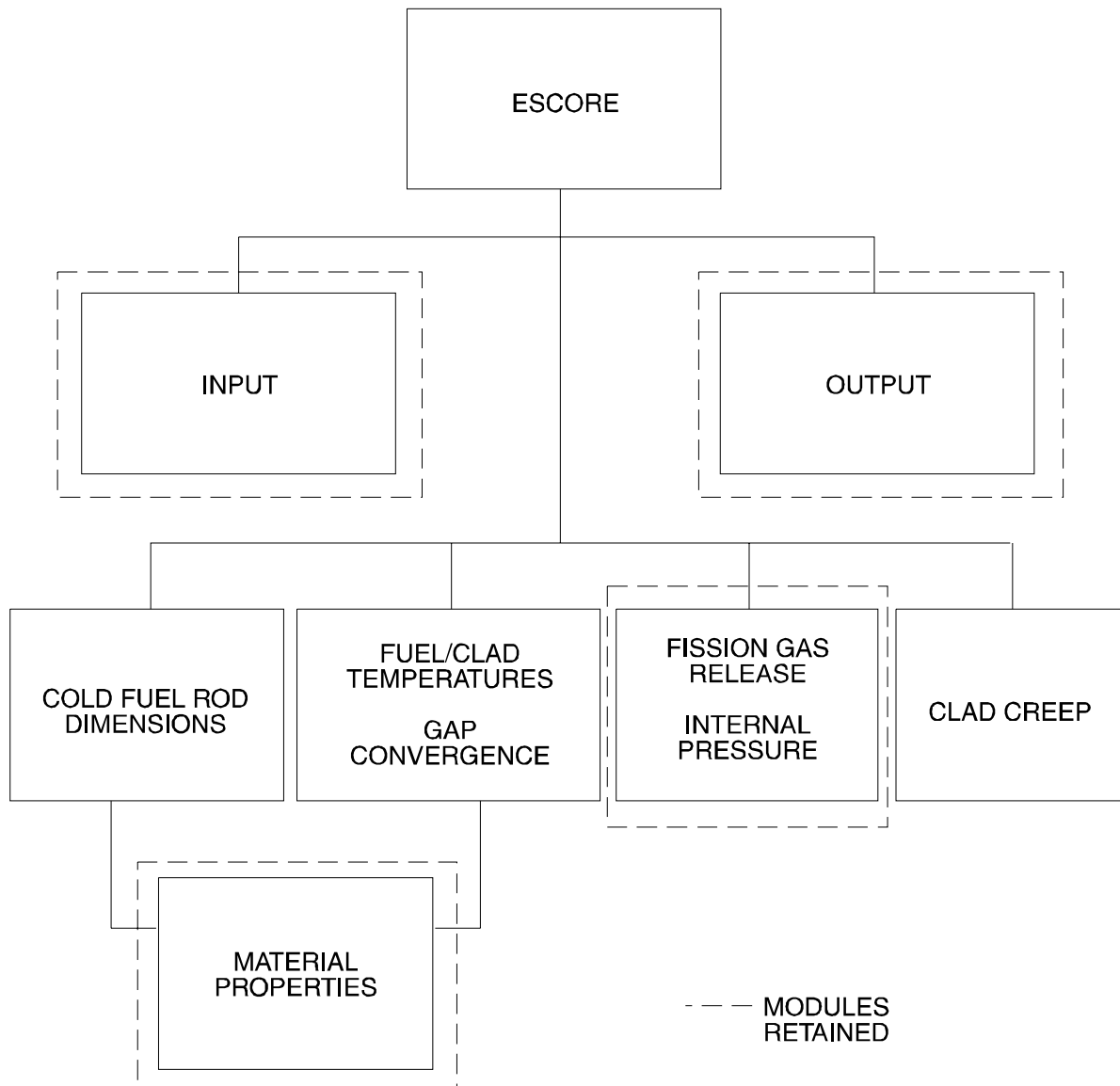


**Figure 1-1**  
**ESCORE Program Architecture**

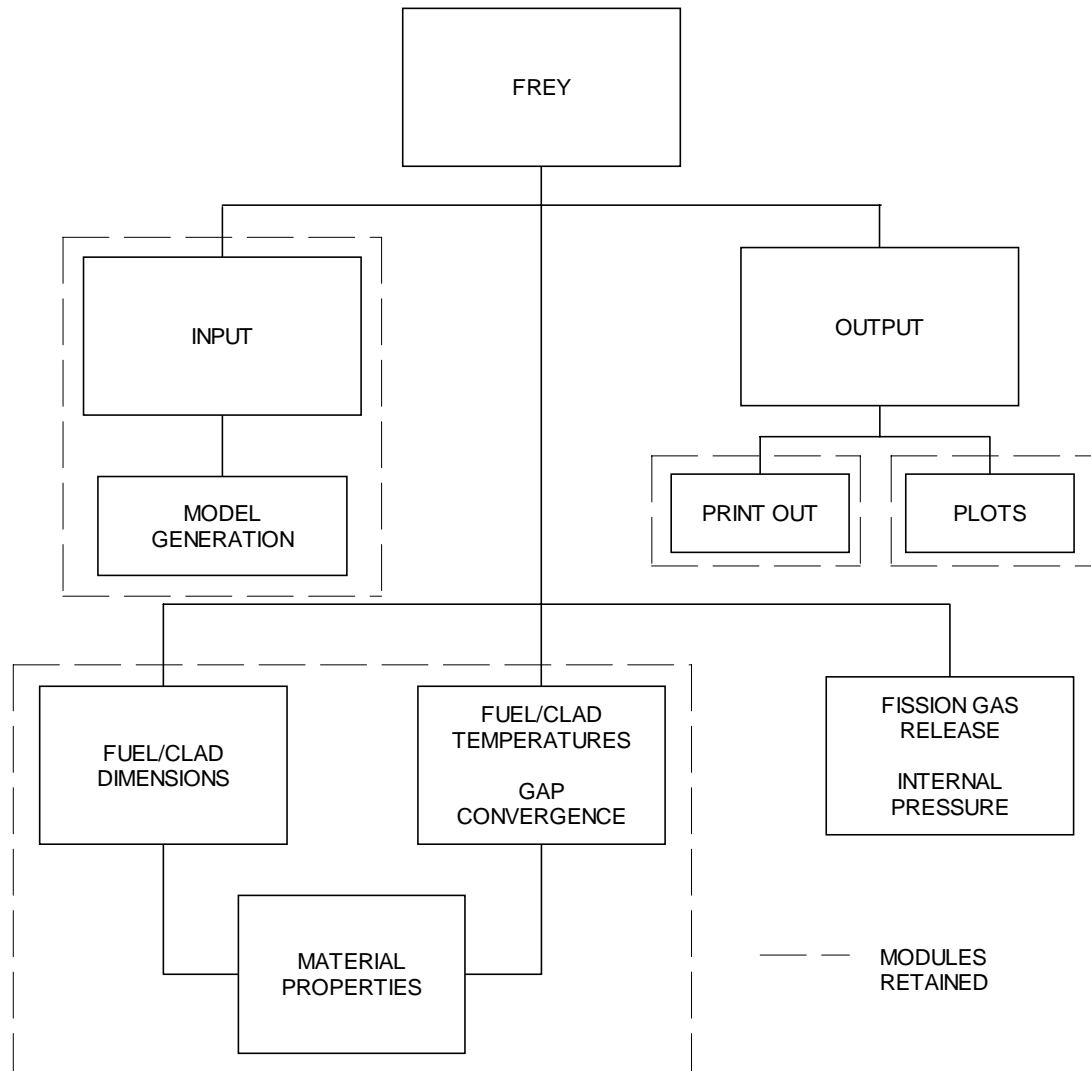
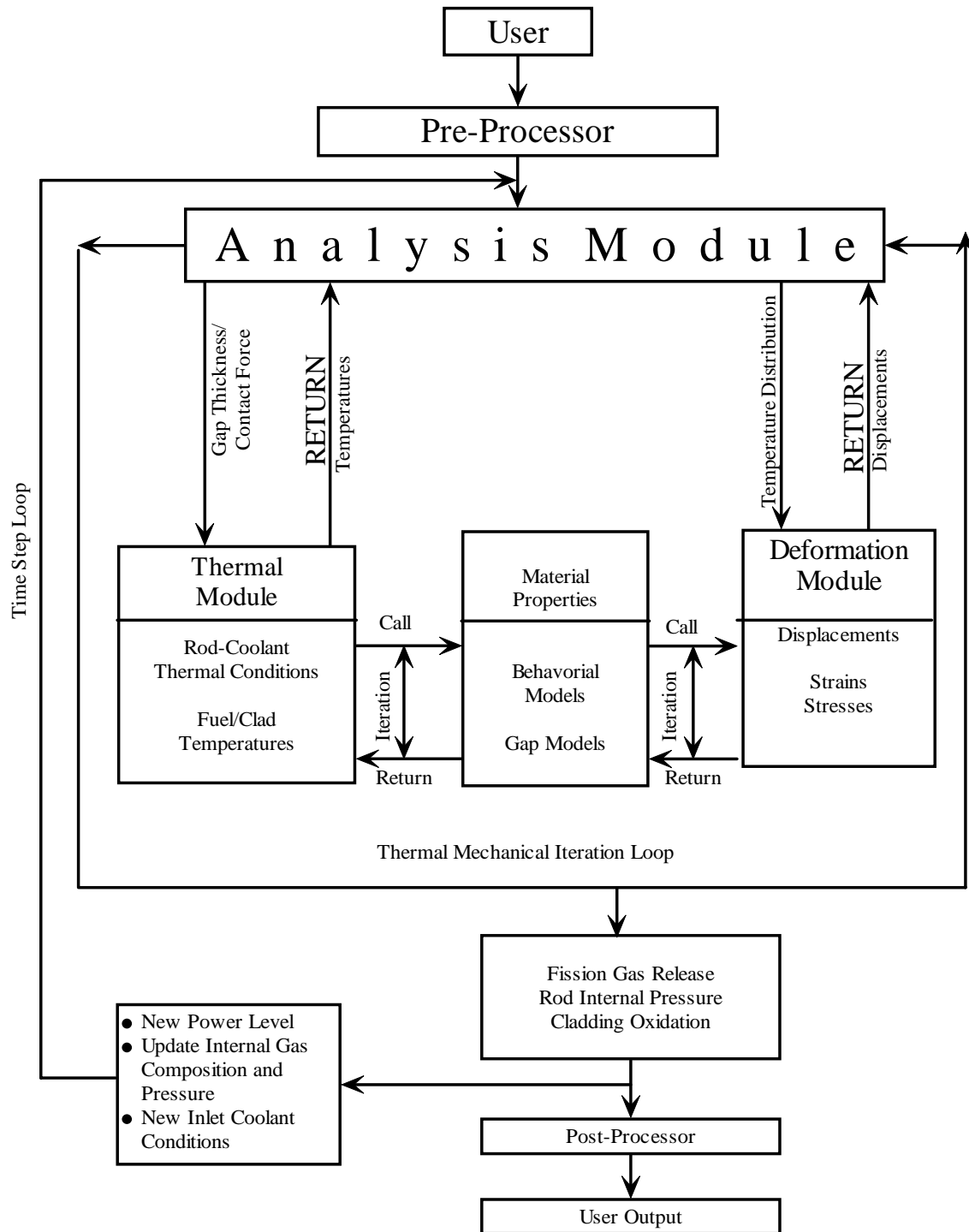


Figure 1-2. FREY Program Architecture

**Figure 1-2**  
**FREY Program Architecture**





**Figure 1-3**  
**FALCON Program Architecture**

*Introduction*

Other important capabilities of FALCON include:

- FALCON is finite element based. The computational structure of the program consists of two compatible grids as shown in Figure 1-4: a full 2D finite element grid, Mode-1; and an axially stacked (1D) radial finite element grid, Mode-2. Both element types have quadratic interpolation functions for temperature and displacements to ensure a consistent discretization accuracy that is equivalent to a five-point finite difference scheme. Each grid contains two sets of points: a "nodal point" set at which the global response variables, temperatures and displacements, are computed; and an internal "integration (Gauss) points" set at which material properties are specified and state variables (stresses, strains, etc.) are computed. The two grids use the same nodal points, but numerical compatibility requires that nine (3x3) Gauss points be used for the 2D grid and three (3) Gauss points be used for the 1D grid for each element. The radial position of the Gauss points and the number and type of state variables per Gauss point will be identical for the two grids.
- The R- $\theta$  (plane) analysis capability in FREY for Pellet/Clad Interaction (PCI) and Stress Corrosion Cracking (SCC) analysis is retained. This capability can be used as a stand-alone or an adjunct to either the 2D or the 1D R-Z (axisymmetric) grids to provide stress/strain concentration factors to account for the local mechanical PCI at pellet cracks. The R- $\theta$ /R-Z coupling can be invoked at any time step in the steady state or the transient analysis, particularly during power ramps.
- The 1D/2D grid and time stepping capabilities described above are constructed to make the transitioning back and forth between steady state and transient analysis automatic and transparent to the user.
- The solution algorithm is similar for the 1D & 2D grids. Both grids have the same formulation for transient heat conduction and the mechanical solution. The choice of steady state versus transient is determined from the input by a default, but a user override is available.
- The FALCON heat transfer correlations for water and the water property models are the same as VIPRE.
- The cladding corrosion program, PFCC, was adapted and incorporated into FALCON.

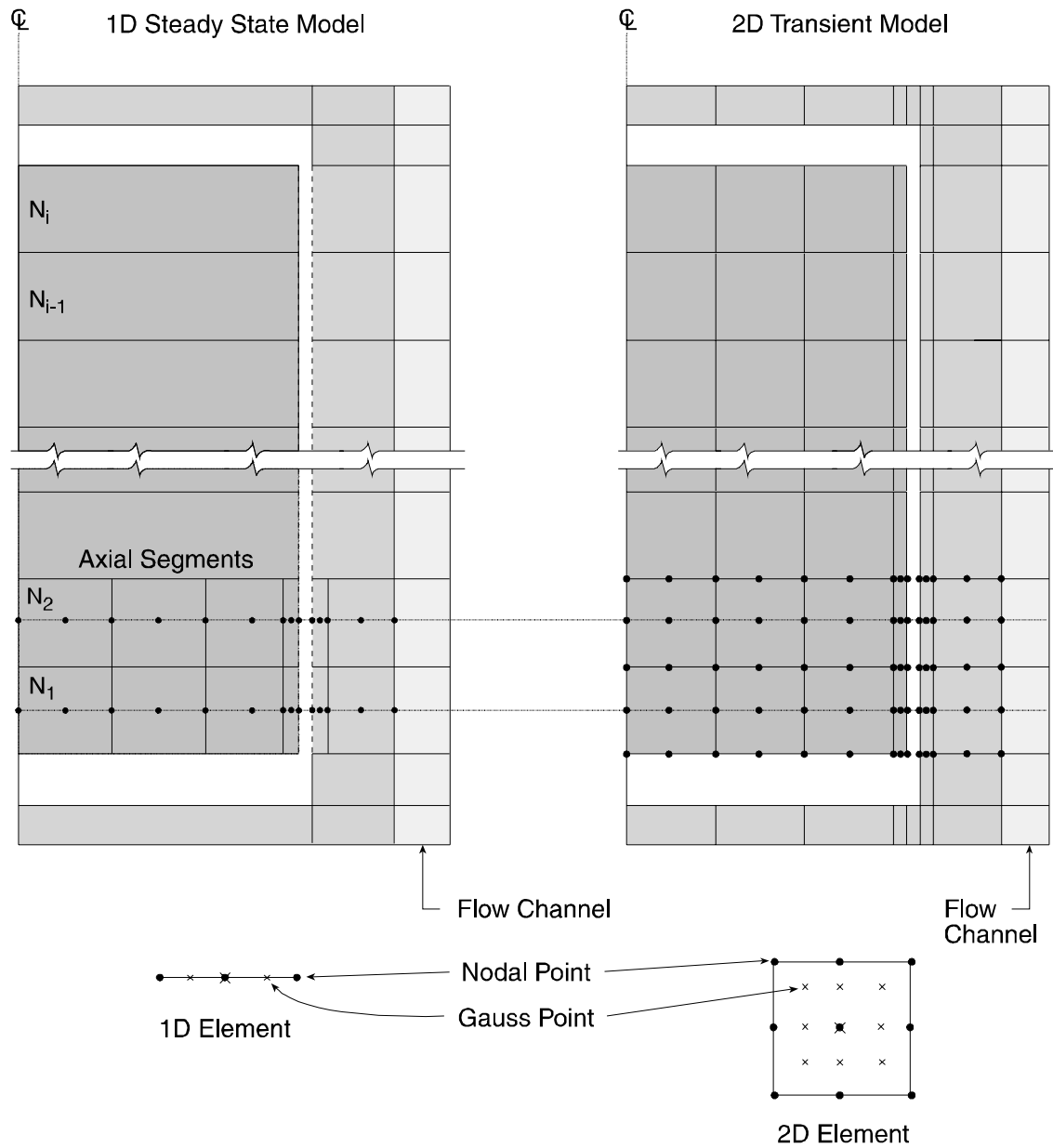


**Figure 1-4**  
**FALCON Steady State and Transient Numerical Models**

*Introduction*

Although FALCON has been specifically developed for the analysis of LWR fuel rods in service, it can be used to solve many problems associated with reactor fuel, such as internally heated rods, BWR channels, and spent fuel. By deactivating the non-applicable input requirements, the knowledgeable user should be able to readily adapt the use of the program to other applications.

FALCON contains appropriate models for the steady state analyses required to define transient initial conditions or in fuel diagnostic evaluations. These models include fission gas release, burnup, fuel cracking and relocation, local gap thickness and conductance, clad and fuel viscoplasticity, fuel hot-pressing, swelling and densification, and pellet-clad interaction (PCI). Because of FALCON's finite element structure, these calculations can be carried out for coupled 1D and 2D full-length rods, short segments, or slices. The geometric models in these analyses consist of R-Z or R- $\theta$  grids, as appropriate, the latter being more suited for PCI analysis. FALCON's PCI analysis capabilities are unique in that it permits the detailed simulation in the R- $\theta$  plane of discrete pellet cracks and pellet-clad interfacial forces. The following is a list of parameters, computed by FALCON, which are generally needed for licensing and fuel performance evaluation[11]:

- Fuel Stored Energy
- Fuel Centerline Temperature
- Fuel Temperature Distribution
- Thermal Margins
- Clad Inner and Outer Surface Temperatures
- Gap Thickness and Conductance Distributions
- Void Volume
- Fission Gas Release Fraction and Composition
- Rod Internal Pressure
- PCI Damage Index
- Outer Surface Oxide Thickness
- Clad Stress Distribution
- Clad Strain Distribution
- Fuel Column and Cladding Axial Growth

Operational transients, which are characterized by small changes in plant variables, and non-LOCA accidents, which include infrequent and limiting fault events, constitute the primary analysis targets for FALCON and thus are well within the range of validity of the material and physical models employed in FALCON. The licensing limits for operational transients are the SAFDLs (Specified Acceptable Fuel Design Limits), which are calculated and output by FALCON. The licensing limits for non-LOCA accidents are peak radially average fuel enthalpy, peak clad temperature, and cladding oxidation. Fuel enthalpy and peak clad temperature are

inherent to the analysis and are printed in the output. Two cladding oxidation models are available to predict high temperature cladding oxidation. The thermal hydraulics model in FALCON allows the code to stand alone without the need for interfacing with system or transient thermal hydraulics programs for problems where closed-channel thermal hydraulics calculations are valid.

The following is a list of parameters calculated by FALCON which are currently needed to evaluate the fuel licensing limits.

- Thermal:
  - Heat Flux
  - Critical Heat Flux Ratio
  - Fuel Enthalpy
  - Fuel Centerline Temperature
  - Cladding Temperatures
- Mechanical:
  - Fission Gas Release
  - Internal Rod Pressure
  - Fuel-Cladding Contact Pressure
  - Cladding Stress
  - Cladding Strain
- Chemical:
  - Cladding Oxidation
  - Cladding Wall Thinning

Transients involving a large-break LOCA are the most limiting applications of FALCON. The program's capabilities in this area are limited to the heatup portion of the LOCA. However, FALCON contains extensive interface capabilities through user input of power, heat transfer coefficients, and bulk temperatures as function of time and axial position, which permits the analysis of a wide range of such transients. A large number of axial nodes can be used, permitting accurate treatment of the strong axial coupling associated with the reflood-quench portion of the LOCA. Also, the R- $\theta$  modeling capability of FALCON makes it possible to analyze the effects of azimuthal variations in temperatures on clad ballooning and rupture.

## 1.4 Purpose

The purpose of this document is to present the theoretical and numerical foundations of FALCON. The mathematical formulation of the governing equations and the physical and material models employed are described in detail. Section 2 gives an introductory description of the finite element method as it pertains to the code. This section should be of special value to readers who are not familiar with finite element analysis. The heat transfer and deformation

*Introduction*

problems are described in detail in Sections 3 and 4. The material and physical models are given in Section 5. The numerical solution procedure is described in Section 6. In order to avoid the cluttering of the main text, derivational details are given in the Appendices.

## 1.5 References

1. Fiero, I. B., et al., "ESCORE-the EPRI Steady-State Core Reload Evaluation Code: General Description," EPRI NP-5100-L-A, April 1991.
2. Rashid, Y. R., Montgomery, R. O., and Zangari, A. J., "FREY-01: Fuel Rod Evaluation System, Volume 1: Theoretical and Numerical Bases," EPRI NP-3277, Revision 3, August 1994.
3. Bremier, S., Walker, C. T., and Manzel, R., "Fission Gas Release and Fuel Swelling at Burnup Higher than 50 MWd/kgU," Proceedings of the OECD/NEA Seminar on Fission Gas Release Behavior in Water Reactor Fuels, Cadarache, France, September 2000.
4. Meyer, R. O., McCardell, R. K., and Scott, H. H., "A Regulatory Assessment of Test Data for Reactivity Accident," Proceedings of the ANS International Topical Meeting on Light Water Reactor Fuel Performance, Portland, Oregon, March 1997.
5. Berna, G. A., et al., "FRAPCON-3: A Computer Code for the Calculation of Steady-State, Thermal-Mechanical Behavior of Oxide Fuel Rods for High Burnup," Pacific Northwest National Laboratory, NUREG/CR-6534, PNNL-11513, December 1997.
6. Cunningham, M. E., et al., "FRAPTRAN: A Computer Code for the Transient Analysis of Oxide Fuel Rods," Pacific Northwest National Laboratory, NUREG/CR-6739, PNNL-13576, August 2001.
7. Chung, H. M., Neimark, L. A., and Kassner, T. F., "Test Plan for High Burnup Fuel Behavior Under Loss-of-Coolant Accident Conditions," Proceedings of the U.S. Nuclear Regulatory Commission, Twenty-Fourth Water Reactor Safety Information Meeting, October 1996, NUREG/CP-0157, January 1997.
8. Burchill, W. E., "Requirements for Analysis of Transient Fuel Rod Behavior during Design Basis Events," EPRI NP-1022, June 1978.
9. Moore, K. V., et al., "RETRAN - A Program for One-Dimensional Transient Thermal-Hydraulic Analysis of Complex Fluid Flow Systems," Volume 1, EPRI CCM-5, December 1978.
10. Stewart, C. W., "VIPRE-01: A Thermal-Hydraulic Code for Reactor Cores, Volume 1: Mathematical Modeling (Revision 2)," NP-2511-CCM, July 1985.
11. "MATPRO - Version 11: A Handbook of Materials Properties for Use in the Analysis of Light Water Reactor Fuel Rod Behavior," NUREG/CR-0497 TREE-1280, February 1979.

# 2

## SPATIAL FINITE ELEMENT MODEL

---

### 2.1 Background

The finite element method has been used for over four decades to solve 2D and 3D initial-boundary value problems in solid mechanics, fluid mechanics and heat transfer. The basic concepts of the finite element method are well documented in many excellent references [1, 2, 3]. The spatial approximations and basic finite element methodology utilized in this report are briefly reviewed in this section and in Appendix A. The reader is assumed to be generally familiar with the finite element method as described in the above cited references.

FALCON solves coupled 1D and 2D plane (R- $\theta$ ) and axisymmetric (R-Z) fuel rod problems, namely the steady state and/or transient heat transfer problems described in Section 3, and the deformation problems described in Section 4. This section describes the basic finite element spatial models used to solve the transient heat transfer and deformation equations. This description is given in general terms in order to lay a foundation for the more detailed derivations given in Sections 3 and 4. Thus, the purpose of this section is to provide a broad overview of the finite element methodology used in FALCON. More detailed derivations are given later.

### 2.2 Element Shape Functions

There are three types of elements available in FALCON: 1D quadratic continuum, 2D bi-linear and bi-quadratic quadrilateral continuum, 2D bi-linear and bi-quadratic triangular continuum, and 1D gap/contact elements. The spatial approximations over the element are expressed as linear combinations of shape functions, which are given below for the three dependent field variables: temperature  $T(x_i, t)$ , horizontal displacement  $U_1(x_i, t)$ , and vertical displacement  $U_2(x_i, t)$ ,

$$T(x_i, t) = \sum_{n=1}^N \hat{\phi}^n(x_i) \theta^n(t) = \sum_{n=1}^N \phi^n(\xi(x_i), \eta(x_i)) \theta^n(t) \quad (\text{eq. 2-1})$$

The geometric relationship between the global coordinates ( $x_i$ ) and local coordinates ( $\xi, \eta$ ) are shown in Figure 2-1.

$$U_j(x_i, t) = \sum_{n=1}^N \hat{\phi}^n(x_i) v_j^n(t) = \sum_{n=1}^N \phi^n(\xi(x_i), \eta(x_i)) v_j^n(t); \quad j = 1, 2 \quad (\text{eq. 2-2})$$

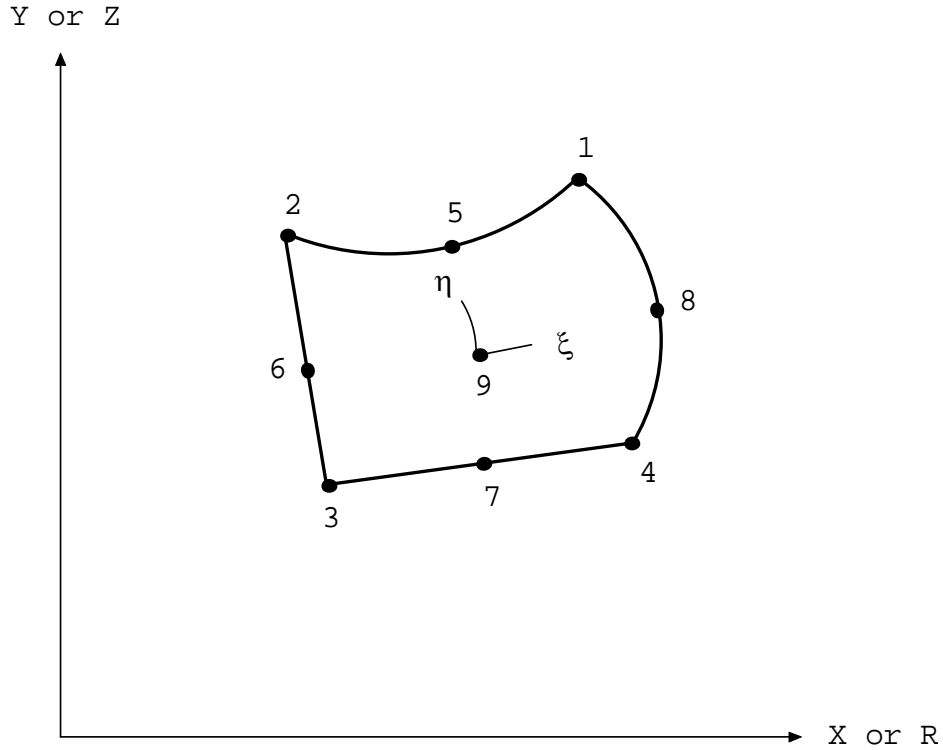


**Figure 2-1**  
**Natural Coordinates for 9-Node Quadrilateral Elements**

A sample of the shape functions,  $\phi^n(\xi, \eta)$ , is given below for the elements shown in Figure 2-2.

9-Node

$$\phi^1(\xi, \eta) = \frac{1}{4}(1+\xi)(1+\eta) - \frac{1}{2} \left[ \frac{1}{2}(1-\xi^2)(1+\eta) + \frac{1}{2}(1+\xi)(1-\eta^2) \right]$$

$$\phi^2(\xi, \eta) = \frac{1}{4}(1-\xi)(1+\eta) - \frac{1}{2} \left[ \frac{1}{2}(1-\xi^2)(1+\eta) + \frac{1}{2}(1-\xi)(1-\eta^2) \right]$$

$\vdots$

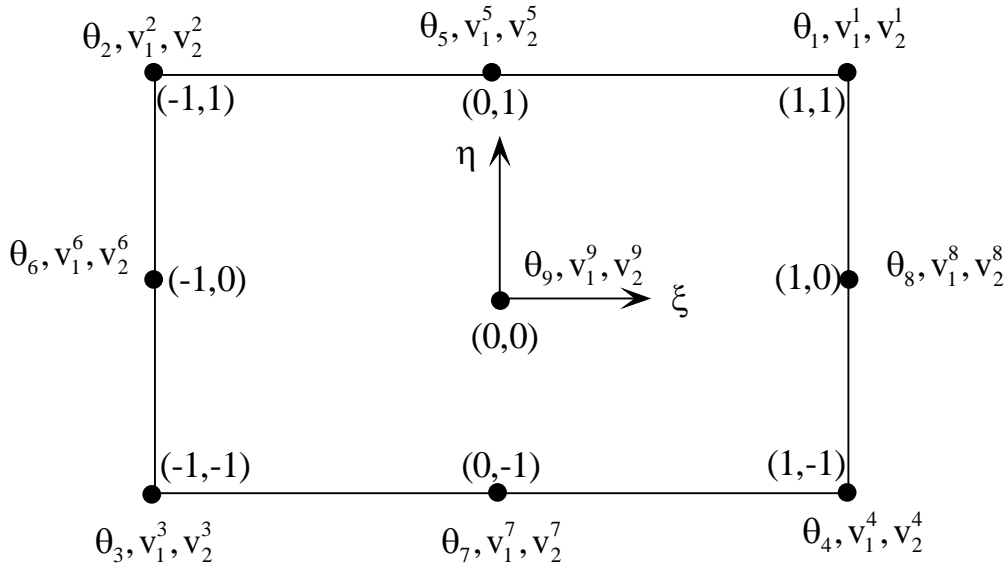
2-Node

$$\phi^1(\xi) = \frac{1}{2}(1+\xi)$$

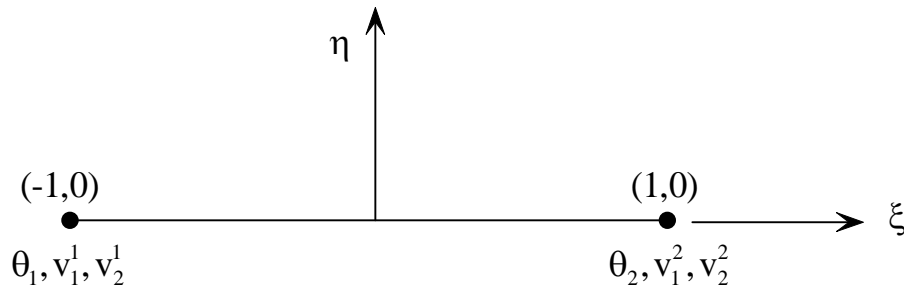
$$\phi^2(\xi) = \frac{1}{2}(1-\xi)$$



As can be observed from these equations, the field variable in the 9-node element is approximated in the continuum element as a quadratic function, thus providing second order accuracy. The remaining finite element spatial equations are given in Appendix A.



N = 9: Fuel/Clad Element



N = 2: Gap/Plenum/Contact Element

**Figure 2-2**  
**Element Shapes and Nodal Variables**

## **2.3 References**

1. Zienkiewicz, O. C., *The Finite Element Method in Engineering Science*, McGraw-Hill, London, 1971.
2. Desai, C. S. and Abel, J. F., *Introduction to the Finite Element Method*, Van Nostrand Reinhold Company, New York, 1972.
3. Gallagher, R. H., *Finite Element Analysis Fundamentals*, Prentice-Hall, New Jersey, 1975.

# 3

## HEAT TRANSFER

---

The fuel rod with its geometric regions, i.e., fuel, gap and clad, is treated as a continuum that is numerically represented in finite element form. The temperatures are calculated at the nodal points from conditions specified for the elements and their boundaries. The sizes, shapes and types of the elements are selected to suit the accuracy requirements and the physical and material characteristics of each region. For example, the fuel and the clad are represented by 9-node elements in which the spatial variation of temperature is a quadratic function. On the other hand, the gap is represented by 2-node elements with linear temperature variation since the heat transfer in this region is governed primarily by a single quantity, namely, the gap conductance. The material properties, namely, fuel and clad conductivities, specific heat and density are, in general, temperature and burnup dependent. A description of the properties models used in FALCON is contained in Section 5. The pellet-cladding gap conductance is calculated using the modified Ross and Stoute model for open gap conditions and the Mikic-Todreas model for solid-solid contact conductance. The fuel rod surface heat transfer is characterized by two time-dependent quantities: the coolant temperature and the heat transfer coefficient. The latter can be either user-specified or alternatively calculated using a closed-channel thermal hydraulics model. Heat generation in the fuel rod includes fission power, decay of fission products, gamma heating, and heat of oxidation.

The governing equations of the overall system are formulated in terms of the nodal temperatures as the primary unknowns. This system is piece-wise linear in time and is solved implicitly with provisions for iteration within each step and/or sub-division of the time steps into smaller substeps. Description of the various thermal models is given in this chapter.

### 3.1 Heat Conduction

The development of the finite element equations for transient heat conduction problems is well documented [1, 2] and will only be briefly reviewed here. The present formulation is restricted to two-dimensional geometries either plane (R- $\theta$ ) or axisymmetric (R-Z). To simplify the derivation of the equations in the following sections, only the 2D plane problem will be treated in detail. Derivation of the axisymmetric equations follow in a straightforward manner.

#### 3.1.1 Basic Equations

The appropriate mathematical description of the heat conduction process in a material region  $\Omega$  is given by

$$\rho C_p \frac{\partial T}{\partial t} - \frac{\partial}{\partial x_i} \left( k_{ij} \frac{\partial T}{\partial x_j} \right) - Q = 0 \quad (\text{eq. 3-1})$$

where  $\rho$  is the material density,  $C_p$  the heat capacity,  $k_{ij}$  the conductivity tensor,  $Q$  the volumetric heat source,  $t$  the time,  $x_i$  the spatial coordinates, and  $T$  the temperature. For the present work, each material is assumed to be homogeneous and either isotropic ( $k_{ij} = K\delta_{ij}$ ) or orthotropic, where  $k_{ij}$  is a diagonal tensor written in terms of the principal material directions. The material properties are functions of temperature; the heat source  $Q$  depends on both time and space.

The boundary of the region  $\Omega$  is defined by  $\Gamma = \Gamma_T + \Gamma_q$ , where  $\Gamma_T$  and  $\Gamma_q$  are parts of the boundary for which the temperature and heat flux are specified. The relevant boundary conditions for eq. 3-1 may then be expressed by

$$T = T_b \quad \text{on} \quad \Gamma_T \quad (\text{eq. 3-2})$$

and

$$q_i n_i + \left( k_{ij} \frac{\partial T}{\partial x_j} \right) n_i + q_c + q_r = 0 \quad \text{on} \quad \Gamma_q \quad (\text{eq. 3-3})$$

where  $T_b$  is an applied boundary temperature,  $q_i$  is the applied heat flux vector,  $n_i$  the unit outward normal to the boundary  $\Gamma_q$ ,  $q_c$  the heat flux due to convection, and  $q_r$  the heat flux due to radiation. Typically, the convective and radiative heat fluxes are given by

$$q_c = h_c (T - T_c) \quad (\text{eq. 3-4})$$

$$q_r = h_r (T - T_r) \quad (\text{eq. 3-5})$$

where  $h_c$  and  $h_r$  are convective and radiative heat transfer coefficients, and  $T_c$  and  $T_r$  are the coolant temperature or inner surface cladding temperature depending on the location. The radiation coefficient is given by

$$h_r = \varepsilon \sigma (T^2 + T_r^2) (T + T_r) \quad (\text{eq. 3-6})$$

in which  $\varepsilon$  is the emissivity,  $\sigma$  is the Stefan-Boltzmann constant, and  $T$  and  $T_r$  are the absolute temperature at a given point and the absolute environment temperature, respectively. Note that the boundary conditions given in equations 3-2 and 3-3 are functions of time.

Equations 3-1 through 3-6 provide a complete description of the boundary value problem for the temperature,  $T$ . When considering the transient heat conduction problem, a suitable set of initial conditions describing the initial spatial distribution of  $T$  is also required.

### 3.1.2 Finite Element Equations

The spatial discretization of the above boundary value problem by use of finite elements may be approached by either of two methods. Historically, the first and most popular approach consists of rewriting the boundary value problem in a variational form [2] for use with the finite element approximation. An equivalent method uses the Galerkin form of the method of weighted residuals [3] to create an integral form of the basic conservation law. This latter method is employed here.

Let the region of interest,  $\Omega$ , be divided into a number of finite elements as shown in Figure 3-1. In the context of FALCON, the region  $\Omega$  refers to fuel, clad, gap or plenum. Each of these regions is represented by finite element types of appropriate shape and nodalization. Within each element, a set of nodal points are established at which the dependent variable (i.e.,  $T$ ) is evaluated. For purposes of developing the equations for these nodal point unknowns, an individual element may be separated from the assembled system.

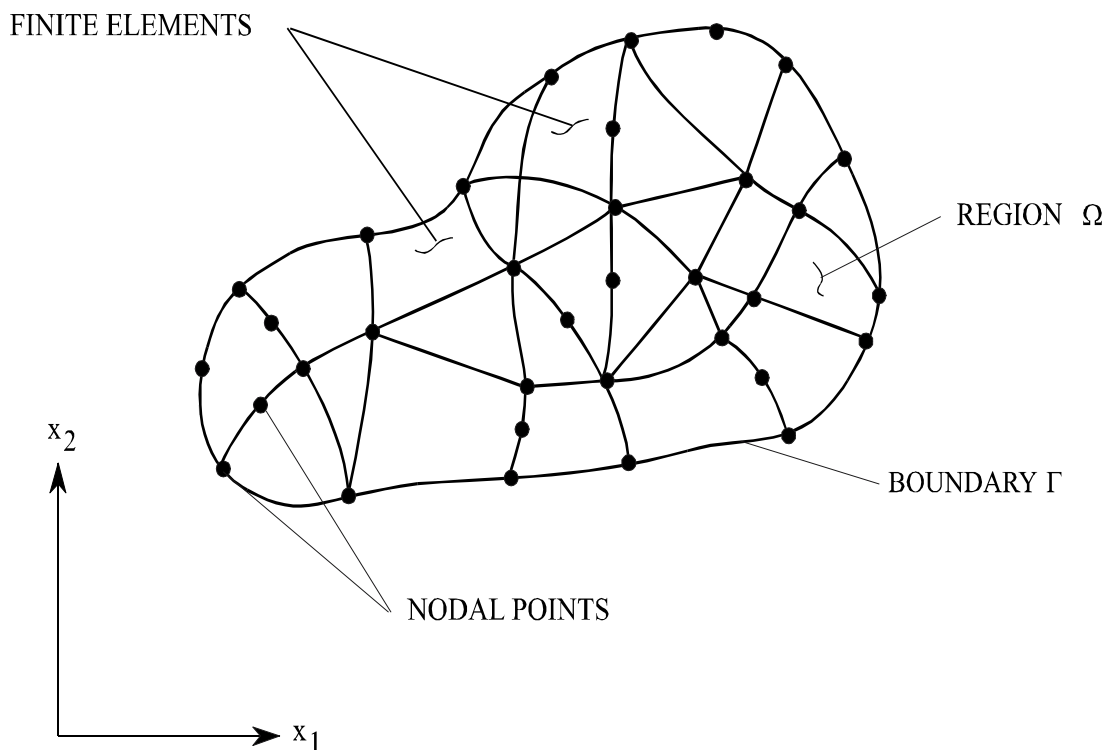


**Figure 3-1**  
**Finite Element Idealization of a Region**

Within each finite element the temperature field is approximated by

$$T(x_i, t) = \sum_{n=1}^N \hat{\phi}^n(x_i) \theta_n(t) = \sum_{n=1}^N \phi_n(\xi(x_i), \eta(x_i)) \theta_n(t) \quad (\text{eq. 3-7})$$

in which the shape functions  $\phi_n(\xi, \eta)$  are quadratic in the parametric coordinates,  $\xi$  and  $\eta$ , as given earlier in Section 2.

In matrix notation, eq. 3-7 becomes

$$T(x_i, t) = \hat{\phi}^T(x_i) \theta(t) \quad (\text{eq. 3-8})$$

In eq. 3-7,  $\phi_n$  is an  $N$  dimensional vector of interpolation (shape) function,  $\theta_n$  is a vector of nodal point temperature unknowns, superscript  $T$  denotes a vector transpose, and  $N$  is the number of nodal points in an element. Substitution of eq. 3-7 into the partial differential eq. 3-1 and boundary conditions eq. 3-3 yields a set of residual equations, due to the approximate nature of eq. 3-7. The Galerkin method guarantees the orthogonality of the residual vectors to the space spanned by the interpolation functions. This orthogonality is expressed by the inner product,

$$\langle \hat{\phi}, R \rangle = \int_{\Omega_e} \hat{\phi} R d\Omega = 0 \quad (\text{eq. 3-9})$$

where  $R$  is the residual for the differential equation, and  $\Omega_e$  is the region enclosed by the element.

Carrying out the above operations explicitly for equations 3-1, 3-3 and 3-8 yields

$$\begin{aligned} \int_{\Omega_e} \hat{\phi} \left\{ \rho C_p \hat{\phi}^T \frac{\partial \theta}{\partial t} - \frac{\partial}{\partial x_j} \left( k_{ij} \frac{\partial \hat{\phi}^T}{\partial x_j} \theta \right) - Q \right\} d\Omega \\ + \int_{\Gamma_e} \hat{\phi} \left\{ q_i n_i + \left( k_{ij} \frac{\partial \hat{\phi}^T}{\partial x_j} \theta \right) n_i + q_c + q_r \right\} d\Gamma = 0 \end{aligned} \quad (\text{eq. 3-10})$$

Equation 3-10 may be rewritten using Green's theorem to give the equation:

$$\begin{aligned} \int_{\Omega_e} \rho C_p \hat{\phi} \hat{\phi}^T \frac{\partial \theta}{\partial t} d\Omega + \int_{\Omega_e} \frac{\partial \hat{\phi}}{\partial x_i} k_{ij} \frac{\partial \hat{\phi}^T}{\partial x_j} \theta d\Omega \\ = \int_{\Omega_e} \hat{\phi} Q d\Omega - \int_{\Gamma_e} \hat{\phi} \{ q_i n_i + q_c + q_r \} d\Gamma \end{aligned} \quad (\text{eq. 3-11})$$

Once the form of the interpolation functions,  $\phi$ , is specified for an element, the integrals in eq. 3-11 may be evaluated. Such an evaluation leads to a matrix equation for each element of the following form,

$$\underset{\approx}{M} \underset{\approx}{\dot{\theta}} + \underset{\approx}{K} \underset{\approx}{\theta} = \underset{\approx}{F_Q} + \underset{\approx}{F} \quad (\text{eq. 3-12})$$

where

$$\underset{\approx}{M} = \int_{\Omega_e} \rho C_p \underset{\approx}{\phi} \underset{\approx}{\phi}^T d\Omega$$

$$\underset{\approx}{K} = \int_{\Omega_e} \frac{\partial \underset{\approx}{\phi}}{\partial x_i} k_{ij} \frac{\partial \underset{\approx}{\phi}^T}{\partial x_j} d\Omega$$

$$\underset{\approx}{F_Q} = \int_{\Omega_e} \underset{\approx}{\phi} Q d\Omega$$

$$\underset{\approx}{F} = \int_{\Gamma_e} \underset{\approx}{\phi} \{q_n + q_c + q_r\} d\Gamma$$

The previous discussion was directed toward the derivation of the equations for a single element. The finite element model for the entire region  $\Omega$  is obtained through assembly of the element matrices by imposing appropriate inter-element continuity requirements on the dependent variable. Such an assembly yields a matrix equation of the form given in eq. 3-12.

### 3.1.3 Boundary Conditions

As noted previously, boundary conditions for heat conduction problems may be of several types. The discrete form of a specified temperature condition is straightforward. For a temperature specified at a nodal point, the equation for that nodal point is replaced by a constraint condition enforcing the boundary value. This type of boundary condition, however, is not usually utilized in fuel rod analysis. More appropriate for the present development is the specification of boundary conditions in terms of various heat fluxes. In eq. 3-11, the boundary fluxes to an element appear in the vector  $\underset{\approx}{F}$  as an integral taken along the element boundary (only element

boundaries coinciding with  $\Gamma$  need be considered as contributions from interior boundaries are cancelled by adjoining elements). In order to understand the procedure for computation of these boundary integrals reference must be made to Figure 3-2 which shows a typical finite element boundary. Considering first the case of an applied normal heat flux to the element, the contribution to  $\underset{\approx}{F}$  is expressed by:

$$\tilde{F}_n = - \int_{\Gamma_e} \phi q_n d\Gamma \quad (\text{eq. 3-13})$$

where  $\phi$  is restricted to the boundary. If the coordinate along the boundary is  $s$ , then

$$d\Gamma = \left[ \left( \frac{\partial x_1}{\partial s} \right)^2 + \left( \frac{\partial x_2}{\partial s} \right)^2 \right]^{1/2} ds = \Delta ds$$

and eq. 3-13 becomes

$$\tilde{F}_n = - \int_{-1}^1 \phi(s) q_n \left[ \left( \frac{\partial x_1}{\partial s} \right)^2 + \left( \frac{\partial x_2}{\partial s} \right)^2 \right]^{1/2} ds \quad (\text{eq. 3-14})$$

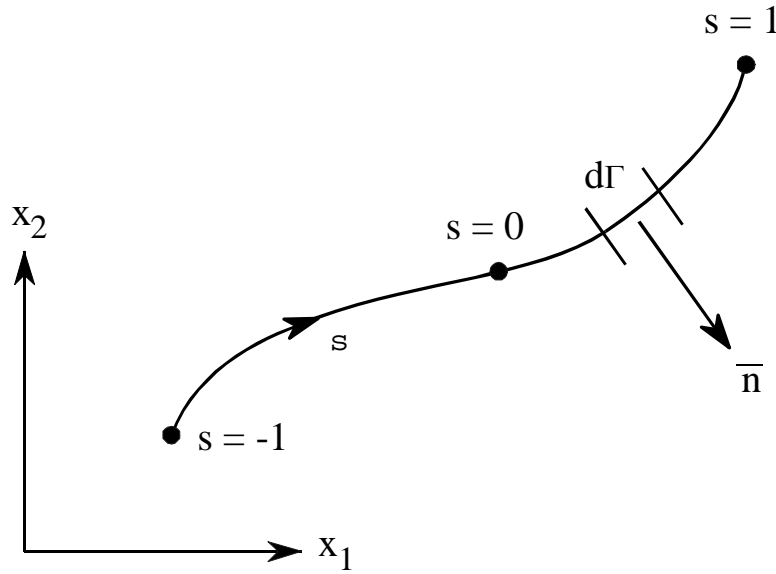


**Figure 3-2**  
**Finite Element Idealization of a Boundary**

Once the distribution of  $q_n$  along the boundary and the shape of the element boundary  $x_i(s)$  are known the computation in eq. 3-14 is straightforward.

The contribution to  $\tilde{F}$  due to convection is

$$\tilde{F}_n = - \int_{\Gamma_e} \phi q_c d\Gamma = \int_{\Gamma_e} \phi h_c (T - T_c) d\Gamma \quad (\text{eq. 3-15})$$



where the definition in eq. 3-4 was employed. The temperature along the element boundary is given by

$$T(s) = \underset{\sim}{\phi}^T \underset{\sim}{\theta}$$

where again  $\phi$  is a boundary or edge function. Using the previous relation for  $d\Gamma$ , eq. 3-15 becomes

$$\underset{\sim}{F}_c = \int_{-1}^1 h_c \underset{\sim}{\phi} \underset{\sim}{\phi}^T \Delta ds \underset{\sim}{\theta} - \int_{-1}^1 h_c \underset{\sim}{\phi} T_c \Delta ds$$

or

$$\underset{\sim}{F}_c = - \underset{\sim}{C} \underset{\sim}{\theta} + \underset{\sim}{F}_{hc} \quad (\text{eq. 3-16})$$

where

$$\underset{\sim}{C} = - \int_{-1}^1 h_c \underset{\sim}{\phi} \underset{\sim}{\phi}^T \Delta ds$$

$$\underset{\sim}{F}_{hc} = - \int_{-1}^1 h_c \underset{\sim}{\phi} T_c \Delta ds$$

Note, in eq. 3-16, the term  $\underset{\sim}{C} \underset{\sim}{\theta}$  contains unknown nodal point temperatures and will thus be moved to the left hand side of the matrix equation in eq. 3-12.

A computation similar to the one above may be carried out for the radiative flux boundary condition to yield

$$\underset{\sim}{F}_r = - \underset{\sim}{R} \underset{\sim}{\theta} + \underset{\sim}{F}_{hr} \quad (\text{eq. 3-17})$$

where

$$\underset{\sim}{R} = - \int_{-1}^1 h_r \underset{\sim}{\phi} \underset{\sim}{\phi}^T \Delta ds$$

$$\underset{\sim}{F}_{hr} = - \int_{-1}^1 h_r \underset{\sim}{\phi} T_r \Delta ds$$

## Heat Transfer

Again, the  $\tilde{R} \tilde{\theta}$  term will be moved to the left-hand side of eq. 3-12, while  $\tilde{F}_{hr}$  is retained on the right-hand side. In eq. 3-17, both  $\tilde{R}$  and  $\tilde{F}_{hr}$  are functions of  $\tilde{\theta}$  since the radiative heat transfer coefficient,  $h_r$  (eq. 3-6), is a function of temperature.

To summarize the modifications to the basic matrix equation (eq. 3-11) due to the application of flux type boundary conditions, equations 3-14, 3-16 and 3-17, may be substituted into eq. 3-12 to yield,

$$\tilde{M} \dot{\tilde{\theta}} + \tilde{K} \tilde{\theta} = \tilde{F}_Q + \tilde{F}_n - \tilde{C} \tilde{\theta} + \tilde{F}_{hc} - \tilde{R} \tilde{\theta} + \tilde{F}_{hr} \quad (\text{eq. 3-18})$$

Rearranging eq. 3-18 allows the final form of the discrete equation to be written as:

$$\tilde{M} \dot{\tilde{\theta}} + \tilde{K}^* \tilde{\theta} = \tilde{F}^* \quad (\text{eq. 3-19})$$

with

$$\tilde{K}^* = \tilde{K} + \tilde{C} + \tilde{R} \quad (\text{eq. 3-20})$$

$$\tilde{F}^* = \tilde{F}_Q + \tilde{F}_n + \tilde{F}_{hc} + \tilde{F}_{hr} \quad (\text{eq. 3-21})$$

In the present context,  $\tilde{M}$ ,  $\tilde{K}^*$  and  $\tilde{F}^*$  are all functions of  $\tilde{\theta}$ ;  $\tilde{K}^*$  and  $\tilde{F}^*$  are time dependent.

## 3.2 Power Generation

FALCON considers heat generation in the pellet, cladding, and coolant when calculating the fuel rod temperature distribution. The sources of heat generation included in FALCON are fission heat in the pellet, gamma heating in the cladding and coolant, decay heat, and heat of oxidation of the cladding. Each of these will be described in the following subsections.

### 3.2.1 Fission Heat Generation

The volumetric heat generation rate is calculated at several spatial positions (integration points) in the fuel, cladding, and coolant elements from the rod average linear power, axial power profile and radial power distribution. From conservation of heat in steady state operation, the volumetric heat generation rate in the pellet from the fission process is given by;

$$\dot{Q}_f(t) = \frac{P(t)}{0.25 \pi D_p^2 (1 - a^2)} f(\alpha, t) g(z, t) (1 - h_{\text{gamma}}) \quad (3-22)$$

where

$\dot{Q}_f(t)$ : Volumetric heat generation rate from fission heating in pellet (W/m<sup>3</sup>)

$P(t)$ : Rod average linear power (W/m)

$a$ :  $D_{pi}/D_p$

$D_{pi}$ : Pellet inner diameter ( $\neq 0$  for hollow pellets) (m)

$D_p$ : Pellet diameter (m)

$f(\alpha, t)$ : Dimensionless normalized radial power distribution

$\alpha$ : Dimensionless radial position =  $2r/D$ , where  $r$  is the radial coordinate of the integration point  $p$

$g(z, t)$ : Dimensionless axial power profile as function of the axial position  $z$  and time  $t$  (input)

$h_{\text{gamma}}$ : Fraction of fuel rod power deposited into the cladding and coolant ( $F_{\text{clad}} + F_{\text{coolant}}$ )

The axial power profile is time-dependent and is treated by FALCON as user input. Three options exist for the determination of the radial power profile: defined by user input, calculated internally using the RADAR-G model [4], or the TUBRNP model [5]. Both of the radial power profile models are described in Appendix E.

A certain fraction of the energy produced by fissions is not deposited in the fuel, but passes into the cladding and the coolant. This energy is normally carried away by the gamma radiation produced during the fission process. As a result, a heat generation term is required for both the cladding and the coolant. This fraction is normally expressed in terms of a percentage of the total fuel rod power. The parameter for the cladding and coolant are treated as user input. The radially uniform volumetric heat generation rate for the cladding is given by

$$\dot{Q}_{\text{clad}}^{\text{gamma}}(t) = \frac{P(t)}{0.25 \pi (D_{\text{co}}^2 - D_{\text{ci}}^2)} g(z, t) F_{\text{clad}} \quad (\text{eq. 3-22a})$$

where

$\dot{Q}_{\text{clad}}^{\text{gamma}}(t)$ : Volumetric heat generation rate from gamma heating in the cladding (W/m<sup>3</sup>)

$D_{\text{co}}$ : Outer cladding diameter

$D_{\text{ci}}$ : Inner cladding diameter

$F_{\text{clad}}$ : Fraction of fuel rod power deposited in the cladding

The volumetric heat generation rate for the coolant is given by

$$\dot{Q}_{\text{coolant}}^{\text{gamma}}(t) = \frac{P(t)}{F_a} g(z, t) F_{\text{coolant}} \quad (\text{eq. 3-22b})$$

where

$\dot{Q}_{\text{coolant}}^{\text{gamma}}(t)$ : Volumetric heat generation rate from gamma heating in the coolant (W/m<sup>3</sup>)

$F_a$ : Coolant channel flow area;  $F_a$  depends on the channel geometry

$F_{\text{coolant}}$ : Fraction of fuel rod power deposited in the coolant

### 3.2.2 Decay Heat

The heat generation due to the radioactive decay of fission products is calculated using the methods described in the 1979 ANS-5.1 Standard [6]. The fission-product decay heat is determined for the thermal fission of <sup>235</sup>U and <sup>239</sup>Pu and fast fission of <sup>238</sup>U as a function of time following shutdown and prior reactor operating conditions. The methods do not consider the decay heat power from other actinide or activation products. In addition, neutron capture by the fission products is not included in the methods. Two types of prior reactor operating periods are considered in the model: (a) constant power, infinite operation ( $T > 10^{13}$  seconds) to establish equilibrium conditions; and (b) variable power, non-equilibrium operation. The total decay heat power is composed of the fission product decay from the three most common fissionable nuclides in an LWR environment. The total decay heat power is given by

$$P_d(t, T) = \sum_{i=1}^3 P_{di}(t, T) \quad (\text{eq. 3-23a})$$

where  $P_{di}$  is the contribution from <sup>235</sup>U, <sup>239</sup>Pu and <sup>238</sup>U,  $t$  is the time after shutdown, and  $T$  is the prior operating time. The fission product decay heat for each individual nuclide is determined for an infinitely long production time ( $T > 10^{13}$  seconds) at a constant rate by

$$F_i(t, \infty) = \sum_{j=1}^{23} \frac{\alpha_{ij}}{\lambda_{ij}} e^{-\lambda_{ij} t} \quad (\text{eq. 3-23b})$$

where  $F_i(t, \infty)$  is the fission product decay heat for nuclide  $i$ , and  $\alpha_{ij}$  and  $\lambda_{ij}$  are a fitting coefficient and the decay constant respectively for the  $j^{\text{th}}$  group of fission products for nuclide  $i$ . Using the total recoverable energy per fission for nuclide  $i$ ,  $Q_i$ , and the power produced by nuclide  $i$  during the production time,  $\gamma_i$ , the contribution to the total decay heat  $P_{di}(t, \infty)$  is

$$P_{di}(t, \infty) = \frac{\gamma_i}{Q_i} F_i(t, \infty) \quad (\text{eq. 3-23c})$$

The decay power resulting from eq. 3-23c is for a constant production rate (power) over an infinitely long operating time (i.e., equilibrium conditions). The decay heat power for equilibrium conditions requires a single value for constant power and the fraction of that power produced from fissioning of nuclide  $i$ .

Normal operating conditions do not satisfy the equilibrium operation criterion ( $T > 10^{13}$ ); therefore, a non-equilibrium approach must be used to properly calculate the decay heat. For a power history which can be represented by a series of constant power intervals, the decay heat contribution from nuclide  $i$  is given by

$$P_{di}(t, T) = \sum_{\alpha=1}^N \frac{\gamma_{i\alpha} F_i(t_{\alpha}, T_{\alpha})}{Q_i} \quad (\text{eq. 3-23d})$$

where  $N$  is the number of time intervals with constant power,  $\gamma_{i\alpha}$  is the power produced by nuclide  $i$  during interval  $\alpha$ , and

$$F_i(t_{\alpha}, T_{\alpha}) = F_i(t_{\alpha}, \infty) - F_i(t_{\alpha} + T_{\alpha}, \infty) \quad (\text{eq. 3-23e})$$

where

$$t_{\alpha} = t + \sum_{\alpha=1}^{N-1} T_{\alpha} \quad (\text{eq. 3-23f})$$

and

$$T = t + \sum_{\alpha=1}^N T_{\alpha} \quad (\text{eq. 3-23g})$$

An example of a power history representation appropriate for use with eq. 3-23d through eq. 3-23g is shown in Figure 3-3. The procedure described above results in the application of the 1979 ANS-5.1 method for decay heat to non-equilibrium reactor operation. The fitting

## Heat Transfer

coefficients and decay constants for each fissionable nuclide is presented in Tables 3-1 through 3-3. The spatial variation of the power throughout the fuel rod is accomplished by assuming that the axial power shape for decay heat production follows the axial power shape prior to reactor shutdown. The radial power profile is assumed to be uniform. This approach provides an approximate power spatial variation within the fuel rod for use in FALCON.

**Table 3-1**  
**Parameters for  $^{235}\text{U}$  Thermal Fissions**

$\alpha$	$\lambda$
$6.5057 \times 10^{-1}$	$2.2138 \times 10^{-1}$
$5.1264 \times 10^{-1}$	$5.1587 \times 10^{-1}$
$2.4384 \times 10^{-1}$	$1.9594 \times 10^{-1}$
$1.3850 \times 10^{-1}$	$1.0314 \times 10^{-1}$
$5.5440 \times 10^{-2}$	$3.3656 \times 10^{-2}$
$2.2225 \times 10^{-2}$	$1.1681 \times 10^{-2}$
$3.3088 \times 10^{-3}$	$3.5870 \times 10^{-3}$
$9.3015 \times 10^{-4}$	$1.3930 \times 10^{-3}$
$8.0943 \times 10^{-4}$	$6.2630 \times 10^{-4}$
$1.9567 \times 10^{-4}$	$1.8906 \times 10^{-4}$
$3.2535 \times 10^{-5}$	$5.4988 \times 10^{-5}$
$7.5595 \times 10^{-6}$	$2.0958 \times 10^{-5}$

$\alpha$	$\lambda$
$2.5232 \times 10^{-6}$	$1.0010 \times 10^{-5}$
$4.9948 \times 10^{-7}$	$2.5438 \times 10^{-6}$
$1.8531 \times 10^{-7}$	$6.6361 \times 10^{-7}$
$2.6608 \times 10^{-8}$	$1.2290 \times 10^{-7}$
$2.2398 \times 10^{-9}$	$2.7213 \times 10^{-8}$
$8.1641 \times 10^{-12}$	$4.3714 \times 10^{-9}$
$8.7797 \times 10^{-11}$	$7.5780 \times 10^{-10}$
$2.5131 \times 10^{-14}$	$2.4786 \times 10^{-10}$
$3.2176 \times 10^{-16}$	$2.2384 \times 10^{-13}$
$4.5038 \times 10^{-17}$	$2.4600 \times 10^{-14}$
$7.4791 \times 10^{-17}$	$1.5699 \times 10^{-14}$

**Table 3-2**  
**Parameters for  $^{239}\text{Pu}$  Thermal Fissions**

$\alpha$	$\lambda$
$2.083 \times 10^{-1}$	$1.002 \times 10^1$
$3.853 \times 10^{-1}$	$6.433 \times 10^{-1}$
$2.213 \times 10^{-1}$	$2.186 \times 10^{-1}$
$9.460 \times 10^{-2}$	$1.004 \times 10^{-1}$
$3.531 \times 10^{-2}$	$3.728 \times 10^{-2}$
$2.292 \times 10^{-2}$	$1.435 \times 10^{-2}$
$3.946 \times 10^{-3}$	$4.549 \times 10^{-3}$
$1.317 \times 10^{-3}$	$1.328 \times 10^{-3}$
$7.052 \times 10^{-4}$	$5.356 \times 10^{-4}$
$1.432 \times 10^{-4}$	$1.730 \times 10^{-4}$
$1.765 \times 10^{-5}$	$4.881 \times 10^{-5}$
$7.347 \times 10^{-6}$	$2.006 \times 10^{-5}$

$\alpha$	$\lambda$
$1.747 \times 10^{-6}$	$8.319 \times 10^{-6}$
$5.481 \times 10^{-7}$	$2.358 \times 10^{-6}$
$1.671 \times 10^{-7}$	$6.450 \times 10^{-7}$
$2.112 \times 10^{-8}$	$1.278 \times 10^{-7}$
$2.996 \times 10^{-9}$	$2.466 \times 10^{-8}$
$5.107 \times 10^{-11}$	$9.378 \times 10^{-9}$
$5.730 \times 10^{-11}$	$7.450 \times 10^{-10}$
$4.138 \times 10^{-14}$	$2.426 \times 10^{-10}$
$1.088 \times 10^{-15}$	$2.210 \times 10^{-13}$
$2.454 \times 10^{-17}$	$2.640 \times 10^{-14}$
$7.557 \times 10^{-17}$	$1.380 \times 10^{-14}$

**Table 3-3**  
Parameters for  $^{238}\text{U}$  Fast Fissions

$\alpha$	$\lambda$
1.2311	3.2881
1.1486	$9.3805 \times 10^{-1}$
$7.0701 \times 10^{-1}$	$3.7073 \times 10^{-1}$
$2.5209 \times 10^{-1}$	$1.1118 \times 10^{-1}$
$7.1870 \times 10^{-2}$	$3.6143 \times 10^{-2}$
$2.8291 \times 10^{-2}$	$1.3272 \times 10^{-2}$
$6.8382 \times 10^{-3}$	$5.0133 \times 10^{-3}$
$1.2322 \times 10^{-3}$	$1.3655 \times 10^{-3}$
$6.8409 \times 10^{-4}$	$5.5158 \times 10^{-4}$
$1.6975 \times 10^{-4}$	$1.7873 \times 10^{-4}$
$2.4182 \times 10^{-5}$	$4.9032 \times 10^{-5}$
$6.6356 \times 10^{-6}$	$1.7058 \times 10^{-5}$

$\alpha$	$\lambda$
$1.0075 \times 10^{-6}$	$7.0465 \times 10^{-6}$
$4.9894 \times 10^{-7}$	$2.3190 \times 10^{-6}$
$1.6352 \times 10^{-7}$	$6.4480 \times 10^{-7}$
$2.3355 \times 10^{-8}$	$1.2649 \times 10^{-7}$
$2.8094 \times 10^{-9}$	$2.5548 \times 10^{-8}$
$3.6236 \times 10^{-11}$	$8.4782 \times 10^{-9}$
$6.4577 \times 10^{-11}$	$7.5130 \times 10^{-10}$
$4.4963 \times 10^{-14}$	$2.4188 \times 10^{-10}$
$3.6654 \times 10^{-16}$	$2.2739 \times 10^{-13}$
$5.6293 \times 10^{-17}$	$9.0536 \times 10^{-14}$
$7.1602 \times 10^{-17}$	$5.6098 \times 10^{-15}$

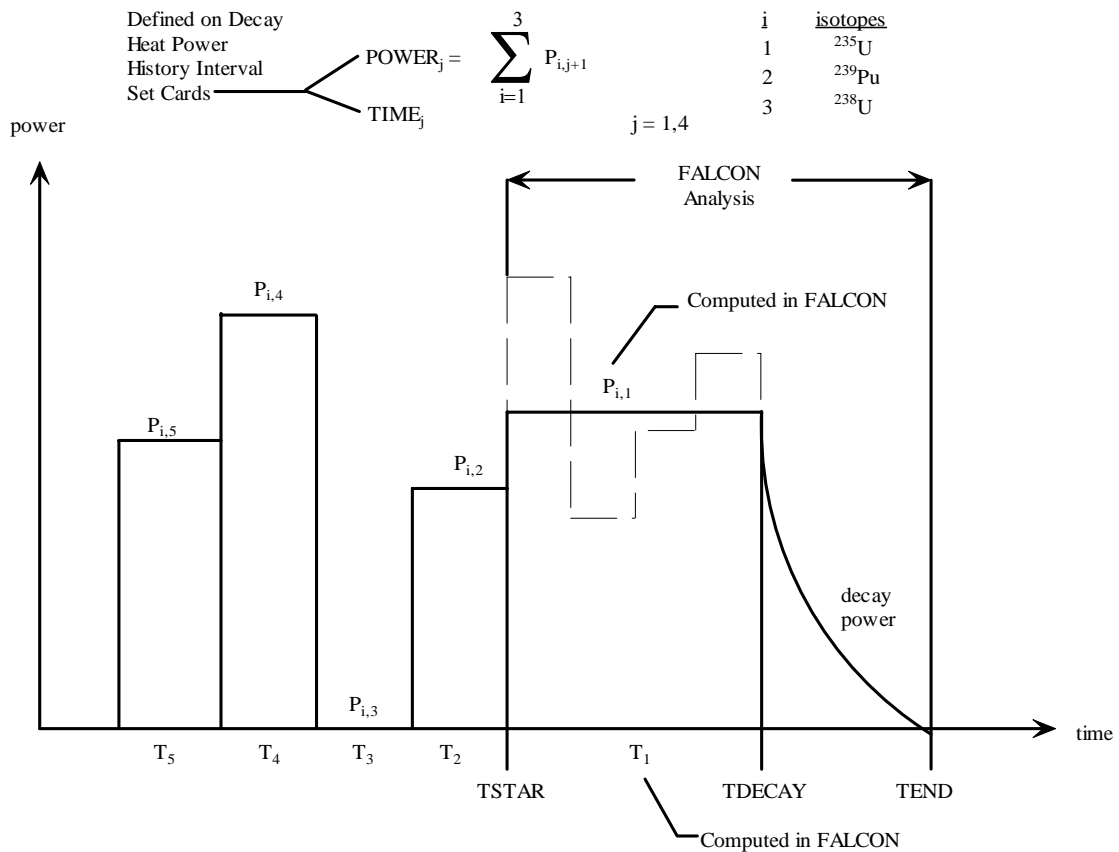


**Figure 3-3**  
Example of a Power History Representation Used in the Decay Heat Model

### 3.2.3 Heat of Oxidation

The linear heat generation in the clad due to the conversion of zirconium to  $\text{ZrO}_2$  is calculated using the results from the high temperature oxidation model according to the following formula:

$$\dot{Q}_0(t) = \frac{2\pi}{3} D_{R0} \rho_Z h_r \Delta Z_0 / \Delta t \quad (\text{eq. 3-24})$$

where

$\dot{Q}_0(t)$ : Linear heat generation rate from oxidation (W/m)

$D_{R0}$ : Original diameter of the rod (m)

$\rho_Z$ : Density of zirconium 6490 kg/m<sup>3</sup>

$h_r$ : Heat of reaction per kg of Zr =  $6.45 \times 10^6$  J/kg

$\Delta t$ : Duration of time step (s)

$\Delta Z_0$ : Change in oxide thickness in the time step  $\Delta t$  (m)

## 3.3 Fuel Rod Voids Heat Transfer

The voids in the fuel rod consist of the plenum, the pellet-cladding gap, and the pellet-pellet interfaces which include pellet dishes and chamfers. These regions are treated as continua in a similar manner to the treatment of the fuel and clad with the exception that two-node elements are used in the voids in place of the eight-node elements for the fuel and the clad. The derivation of relevant element matrices, namely, the conductivity matrices, follows directly from the derivations presented earlier in this section, but making use of the special conductance characteristics of the gap and gas mixture. Because of the small heat capacity of the gases compared to the fuel and clad, the capacity matrices for the gap elements are null matrices.

### 3.3.1 Gap Conductance

As was mentioned earlier, the pellet-cladding gap is treated mathematically as a continuum, which permits spatial variation of the gap conductance in both axisymmetric (r-z) or plane (r- $\theta$ ) geometries. By the same consideration, pellet-cladding gap opening and closure is handled automatically as time- and space-dependent phenomenon. The pellet-cladding gap conductance is composed of two components: heat transfer across a gas gap and heat transfer through solid-solid contact. The pellet-cladding gap conductance is applied locally, element by element and the status (opened vs. closed) is treated separately at each location. The open gap conductance is based on the Ross and Stoute [7] model, and the solid-solid contact conductance is based on the Mikic-Todreas model [8] as modified by Lanning and Hann in BNWL-1894 [9]. The model distinguishes between open and closed gap and is described below.



### 3.3.1.1 Open Gap

In a locally open gap, heat is transferred across the gas gap by conduction through the gas and by radiation. The heat transfer coefficient across the gas gap is determined by the equation:

$$h_g = \frac{K_g}{t_g + d_{\text{rough}} + (g_1 + g_2)} + h_r \quad (\text{eq. 3-25})$$

where

- $h_g$ : Pellet-cladding gap conductance ( $\text{W/m}^2\text{-K}$ )
- $K_g$ : Conductivity of the gas mixture ( $\text{W/m-K}$ )
- $t_g$ : Mechanical gap width calculated in deformation solution (m)
- $g_1$ : Temperature jump distance at cladding inside surface (m)
- $g_2$ : Temperature jump distance at fuel outside surface (m)
- $h_r$ : Radiant heat transfer conductance
- $d_{\text{rough}}$ : Combination of fuel and cladding surface roughness (can be input by user to override default combination). The default combination is as follows:
  - $d_{\text{rough}} = 3.2 (R_f + R_c)$
  - $R_f$  = fuel surface roughness (m)
  - $R_c$  = cladding surface roughness (m)

The thermal conductivity of the gas mixture ( $K_g$ ) is calculated using the thermal conductivity of each gas species present within the fuel rod void volume and a gas mixing approach developed by Brokaw for monatomic gases [10]. The approach by Brokaw uses the molecular weight and mole fraction of the individual gas species to calculate the thermal conductivity of a gas mixture. A detailed description of the thermal conductivity model for gas mixtures is contained in the MATPRO Version 11 Rev. 0 document [11]. In determining the gas mole fractions, FALCON considers instantaneous gas communication within the different fuel rod void volumes and the mole fractions of the various gas species is assumed uniform throughout the rod. A total of seven different gases are included in the gap conductance model in FALCON, including the monatomic gases, helium, argon, xenon, and krypton, as well as, nitrogen, hydrogen, and steam. These gas species span the expected range of internal gases that may be present within a fuel rod at manufacture and following operation.

The radiant heat transfer coefficient is computed using the following equation:

$$h_r = \sigma F_e (T_f^2 + T_c^2) (T_f + T_c) \quad (\text{eq. 3-26})$$

where

- $h_r$ : Radiant heat transfer conductance ( $\text{W/m}^2\text{-K}$ )

Heat Transfer

- $\sigma$ : Stefan-Boltzmann constant ( $\text{W/m}^2\text{-K}^4$ )
- $F_e$ : Emissivity factor (-)
- $T_f$ : Temperature of outside surface of fuel (K)
- $T_c$ : Temperature of inside surface of cladding (K)

The emissivity factor is computed by the equation [12]:

$$F_e = \left[ \frac{1}{\epsilon_f} + \frac{r_f}{r_c} \left( \frac{1}{\epsilon_c} - 1 \right) \right]^{-1} \quad (\text{eq. 3-27})$$

where

- $F_e$ : Emissivity factor
- $\epsilon_f$ : Emissivity of fuel surface determined from MATPRO-11 [11]
- $\epsilon_c$ : Emissivity of cladding inside surface determined from MATPRO-11 [11]
- $r_f$ : Outside radius of fuel
- $r_c$ : Inside radius of fuel

The temperature jump distance term ( $g_1 + g_2$ ) is computed using an approach developed by Kennard. The Kennard model was selected for use in FALCON based on a review of temperature jump distance models published by Lanning and Hann [9]. The equation for temperature jump distance used in FALCON is:

$$g_1 + g_2 = 2 \left[ 2878 \left( \frac{2 - a_{mix}}{a_{mix}} \right) \left( \frac{K_{gas} \sqrt{T_{gas}}}{P} \right) \left( \frac{1}{\sum_{i=1}^7 \frac{f_i}{M_i}} \right)^{1/2} \right] \quad (\text{eq. 3-28})$$

where

- $(g_1 + g_2)$ : Jump distance (cm)
- $K_{gas}$ : Thermal conductivity of the gas mixture (cal/sec-cm-C)
- $P$ : Pressure of gas (dynes/cm<sup>2</sup>)
- $f_i$ : Mole fraction of i-th gas species
- $T_{gas}$ : Temperature of gas (K)
- $M_i$ : Molecular weight of i-th gas species
- $a_{mix}$ : Accommodation coefficient for the gas mixture

The accommodation coefficient for the gas mixture is calculated using expressions developed by Ullman for both helium and xenon gas and a linear interpolation based on the effective molecular weight of the gas [9]. The accommodation coefficients for helium and xenon gases are a function of the gas temperature and are given by

$$a_{He} = 0.425 - 2.3 \times 10^{-4} T_{gas} \quad (\text{eq. 3-29})$$

$$a_{Xe} = 0.749 - 2.5 \times 10^{-4} T_{gas} \quad (\text{eq. 3-30})$$

For a gas mixture or gases other than helium and xenon, the accommodation coefficient is given by

$$a_{mix} = a_{He} + \frac{(a_{Xe} - a_{He})(M_{mix} - M_{He})}{M_{Xe} - M_{He}} \quad (\text{eq. 3-31})$$

where

$M_{He}$ : Molecular weight of helium

$M_{Xe}$ : Molecular weight of xenon

$M_{mix}$ : Molecular weight of gas mixture given by  $\sum_{i=1}^7 f_i M_i$

In the calculation of the accommodation coefficient, the relationships for helium and xenon shown in equations 3-29 and 3-30 are applicable to gas temperatures in the range of 500 to 1000 K, and therefore, the gas temperature is limited to a maximum of 1000 K in FALCON for this calculation. Furthermore, the temperature jump distance calculated in eq. 3-28 represents an average for the cladding and fuel surfaces, requiring the factor of 2 included in eq. 3-28.

### 3.3.1.2 Solid-Solid Contact

Once pellet-cladding contact occurs, the equation for solid-solid contact conductance used in FALCON is the model developed by Mikic and Todreas [8] and modified by Lanning and Hann [9]. The modified Mikic and Todreas equation provides a lower bound fit to the gap conductance data measured by Ross and Stoute for  $\text{UO}_2$ -metal contact [9].

The criterion used to define gap closure in FALCON and change the calculation of the gap conductance from the Ross and Stoute model for an open gap to the modified Mikic and Todreas model for a solid-solid conductance is based on a minimum gap size. Gap closure is assumed to occur once the effective gap ( $\Delta X_{R-S}$ ) used in the Ross and Stoute model given by:

$$\Delta x_{R-S} = t_g + d_{\text{rough}} + (g_1 + g_2) \quad (\text{eq. 3-32})$$

becomes smaller than the zero interfacial pressure effective gap ( $\Delta X_{M-T}$ ) used in the modified Mikic-Todreas model given by:

$$\Delta x_{M-T} = 1.8[2(R_f + R_c) + (g_1 + g_2)] - 1.2 \times 10^{-6} \quad (\text{eq. 3-33})$$

The equation for the modified Mikic-Todreas gap conductance model is given by

$$h_g = \frac{A_m K_m \left(\frac{P_i}{H}\right)^n}{R \exp(5.738 - 0.528 R_1)} + \frac{K_g}{1.8[C(R_f + R_c) + (g_1 + g_2)] - 1.2 \times 10^{-6}} + h_r \quad (\text{eq. 3-34})$$

where

$h_g$ : Pellet-cladding gap conductance (W/m<sup>2</sup>-K)

$A_m = 0.5785$  – Interfacial pressure model constant (deceased by a factor of 4 from original Mikic-Todreas model [9])

$$R = (R_f^2 + R_c^2)^{1/2}$$

$$R_1 = \log(R_f^*)$$

$R_f^*$ : Fuel surface roughness in micro-inches

$$n = \begin{cases} 0.5 & \text{for } \frac{P_i}{H} < 10^{-4} \\ 1.0 & \text{for } \frac{P_i}{H} \geq 10^{-2} \end{cases}$$

$$\frac{P_i}{H} = 0.01 \quad \text{for } 10^{-4} \leq \frac{P_i}{H} < 10^{-2}$$

$$K_m = \frac{2K_f K_c}{K_f + K_c} \quad (\text{W/m-K})$$

$K_f$ : Fuel conductivity (W/m-K)

$K_c$ : Cladding conductivity (W/m-K)

$P_i$ : Interfacial pressure between fuel and cladding (psi)

$R_c$ : Arithmetic mean roughness height of cladding (m)

$R_f$ : Arithmetic mean roughness height of fuel (m)

$H$ : Meyer-Hardness of cladding (kg/cm<sup>2</sup>) determined from MATPRO-11

$K_g$ : Thermal conductivity of gas (W/m-K) determined from MATPRO-11

The coefficient,  $C$ , in eq. 3-34 is computed by the empirical equation:

$$C = 1.98 e^{-0.00125 P_i} \quad (\text{eq. 3-35})$$

where

$P_i$ : Interfacial pressure between fuel and cladding ( $\text{kg/cm}^2$ )

No limit is placed on the interfacial pressure used in eq. 3-34 and eq. 3-35. The ratio of interfacial pressure to Meyer hardness is limited to values less than unity. This insures that the interfacial pressure does not exceed the Meyer hardness.

The gap conductance for closed gap conditions is composed of three separate terms as shown in eq. 3-34. The first term represents the solid-solid conductance across contact points in the pellet-cladding gap. The efficiency of heat conduction by contact is a function of the interfacial pressure and the size and shape of the pellet and cladding surface roughnesses. The second term in eq. 3-34 represents heat conduction across the remaining gas voids in the gap. The size of the effective gas gap in the denominator of the second term is a function of the surface roughness and the temperature jump distances. To improve numerical stability, a minimum effective gas gap of 2 microns is used in the modified Mikic-Todreas model at high interfacial pressures. The third term in eq. 3-34 represents the radiative heat transfer between two cylindrical surfaces and is calculated by eq. 3-26.

### 3.3.2 Pellet-Pellet Contact Conductance

Axial heat flow in the fuel column is generally small by comparison with the radial heat flow. However, discontinuities in the fuel column due to individual pellet geometries, pellet hour-glassing and pellet dishing create local axial perturbation in the temperature field. Also axial power variation introduces axial heat flow that is interrupted by these local variations. It is important, therefore, to give proper treatment of the pellet-pellet conductance, which is done by providing contact elements of very small dimensions between pellets. The element thermal properties are then derived in much the same way as the gap elements utilizing the same gap conductance model but substituting the fuel-fuel for the fuel-clad properties. This type of treatment may be approximate, but it is reasonable in view of the complete lack of data on pellet-pellet conductance measurement. On this basis, then, the pellet-pellet conductance is calculated by eq. 3-34. In the case of pellet separation, such as might occur at the outer edges due to pellet-end convexity, the conductance is calculated by eq. 3-25. In the event that a large axial gap is formed in the fuel column, the pellet-pellet conductance is dominated by the radiation component. It should be pointed out, however, that in the absence of clad collapse into the axial gap, pellet contact is an initial and low power condition, whereas pellet separation is a deformation-induced high power condition.

In constructing the finite element grid for the fuel column, it is not necessary to model each individual pellet, and in fact, such modeling would be prohibitive in computer cost. The fuel can be modeled as a continuous column with no gaps, or gaps can be introduced periodically to account for pellet dishes gas space. This is referred to as lumping of the gas volume in the fuel

column and is conveniently done by assigning the appropriate dimensions to the pellet-pellet contact elements; the code automatically adjusts the conductivities to the appropriate values for small gap conditions.

### 3.3.3 Plenum Heat Transfer

The plenum is modeled as a continuum in the form of finite elements with appropriate thermal and mechanical properties of the spring material and stored gases. The spring conductivity and radiation are the major contributors to the plenum conductance model. Treating the plenum as a large gap, and ignoring the temperature jump distances, one obtains from eq. 3-25

$$K_{PL} = K_g + h_r L + K_s \quad (\text{eq. 3-36})$$

where

- $K_{PL}$ : Conductivity of plenum element
- $h_r$ : Radiant heat transfer coefficient, eq. 3-26
- $L$ : Length of plenum spring
- $K_s$ : Conductivity of the spring material
- $K_g$ : Conductivity of the gas

## 3.4 Fuel Rod Surface Heat Transfer

This sub-section describes the thermal boundary conditions required to model the heat flux between the clad and the coolant. The heat flux is a function of the local thermal-hydraulic conditions of the coolant which are simulated in a single channel enthalpy rise model described below.

### 3.4.1 Coolant Enthalpy Model

A coolant enthalpy rise model is used in FALCON to determine the coolant enthalpy (or temperature) and mass flow rate distributions along the fuel rod flow channel. The coolant channel information is required in calculating the rod-to-coolant heat transfer coefficients which, along with the coolant temperature, provide the thermal boundary conditions for the cladding and pellet temperature calculations. As an option, the coolant enthalpy model can also be deactivated by the user provided one of the following boundary conditions are supplied: (1) the heat transfer coefficient and coolant (bulk) temperature distribution, (2) the wall heat fluxes, or (3) the clad surface temperatures.

The coolant enthalpy rise model in FALCON has the ability to treat two different fluids: water and sodium. For water, FALCON models both single-phase (liquid or vapor) and two-phase fluid flow and heat transfer. A complete representation of the forced convection boiling curve for water is included in the coolant model used in FALCON. The heat transfer and critical heat flux correlations in FALCON are consistent with the heat transfer correlations used in the

RETRAN and VIPRE codes [13, 14]. A description of the heat transfer and critical heat flux correlations is contained in Appendix B. The coolant enthalpy model for sodium only considers single-phase (liquid) fluid flow and convective heat transfer. The forced convection heat transfer correlation by Lyon is used in FALCON to calculate the clad-to-sodium heat transfer coefficient [15]. The model is described in Appendix B.

Equations of state for both phases of water and liquid sodium are required as part of the coolant enthalpy model. The equations of state for water used in FALCON were obtained for the RETRAN code package [13]. The water properties are discussed in Appendix F. The liquid sodium thermophysical properties used in FALCON include heat capacity, enthalpy, density, thermal conductivity, and viscosity. These properties were obtained from the ANL publications on thermophysical properties of sodium developed as part of the Liquid Metal Fast Breeder Reactor (LMFBR) program [16]. The liquid sodium thermophysical properties are described in Appendix F.

The coolant channel model is based on a homogeneous closed channel approach, with thermal equilibrium between the liquid and vapor phases. These assumptions do not provide for energy or momentum transfer to other channels. Therefore, the conservation of mass (continuity equation) and the conservation of energy (energy equation) are used to determine the enthalpy and velocity distributions along the channel without requiring the solution of the conservation of momentum equation. This approach simplifies the required computations; however, no consideration is given to pressure losses or lateral momentum or energy transfer to adjacent channels which may be of importance for fuel rod bundle flow. In addition, the pressure/flow feedback is not modeled (i.e., no flow oscillations). A total pressure drop for the channel can be input that is assumed to vary linearly along the rod. The coolant channel is subdivided into control volumes, as shown in Figure 3-4, each of which coincides with a clad element. The input inlet conditions for the mass flow rate, fluid temperature or enthalpy, and pressure are used to initialize the model at the lower plenum. For each control volume, the inlet conditions at the lower interface are used to solve for the exit conditions at the upper interface.

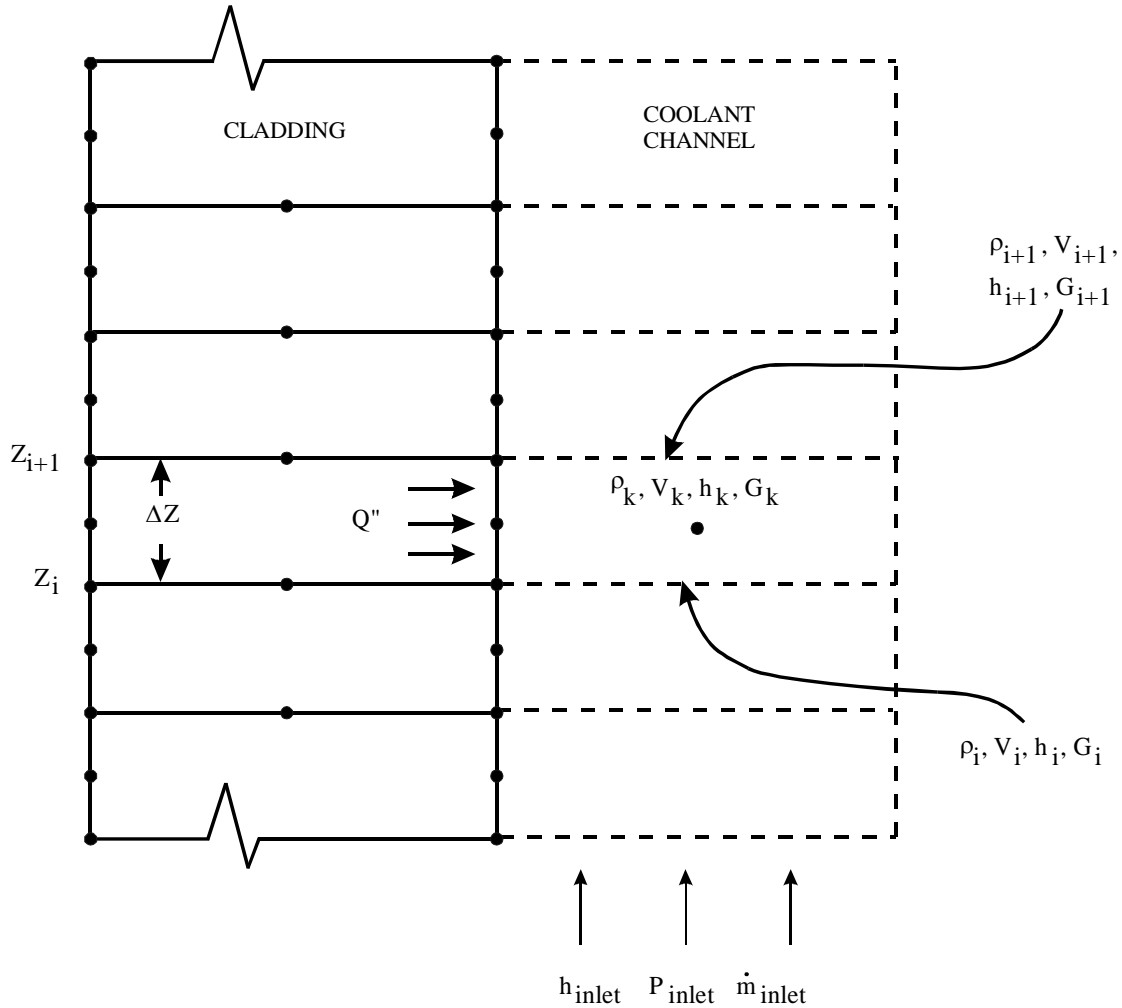


**Figure 3-4**  
**Coolant Channel Nodalization**

The following conservation equations provide the basis for the coolant model in FALCON. A one-dimensional approach in the axial direction is used; therefore, all components in the lateral directions ( $x, y$ ) are set to zero. The conservation of mass and energy equations in the axial direction ( $z$ ) can be written as follows.

Continuity Equation:

$$\frac{\partial \rho}{\partial t} = \frac{\partial}{\partial z} (\rho V) = 0 \quad (\text{eq. 3-37})$$

Energy Equation:

$$\frac{\partial}{\partial t} \left[ \rho \left( u + \frac{1}{2} V^2 \right) \right] + \frac{\partial}{\partial z} \left[ \rho V \left( u + \frac{1}{2} V^2 + g z \right) \right] + \frac{\partial}{\partial z} [\rho V] = Q \quad (\text{eq. 3-38})$$



where  $\rho$  is density,  $V$  is velocity,  $u$  is the coolant specific energy,  $p$  is the pressure,  $Q$  is the heat energy, and  $g$  is the gravitational acceleration. The assumption of homogeneous equilibrium flow (i.e.,  $V_g = V_\ell = V$ ) requires that only one system of equations be used to determine the enthalpy at each control volume. The time derivative terms are dropped from the equations for steady state conditions. The numerical integration of these equations is given in Appendix B.

### 3.4.2 Heat Transfer Correlations

A heat transfer coefficient is calculated for each coolant channel control volume from empirical correlations for the appropriate heat transfer regime and fluid type. The mathematical expressions for both the water and sodium heat transfer correlations are given in Appendix B. Figure 3-5 shows a map of the boiling regimes with the applicable heat transfer correlations. The selection criteria for the appropriate heat transfer correlation are described in Table 3-4 for water. For water coolant applications, the critical heat flux (CHF) is calculated for each coolant channel control volume using the input specified CHF model and the current coolant conditions prior to the heat transfer coefficient calculation. These values are then used as part of the selection criteria. The CHF correlations are also given in Appendix B. No consideration is given in FALCON to the boiling or voidage for sodium coolant. The assumption is made that the sodium remains as a liquid under all heat transfer and flow regimes.

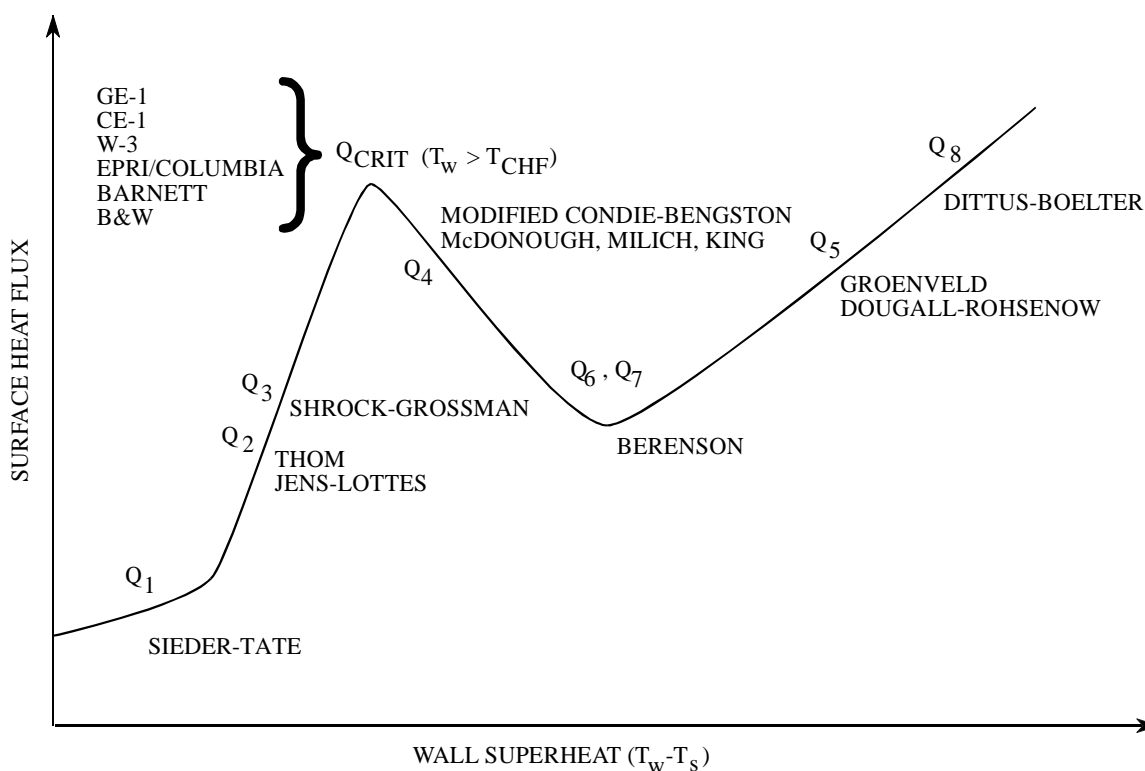


**Figure 3-5**  
**Schematic Representation of the Boiling Curve**

## Heat Transfer

**Table 3-4**  
**Heat Transfer Modes and Corresponding Correlations for Water**

Heat Transfer Mode	Correlation	Selection Criteria
1: Single Phase Liquid	Sieder-Tate	$T_w < T_{sat}, \chi = 0.0, Q_2 < Q_1 < Q_{CHF}$
2: Fully Developed Sub-Cooled Boiling  Fully Developed Saturated Boiling	Thom  Jens-Lottes	$Q_1 < Q_2 < Q_{CHF}, \alpha < 0.999$
3: Forced Convection Vaporization	Shrock & Grossman	$Q_1, Q_2, Q_3 < Q_{CHF}, \alpha > 0.999$
4: Forced Convection Transition Boiling	McDonough, Milich & King Modified Condie-Bengston	$T_w > T_{CHF}$
5: Forced Convection Stable Film Boiling	Groeneveld Dougall-Rohsenow	$T_w > T_{CHF}, Q_5 > Q_4$
6: Pool Transition and Stable Film Boiling	Berenson	$G < 200000, \Delta T_w < \Delta T_{min}$
7: Pool Transition and Stable Film Boiling	Berenson	$G < 200000, \Delta T_w \geq \Delta T_{min}$
8: Single Phase Vapor	Dittus-Boelter	$\chi = 1.0$
<p>where</p> <p><math>Q_i</math>: Heat flux for the <math>i^{th}</math> heat transfer mode</p> <p><math>Q_{CHF}</math>: Critical heat flux</p> <p><math>T_w</math>: Wall (clad outer surface) temperature</p> <p><math>T_{sat}</math>: Saturation temperature</p> <p><math>\Delta T_w = T_w - T_{sat}</math>: Wall superheat</p> <p><math>\Delta T_{min} = (T_w - T_{sat})_{min}</math>: Wall superheat at minimum heat flux</p> <p><math>\alpha</math>: Vapor volume fraction</p> <p><math>\chi</math>: Thermodynamic quality</p>		

### 3.4.3 Model Assumption Implications

The formulation of the coolant channel model in FALCON is based on four important assumptions: (1) closed channel, (2) homogeneous flow, (3) thermal equilibrium between phases, and (4) no pressure/flow feedback. The assumptions used in the coolant channel model have certain implications on the coolant conditions calculated by FALCON when using this model. The closed channel approach ignores the lateral transfer of momentum, energy or mass that occurs within a fuel rod bundle. By not considering the rod-to-rod exchange, the enthalpy (temperature) increase along the length of the channel is larger using the FALCON model. The presence of flow diversion in the lateral direction within a rod bundle is influenced by the radial power profile within the assembly, non-uniform inlet conditions, and void generation within the assembly. The occurrence of these conditions will result in incorrect heat transfer conditions to be calculated using the closed channel approach for rod assemblies. The homogeneous flow assumption requires the flow velocity of the different phases, namely liquid and vapor, to be equal. Therefore, no slip between the phases is included in the FALCON coolant model. The consequence of this assumption is that the flow quality and void fraction will not be predicted correctly, possibly resulting in the selection of the improper heat transfer mode and error in the magnitude of the heat transfer coefficient. The prediction of departure from nucleate boiling (DNB) will be impacted by the homogeneous flow assumption. The requirement of thermal equilibrium mandates that the different phases must be at the same temperature for boiling conditions (saturation). The inability to explicitly handle the simultaneous occurrence of superheated vapor and sub-cooled or saturated liquid will influence the heat transfer coefficient, particularly in the post-dryout regime. Two post-dryout heat transfer correlations used in FALCON do treat the thermal non-equilibrium conditions using an empirical approach. However, the application of these correlations to fuel rod assemblies is limited. The final major inadequacy in the FALCON coolant model is the lack of a pressure/flow feedback methodology. The pressure drop due to flow-induced resistance (for example, void generation, space grids, etc.) is not considered in FALCON. Therefore, the occurrence of flow oscillations and the heat transfer conditions associated with these flow conditions will not be modeled properly when using FALCON.

The impact of the assumptions on the method for using FALCON depends on the user's application. For licensing analysis, the coolant channel model is only applicable to pre-DNB heat transfer conditions. The coolant model should not be used for predicting the time and location of DNB for transients expected to experience these conditions. Instead, to use FALCON in determining the fuel rod response during post-DNB operation, the heat transfer correlations (HTC) and coolant conditions should be obtained from an assembly thermal-hydraulics program which properly considers the complex post-DNB flow conditions within a fuel rod assembly. The spatial and temporal variations of the HTC's can be input to yield an accurate thermal boundary condition to investigate the thermal and mechanical response of the fuel rod during the transient of interest.

The coolant channel model in FALCON is adequate for scoping calculations and for single rod/single channel experiments similar to those used to benchmark the program. For these conditions, judicious selection of the appropriate heat transfer and critical heat flux correlations which comply with the conditions to be analyzed will provide the user with reasonable results.

This later method was used in the verification and validation of the program with satisfactory success.

### 3.5 References

1. Wilson, E.L. and Nickell, R.E., "Application of the Finite Element Method to Heat Conduction Analysis," Nuclear Engineering and Design, Vol. 4, 1966, pp. 276-286.
2. Comini, G., del Guidice, S., Lewis, R.W. and Zienkiewicz, O.C., "Finite Element Solution of Non-Linear Heat Conduction Problems with Special Reference to Phase Change," International Journal of Numerical Methods in Engineering, Volume 8, 1974, pp. 613-624.
3. Finlayson, B.A., The Method of Weighted Residual and Variational Principles, Academic Press, New York, 1972.
4. Thomas, G.M. and Hesketh, K.W., "RADAR-G - A Routine for Calculating Radial Power Profiles in Thermal Reactor Fuel," BNFL, EPRI Contract 18362, November 1986.
5. Lassman, K., O'Carroll, C., van de Loor, J., Walker, C. T., "The Radial Distribution of Plutonium in High Burnup  $\text{UO}_2$  Fuel," J. Nuc. Mat. 208, 1994, pp. 2232-231.
6. "American National Standard for Decay Heat Power in Light Water Reactors," ANSI/ANS-5.1 - 1979.
7. Ross, A.M. and Stoute, R.L., "Heat Transfer Coefficient between  $\text{UO}_2$  and Zircaloy-2," CRFD-1075, Chalk River, Ontario, June 1962.
8. Todreas, N. and Jacobs, G., "Thermal Conductance of Reactor Fuel Elements," Nuclear Science and Engineering, 50, 1973, p. 283.
9. Lanning, D.D. and Hann, C.R., "Review of Methods Applicable to the Calculation of Gap Conductance in Zircaloy Clad  $\text{UO}_2$  Fuel Rods," Battelle Pacific Northwest Laboratories, BNWL-1894, April 1975.
10. Brokaw, R.S., "Alignment Charts for Transport Properties, Viscosity, Thermal Conductivity, and Diffusion Coefficients for Nonpolar Gases and Gas Mixtures at Low Density," Lewis Research Center, NASA-TR-R-81 (1960)
11. MATPRO - Version 11: A Handbook of Materials Properties for Use in the Analysis of Light Water Reactor Fuel Rod Behavior, NUREG/CR-0497 TREE-1280, February 1979.
12. Bird, R.B., Stewart, W.E., Lightfoot, E.N., Transport Phenomena, John Wiley & Sons, New York, 1960, p. 445.
13. "RETRAN - A Program for One-Dimensional Transient Thermal-Hydraulic Analysis of Complex Fluid Flow Systems," Volume 1, EPRI CCM-5, December 1978.
14. Stewart C.W., et al., "VIPRE-01, A Thermal-Hydraulic Analysis Code for Reactor Cores: Volume 1, Mathematical Modeling," EPRI NP-2511, August 1982.
15. Lyon, R.M., "Liquid Metal Heat-Transfer Coefficients," Chem. Eng. Prog. 47, 75, 1951.
16. Fink, J.K., Leibowitz, L., "Thermophysical Properties of Sodium," ANL-CEN-RSD-79-1, Argonne National Laboratory Report, 1979.

# 4

## DEFORMATIONS

---

The system of equations which characterizes the deformation of a fuel rod consists of the strain-displacement relations, the stress-strain constitutive relations, the boundary conditions and the equilibrium equations. The strain-displacement relations govern the kinematic behavior of the fuel rod and, hence, are of critical importance to the modeling of the large deformation ballooning behavior of the cladding. Consequently, large or finite strain theory is utilized for the cladding and small (infinitesimal) strain theory is used for the fuel where the deformations remain small.

The stress-strain constitutive relations govern the nonlinear material behavior and are derived consistently with the large strain theory. The material data utilized in these equations are obtained from MATPRO-11 [1]. The material behavior represented covers the entire range from initial elastic response to the elastic-plastic-creep strain-rate dependent (viscoplastic) response in the high power and high temperature regimes.

The equilibrium equations are derived in incremental form from the principle of virtual work subject to the appropriate boundary conditions. They consist of piecewise linear algebraic equations, whose matrix of coefficients relates the unknown nodal displacements to the known nodal forces; this matrix is positive-definite symmetric. These equations are solved implicitly in a sophisticated iterative time-stepping procedure.

Finite element large strain theory in FALCON is formulated in an Updated Lagrangian coordinate system. In this coordinate system, the appropriate stress/strain conjugate measures are the Cauchy (or true) stress and Euler (or log) strain, and a consistent constitutive material description is given as the relation between the Jaumann (or co-rotational) rate of the Cauchy stress and the rate of deformation tensors. The relevant derivations are given in the following paragraphs.

The first set of equations to be defined is the field equations which consist of the displacement approximations, the strain-displacement relations and the stress-strain relations. The stresses and strains are defined at the integration points and, hence, they account for the effects of temperature variations through the element. The field equations are then used together with the appropriate boundary conditions to derive the governing (equilibrium) equations from the virtual work variational principle. The detailed derivations of these equations for the finite element system are lengthy and are included, therefore, in Appendix C. In this section, we present equations that are necessary to illustrate the important features of the deformation model and the numerical structure of the equilibrium equations.

## 4.1 Displacement Approximations

The strain-displacement relations for the cladding are based on the large deformation theory. This permits the cladding to undergo ballooning (or collapse) under PCMI and/or differential pressure. These states of large deformations evolve in a continuous manner in the solution; hence, the artificial switch to a "ballooning model" is avoided. The fuel deformations, on the other hand, remain small; therefore, the strain-displacement relations for the fuel elements do not include the nonlinear terms. These features are illustrated in the following equations.

Consider the 2D problem of plane and axisymmetric geometry for which the finite element shown in Figure 2-1 is used. The following notation is adopted:

- $X_i$ : Original coordinates (referred to the initial configuration) of a material point
- $x_i$ : Deformed coordinates
- $U_i$ : Displacements relative to original coordinates
- $dU_i$ : Increments of displacement (within a time step)

then

$$\begin{aligned} x_i &= X_i + U_i \\ dx_i &= dU_i \end{aligned} \quad (\text{eq. 4-1})$$

For the element shown in Figure 2-1, variables are represented in terms of their nodal values and shape functions as follows:

$$\begin{aligned} x_i &= \sum_{n=1}^N \phi_n x_i^n \\ U_i &= \sum_{n=1}^N \phi_n v_i^n \\ dU_i &= \sum_{n=1}^N \phi_n dv_i^n \end{aligned} \quad (\text{eq. 4-2})$$

where  $n$  ranges over the number of nodes ( $N$ ) in the element which, as described in Section 2, for example, is 8 for bi-quadratic quadrilaterals and 6 for bi-quadratic triangles;  $x_i^n$  is the  $i^{\text{th}}$  coordinate of node  $n$ ,  $v_i^n$  is the  $i^{\text{th}}$  displacement component of node  $n$ , and similarly for the displacement increment  $dv_i^n$ . As described in Section 2, the shape functions are continuous functions of the natural (parametric) coordinates within the element.

The displacement shape functions are linear or quadratic in the parametric coordinates  $\xi$  and  $\eta$ , and are identical to the temperature shape functions; the difference is that the amplitudes are the

nodal temperatures and the nodal displacements for the thermal and deformation problems, respectively. The displacement approximations for the fuel/clad elements are given below, using eq. 4-2 and introducing time and position dependence.

$$U_i(x_j, t) = \sum_{n=1}^N \hat{\phi}^n(x_j) v_i^n(t) = \sum_{n=1}^N \phi_n(\xi(x_j), \eta(x_j)) v_i^n(t) \quad (\text{eq. 4-3})$$

where  $U_i(x_j, t)$  is the  $i^{\text{th}}$  displacement at position  $x_j$  and time  $t$ . The specific form of the shape functions  $\phi^n(\xi, \eta)$  was given in Section 2. In matrix form the equations in eq. 4-2 are written as

$$\begin{aligned} x_i &= \phi^T \underline{x}_i \\ U_i &= \phi^T \underline{U}_i \\ dU_i &= \phi^T d\underline{U}_i \end{aligned} \quad (\text{eq. 4-4})$$

It is necessary to distinguish between the quantity  $x_i$  which is the  $i^{\text{th}}$  component of the deformed coordinate as continuous function (of  $\xi$  and  $\eta$ ) over the element and  $\underline{x}_i$  which is a vector

consisting of the nodal values of the deformed coordinates. The same is true for the other variables in eq. 4-4.

## 4.2 Strain-Displacement Relations

The deformation gradients are:

$$\varepsilon_{ij} = \frac{1}{2} \left[ \frac{\partial x_k}{\partial x_i} \frac{\partial x_k}{\partial x_j} - \delta_{ij} \right] - \varepsilon_{ij}^f \quad (\text{eq. 4-5})$$

where  $\varepsilon_{ij}^f$  are the free expansion strains and  $\delta_{ij}$  is the Kronecker delta. The explicit form of eq. 4-5 for the axisymmetric geometry is as follows:

$$\begin{aligned}
\varepsilon_{RR} &= \frac{\partial U_R}{\partial R} + \frac{1}{2} \left[ \left( \frac{\partial U_R}{\partial R} \right)^2 + \left( \frac{\partial U_Z}{\partial R} \right)^2 \right] - \varepsilon_{RR}^f \\
\varepsilon_{ZZ} &= \frac{\partial U_Z}{\partial Z} + \frac{1}{2} \left[ \left( \frac{\partial U_R}{\partial Z} \right)^2 + \left( \frac{\partial U_Z}{\partial Z} \right)^2 \right] - \varepsilon_{ZZ}^f \\
\varepsilon_{\theta\theta} &= \frac{U_R}{R} + \frac{1}{2} \left( \frac{U_R}{R} \right)^2 - \varepsilon_{\theta\theta}^f \\
\varepsilon_{R\theta} &= \varepsilon_{Z\theta} = 0
\end{aligned} \tag{eq. 4-6}$$

The squared terms in equations 4-5 and 4-6 are responsible for producing smoothly changing large strains. Without these terms, ballooning could not be correctly predicted. The fuel strain-displacement relations are confined to the linear terms in eq. 4-6.

### 4.3 Stress-Strain Relations

The stress-strain relations are presented in this section with more detailed derivations given in Appendix C. Consider a material element where it is assumed the strain rate tensor  $\dot{\varepsilon}_{ij}$  can be expressed as the sum of four components: elastic, time-independent plastic, creep, and free expansion, namely

$$\dot{\varepsilon}_{ij} = \dot{\varepsilon}_{ij}^e + \dot{\varepsilon}_{ij}^p + \dot{\varepsilon}_{ij}^c + \dot{\varepsilon}_{ij}^f \tag{eq. 4-7}$$

Note the free expansion term is due to the combined effects of temperature and irradiation induced swelling and densification. With view towards deriving stress-strain relations in incremental form, eq. 4-7 can be expressed as

$$\Delta \varepsilon_{ij} = \Delta \varepsilon_{ij}^e + \Delta \varepsilon_{ij}^p + \Delta \varepsilon_{ij}^c + \Delta \varepsilon_{ij}^f \tag{eq. 4-8}$$

#### 4.3.1 Elastic Relations

The elastic strains are related to the incremental stress by

$$\Delta \varepsilon_{ij}^e = \Delta (C_{ijkl} \sigma_{kl}) = C_{ijkl} \Delta \sigma_{kl} + \Delta C_{ijkl} \sigma_{kl} \tag{eq. 4-9}$$

Equation 4-9 admits the variation of the elastic material tensors  $C_{ijkl}$  with temperature and neutron flux, however, such variations are usually small. For isotropic material, we have



$$C_{ijk\ell} = \frac{1-\nu}{E} \delta_{ik} \delta_{j\ell} - \frac{\nu}{E} \delta_{ij} \delta_{k\ell} \quad (\text{eq. 4-10})$$

where  $E$  is Young's modulus and  $\nu$  is Poisson's ratio.

### 4.3.2 Creep Relations

We direct our attention next to the creep strain rates  $\dot{\epsilon}_{ij}^c(t)$ . The uniaxial creep strain rate is represented by the following equation:

$$\dot{\epsilon}^c = \dot{J} \sigma \quad \text{and} \quad \dot{J} = \dot{J}(\sigma, T, \dots) \quad (\text{eq. 4-11})$$

where  $J(\sigma, t)$  is the creep compliance. Note that  $J$  is an explicit function of many other variables such as temperature, flux and fluence. This equation is generalized to multiaxial relations by

$$\dot{\epsilon}_{ij}^c(t) = \dot{J} B_{ijk\ell} \nabla \sigma_{k\ell} \quad (\text{eq. 4-12})$$

where the Jaumann rate  $\nabla \sigma_{k\ell}$  of the Cauchy stress is used to preserve invariance of the creep law. For isotropic creep behavior

$$B_{ijk\ell} = (0.5 + \nu_0) \delta_{ik} \delta_{j\ell} - (0.5 - \nu_0) \delta_{ij} \delta_{k\ell} \quad (\text{eq. 4-13})$$

In this equation,  $\nu_0$  is a material constant which governs the creep volume change generally exhibited by the fuel material. For the cladding,  $\nu_0$  is zero. The hot pressing behavior of the fuel is represented by  $\nu_0$  and is calculated by [2].

$$\nu_0 = \frac{1}{4} \left( \frac{3}{2} \right)^n \left[ \frac{1}{0.74/p^{1/n} - 1} \right]^n \quad (\text{eq. 4-14})$$

where  $n$  is 3 and  $p$  is the porosity of the fuel, excluding crack porosity. Further discussion of  $\nu_0$  is given in Appendix C.

### 4.3.3 Time-Independent Elastic-Plastic Relations

A general yield criterion can be expressed as

$$F(\sigma_{ij}, \epsilon_{ij}^p, K) = 0 \quad (\text{eq. 4-15})$$

## Deformations

where  $\sigma_{ij}$  and  $\varepsilon_{ij}^p$  are the stresses and plastic strains, respectively, and  $K$  is a material parameter, such as the yield stress, which depends on the effective plastic strain, temperature, neutron flux, etc. The plastic strain increments obey a flow rule of the form

$$\Delta \varepsilon_{ij}^p = \lambda \left( \partial F / \partial \sigma_{ij} \right) \quad (\text{eq. 4-16})$$

where  $\lambda$  is a positive scalar function which depends on the state of stress, strain, temperature, hardening, and neutron flux. The stress state must satisfy the following condition:

$F < 0$  for elastic state

$$\left. \begin{aligned} F &= 0 \\ \frac{\partial F}{\partial \sigma_{ij}} d\sigma_{ij} + \frac{\partial F}{\partial K} dK &\geq 0 \end{aligned} \right\} \text{ for plastic state}$$

Equation 4-15 is too general, and to reduce it to a form which can be used in analysis the yield function  $F$  must be defined. In doing so, we must also define the type of hardening the material exhibits during plastic flow. For the fuel material we adopt combined Mohr-Coulomb and von Mises yield conditions [3], and for the cladding material we use Prager's kinematic hardening rule [4] in the following derivations. The yield function  $F$  is given by

$$F = J_2 + \beta I_1^2 - K^2 = 0 \quad (\text{eq. 4-17})$$

where  $I_1$  and  $J_2$  are the stress invariants defined below using the stress tensor  $\sigma'_{ij}$  where

$$\sigma'_{ij} = \sigma_{ij} - \alpha_{ij} \quad (\text{eq. 4-18})$$

in which  $\sigma_{ij}$  are the applied stresses and  $\alpha_{ij}$  are the yield surface translations (see Appendix C). The definitions of  $I_1$  and  $J_2$  are as follows:

$$I_1 = \sigma'_{ii} \quad (\text{eq. 4-19})$$

$$J_2 = \frac{1}{2} S'_{ij} S'_{ij} \quad (\text{eq. 4-20})$$

where

$$S'_{ij} = \sigma'_{ij} - \frac{1}{3} \sigma'_{kk} \delta_{ij} \quad (\text{eq. 4-21})$$

which is the deviatoric part of the tensor  $\sigma'_{ij}$ . The parameter  $\beta$  in eq. 4-17 is a material constant which governs the plastic volume change of the material and enhances the yield stress as a function of the confining stress. The time-independent plastic dilatation is given by

$$d\varepsilon_{ii}^p = 6\beta \lambda I_1 \quad (\text{eq. 4-22})$$

If the plastic volume change is zero, as is the case for the cladding,  $\beta = 0$ . Hence the yield function (eq. 4-22) reduces to the ordinary von Mises condition. However, for the fuel material,  $\beta$  is the plastic hot pressing parameter and is given by the following equation [2]:

$$\beta = \left[ \frac{Y(p_0)/Y_s}{2\sqrt{3} \ln(0.74/p)} \right]^2 \quad (\text{eq. 4-23})$$

where  $p_0$  is the as-manufactured porosity,  $p$  is the current porosity,  $Y(p_0)$  is the initial yield strength and  $Y_s$  is the yield strength of solid (100% dense)  $\text{UO}_2$ . This equation is further discussed in Appendix C. In FALCON,  $\beta = 0.005$  for the fuel material (see Appendix C), representing a small but non-trivial plastic volume reduction component. As mentioned above, the two parameters  $v_0$  in eq. 4-13 and  $\beta$  in eq. 4-17 govern the hot pressing behavior of the fuel. The  $\alpha_{ij}$ 's can be obtained from

$$\alpha_{ij} = \int C d\varepsilon_{ij}^p \quad (\text{eq. 4-24})$$

where  $C$  is a material parameter and is equal to  $2/3 E'$ , where  $E'$  is the slope of the stress-plastic strain curve in simple tension. The parameter  $K$  in eq. 4-17 is related to the uniaxial yield stress  $\sigma_y$  by

$$K = \sigma_y / \sqrt{3} \quad (\text{eq. 4-25})$$

#### 4.3.4 Pellet-Cladding Mechanical Interaction (PCMI)

Pellet-cladding mechanical interaction, which occurs when fuel pellets come in contact with the clad, is a highly complex mechanism and requires careful treatment. Its effects on the fuel rod response may be summarized as follows:

1. Contact conductance can be significantly higher (by an order of magnitude) than the open-gap conductance because of the interfacial pressure.
2. This change in gap conductance (from open to closed gap or vice versa) occurs suddenly in an incremental steady state analysis; and the sudden change in heat transfer can produce sudden changes in deformations leading to oscillations.
3. The interaction is not frictionless; consequently, a stick-slip condition develops which, under certain conditions, can lead to the well known PCI failures.

*Deformations*

4. The effects of fuel-clad interaction are not limited to steady state power operations, but can influence transients such as power-coolant mismatch to the extent that DNB can be triggered by a combination of improved heat flow to the cladding and reduced cooling.
5. The formation of axial gaps in the fuel column is the consequence of combined fuel densification, power cycling and fuel-clad interaction.
6. Not all fuel-clad mechanical interaction effects are harmful; for example, FCMI-enhanced heat transfer immediately preceding a rod withdrawal transient may be sufficient to keep the fuel enthalpy within acceptable limits.

Analytical treatments of FCMI vary widely in fuel modeling codes. Because of its very nature, an adequate treatment of this mechanism requires, at least, a fully two-dimensional representation. The approach adopted in FALCON is unique in this regard, and furthermore, the use of gap elements makes the analytical treatment of FCMI highly tractable. This spatial representation of the fuel-clad interface renders the mathematical description of the problem very simple. Its implementation in the code, however, is rather complex.

A fuel-clad gap element is initially assigned zero stiffness until the local gap indicates closure. This is judged by the following criterion:

$$\begin{aligned} 1 + \varepsilon_{\text{gap}} > 0 & \quad \text{gap is open} \\ 1 + \varepsilon_{\text{gap}} \leq 0 & \quad \text{gap is closed} \end{aligned}$$

where  $\varepsilon_{\text{gap}}$  is the strain calculated in the gap element (change in gap size divided by original gap size). Once the gap is closed, the gap element is assigned stiffness properties in the usual finite element sense based on a two-dimensional state of stress; normal contact normal stress  $\sigma$ , and shear stress  $\tau$ . Thus, the stiffness matrix for a gap element is calculated as follows

$$\begin{bmatrix} \sigma \\ \tau \end{bmatrix} = \begin{bmatrix} e_1 E & 0 \\ 0 & e_1 e_2 G \end{bmatrix} \begin{bmatrix} \varepsilon_{\text{gap}} \\ \gamma_{\text{gap}} \end{bmatrix} \quad (\text{eq. 4-26})$$

where  $E$  and  $G$  are the pseudo elastic and shear moduli, respectively, for the gap element. They are assigned sufficiently high values relative to the moduli of the fuel and clad to maintain small relative displacements between the fuel and clad surfaces while in contact. The values for the gap moduli are carefully chosen so that the interaction stresses ( $\sigma$  and  $\tau$ ) are independent of the moduli. The multipliers  $e_1$  and  $e_2$  are defined as follows:

$$\begin{aligned} e_1 &= \begin{cases} 0 & \text{for open gap} \\ 1 & \text{for closed gap} \end{cases} \\ e_2 &= \begin{cases} 0 & \text{slip condition } \tau \geq \mu \sigma \\ 1 & \text{stick condition } \tau < \mu \sigma \end{cases} \end{aligned}$$

In the above,  $\mu$  is the coefficient of friction between irradiated fuel and cladding. The out-of-pile experimental value of this parameter is about 0.5. The in-reactor value, however, is expected to

be higher (to account for cracking) and a typical value of unity is usually used. Under certain conditions, pellet-clad interlocking can develop as a result of eccentrically positioned fuel column, fuel chips, material bonding, etc., where no significant relative slip can occur. This situation can be simulated in the analysis by specifying high value ( $> 100$ ) for  $\mu$ .

The fuel-fuel contact elements and the plenum springs are treated in the same manner.

#### 4.3.5 Incremental Stress-Strain Relations

The complete derivation of the incremental stress-strain relations is rather lengthy and is therefore included in Appendix C. It is sufficient in this section to state the final result in the following form:

$$\Delta \tilde{\sigma} = \tilde{H} \Delta \tilde{\varepsilon} - \tilde{R} \quad (\text{eq. 4-27})$$

where  $\tilde{H}$  is the material constitutive matrix and  $\tilde{R}$  is an internal stress vector.

### 4.4 Equilibrium Equations

The equilibrium equations are derived for the finite element system using the variation of the principle of virtual work. The details of the derivations are given in Appendix C. The final results are stated here as follows:

$$\Delta \tilde{F} = \tilde{K} \Delta \tilde{v} \quad (\text{eq. 4-28})$$

where  $\Delta \tilde{F}$  is the incremental nodal force vector,  $\Delta \tilde{v}$  is the incremental nodal displacement vector and  $\tilde{K}$  is the tangent stiffness matrix. Both  $\Delta \tilde{F}$  and  $\tilde{K}$  are dependent upon the thermal and deformation states of the fuel rod; hence, the solution of eq. 4-28 may be sensitive to the step size. This is discussed in Section 6.

## 4.5 References

1. Hagrman, D. L., "MATPRO - Version 11: A Handbook of Materials Properties for Use in the Analysis of Light Water Reactor Fuel Rod Behavior," NUREG/CR-0497 TREE-1280, February 1979.
2. Rashid, Y. R., Tang, H. T., Johansson, E. B., "Mathematical Treatment of Hot Pressing of Reactor Fuel," *Nuclear Engineering and Design*, Vol. 29, No. 1, November 1974.
3. Drucker, D. C. and Prager, W., "Soil Mechanics and Plastic Analysis or Limit Design," *Quarterly of Applied Mathematics* 10, 1952, pp. 157-165.
4. Prager, W., "The Theory of Plasticity: A Survey of Recent Achievements," *Proc. Inst. Mech. Eng.* 169, 1955, p. 41.

# 5

## MATERIAL AND PHYSICAL MODELS

---

This section presents an overview of the material and physical models used in FALCON to represent the behavior of the  $\text{UO}_2$  pellet, Zircaloy cladding, and the internal gas during normal operation and transient events. The most important part of any fuel rod analysis program is the material property models and behavioral models used to represent the response of a fuel rod to the irradiation environment. Integrating the interplay of these models through the numerical analysis method and geometric representation is the main objective of a fuel rod analysis program. More than forty material property and behavioral models are used in FALCON to calculate the thermal and mechanical behavior of the pellet and cladding. Only the main models of specific interest are described below. Further details of all the material property and behavioral models used in FALCON can be found in the references contained at the end of this section.

The material properties and behavior models used in FALCON were obtained from a variety of sources, including the MATPRO–11, Rev. 0 and Rev. 2 packages developed by the US NRC [1, 2], models published in the open literature or developed through industry research activities such as the Nuclear Fuel Industry Research (NFIR) program [3], and several from the ESCORE code package [4]. A listing of the thermal and mechanical properties models and the behavioral models used in FALCON are shown in Tables 5-1 through 5-3, along with an indication of the source of the model and some of the primary model dependencies.

The models shown in Tables 5-1 through 5-3 provide the material properties for use directly in the finite element matrices or to quantify parameters of the constitutive theory described in Sections 3 and 4 of this document. Because of the dependence of the material properties on spatially and temporally varying quantities, such as temperature, fast fluence, burnup, stress level, etc., the material property routines are called at each time and iteration step, and for each integration point in the element. This allows a much greater degree of material variability than is indicated by the mesh density.

## Material and Physical Models

**Table 5-1**  
**Thermal Property Models Used in FALCON**

<i>Material</i>	<b>Property</b>	<b>Source</b>	<b>Primary Dependency</b>
Fuel	Specific Heat Capacity Thermal Conductivity Emissivity Melting Temperature	MATPRO MATPRO and Literature MATPRO Literature	Temperature, Stoichiometry Temperature, Burnup, Porosity, Gadolinia Temperature Temperature, Burnup
Cladding	Specific Heat Capacity Zircaloy Thermal Conductivity ZrO <sub>2</sub> Thermal Conductivity Zirconium Dioxide Emissivity Melting Temperature	MATPRO MATPRO Literature and MATPRO MATPRO MATPRO	Temperature Temperature Temperature Temperature, Oxide Layer Thickness
Gap	Gas Thermal Conductivity Gas Viscosity Temperature Jump Distance	MATPRO MATPRO Literature	Temperature, Gas Molar Fractions Temperature, Pressure, Gas Molar Fractions Temperature, Pressure, Gas Molar Fractions



**Table 5-2**  
**Mechanical Property Models Used in FALCON**

<i>Material</i>	<b>Property</b>	<b>Source</b>	<b>Dependency</b>
Fuel	Thermal Expansion Young's and Shear Modulus Compressive Yield Stress Fracture Strength Thermal/Irradiation Creep Densification Swelling Relocation	MATPRO MATPRO Literature MATPRO MATPRO MATPRO and ESCORE Literature ESCORE	Temperature, PuO <sub>2</sub> content Temperature Temperature Temperature Temperature, fission rate stoichiometry, stress Temperature, Burnup, initial density Burnup Burnup, power level
Cladding	Thermal Expansion Young's Modulus Shear Modulus Yield Stress Plastic Strain Hardening Annealing Meyer Hardness Thermal/Irradiation Creep Irradiation Growth	MATPRO MATPRO MATPRO MATPRO MATPRO MATPRO MATPRO MATPRO, ESCORE, Literature MATPRO, ESCORE, Literature	Temperature Temperature, Fluence, Cold Work, Oxygen Content Temperature, Fluence, Cold Work, Oxygen Content Temperature, Fluence, Cold Work, Oxygen Content Temperature, Fluence, Cold Work, Oxygen Content Temperature Temperature Temperature, Fluence, Fast Flux, Cold Work, stress Temperature, Cold Work, Fluence

**Table 5-3**  
**Behavioral Models Used in FALCON**

<i>Material</i>	<b>Behavioral Models</b>	<b>Source</b>	<b>Dependency</b>
Fuel	Steady State Fission Gas Release Transient Fission Gas Release Radial Power Distribution High Burnup Structure	Literature Literature Literature Literature	Temperature, Burnup, Grain Size Temperature, Burnup Grain Size Burnup, Enrichment, Plutonium Content, Gadolinia content Burnup
Cladding	Low Temperature Oxidation (Water) High Temperature Oxidation (Steam) Phase Transformation Stress Corrosion Cracking High Temperature Rupture	Literature MATPRO MATPRO Literature Literature	Temperature, Cladding, Type, Coolant Chemistry, Fluence Temperature Temperature Temperature, Stress, Cladding Type Temperature and Stress
Gap	Open and Solid Gap Conductivity	Literature	Gap Size, Interfacial Pressure, Gas Molar Fractions

## 5.1 UO<sub>2</sub> Fuel Material Properties & Behavioral Models

### 5.1.1 Melting Temperature Model

The UO<sub>2</sub> melting temperature expression used in FALCON includes the effect of local burnup. The model is based on recent data obtained from irradiated UO<sub>2</sub> material and analytical evaluations for mixed chemical compositions. The newer expression used in FALCON was selected instead of the older MATPRO model. The burnup dependency of the UO<sub>2</sub> melting temperature expression in MATPRO-11 is based on experiments conducted by Christensen in 1965 [5]. The burnup dependency of the melting temperature in the MATPRO-11 model is considerably stronger than that observed in recent experiments on high burnup fuel.

A recent review of the UO<sub>2</sub> melting temperature data by Philipponeau at CEA and experiments by Yamanouchi and Komatsu from NFD have shown that burnup has only a limited impact on the UO<sub>2</sub> melting temperature [6, 7, 8]. Measurements by Yamanouchi on UO<sub>2</sub> and UO<sub>2</sub>-2wt%Gd<sub>2</sub>O<sub>3</sub> fuel samples irradiated to 30 GWd/MTU found no decrease in the UO<sub>2</sub> melting temperature with burnup. Komatsu conducted measurements on mixed oxide UO<sub>2</sub>-20wt% PuO<sub>2</sub> fuel specimens up to a burnup 200 GWd/MTM. A slight decrease of the melting temperature was observed above 50 GWd/MTM for the mixed oxide material. Figure 5-1 shows a comparison of the Yamanouchi UO<sub>2</sub> data with earlier measurements by Christensen [5], and Figure 5-2 shows a comparison of the UO<sub>2</sub>-20wt% PuO<sub>2</sub> from Komatsu with earlier data from Krankota and Craig [9].

Phillipponeau conducted a theoretical evaluation using a mixed chemical composition of U, Pu, and fission products [6, 10]. Using the ideal solid solution method to evaluate the melting temperature of a mixed chemical composition material, Phillipponeau was able to evaluate the separate effects of solid fission products and Pu on the melting temperature. For UO<sub>2</sub>, the decrease in the melting temperature was determined to be 7.6°C/10 GWd/MTU. In comparison to the data for both UO<sub>2</sub> and UO<sub>2</sub>-20wt%PuO<sub>2</sub>, the decrease with burnup determined by Phillipponeau appears to over-estimate the burnup impact on the UO<sub>2</sub> melting temperature. The UO<sub>2</sub> melting temperature expression recommended by Phillipponeau is given by:

$$T_m(\text{UO}_2) = 2847^\circ\text{C} - 7.6^\circ\text{C}/10 \text{ GWd/MTU} \quad (\text{eq. 5-1})$$

Equation 5-1 is used in FALCON to calculate the UO<sub>2</sub> melting temperature as a function of local burnup. The local burnup at each nodal location is obtained from the radial burnup distribution calculated using either the RADAR-G or TUBRNP models, or defined via input. As a result, the UO<sub>2</sub> melting temperature can vary across the radius of the pellet and the axial dimension of the fuel column.

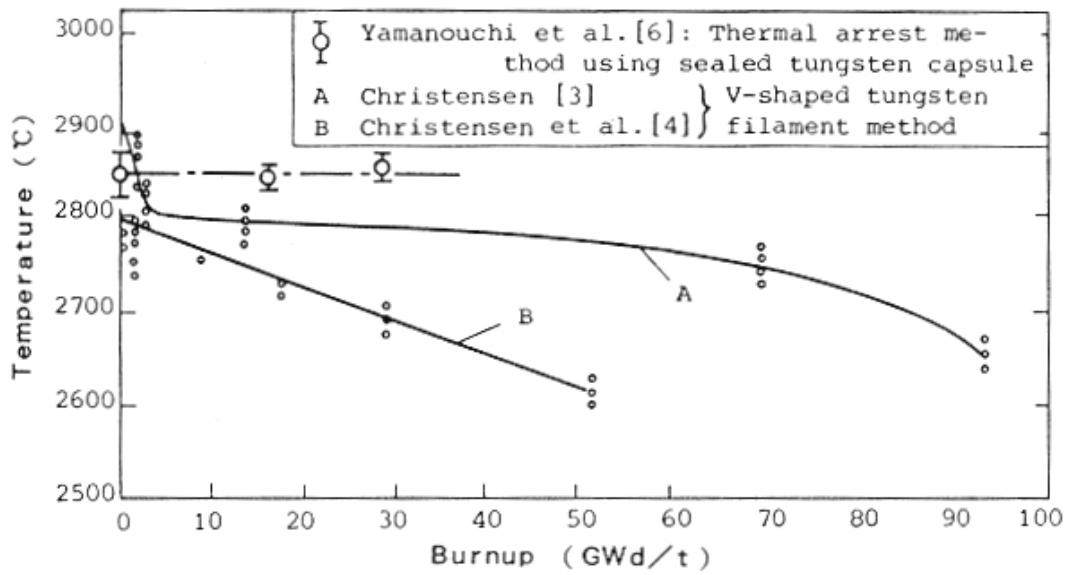


**Figure 5-1**  
**Comparison of Yamanouchi  $\text{UO}_2$  Melting Temperature Data to Earlier Measurements by Christensen [5]. References in Figure Are Defined in Reference 5. Yamanouchi Measurements Display No Burnup Dependency out to 30  $\text{GWd/MTU}$ .**

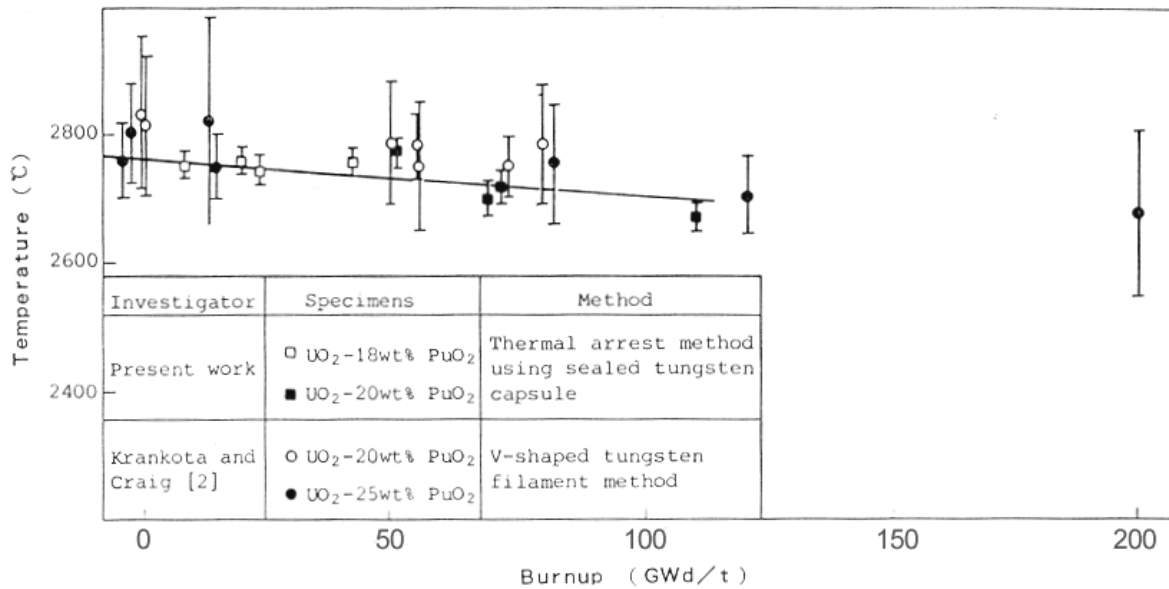


**Figure 5-2**  
**Comparison of Komatsu Data for Mixed Oxide Melting Temperature Data to Earlier Measurements by Krankota and Craig [9]. The Data Show a Slight Burnup Dependency beyond a Burnup of 50  $\text{GWd/MTU}$ .**

### 5.1.2 Thermal Conductivity

The uranium dioxide (UO<sub>2</sub>) thermal conductivity is required to calculate the temperature distribution across the fuel pellet. The thermal conductivity of unirradiated uranium dioxide is primarily a function of temperature, porosity, stoichiometry and the presence of additives such as gadolinia. Irradiation experiments performed with fuel rods containing fuel centerline thermocouples have shown a progressive degradation of the UO<sub>2</sub> thermal conductivity as a consequence of irradiation damage and build up of fission products [11]. Furthermore, recent separate effects tests conducted to measure the thermal diffusivity of irradiated miniature fuel specimens have found a strong impact of burnup on the UO<sub>2</sub> thermal conductivity. Because thermal conductivity has a direct effect on fuel temperatures and thus fuel performance, it is important to include the degradation with burnup in fuel analysis methods. Several different UO<sub>2</sub> thermal conductivity models have been developed and incorporated into other fuel performance codes [12-14].

Two different UO<sub>2</sub> thermal conductivity models are available in FALCON. First, the MATPRO-11 Rev. 0 model combined with a burnup degradation factor from ESCORE is available in FALCON [1, 4]. Second, the model developed by Turnbull from thermal diffusivity measurements performed under the Nuclear Fuel Industry Research (NFIR) program has been incorporated into FALCON [15]. A brief description of each model is given below.

#### 5.1.2.1 MATPRO Revision 11 Model Modified for Burnup

The MATPRO-11 expression consists of a low temperature term representing phonon-phonon and phonon-defect scattering and a high temperature term representing electronic conduction. The equations from MATPRO-11 for UO<sub>2</sub> thermal conductivity are [1]:

$$k_{\text{mat}} = P \left[ \frac{K_1}{K_2 + T} + K_3 e^{K_4 T} \right] \quad \text{for } T < 1650 \text{ } ^\circ\text{C} \quad (\text{eq. 5-2})$$

$$k_{\text{mat}} = P \left[ K_5 + K_3 e^{K_4 T} \right] \quad \text{for } 1650 \text{ } ^\circ\text{C} \leq T < T_{\text{melt}} \quad (\text{eq. 5-3})$$

where

$k_{\text{mat}}$ : Unirradiated thermal conductivity (W/m-K)

P: Porosity correction factor (unitless)

T: Temperature (°C)

$K_1 = 4040$

$K_2 = 464$

$K_3 = 0.1216$

$K_4 = 1.867 \times 10^{-3}$

$K_5 = 1.91$

The porosity correction factor, P, is given by

$$P = \frac{1 - \beta(1 - D)}{1 - \beta(1 - 0.95)} \quad (\text{eq. 5-4})$$

where

$\beta$ : Porosity coefficient ( $2.58 - 0.58 \times 10^{-3} T$ )

D: Fraction of theoretical density (unitless)

T: Temperature ( $^{\circ}\text{C}$ )

The thermal conductivity model from MATPRO-11 was developed from a large database of thermal conductivity measurements on unirradiated  $\text{UO}_2$  material [1]. Although most of the data used to develop the MATPRO-11 expressions were obtained in the 1960's and 1970's, a recent review by Baron demonstrates that the model continues to agree well with recent thermal diffusivity measurements up to 2200 K on unirradiated  $\text{UO}_2$  material [16].

FALCON uses the expressions given in equations 5-2 through 5-4 to calculate the  $\text{UO}_2$  thermal conductivity as a function of the local temperature and porosity at each integration point within the fuel element grid. However, the expression from MATPRO-11 does not consider the effect of burnup on the thermal conductivity of irradiated material.

FALCON includes a burnup reduction factor on the  $\text{UO}_2$  thermal conductivity that is applied to the expressions given in equations 5-2 and 5-3. To be consistent with the EPRI steady state fuel performance code ESCORE, the burnup reduction factor from ESCORE has been incorporated into FALCON [4, 17]. The burnup reduction factor from ESCORE was derived from fuel centerline thermocouple measurements in Halden as a multiplier on the total thermal conductivity. The  $\text{UO}_2$  thermal conductivity model for irradiated material in FALCON is:

$$k_{\text{irr}} = (T, P, \text{Bu}) = k_{\text{mat}}(T, P) \cdot f(\text{Bu}) \quad (\text{eq. 5-5})$$

where

$$\begin{aligned} f(\text{Bu}) &= 1 - 5.0 \times 10^{-6} \text{Bu} & 0 \leq \text{Bu} \leq 2.0 \times 10^4 \\ f(\text{Bu}) &= 0.9 - 4.0 \times 10^{-6} (\text{Bu} - 2 \times 10^4) & 2.0 \times 10^4 < \text{Bu} \leq 3.0 \times 10^4 \\ f(\text{Bu}) &= 0.86 & 3.0 \times 10^4 < \text{Bu} \end{aligned}$$

and

Bu: Pellet average burnup (MWD/MTU)

The burnup reduction factor in FALCON is applied to both the low-temperature and high temperature expressions from MATPRO-11. As shown above, the maximum reduction in  $\text{UO}_2$  thermal conductivity used in FALCON is 14% at pellet average burnup levels above 30 GWd/MTU. Recent thermal diffusivity measurements and centerline thermocouple measurements on fuel material with burnup levels above 40 GWd/MTU show that the burnup

effect on thermal conductivity continues to increase, particularly at temperatures below 1000 K [11, 13, 18]. Reductions as high as 40% have been observed at a burnup level of 60 GWD/MTU at temperatures below 1000 K. At temperature levels above 1000 K, the influence of burnup on the  $\text{UO}_2$  thermal conductivity decreases to less than 20% at 1500 K and 10% at 2500 K, based on the Wiesenack model [11, 16]. Unfortunately, no data exist on the thermal conductivity of irradiated  $\text{UO}_2$  at temperature levels above 2000 K. The application of the burnup reduction factor to the high temperature term in eq. 5-3 may overestimate the reduction in thermal conductivity at high temperatures. This only affects FALCON calculations for transients and postulated accidents that result in fuel temperatures above 2000 K.

### 5.1.2.2 NFIR Thermal Conductivity Model

The NFIR thermal conductivity model provides a more accurate treatment of the burnup and burnable poison additives impact on fuel thermal conductivity than the MATPRO-11 model discussed above. The NFIR thermal conductivity model in FALCON is a modified version of an empirical expression developed by Tony Turnbull from thermal diffusivity measurements performed using miniature  $\text{UO}_2$  specimens irradiated to burnup levels between 28 and 80 GWd/MTU [15]. Details of the original thermal conductivity expression are contained in Reference 15. The empirical model developed by Turnbull was modified to include the effects of gadolinia additives in the fuel using recent thermal diffusivity measurements on unirradiated and irradiated  $\text{UO}_2\text{-Gd}_2\text{O}_3$  miniature specimens with gadolinia enrichments between 4% and 12%.

As mentioned above, heat conduction through solids typically occurs as a combination of lattice conduction by phonons and electron conduction. Based on this, the general formula for thermal conductivity is given by:

$$K = K_{\text{ph}} + K_{\text{el}} \quad (\text{eq. 5-6})$$

The lattice conduction by phonons ( $K_{\text{ph}}$ ) is represented empirically by:

$$K_{\text{ph}} = \frac{1}{A + B T} \quad (\text{eq. 5-7})$$

where the model coefficient A describes the effect of phonon scattering by lattice impurities or discontinuities and the model coefficient B describes the effects of phonon-phonon collisions.

The electron conduction ( $K_{\text{el}}$ ) is given by:

$$K_{\text{el}} = C e^{D T} \quad (\text{eq. 5-8})$$

where the model coefficients C and D have been determined empirically by Christensen.

In  $\text{UO}_2$ , the primary mode of heat transfer is through lattice conduction by phonon processes at temperatures below 1600°C. Heat transfer by electron conduction begins beyond 1600°C, once

the mobility increases for electron-vacancy pairs. Since fuel rods normally operate at temperatures below 1600°C, the main focus of recent experiments and analytical work has been to identify the impact of burnup on the lattice conduction processes. Burnup accumulation causes an increase in the irradiation damage and fission product impurities within the  $\text{UO}_2$  matrix. These factors increase the number of phonon scattering sites, resulting in a decrease in the thermal conductivity.

Thermal diffusivity experiments on both irradiated  $\text{UO}_2$  and unirradiated  $\text{UO}_2$  material containing simulated fission products indicate that both the coefficients A and B in eq. 5-7 are a function of burnup [12, 19]. Turnbull used experimental results obtained from thermal diffusivity measurements on  $\text{UO}_2$  samples irradiated at temperatures below 800°C and burnups between 28 and 67 GWd/MTU to determine the coefficients A and B as a function of burnup. The thermal diffusivity experiments used by Turnbull to develop the burnup dependency of the A and B coefficients displayed a measurable recovery of the thermal conductivity upon heating to temperatures above 800°C due to annealing of fission products and point defects [15]. As a result, the coefficients A and B have a complex burnup dependency that includes an empirical function representing the thermal recovery process. The resulting thermal conductivity as a function of burnup is given by;

$$K(\text{Bu}) = (1 - F) \cdot K_{\text{start}} + F \cdot K_{\text{end}} + K_{\text{el}} \quad (\text{eq. 5-9})$$

where  $K_{\text{start}}$  is the lattice conductivity before thermal recovery,  $K_{\text{end}}$  is the lattice conductivity after recovery, F is the empirically-derived thermal recovery function, and  $K_{\text{el}}$  is given by eq. 5-8. The lattice conductivity before thermal recovery is given by;

$$K_{\text{start}} = \frac{1}{A_1 + A_2 \cdot \text{Bu} + A_3 \cdot \text{Bu}^2 + [B_1 - B_2 \cdot \text{Bu}] \cdot T} \quad (\text{eq. 5-10})$$

where the model coefficients  $A_1$ ,  $A_2$ ,  $A_3$ ,  $B_1$ , and  $B_2$  are shown in Table 5-4, Bu is the local burnup in GWd/MTU, and T is temperature in °C. Similarly, the lattice conductivity after thermal recovery is given by;

$$K_{\text{end}} = \frac{1}{A_1 + A_4 \cdot \text{Bu} + [B_1 - B_3 \cdot \text{Bu}] \cdot T} \quad (\text{eq. 5-11})$$

where the model coefficients  $A_4$  and  $B_3$  are shown in Table 5-4.

The thermal recovery function, F, was developed to represent the transition between no recovery of irradiation damage and full recovery of irradiation damage. The function is given by;

$$F = 0.5 \left( 1 + \tanh \left( \frac{T - 900}{150} \right) \right) \quad (\text{eq. 5-12})$$

As can be seen by eq. 5-12, the thermal recovery process is completed by ~1200°C.



As mentioned previously, burnable poison additives to the  $\text{UO}_2$  matrix also impacts the thermal conductivity. Similar to burnup, the effect of alloying additions such as gadolinium is primarily limited to the lattice conductivity where the gadolinium impurities increase phonon scattering sites. To account for the impact of  $\text{Gd}_2\text{O}_3$ , equations 5-9 through 5-11 were modified to include the effects of gadolinium on the A and B coefficients. In modifying the thermal conductivity model developed by Tony Turnbull, it was assumed that the effect of burnup and gadolinium additions on the lattice conductivity can be summed together. Based on this assumption, the new form of the phonon conductivity equations 5-10 and 5-11 become:

$$K_{\text{ph}} = \frac{1}{A(\text{Bu}) + A'(\text{Gd}) + (B(\text{Bu}) + B'(\text{Gd}))T} \quad (\text{eq. 5-13})$$

where the coefficients  $A(\text{Bu})$  and  $B(\text{Bu})$  are the same as that shown in Eqs 5-10 and 5-11. Several datasets of thermal diffusivity measurements on unirradiated  $\text{UO}_2\text{-Gd}_2\text{O}_3$  samples with gadolinia concentrations ranging between 2 and 12 wt% were used to develop the coefficients  $A'$  and  $B'$  in eq 5-13. These datasets are described in References 20-22. The  $A'$  coefficient as a function of gadolinium is given by;

$$A'(\text{Gd}) = (A_5 + A_6 \cdot \text{Gd} + A_7 \cdot \text{Gd}^2 + A_8 \cdot \text{Gd}^3) \quad (\text{eq. 5-14})$$

where Gd is the initial gadolinium concentration in wt% and the coefficients  $A_5$ ,  $A_6$ ,  $A_7$ , and  $A_8$  are shown in Table 5-4. Furthermore, the  $B'$  coefficient as a function of gadolinium is given by;

$$B'(\text{Gd}) = B_1 \cdot e^{B_4 \cdot \text{Gd}} \quad (\text{eq. 5-15})$$

where the coefficient  $B_1$  and  $B_4$  are shown in Table 5-4.

**Table 5-4**  
**Model Coefficients for the Modified NFIR UO<sub>2</sub> Thermal Conductivity Model**

Model Constant	Value
A1	9.592E-2
A2	6.14E-3
A3	-1.4E-5
A4	2.6E-3
A5	1.197E-1
A6	1.214167E-2
A7	5.40625E-4
A8	-5.182292E-5
B1	2.5E-4
B2	-1.81E-6
B3	-2.7E-7
B4	-1.268763E-2
C	1.32E-2
D	1.88E-3

Thermal diffusivity measurements are also available for irradiated UO<sub>2</sub>-Gd<sub>2</sub>O<sub>3</sub> material in the burnup range between 28 and 60 GWd/MTU [23-24]. Comparison of eq. 5-13 with the data from irradiated gadolinia samples in Reference 23 and 24 and analysis of instrumented UO<sub>2</sub>-Gd<sub>2</sub>O<sub>3</sub> fuel rods in Halden found that the combined effects of gadolinium and burnup included in eq. 5-13 resulted in a lower thermal conductivity than expected from the data or thermocouple measurements. As a result, a burnup adjustment factor was developed that decreases the gadolinium effect for irradiated fuel at burnup levels greater than 28 GWd/MTU. It was found that the gadolinium impact on thermal conductivity diminishes as burnup accumulates. The burnup adjustment factor is multiplied on the coefficient A' shown in eq 5-14 and is given by.

$$\eta_{gd} = 0.26 \cdot e^{\frac{28.5875}{Bu+19.8085}} \quad (\text{eq. 5-16})$$

where Bu is the burnup in GWd/MTU. Equation 5-16 is applied at burnup levels beyond 28 GWd/MTU.

The modified NFIR model shown above was normalized to material with 95% theoretical density. For application to material with a different amount of porosity, eq. 5-4 is used to account for porosity effects. The modified NFIR model is used to calculate the thermal conductivity at each integration point within the fuel element model used in FALCON. As a

result, the local burnup corresponding to the radial position of the integration point is used in the NFIR model. This burnup value is calculated based on the radial power distribution.

The fuel centerline temperature calculated by FALCON for two instrumented fuel rods irradiated in the Halden reactor are presented in Figures 5-3 and 5-4 to highlight the differences between the modified MATPRO and modified NFIR thermal conductivity models [25]. Figure 5-3 shows the results for the  $\text{UO}_2$  rod A1 in IFA-515.10 irradiated to a burnup of  $\sim 75$  GWd/MTU. The FALCON results using the modified NFIR model shows excellent agreement with the thermocouple data, validating the burnup dependency of the thermal conductivity. However, the modified MATPRO model results in an under-prediction of the fuel centerline temperature at rod average burnup levels beyond 20 GWd/MTU. These results indicate that the burnup degradation factor used in the modified MATPRO model is insufficient for this case.

Figure 5-4 shows the results for the  $\text{UO}_2\text{-Gd}_2\text{O}_3$  rod A2 in IFA-515.10 irradiated to a burnup of 92 GWd/MTU. The FALCON results using the modified NFIR models show good agreement with the thermocouple data at burnup levels up to 70 GWd/MTU. Beyond this burnup range, the FALCON results are 150 to 200°C higher than the measured data. These differences could be attributed to errors in the thermocouple measurements. These results validate the combined effects of burnup and gadolinium contained in the modified NFIR model.

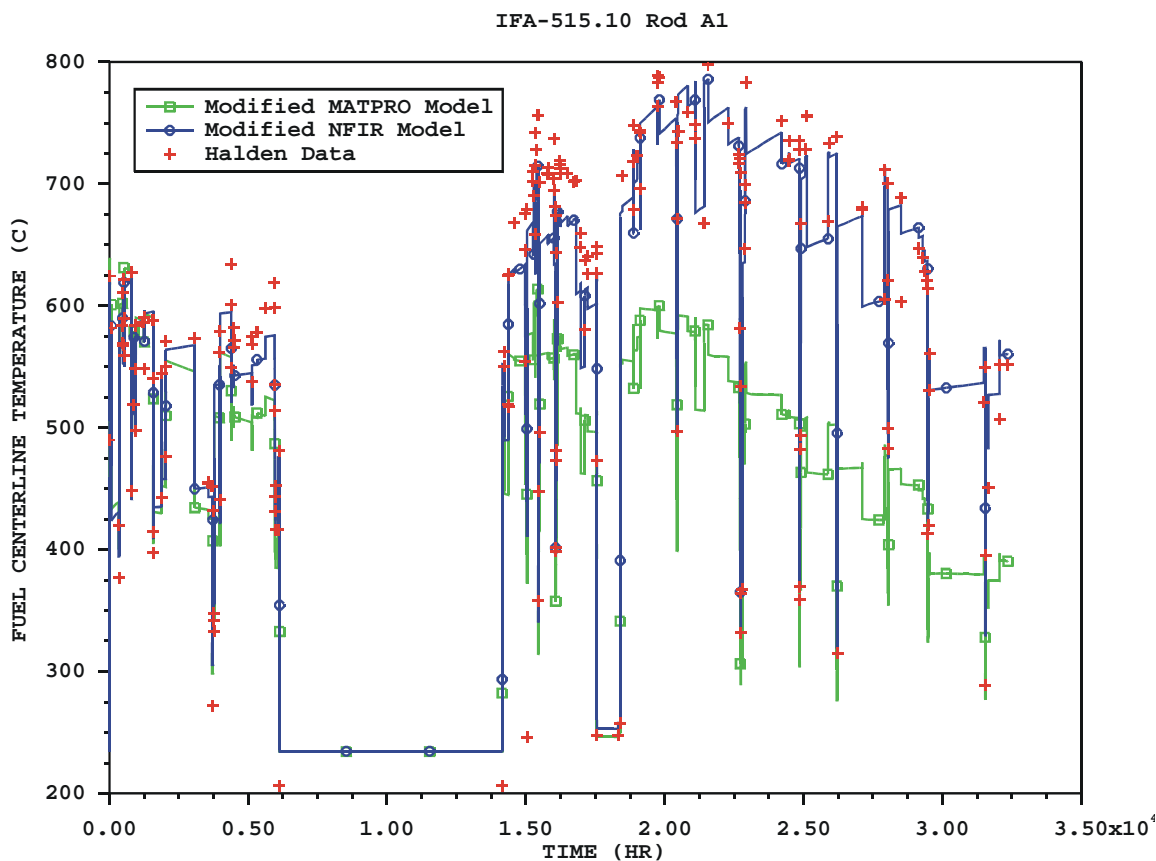


**Figure 5-3**  
**Comparison of Fuel Centerline Temperature as a Function of Irradiation Time for IFA 515.10, Rod A1 ( $\text{UO}_2$  Rod) for the MATPRO and NFIR Fuel Thermal Conductivity Models**

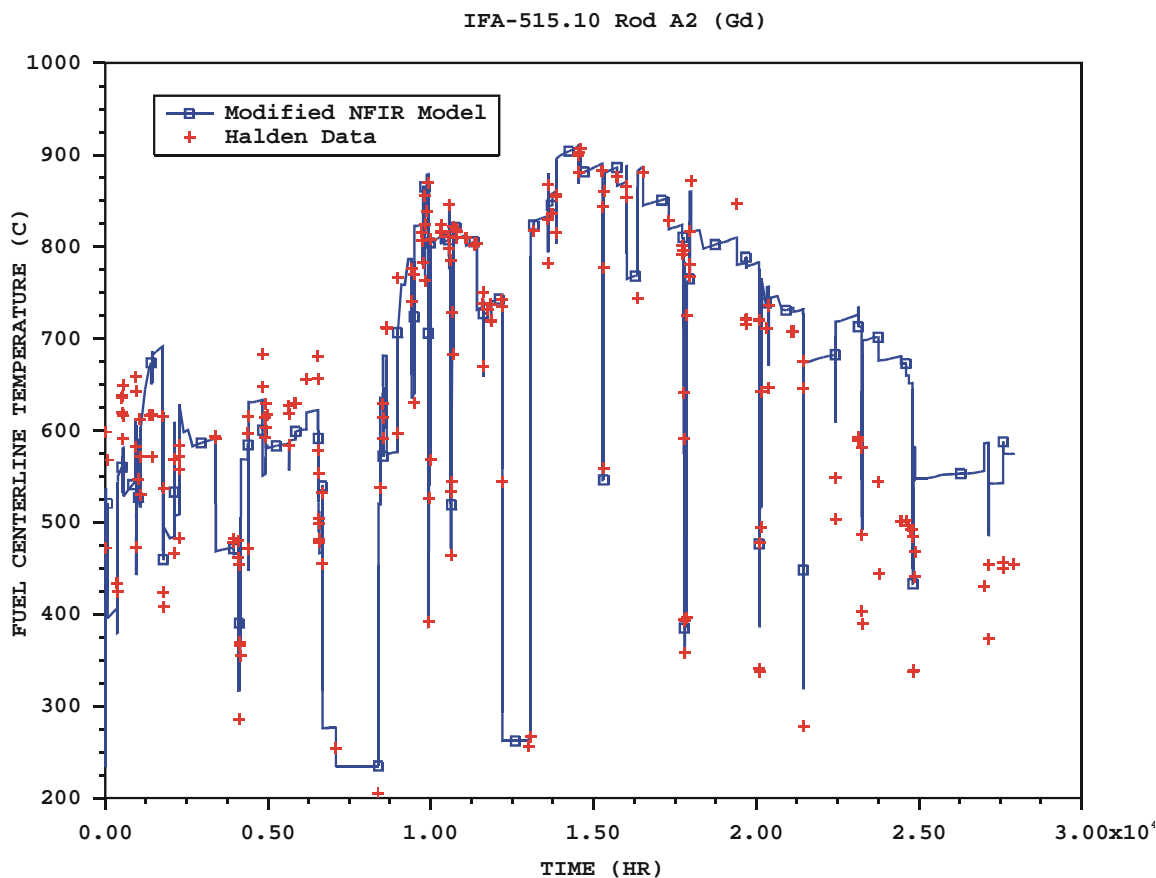


**Figure 5-4**  
**Comparison of Fuel Centerline Temperature as a Function of Irradiation Time for IFA**  
**515.10, Rod A2 (UO<sub>2</sub>-Gd<sub>2</sub>O<sub>3</sub> Rod) for the modified NFIR Fuel Thermal Conductivity Model**

### 5.1.3 Swelling Model

Fuel swelling is the phenomenon that occurs when fission product atoms force themselves into the lattice structure of the fuel and displace more volume than their fissile parents. Approximately, half of the solid fission products remain interstitially in the fuel lattice after formation, causing volumetric swelling. Gaseous fission products can also accumulate in the fuel lattice and result in a positive volume change. At low fuel temperatures, gaseous swelling is limited. As the fuel temperature rises, the fission gas bubbles agglomerate and grow in size, displacing more fuel. At even higher temperatures, fission gas release from the fuel matrix to the rod open void volumes counteracts the bubble growth and fuel displacement, thus decrease the swelling rate. At the highest temperatures, essentially all of the fission gas is released and no gaseous swelling is observed.

Fuel swelling is also dependent on the high burnup structure formation in the outer periphery of the fuel pellet. This region is termed the “rim region” and is often characterized by high concentration of porosity. The increase in porosity is associated with an increase in bubble size, which have an obvious influence on the overall fuel pellet dimensional changes. Recent data from Bremier et al. [26] indicates that the fuel swelling rate changes dramatically beyond local

burnup of ~70 GWd/MTU as shown in Figure 5-5. The FALCON fuel swelling model was developed using the work of Turnbull [27] and several data sets including NFIR U- and G- series data (excluding the gadolinium [Gd]-doped fuel), and EDF UO<sub>2</sub> data from Blanpain, et al. [28]. A linear correlation was developed for the entire dataset as,

$$d(\%TD) = 96.14 - 5.64E-2 * BU(MWd/KgU) \quad (\text{eq. 5-17})$$

For high burnup (>60 MWd/KgU), the following correlation, derived from the local correlation of Lassmann, HBRP, and Une [29] high restraint swelling data, is used

$$d(\%TD) = 93.35 - 0.171 * (BU(MWd/KgU) - 60) \quad (\text{eq. 5-18})$$

These correlations apply to solid swelling of irradiated UO<sub>2</sub> and apart from the porosity generated by rim restructuring, do not include intra-granular gas bubble swelling. Based on the above correlations, the change in density corresponds simply to the volume increase according to the following equation

$$\left( \frac{\Delta V}{V} \right)_{ur} = d_{t_0} / d_{t_1} - 1 \quad (\text{eq. 5-19})$$

Where,  $\left( \frac{\Delta V}{V} \right)_{ur}$  is the unrestricted volumetric swelling, and  $d_{t_0}$  and  $d_{t_1}$  are UO<sub>2</sub> pellet density at two successive time steps obtained from equations 5-17 and 5-18. The local burnup at the radial position of the integration points is used to calculate the solid swelling. Results using these correlations in FALCON is also shown in Figure 5-5.

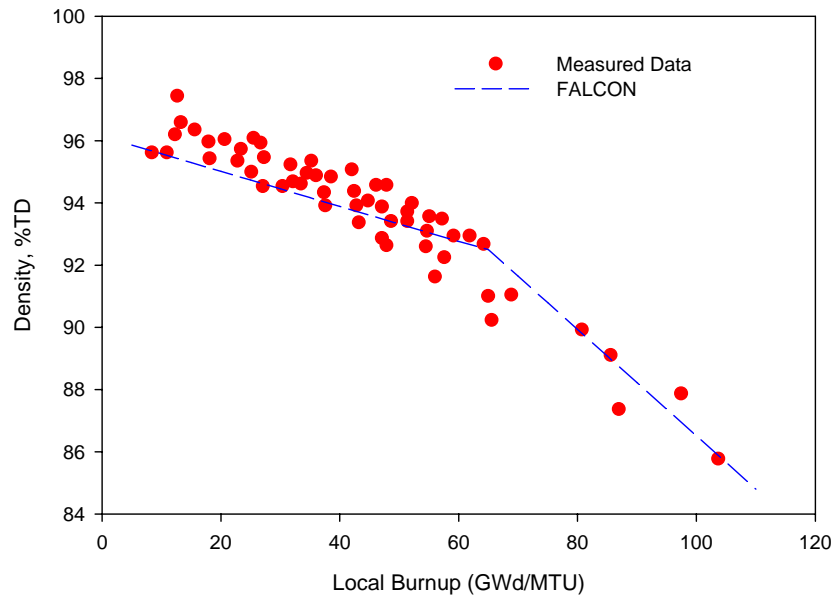


**Figure 5-5**  
**Comparison of Measured Density to the FALCON Fuel Swelling Model as Function of Burnup for UO<sub>2</sub> fuel.**

Accommodation of fuel swelling is the redistribution of expanding fuel into fuel internal void volumes, porosity, dishes, etc. As long as sufficient porosity is available, swelling is accommodated by the fuel pore spaces. Anselin, et al. [30] found a maximum solid swelling rate of 0.13% ( $\Delta V/V$ ) per  $10^{26}$  fissions/ $m^3$  if the fuel completely utilizes the vacancies created or 0.54% ( $\Delta V/V$ ) per  $10^{26}$  fissions/ $m^3$  if none of the vacancies is utilized. Based on these observations, FALCON unrestricted volumetric swelling rate is adjusted for all operating conditions as follows

$$\left(\frac{\Delta V}{V}\right)_r = 0.9 \left(\frac{\Delta V}{V}\right)_{ur} \quad (\text{eq. 5-20})$$

Where  $\left(\frac{\Delta V}{V}\right)_r$  is the restricted volumetric swelling rate. When the fuel-cladding contact is established, the contact pressure restrains the fuel swelling. Turnbull [31] pointed out that restrained fuel swelling is less dependent on both temperature and burnup and virtually unaffected by the level of restraint. Moreover, the effect of restraint is of relevance to different pellet geometries since the hydrostatic pressure is very dependent on the volume available to accommodate the change in pellets. Based on Bettis data [32], 50% of the gaseous swelling is accommodated with pellet-clad interaction. Due to the limited compressibility of solid fission products, only 10% of solid swelling can be accommodated. More recently, Une [29] also explained the effect of PCI restraint on the rim porosity and bubble growth. Fuel pellets with weak restraint force showed larger bubbles (5-6  $\mu m$ ) and high porosity (15-18%) in the rim region, whereas, bubbles size decrease to 2-3 microns and porosity to 7-8% for pellets with strong restrain force. For computational simplicity, a total of 30% swelling accommodation is considered in FALCON calculations and assumed that the rate of accommodation remains constant once a contact pressure is established and is maintained, i.e., the rate of accommodation is not a function of the level of contact pressure. As a result, the specific volume change once pellet-clad contact occurs takes the following form;

$$\left(\frac{\Delta V}{V}\right)_r = 0.7 \left(\frac{\Delta V}{V}\right)_{ur} \quad (\text{eq. 5-21})$$

where the unrestrained swelling is given by eq. 5-17.

#### 5.1.4 **Densification**

Fuel densification is a phenomenon that rapidly removes as-fabricated internal porosity when fuel pellets are irradiated in a reactor. First-generation fuel had a propensity to densify by as much as 4% of theoretical density within the first few thousand MWd/MTU burnup. Recognition of densification mechanisms in the early 1970s led to the development of fuels that are more stable to densification in reactor, and which densify by much less than 1% of theoretical density. Densification causes fuel pellet dimensions to decrease. Pellet dimensional changes have a direct impact on gap conductance and fuel temperature during operation. FALCON contains two models to calculate fuel densification. First, the densification model

from the ESCORE code has been incorporated into FALCON. Second, the densification model from MATPRO is included for completeness. Each of these models are described below.

#### 5.1.4.1 ESCORE Model

The ESCORE model has two options to calculate fuel densification, one that is temperature dependent and one that is temperature independent [4]. The options are the same for fuel average temperatures above 750°C. Below 750°C, the temperature-dependent options give lower densification rates as the temperature is reduced.

Both densification options, are based on two quantities:  $\Delta\rho_D$ , the total amount of densification that can occur as a percent of fuel theoretical density and  $Bu_D$ , the burnup at which densification is complete. These quantities are defined via input. The total densification can be based, for example, on the use of either the NRC-approved thermal resinter test of 24 hours at 1700°C, or a fuel vendor's NRC-approved resinter test conducted for the specific fuel supplied. Typically, most of the fuel densification occurs relatively quickly. Usually, the densification process is more than 75% complete within the first few thousand MWd/MTU burnup. Complete densification typically occurs by about 5000 MWd/MTU.

For each of the two models, the total accrued specific-volume change due to densification at constant temperature operation is:

$$(\Delta V/V_0)_D = \Delta\rho_D [\exp\{Bu \cdot \ln(0.010)/(C \cdot Bu_D)\} - 1] \quad (\text{eq. 5-22})$$

where  $Bu$  is the pellet average, (MWd/MTU).

For the temperature-independent densification model, the value of  $C$  is:

$$C = 1.0 \quad (\text{eq. 5-23})$$

For the temperature-dependent densification model:

$$C = \begin{cases} 1.0 & \text{for } T_f \geq 750^\circ\text{C} \\ 7.2 - 4.3(T_f - 25)/500 & \text{for } T_f < 750^\circ\text{C} \end{cases} \quad (\text{eq. 5-24})$$

where:

$T_f$  : local temperature at an integration point (°C).

The densification model as described above is qualified for application at constant temperature operation. Since fuel temperatures change during the period of fuel densification, a method is required to determine the incremental densification that occurs during each timestep. This increment is then added to the previously accrued specific-volume change due to densification. Further details regarding the ESCORE densification model can be found in Reference [4].

#### 5.1.4.2 MATPRO Model

The MATPRO-11 Rev. 0 densification model calculates fuel dimensional changes due to irradiation induced densification of  $\text{UO}_2$  and  $(\text{U,Pu})\text{O}_2$  fuels during the first few thousand hours of water reactor operation [1]. Densification is calculated as a function of fuel burnup, temperature, and initial density.

The data used to develop the MATPRO densification model were taken from irradiated fuel which also experienced solid swelling. If fuel densification is much greater than swelling during the first thousand hours of irradiation, then as a first approximation, swelling can be neglected during this period. This assumption was made in the development of the MATPRO densification model.

The MATPRO densification model uses one of two methods to calculate the maximum density change during irradiation. The density change observed during a resintering test (1700°C for more than 24 hours) in a laboratory furnace is the preferred input for the densification model. If a resintering density change is not input, the model uses the initial unirradiated density of the fuel and the fuel fabrication sintering temperature. These inputs are used in the following equations to calculate the maximum densification length change during irradiation.

If a nonzero value for the resintering density change is input:

$$\begin{aligned} \left(\frac{\Delta L}{L}\right)_m &= (0.0015) \cdot \Delta\rho_{\text{SNTR}} \quad \text{for } T_f < 1000 \text{ K} \\ \left(\frac{\Delta L}{L}\right)_m &= -(0.00285) \cdot \Delta\rho_{\text{SNTR}} \quad \text{for } T_f \geq 1000 \text{ K} \end{aligned} \quad (\text{eq. 5-25})$$

If zero is input for the resintering density change:

$$\begin{aligned} \left(\frac{\Delta L}{L}\right)_m &= \frac{-22.2(100 - \rho_{\text{TD}})}{T_{\text{SINT}} - 1453} \quad \text{for } T_f < 1000 \text{ K} \\ \left(\frac{\Delta L}{L}\right)_m &= \frac{-66.6(100 - \rho_{\text{TD}})}{T_{\text{SINT}} - 1453} \quad \text{for } T_f \geq 1000 \text{ K} \end{aligned} \quad (\text{eq. 5-26})$$

where

$\left(\frac{\Delta L}{L}\right)_m$ : Maximum possible dimension change of fuel due to irradiation (percent)

$\rho_{\text{TD}}$ : Theoretical density (percent)

$T_f$ : Fuel temperature (K)

$T_{\text{SINT}}$ : Sintering temperature (K)

$\Delta\rho_{\text{SNTR}}$ : Resintered fuel density change ( $\text{kg/m}^3$ ).



Densification as a function of burnup is calculated using

$$\frac{\Delta L}{L} = \left( \frac{\Delta L}{L} \right)_m + \exp[-3(\text{Bu} + B_o)] + 2.0 \exp[-35(\text{Bu} + B_o)] \quad (\text{eq. 5-27})$$

where

$\frac{\Delta L}{L}$  : Dimension change (percent)

Bu: Pellet average burnup (MWd/kgU)

$B_o$ : Constant determined by the sub-code to fit the boundary condition:  
 $\Delta L / L = 0$  when  $\text{Bu} = 0$ .

The MATPRO densification model uses eq. (5-27) to calculate total densification and then subtracts the densification from the previous time step to obtain the incremental densification. Further details of the MATPRO densification model can be found in Reference [1].

### 5.1.5 Relocation

During normal operation of LWR pellet fuel, the large radial temperature gradients cause thermal stresses within the fuel matrix that may exceed the material fracture stress. At sufficient power levels, pellet cracking occurs due to the thermal gradients. Cracking of the fuel pellets causes some of the original fuel-cladding gap to be re-distributed into the pellet in the form of radial cracks. This process is termed fuel relocation and it can impact the pellet temperatures by decreasing the pellet-cladding gap. Experimental data indicate that fuel relocation is a function of the fuel rod design (pellet diameter and gap thickness) and operating conditions (power level, power cycles, and burnup). Because of the consequences on fuel temperatures, fuel rod modeling codes must consider fuel relocation in the thermal calculations.

FALCON includes two different fuel relocation models for use in analyzing fuel rods. In addition, the user can specify via input the initial fuel relocation. The two models available in FALCON are the HEDL model and the ESCORE model. Each of these models are described below.

#### 5.1.5.1 HEDL Model

The HEDL fuel relocation model is provided in FALCON as an option to initialize analyses which start at a non-zero burnup [33]. The HEDL model can be used to estimate the amount of gap closure due to fuel swelling, cracking, and cladding creepdown that occurred during the prior irradiation history.

Data on fuel relocation in LWR power reactors tend to be either proprietary or in a qualitative form unsuitable for model parameterization. The basis for the HEDL relocation model is data from post-irradiation gap thickness measurements from which the following formula was derived [33]:

$$G = G_0 - A_1 \cdot Q \cdot G_0 \cdot (Q - A_2) \cdot (1 - e^{-C}) - A_3 G_0 (1 - e^{-A_4 Q \cdot B}) - A_5 B \quad (\text{eq. 5-28})$$

where

G: Diametral gap (mils)

G<sub>0</sub>: As-manufactured gap (mils)

B: Burnup (MWd/KgU)

Q: Linear power averaged over the time period during which the burnup, B, was accumulated (KW/ft)

C: Number of reactor cycles

$$A_1 = 0.0005224$$

$$A_2 = 5.835$$

$$A_3 = 0.365$$

$$A_4 = 0.0914$$

$$A_5 = 0.00347$$

These values of A<sub>i</sub>'s are based on adopting British units for the variables in eq. 5-28. This equation defines the average initial cold gap which is further modified by the axial power profile on the assumption that fuel relocation is proportional to local power. The results of eq. 5-28 are applied as an initial cold gap to establish the fuel-cladding gap conditions prior to the actual analysis. Modification of the relocation equation by the axial power profile factor is given by

$$G(z, t_0) = P(z) G(t_0) \quad (\text{eq. 5-29})$$

where

G(z, t<sub>0</sub>): Diametral gap at elevation z and time of the start of the analysis t<sub>0</sub>

P(z): Normalized axial power profile such that [P(z)]<sub>max</sub> = unity

G(t<sub>0</sub>): Obtained from eq. 5-28

### 5.1.5.2 ESCORE Relocation Model

The ESCORE fuel relocation model calculates the change in pellet outer diameter caused by pellet relocation during operation [4]. The model considers the effects of power, as-fabricated pellet diameter, as-fabricated gap thickness, and burnup. The model was developed from pellet mean-diameter measurements on fuel rods operated at power level between 8 and 22 kw/ft and to burnup levels between 0 and 11,500 MWd/MTU. The resulting correlation is given as follows;

$$(\% \Delta D / D_o)_{REL} = 0.80 Q (\% G_t / D_o) (0.005 B_u^{0.3} - 0.20 D_o + 0.3) \quad (\text{eq. 5-30})$$

with:

$$Q = \begin{cases} 0 & \text{for } q' \leq 6 \text{ kW / ft} \\ (q' - 6)^{1/3} & \text{for } 6 \text{ kW/ft} < q' \leq 14 \text{ kW / f} \\ (q' - 10)/2 & \text{for } q' > 14 \text{ kW / f}_t \end{cases} \quad (\text{eq. 5-31})$$

where:

$(\% \Delta D/D_o)_{\text{REL}}$ : Percentage change in diameter due to relocation,

$D_o$ : As-fabricated cold diameter of the pellet (in),

$q'$ : Pellet average linear heat rating (kW/ft),

$BU_t$ : Pellet average fuel burnup (MWd/MTU), and

$G_t$ : As-fabricated cold diametral gap (in)

The fuel relocation calculated by eq. 5-30 is applied incrementally within FALCON. This is done by calculating the fuel relocation using eq. 5-30 at the burnup for the current step and subtracting the previous step fuel relocation. If the gap is not closed in the previous step ( $t-\Delta t$ ), but would close with interference for the current time step ( $t$ ) using the incremental fuel relocation value, then a smaller value of relocation is chosen, sufficient to close the gap at the current time step. Once the gap is closed no further relocation is considered unless gap reopening occurs at a later time. The implementation of the ESCORE relocation model into FALCON does not include recovery of relocation strain following gap closure.

### 5.1.6 High Burnup Rim Structure

At a local burnup of 60~75 GWd/MTU, a characteristic microstructure is observed along the outer periphery of the fuel. This high burnup structure (HBS), sometimes referred to as the “rim region” and is often characterized by a high concentration of porosity, loss of definable grain structure, and depletion of fission gas from the  $\text{UO}_2$  matrix into a large collection of fission gas bubbles that are typically 1  $\mu\text{m}$  in diameter. The widespread formation of the high burnup structure in the pellet outer periphery can significantly enhance the thermal fission gas release from this region, as well as, cause an increase in the local fuel swelling. Moreover, this porous rim region can also degrade the  $\text{UO}_2$  thermal conductivity, which has an influence on the fuel temperatures.

A simple model has been implemented into FALCON based on a correlation developed by Lassmann, et al. [34] to calculate the thickness of the high burnup structure at the pellet periphery. This model calculates the rim thickness when the pellet local burnup exceeds a threshold value defined to be 75 GWd/MTU in FALCON. The rim region thickness is calculated based on the radial burnup distribution. The radial burnup distribution is calculated at discrete points in FALCON and the resolution of these points are defined by the user and are independent of the finite element mesh used in the fuel column. Instead of using a linear interpolation to identify the radial position of the HBS threshold burnup, an exponential function is used that

considers the non-linear variation of burnup in the pellet periphery. This function is given below;

$$\text{Rim Width} = \left[ 0.33 \log \left( \frac{B}{6.48 \times 10^6 - A} \right) \right]^{2.22} \quad (\text{eq. 5-32})$$

Where,

$$A = \frac{BU_{in} * e^{-3(RF_{out} - R_{out})^{0.45}} - BU_{out} * e^{-3(RF_{out} - R_{in})^{0.45}}}{e^{-3(RF_{out} - R_{out})^{0.45}} - e^{-3(RF_{out} - R_{in})^{0.45}}}$$

$$B = \frac{BU_{out} - BU_{in}}{e^{-3(RF_{out} - R_{out})^{0.45}} - e^{-3(RF_{out} - R_{in})^{0.45}}}$$

$BU_{in}$  and  $BU_{out}$  are the local burnup in MWs/KgU for two corresponding radial positions of a pellet section.  $RF_{out}$  is the pellet outer radius;  $R_{in}$  and  $R_{out}$  are the inner and outer radius in meters for the two radial positions for the burnup values. When the inner burnup ( $BU_{in}$ ) is equal to the threshold burnup, the entire zone becomes rim and the rim thickness is calculated simply by subtracting the inner radius ( $R_{in}$ ) from the pellet outer radius.

The penetration of the high burnup structure to the fuel pellet increases smoothly with burnup. However, the progression of the re-structuring process and the propagation of the rim zone inwards cannot be correlated to local burnup alone. The local fuel temperature, which controls the dislocation annealing, can also limit the inward propagation of the high burnup structure [35]. The present model neglects the effect of temperature on the growth of the rim zone inward towards the pellet center. Future development of this model is planned to limit the inward growth of the rim region based on the local pellet temperature when more data become available.

## 5.2 Internal Void Volume and Gas Pressure

The internal gas pressure calculation is based on the ideal gas law and instantaneous gas communication between the internal void volumes. The interval void volumes considered in FALCON for internal gas pressure calculations include the upper and lower plena, the fuel-cladding gap, open fuel cracks, open porosity, and user definable fuel-to-fuel pellet gaps. The internal gas pressure calculation includes changes in the internal void volumes due to deformations, such as pellet-cladding gap closure, fuel crack closure, etc. Also changes in the initial internal gas inventory due to fission gas release are included in the gas pressure calculation.

The gas pressure is calculated from the ideal gas law as;

$$P = R \cdot \sum_N \left( \frac{T_i}{V_i} \right) \quad (\text{eq. 5-33})$$

where  $N$  is the number of void volume regions  $P$  is the internal pressure,  $R$  is the specific gas constant,  $T_i$  is the temperature of the  $i^{\text{th}}$  internal void volume, and  $V_i$  is the volume of the  $i^{\text{th}}$  void volume. The specific gas constant is defined as the ratio of the universal gas constant  $R_u$  and the molar mass,  $M_g$ , ie.,

$$R = \frac{R_u}{M_g}$$

The initial molar mass is calculated from the as-manufactured fill pressure, fill temperature and initial void volume. The amount of fission gas moles released to the internal void volume is added to the initial molar mass to yield the total gas moles within the rod,  $M_g$ .

The temperature and volume for each of the internal void volume locations is calculated in FALCON. For the upper and lower plena, the fuel-cladding gap, and the user defined fuel-to-fuel gaps, 2-node elements are used to represent these regions. The gas temperature used in the gas pressure calculations for these void volumes is a linear average of the two nodes. The void volume for each element is calculated using the deformed coordinates of the element. Because multiple elements are used in the fuel-cladding gap, a distribution of temperatures and void volumes are used in the pressure calculation.

The void volume associated with open fuel cracks is defined at each integration point within the fuel column finite element mesh based on the cracking strain calculated in the deformation solution. The gas temperature within the cracks is assumed equal to the fuel temperature at each integration point. The contribution of the open fuel cracks to the rod internal pressure is obtained by summing the volumes and temperature from all the integration points in the fuel. Similarly, the open porosity void volume is distributed across the fuel pellet radius and the pressure contribution is calculated for each integration point using the local temperature. The fuel crack and open porosity void volume is included in the pressure calculation performed in eq. 5-33. At this time, dish and chamfer void volume is not included in the rod internal pressure calculation, unless explicitly represented using two-node fuel-to-fuel gap elements.

The internal void volume and gas pressure calculation is performed at the end of the timestep following completion of the thermal solution, mechanical solution, and fission gas release calculations.

## 5.3 Clad Material Properties & Behavioral Models

### 5.3.1 Zircaloy and $ZrO_2$ Thermal Conductivity

FALCON uses the Zircaloy thermal conductivity model from MATPRO to determine the cladding thermal conductivity as a function of temperature which is used to form the matrices in the heat conduction solution described in Section 3.1. In calculating the cladding temperature distribution, the resistance to heat flow caused by the presence of an oxide layer on the outer surface is not considered in FALCON. However, the zirconium oxide thermal conductivity is used within the cladding oxidation model described in Section 5.3.5.1 to calculate the metal-oxide interface temperature. For this model, two options are available to calculate the thermal conductivity of zirconium oxide. First, the zirconium oxide thermal conductivity model from the most recent version of MATPRO is used in FALCON. Second, recent measurements obtained in the NFIR program have been used to establish the  $ZrO_2$  thermal conductivity. The following briefly summarizes the cladding and oxide thermal conductivity models used in FALCON.

#### 5.3.1.1 Zircaloy Thermal Conductivity

The MATPRO-11 Rev. 2 Zircaloy thermal conductivity model used in FALCON is a function of temperature [2]. For temperature below 2098 K, the thermal conductivity is given by;

$$K = 7.51 + 2.09 \times 10^{-2} T - 1.45 \times 10^{-5} T^2 + 7.67 \times 10^{-9} T^3 \quad (\text{eq. 5-34})$$

For temperature greater than 2098 K, the thermal conductivity is;

$$K = 36 \quad (\text{eq. 5-35})$$

where

K: Thermal conductivity at Zircaloy (W/m-K)

T: Temperature (K)

Good agreement is found between eq. 5-34 and measured data up to temperatures of about 1800 K. The thermal conductivity for liquid Zircaloy was estimated based on the ratio of solid state conductivities to liquid-state conductivities for metals with a body-centered cubic lattice. Additional information on the Zircaloy thermal conductivity model can be found in Reference [2].

#### 5.3.1.2 Zirconium Oxide ( $ZrO_2$ ) Thermal Conductivity

FALCON includes the NFIR and MATPRO models to calculate the zirconium oxide ( $ZrO_2$ ) thermal conductivity as a function of temperature. The NFIR model is based on a series of in-pile experiments performed in the Halden test reactor that were designed to determine the thermal conductivity of external oxide layers on fuel rods [36]. In the NFIR experimental program, the  $ZrO_2$  thermal conductivity was estimated using cladding elongation measurements

during power ramps as a representation of cladding temperature changes. By comparing the cladding elongation of a fuel rod with an external oxide to a reference rod without an external oxide, the thermal impact of the oxide layer was determined. Experiments were performed at oxide layer thicknesses between 30 and 82  $\mu\text{m}$ . In determining the thermal conductivity from the measured data, considerations were made for external crud layers, power increases, power decreases, and oxide layer thickness. The results of the experiments found that the thermal conductivity of  $\text{ZrO}_2$  is independent of oxide thickness and temperature in the temperature range between 240°C and 300°C. The NFIR model provides a constant thermal conductivity value of 2.7 W/m-K.

The MATPRO-11 Rev. 2 model for Zircaloy oxide thermal conductivity is based on several different data sources of thermal conductivity measurements [2]. These measurements were performed using a variety of oxide morphologies (stabilized oxides, nodular, and black) and oxide formation techniques (steams oxidation and plasma sputtering).

Using thermal diffusivity measurements, the thermal conductivity was determined for the different oxide types as a function of temperature. The MATPRO model used primarily data from tests with black oxide layers to develop the thermal conductivity as a function of temperature. The resulting correlation is;

$$K_{\text{ox}} = 0.835 + 1.81 \times 10^{-4} T \quad (\text{eq. 5-36})$$

where

$K_{\text{ox}}$ : Oxide thermal conductivity (W/m-K)

T: Oxide temperature (K)

The correlation above is applicable to solid Zircaloy oxide found on fuel rods. Further information on the MATPRO Zircaloy oxide model can be found in Reference [2].

### 5.3.2 Elasticity & Plasticity

The mechanical properties used in FALCON for the clad are based on MATPRO-11 Rev. 0 [1]. These properties are known to only partially represent the material behavior of irradiated cladding across the entire range of alloy types and environmental conditions encounter in a reactor under normal and off normal conditions. However, they have been accepted as a suitable basis for licensing calculations for fuel rods under typical steady state (operational) conditions. The important clad mechanical properties include Young's modulus, Poisson's ratio, coefficient of thermal expansion, the yield stress and hardening law, and the creep and irradiation growth creep. In FALCON, all these clad mechanical properties, except creep and irradiation growth, are based on the MATPRO-11 Revision 0 models [1].

### 5.3.3 Thermal/Irradiation Creep

FALCON includes the thermal and irradiation creep rate of the Zircaloy material in the calculation of the cladding stress and strain behavior during normal operation, off-normal conditions, and accidents. For steady state operation and power ramp conditions where the cladding temperature remains below 450°C, four different Zircaloy alloy creep models are available in FALCON. The models include the MATPRO-11, Rev. 0 model, the ESCORE model, a modified version of the MAPTRO-11, Rev. 2 model, and the Limbäck and Andersson model. FALCON also includes a high temperature creep model developed from MATPRO-11, Rev.0 that is used for accident conditions at temperatures greater than 450°C. The following summarizes the key points of the ESCORE creep model, the modified MATPRO Rev. 2 model, and the Limbäck and Andersson model. Additional information on the low and high temperature MATPRO Rev. 0 models can be found in Reference [1].

The general approach used in FALCON is to compute the cladding creep rate using two terms, irradiation-induced creep and thermal creep. The total cladding creep rate is then the sum of the contributions from these two components. The thermal creep rate is further broken down into primary and secondary creep rate components. For normal operating conditions, the cladding diametral creep down process is controlled by irradiation-induced creep deformations. Thermal creep is the controlling creep process that causes stress relaxation and cladding deformations for operational transients that result in PCMI. Also, under spent fuel storage conditions, the neutron flux is negligible and therefore thermal creep is the dominant cladding creep process. The models used in FALCON for the diametral creep of Zircaloy cladding are dependent on the time, temperature, stress, and fast-neutron flux. Each model also includes a dependence on the material metallurgical condition.

#### 5.3.3.1 ESCORE

The ESCORE model for diametral creep of Zircaloy cladding is dependent on operating conditions of time, temperature, stress, and fast-neutron flux and on material metallurgical conditions of yield strength and texture[4]. Two components of creep are included. The first describes irradiation-independent thermal creep and the second describes irradiation-induced creep.

The ESCORE creep model has the following form prior to differentiating with respect to time:

$$\varepsilon^c = \varepsilon_{Th}^c + \varepsilon_{Ir}^c \quad (\text{eq. 5-37})$$

$$\varepsilon_{Th}^c = A_1 \left[ \sinh \left( A_2 \sigma_{\theta}^{A_3} \right) \right]^{A_4} t^{A_5} \sigma_{yield}^{A_6} \exp(-A_7/T) \quad (\text{eq. 5-38})$$

$$\varepsilon_{Ir}^c = B_1 t^{B_2} \phi^{B_3} \sigma_{\theta}^{B_4} [\exp(-B_5/T)] \sigma_{yield}^{B_6} [\cos \theta_{max}]^{B_7} \quad (\text{eq. 5-39})$$



where

- $\varepsilon$ : Diametral strain,  $\Delta D/D$  (m/m),
- $t$ : Time of exposure (hrs),
- $\phi$ : Fast neutron flux for  $E > 1$  MeV ( $\text{n/cm}^2\text{-sec}$ ),
- $\sigma_\theta$ : Midwall hoop stress (MPa),
- $T$ : Cladding temperature (K)
- $\sigma_y$ : Cladding yield strength at room temperature (MPa), and
- $\cos \theta_{\max}$ : Cosine of angle of maximum intensity of basal pole or radial direction, normal to axial direction.

The constants in the creep equations have the following values:

<u>Constant</u>	<u>Value</u>	<u>Constant</u>	<u>Value</u>
$A_1$	$1.388 \times 10^8$	$B_1$	$2.35 \times 10^{-21}$
$A_2$	$3.29 \times 10^{-5}$	$B_2$	0.811
$A_3$	2.28	$B_3$	0.595
$A_4$	0.997	$B_4$	1.352
$A_5$	0.770	$B_5$	22.91
$A_6$	0.956	$B_6$	1.58
$A_7$	$23 \times 10^3$	$B_7$	2.228

The creep model was obtained from a regression fit of available LWR creep data. These data were obtained from fueled and non-fueled rods irradiated in PWRs and in BWRs, all of which were subjected to compressive stresses. Data were also obtained from ex-reactor thermal creep tests with samples subjected to tensile or compressive stresses and from tensile irradiation tests of pressure tubing. With the exception of the pressure tube data, all data pertained to production fuel cladding typical of that employed in the fabrication of modern LWR fuel. In all cases, only those post-irradiation data were utilized for which pre-irradiation characterization data were also available. The data were obtained from fueled and non-fueled rods with little or no cladding contact with the fuel or mandrels. Thus the modifying influence of contact on creep down was minimized. Also, the measurements were obtained away from grid locations, generally at mid-span positions, to preclude any restraining effects of grids. Equation 5-38 is based on the ex-reactor, thermal-creep model described by Gorscak and Pfenningworth [37]. The effects of material metallurgy are reflected by the addition of the term:  $\sigma_{\text{yield}}^{A_6}$ , which produces a dependence of creep on the material yield strength [38]. Due to the unavailability of data on yield strength at elevated temperatures, the yield strength at room temperature is used in the model. Equation 5-39 is based on the form of the low-temperature irradiation-creep model developed by Franklin [38].

The form of the ESCORE creep model shown in equations 5-37, 5-38, and 5-39 provides the creep strain for time invariant conditions of stress temperature and flux. However, the

incremental analysis approach in FALCON and the real life conditions in a fuel rod requires time-varying conditions. Two approaches can be used to convert the model to time varying conditions: the time-hardening law or the strain hardening law. Experience has shown that the strain-hardening law provides better representation of creep deformation under time-varying conditions. Using the strain hardening approach, the ESCORE creep model becomes;

$$\begin{aligned} d\varepsilon_{\text{Total}} / dt = & LA_5 [\varepsilon_{\text{Thermal}} / L]^{[(A_5-1)/A_5]} \\ & + MB_2 [\varepsilon_{\text{Irradiation}} / M]^{[(B_2-1)/B_2]} \end{aligned} \quad (\text{eq. 5-40})$$

where:

$$L = A_1 \left[ \sinh(A_2 \sigma_{\text{hoop}}^{A_3}) \right]^{A_6} \sigma_{\text{yield}}^{A_4} \exp(-A_7 / T) \quad (\text{eq. 5-41})$$

$$M = B_1 \phi^{B_3} \sigma_{\text{hoop}}^{B_4} \exp(-B_5 / T) \sigma_{\text{yield}}^{B_6} (\cos \theta_{\text{max}})^{B_7}$$

Equations 5-40 and 5-41 have been incorporated into FALCON for calculating the thermal and irradiation growth of Zircaloy alloy cladding

### 5.3.3.2 MATPRO Rev 2 Cladding Creep Model

The MATPRO-11 Revision 2 cladding creep model was developed primarily to address irradiation-induced cladding creep down and is based on data from the HOBBIE-1 tests conducted jointly by the US NRC and Engergieonderzoek Centrum Nederland (ECN)[39]. In the tests conducted in the High Flux Reactor at Petten, measurements were made of the in-pile creep down displacements as a function position and time during irradiation. Using this data, the MATPRO-11 Revision 2 model was developed as a function of temperature, fast neutron flux, and compressive hoop stress. A detailed description of the MATPRO-11 Revision 2 irradiation creep model can be found in Reference [2]. The MATPRO-11 Revision 2 model does not depend on the material metallurgical condition of the cladding. To increase the applicability of the model in FALCON, a cold work dependency was introduced into the model using data sets of stress-relief annealed cladding with varying degrees of cold work and fully recrystallized cladding. The material dependency was developed using irradiation creep data obtained by Gilbon and Franklin [38, 39] Adding a material heat treatment consideration to the model improved the performance of the model and although the model represents well the data from the HOBBIE-1 experiment, the modified MATPRO Revision 2 model has not been extensively compared to creep down data from commercial fuel rods. The primary application of this model is for steady state analysis.

### 5.3.3.3 Limbäck and Andersson Cladding Creep Model

The Limbäck and Andersson model has recently been developed to represent the effects of metallurgical condition on both the in-pile and out-of-pile creep behavior of Zircaloy cladding [41]. This model includes three key elements: a thermal creep rate expression based on the

Matsuo formulation [42], an irradiation hardening effect on the thermal creep rate based on the model of Hoppe [43], and an irradiation-induced creep rate expression. The out-of-pile thermal creep tests used to develop the model included both cold work stress relieved (CWSR) Zircaloy-4 (Zr-4) and both partially recrystallized annealed (PRXA) and recrystallized annealed (RXA) Zircaloy-2 (Zr-2) cladding material. As a consequence of using this wide array of materials, the model coefficients in the Limbäck and Andersson model depend on the metallurgical condition of the cladding. Further, the Franklin data for in-pile creep of CWSR and RXA cladding material were used to develop the model coefficients for the irradiation-induced creep rate expression [38].

The general form of the Limbäck and Andersson model is; summarized below;

$$\dot{\epsilon}_s = A \cdot \frac{E}{T} \left( \sinh \frac{a_i \sigma_\theta}{E} \right)^n \cdot e^{-Q/R^T} \quad (\text{eq. 5-42})$$

$$\epsilon_\rho^s = B \cdot \dot{\epsilon}_s^b [2 - \tanh(D \cdot \dot{\epsilon}_s)]^d \quad (\text{eq. 5-43})$$

$$\epsilon_{th} = \epsilon_\rho^s [1 - \exp(-c \sqrt{\dot{\epsilon}_s} \cdot t)] + \dot{\epsilon}_s \cdot t \quad (\text{eq. 5-44})$$

where

- $\dot{\epsilon}_s$ : Steady state creep rate
- $\epsilon_\rho^s$ : Saturation value for the primary creep
- $\epsilon_{th}$ : Total thermal creep strain
- A: Model constant dependent on alloy heat treatment
- E: Young's Modulus
- B: Constant (0.0216)
- b: Constant (0.109)
- $\sigma_\theta$ : Hoop stress
- n: Model constant dependent on alloy heat treatment
- Q: Thermal creep activation energy (205 KJ/mol)
- R: Universal gas constant
- C: Constant (52)
- D: Model constant (35,500)
- d: Model constant (-2.05)

Irradiation hardening of thermal creep is included in the Limbäck-Andersson model through the  $a_i$  term. The development of irradiation damage that hinders dislocation motion is modeled as a function of fast fluence, similar to Hoppe [43] as:

$$a_i = a[1 - A_1[1 - \exp(-A_2 \cdot \Phi^{A_3})]]$$

where

$\Phi$ : Fast neutron fluence  $E > 1\text{MeV}(\text{n}/\text{cm}^2)$

$a$ : Model constant (650)

$A_1$ : Model constant (0.56)

$A_2$ : Model constant ( $1.4 \times 10^{-27}$ )

$A_3$ : Model constant (1.3)

As can be seen, the thermal creep equations include both primary creep, the first term in Eq. 5-44, and secondary (state-state) creep, the second term in Eq. 5-44. The incremental analysis approach in FALCON requires the creep rate to account for time-varying temperature and stress conditions. As a result, the strain hardening law has been used to reformulate the primary creep given by the first term in Eq. 5-44. The result for the primary creep rate is

$$\dot{\epsilon}_\rho = 0.5C^2 \dot{\epsilon}_s \epsilon_\rho^s \left[ \frac{1 - \epsilon_\rho / \epsilon_\rho^s}{\ln(1 - \epsilon_\rho / \epsilon_\rho^s)} \right]$$

where

$\dot{\epsilon}_\rho$ : Primary creep rate

$\epsilon_\rho$ : Accumulated primary creep

The irradiation-induced creep model is based on a model development by Hoppe which states that the irradiation creep rate is proportional to the current fast flux,  $\phi$ , and stress and is given by Reference [43];

$$\dot{\epsilon}_i = C_0 \phi^{C_1} \sigma_\theta^{C_2} \quad (\text{eq. 5-45})$$

where

$C_0$ : Model constant dependent on alloy heat treatment

$C_1$ : Model constant (0.85)

$C_2$ : Model constant (1.0)

The model coefficients in eq. 5-45 were calibrated for stress-relieved annealed and recrystallized cladding material using the data of Franklin Reference [38]. The total creep rate is given by

$$\dot{\epsilon}_t = \dot{\epsilon}_s + \dot{\epsilon}_p + \dot{\epsilon}_i$$

Further details about the Limbäck and Andersson model can be found in Reference [41]

### 5.3.4 Irradiation Growth

The change in cladding elongation by irradiation-induced growth is calculated by FALCON for use in steady state fuel performance evaluations. Currently, three models are available to calculate the incremental change in the axial dimension caused by irradiation-induced growth; the MATPRO-11 Revision 2 model, the ESCORE model, and the Franklin model. Each of these models are summarized below.

#### 5.3.4.1 MATPRO-11 Revision 2 Model

The MATPRO-11 Revision 2 model calculates the fractional change in length of zircaloy tubes due to irradiation-induced growth including the effects of fast neutron fluence, tubing texture, cladding temperature, and cold work. The model can be applied to both Zircaloy-2 and Zircaloy-4. The datasets used to develop the model included both Zircaloy-2 and Zircaloy-4 material irradiated to fluence levels of approximately  $1 \times 10^{25} \text{ n/m}^2$  ( $>1 \text{ MeV}$ ).

The following equation has been developed to model the irradiation growth of zircaloy tubes at temperatures between 40 and 360°C (the normal range of cladding temperatures in LWRs).

$$\Delta L/L = A[\exp(240.8/T)](\phi t)^{1/2}(1 - 3f_z)(1 + 2.0CW) \quad (\text{eq. 5-46})$$

where

$\Delta L/L$ : Fractional change in length due to growth

$A = 1.407 \times 10^{-16} (\text{n/m}^2)^{-1/2}$

$T$ : Cladding temperature (K)

$\phi$ : Fast neutron flux ( $\text{n/m}^2\text{s}$ ) ( $E > 1.0 \text{ MeV}$ )

$t$ : Time(s)

$f_z$ : Texture factor for the tubing axis

$CW$ : Cold work (fraction of cross-sectional area reduction)

The parameter  $f_z$  is the effective fraction of cells aligned with their  $\langle 0001 \rangle$  axis parallel to the tubing axis, as determined by X-ray diffraction analysis. A value of  $f_z = 0.05$  is typical. Limited testing of the MATPRO-11 Revision 2 model has shown that it works well for Zircaloy-2. However, it tends to under predict irradiation growth for Zircaloy-4 at fluence levels beyond  $1 \times 10^{25} \text{ n/m}^2$ . A more detailed description can be found in Reference 2.

### 5.3.4.2 ESCORE Model

The stress-free axial growth of Zircaloy-2 and Zircaloy-4 is described in the ESCORE model by an equation of the form [4]:

$$\Delta L / L = A(\phi_1 t)^n \quad (\text{eq. 5-47})$$

where:

$\Delta L / L$ : Axial growth strain (m/m),

$\phi_1 t$ : Fast neutron fluence ( $E > 1 \text{ MeV}$ ,  $\text{n/cm}^2$ ), and

$A, n$ : Model constants that depend on cladding metallurgical state

The model coefficients were developed as a function of cladding type using irradiation growth data obtained in an early EPRI program [38]. This program evaluated growth data from fuel rods manufactured by General Electric (GE), Combustion Engineering (C-E), Westinghouse (W), Babcock and Wilcox (B&W), and Exxon. The C-E, W, and B&W fuel rods were irradiated in PWR's while the Exxon and GE fuel rods were irradiated in BWR's. The fuel rods experienced fluences to  $10 \times 10^{21} \text{ n/cm}^2$  ( $E > 1 \text{ MeV}$ ).

The results of the EPRI evaluation show that the growth behavior of the W, C-E, and Exxon fuel rods was similar. These fuel rods all used stress-relief annealed cladding. Although the B&W cladding is also in the stress-relief annealed condition, the growth of the B&W fuel rods was lower than for fuel rods with similar cladding produced by other vendors. The growth of the GE fuel rods, which used fully-annealed cladding, was lower than that of the fuel rods with stress-relief annealed cladding. The model coefficient  $A$  and  $n$  for the various vendor fuel rods are given below:

Fuel Rod Vendor	$A$	$n$
C-E, EXXON, W	$3 \times 10^{-20}$	0.794
B&W	$7.3 \times 10^{-25}$	1
GE	$1.82 \times 10^{-15}$	0.564

A more detailed description of the ESCORE model is contained in Reference [4].

### 5.3.4.3 FRANKLIN Model

D. G. Franklin proposed a model, based on high-fluence PWR data, in which axial growth is proportional to the fluence raised to the 0.845 power [38]. The model uses the same set of axial elongation measurements used to develop the ESCORE model coefficients. The Franklin model is given by;

$$\frac{\Delta L}{L} = 9.09 \times 10^{-25} (\phi t)^{0.845} \quad (\text{eq. 5-48})$$

where

$\frac{\Delta L}{L}$ : Axial growth strain (unit less)

$\phi t$ : Fast neutron fluence  $E > 1$  MeV ( $n/cm^2$ )

The Franklin model has been found to represent well the irradiation growth of Zircaloy-4 in a stress-relieved annealed condition. For recrystallized Zircaloy-2 material used in BWR's, the Franklin model over-predicts the irradiation growth. For application of the Franklin model to recrystallized Zircaloy-2 material, a factor of 0.5 is applied in FALCON to the model shown in eq. 5-48.

### 5.3.5 Oxidation

FALCON calculates both low temperature oxidation associated with normal operation under typical reactor coolant temperature, pressure, and chemistry conditions and high temperature oxidation associated with accidents that result in steam conditions. The low temperature oxidation is calculated using either the CORROS model provided in MATPRO-11 Rev. 2 or the PFCC EPRI/SLI model. Considerations are made for cladding alloy type, alloy composition, and coolant chemistry effects for low temperature oxidation. The high temperature oxidation layer buildup is calculated using either the Cathcart or Leistikow equations for best estimate calculations or the Baker-Just equation for licensing calculations. The selection of different reaction rates are provided as a user option. Linear heat generation due to the exothermic zirconium-water reaction is also calculated. Clad oxidation kinetics at both the outer surface and the inner surface (after cladding failure) are calculated for the R-Z geometry models. Cladding oxidation is not considered for R- $\theta$  geometry models.

The effect of cladding oxidation on the thermomechanical solution appears in two areas. First, the metal-water reaction heat generation is included in the thermal solution in the form of linear power source at the outer clad surface. Second, the effect of the  $ZrO_2$  layer on the mechanical deformations is treated as an effective thickness reduction.

Inner surface oxidation following clad rupture is considered, at present, to take place over the failure region which is assumed to extend axially one element in height and fully around the circumference. All failed elements are included in these calculations. The oxidation rate, oxidation linear heat generation, and oxide thickness buildup at the inner surface are based on the same models and assumptions used for the outer surface.

The phase transformation of Zircaloy cladding is also calculated in FALCON as a function temperature and oxygen content. This calculation is performed for the high temperature oxidation process using the models provided in MATPRO-11 Rev. 2 [2].

#### 5.3.5.1 Low Temperature Oxidation

Low temperature (523K to 673K) oxidation is calculated in FALCON for normal operating conditions using either the CORROS model from MATPRO-11 Rev. 2 [2] or the EPRI/SLI

Material and Physical Models

model from the PFCC code [44]. Both models consider that cladding oxidation under normal LWR conditions occurs in two stages, depending on the oxide layer thickness. The pre-transition oxidation follows a cubic time dependence up to the transition oxide thickness (typically 2μm). The post-transition oxidation beyond the transition oxide thickness follows a linear time dependence. The rate equations for low temperature oxidation are give by;

Pre transition;

$$\frac{d(S^3)}{dt} = K_{pre} \exp\left(\frac{-Q_{pre}}{R_u T_i}\right) \quad \text{for } S < S_{trans} \quad (\text{eq. 5-49})$$

Post-Transition;

$$\frac{d(S)}{dt} = K_{post} \exp\left(\frac{-Q_{post}}{R_u T_i}\right) \quad \text{for } S > S_{trans} \quad (\text{eq. 5-50})$$

where;

S is the oxide thickness

- $T_i$ : Metal-oxide interface temperature
- $K_{pre}$ : Rate constant for pre-transition oxidation
- $K_{post}$ : Rate constant for post-transition oxidation
- $Q_{pre}$ : Activation energy for pre-transition oxidation
- $Q_{post}$ : Activation energy for post-transition oxidation
- $R_u$ : Universal gas constant
- $S_{trans}$ : Transition oxide thickness

The model coefficient  $K_{pre}$ ,  $K_{post}$ ,  $Q_{pre}$ , and  $Q_{post}$  are calculated by the CORROS and EPRI/SLI models based on several parameters, including alloy type (Zircaloy-2 or Zircaloy-4), coolant conditions, and temperature. For the CORROS model, the main parameters of interest are the reactor type (BWR vs. PWR) and temperature.

The EPRI/SLI model is only applicable to PWR coolant conditions. The model coefficients in the EPRI/SLI model contain factors that are a function of coolant lithium content, alloy tin and iron content, hydrogen content, and fast flux. Studies have shown that the EPRI/SLI model is a best-estimate oxidation model for PWR conditions and Zircaloy-4 cladding. The model has been applied to fuel rods with burnup levels exceeding 60 GWd/MTU and oxide thickness levels beyond 100 μm.

The metal-oxide interface temperature,  $T_i$ , is calculated assuming steady-state heat conduction across the oxide thickness as;



$$T_i = T_s + \frac{q'' S}{K_{ox}}$$

where

$T_s$ : Outer space oxide temperature

$q''$ : Surface heat flux

$K_{ox}$ : Thermal conductivity of the oxide layer

As discussed in Section 5.3.1 FALCON has several different options to calculate the oxide layer thermal conductivity. Testing of the EPRI/SLI model used the recommended value of  $K_{ox}=1.5$  w/m-K for PWR applications [44]. The CORROS model has primarily been applied to BWR applications. For this case, the MATPRO model for oxide thermal conductivity has been used in FALCON.

Further description of the CORROS and EPRI/SLI oxidation models can be found in Reference 2 and 44, including detailed descriptions of the model coefficients and the adjustment factors.

### 5.3.5.2 High Temperature Oxidation

Zirconium alloys experience an accelerated oxidation rate at temperatures above 900°C when exposed to steam. FALCON contains a high temperature (800 to 1800°C) oxidation model for the analysis of clad outer and inner surface oxide formation during accident conditions. The basis for the high temperature oxidation model is the COXIDE model from the MATPRO-11 Rev. 2 package [2]. The COXIDE model calculates the formation of  $ZrO_2$  on the cladding outer surface due to reaction with steam coolant and the formation  $ZrO_2$  on the cladding inner surface due to reactions with steam coolant, or  $UO_2$  when pellet-clad contact has been established. The model also calculates the total weight gain caused by oxidation, the thickness of the oxygen-stabilized alpha phase layer and the beta-phase layer.

Experimental data show that the oxide formation at high temperature follows a parabolic rate law, indicating that oxygen diffusion across the oxide layer is the rate controlling step. Based on these observations, the rate equation for oxide thickness ( $X_o$ ), weight gain ( $W_o$ ), or alpha layer thickness ( $X_\alpha$ ) can be written as;

$$\frac{d(Z)}{dt} = \frac{K_n}{Z} \exp\left(\frac{-Q_n}{T}\right) \quad (\text{eq. 5-51})$$

where

$Z$ : Kinetic parameter of interest ( $X_o$ ,  $X_\alpha$ ,  $W_o$ )

$K_n$ : Rate constant for the kinetic parameter

$Q_n$ : Activation for the kinetic parameter

$T$ : Temperature

*Material and Physical Models*

The rate constants used in FALCON for the oxide layer, alpha layer, and weight gain are summarized in Table 5-4 for all the rate constants available in the code. The default MATPRO-11 Rev. 2 rate constant is labeled COXIDE. In addition, rate constants measured by Cathcart-Pawel, Baker-Just, Leistikow, and Urbanic-Heidrick are available for use in the model [45]. Experience has shown that the Cathcart-Pawel and Leistikow rate constants provide a best-estimate calculate of the oxidation rate alpha layer formation, and weight gain.

The rate constants shown in Table 5-5 are used to calculate the outer surface oxidation and cladding failure due the inner surface oxidation. The COXIDE model also considers the formation of alpha layers on the cladding inner surface for oxygen released from the fuel pellet, if the pellet-cladding gap is closed. Further details of the Zircaloy-UO<sub>2</sub> reaction model can be found in Reference [2].

**Table 5-5**  
**High Temperature Oxidation Rate Constants used in FALCON**

	Oxide Layer ( $X_o$ ) (m)		Alpha Layer ( $X_\alpha$ ) (m)		Weight Gain ( $W_o$ ) (kg/m <sub>2</sub> )	
	$2 \cdot K_o$	$Q_o$	$2 \cdot K_\alpha$	$Q_\alpha$	$2 \cdot K_w$	$Q_w$
COXIDE [2]						
T<1853 K	$2.25 \times 10^{-6}$	18,063	$1.523 \times 10^{-4}$	24,228	33.6	20,065
T>1853 K	$2.07 \times 10^{-6}$	16,014	$1.523 \times 10^{-4}$	24,228	10.852	16610
Cathcart [45]	$2.25 \times 10^{-6}$	18,063	$1.523 \times 10^{-4}$	24,228	33.6	20,065
Baker-Just [46]	$1.04 \times 10^{-4}$	22,900	--	--	409.9	22,899
Leistikow [47]	$7.84 \times 10^{-6}$	20,214	$5.084 \times 10^{-5}$	21,922	52.418	20,962
Urbanic & Heidrick [48]						
T<1853 K	$1.296 \times 10^{-7}$	13,586	$1.521 \times 10^{-5}$	19,830	3.654	16,820
T>1853 K	$2.074 \times 10^{-6}$	16,014	$1.521 \times 10^{-5}$	19,830	10.851	16,610

The heat of reaction is used in the cladding temperature calculation as described in Section 3.2.3. The COXIDE model is used to calculate the heat generation rate based on the rate constants shown in Table 5-5.

The beta layer thickness ( $X_\beta$ ) is calculated in FALCON using the following equation;

$$X_\beta = t_i - X'_\alpha - \frac{2}{3} X'_0 \quad (\text{eq. 5-52})$$

where

- $t_i$ : Initial cladding wall thickness
- $X'_\alpha$ : Summation of the inner and outer surface alpha layers
- $X'_0$ : Summation of the inner and outer surface oxide layers

The Equivalent Clad Reacted (ECR) represents the amount of cladding wall thickness consumed during the oxidation process. Assuming all the oxygen reacted with the cladding forms  $\text{ZrO}_2$ , the formula used in FALCON to calculate the ECR is given by;

$$\text{ECR} = \frac{2.85 w_o}{\rho_{\text{Zr}} t_w} \times 100 \quad (\text{eq. 5-53})$$

where

- ECR: Equivalent cladding reacted in percent
- $w_o$ : Weight gain ( $\text{kg/m}^2$ )
- $\rho_{\text{Zr}}$ : Density of zirconium
- $t_w$ : Cladding wall thickness adjusted for deformation and metal loss from low temperature oxidation

The coefficient 2.85 arises from the ratio of zirconium to oxygen moles in the reaction process. A more detailed description of the COXIDE model from MATPRO-11 Rev. 2 can be found in Reference [2].

## 5.4 Failure

FALCON has the capability to calculate parameters that can be used to evaluate the potential for cladding failure caused by a combination of thermal and mechanical forces. Three separate cladding failure regimes are considered in FALCON. For power ramp conditions, FALCON contains a pellet-cladding interaction (PCI) failure model to address the failure mechanism of intergranular stress corrosion cracking (ISCC). FALCON also calculates cladding failures by cladding ballooning and rupture for high temperature conditions associated with a loss-of-coolant accident (LOCA). Finally, FALCON calculates the potential for cladding failure by mechanical fracture resulting from pellet-cladding mechanical interaction (PCMI) during rapid power ramps or power pulses associated with reactivity initiated accidents (RIA).

Two different approaches are used in FALCON to calculate the cladding failure potential. First, the failure models for PCI and high temperature cladding rupture are based on a time-temperature-stress failure approach using the cumulative damage concept. This concept assumes that the material undergoes cumulative damage due to sustained stress: the higher the stress, the shorter the time to failure. Therefore, an applied stress of magnitude,  $\sigma_0$ , lasting for a fraction of time,  $\Delta t$ , will cause the accumulation of fractional change,  $\Delta D$ , as

$$\Delta D = \frac{\Delta t}{t_f(\sigma_0)} \quad (\text{eq. 5-54})$$

where  $t_f(\sigma_0)$  is the time to failure had the stress,  $\sigma_0$ , been applied for the total time. Equation 5-54 depends implicitly on the temperature, hence for a given constant temperature,  $T_0$ , eq. 5-54 takes the form

$$\Delta D(\sigma_0, T_0) = \frac{\Delta t}{t_f(\sigma_0, T_0)} \quad (\text{eq. 5-55})$$

In FALCON, the fractional damage is calculated at each time step,  $n$ , by the following:

$$\Delta D_n(\sigma_0^n, T_0^n) = \frac{\Delta t_n}{t_f^n(\sigma_0^n, T_0^n)}$$

and cladding failure is assumed to occur when the total cumulative damage,  $D$ , given by

$$D = \sum_{i=1}^n \Delta D_i$$

reaches a threshold value. Generally, a threshold value of unity is used in FALCON which represents a best-estimate failure probability. The cumulative damage concept has been applied to stress-corrosion cracking of Zircaloy cladding with reasonable success [49]. Bocek used it to develop a model to predict clad rupture under transient temperature and stress ramps [50].

Second, the failure model for mechanical fracturing by PCMI uses a critical limit state approach based on the cladding strain energy density. In this approach, a cladding response parameter is selected and compared to a limit value. Cladding failure is assumed once the response parameter exceeds this limit value. Candidate response parameters include strain, stress, and strain energy density. Because the limit states for strain or stress are strongly dependent on the method used to obtain them, the strain energy density was selected for use in FALCON for evaluating the potential for failure by PCMI.

#### 5.4.1 High Temperature Transient Failure Model (Burst)

Equation 5-55 is valid for constant stress and constant temperature. Under these conditions the failure time,  $t_r$ , can be determined experimentally as a family of curves described by various values of  $\sigma_0$  and  $T_0$ . However, the ultimate application of this concept is to time varying stress and temperature. Furthermore, the independent variables  $\sigma$  and  $T$  in the analysis problem are inhomogeneous local quantities whereas in the experiment they are generally uniform gross quantities. Hence, in order to derive a useful relationship for application to transient problems with spatially varying stresses and temperature, we first express eq. 5-55 in differential form and substitute the strain, which is a more appropriate measure of the material local response, in place of the stress as follows:

$$dD(\epsilon, T) = \frac{\partial D}{\partial \epsilon} d\epsilon + \frac{\partial D}{\partial T} dT \quad (\text{eq. 5-56})$$

and giving the failure condition as

$$D = \int dD(\epsilon, T) \geq 1 \quad (\text{eq. 5-57})$$

Equation 5-8 can be further simplified as

$$D = \int_0^t \frac{\partial D}{\partial \epsilon} \dot{\epsilon} dt + \int_0^t \frac{\partial D}{\partial T} \dot{T} dt \leq 1 \quad (\text{eq. 5-58})$$

Let  $\partial D / \partial \epsilon = \alpha_1 / \epsilon_B$  and  $\partial D / \partial T = \alpha_2 / T_B$ , then eq. 5-58 becomes

$$D = \alpha_1 \int_0^t \frac{\dot{\epsilon} dt}{\epsilon_B} + \alpha_2 \int_0^t \frac{\dot{T} dt}{T_B} \leq 1 \quad (\text{eq. 5-59})$$

where  $\epsilon_B$  is the rupture strain at constant temperature,  $T_B$  is the rupture temperature at constant stress and constant heating rate, and  $\alpha_1$  and  $\alpha_2$  are constants determined from experimental data.

This equation gives the failure condition in terms of the strain and heating rates and two experimentally determined parameters  $\epsilon_B$  and  $T_B$ . These parameters are determined from work by Cheung and Rosinger [51] and Erbacher [52] who derived expressions for the burst stress  $\sigma_B$  and burst strain  $\epsilon_B$  for pressurized tube experiments as follows:

$$\sigma_B = a e^{-bT_B} \quad (\text{eq. 5-60})$$

$$\varepsilon_B = \frac{1}{2} \ln \left( \frac{P_0}{P_B} \frac{a}{\sigma_0} e^{-bT_B} \right) \quad (\text{eq. 5-61})$$

where

$$\begin{aligned} a &= 4.03 \times 10^3 & b &= 2.695 \times 10^3 & \text{for } T_B \leq 1085 \text{ K} \\ a &= 1.51 \times 10^{-8} & b &= 1.24 \times 10^{-2} & 1085 \text{ K} < T_B < 1248 \text{ K} \\ a &= 1.19 \times 10^3 & b &= 3.016 \times 10^{-3} & 1248 \text{ K} \leq T_B \leq 1873 \text{ K} \end{aligned}$$

In these equations,  $a$  and  $b$  are experimental constants,  $T_B$  is the burst temperature,  $P_B$  is the burst pressure and  $P_0$  is the initial pressure. It is important to note that these expressions are valid for pressurized tubes in which the primary forcing function is the internal pressure which gives rise to stress and strain states that are uniform along the tube and across the thickness; furthermore, the heating rate is constant. To go from these conditions to inpile fuel rods, we make use of the large-deformation long cylinder solution and equations 5-58, 5-59, and 5-60 give the following final expression for the damage factor:

$$D = \int_0^t \frac{1.5 \dot{\varepsilon} dt}{\alpha \omega \ln[ae^{-bT_B} e^{2\varepsilon}/\sigma]} + \int_0^t \frac{\dot{T} dt}{(T_B - T_0)\omega} \quad (\text{eq. 5-62})$$

where  $T_0$  is the initial temperature,  $a$  and  $\omega$  are experimental constants which represent material property dependence of irradiation conditions and phase transition, and the other parameters are defined as before. The independent variables in this equation, namely  $\varepsilon$ ,  $\dot{\varepsilon}$ , and  $\sigma$ , are computable local quantities. The new parameters  $\alpha$  and  $\omega$  are given by

$$\alpha = \begin{cases} \left( \frac{0.33 + e^{-21c}}{1.33} \right) \left( \frac{1 + 2e^q}{3} \right) & \text{for } T_B \leq 1090 \text{ K} \\ 1 & \text{otherwise} \end{cases}$$

where  $c$  is the material cold work ratio and  $q$  is the fast fluence,  $n/m^2/10^{23}$ , and

$$\omega = \begin{cases} 3.17 e^{-1.119 \times 10^{-3} T_B} & T_B \leq 1090 \text{ K} \\ 4828.3 e^{-7.843 \times 10^{-3} T_B} & 1090 \text{ K} < T_B \leq 1170 \text{ K} \\ 3.1385 \times 10^{-6} e^{1.0237 \times 10^{-2} T_B} & 1170 \text{ K} < T_B \leq 1248 \text{ K} \\ 0.4779 e^{6.7523 \times 10^{-4} T_B} & T_B > 1248 \text{ K} \end{cases}$$

Further details of this model are given in Reference [53].

Equation 5-62 is applied incrementally and the integration is carried out in time for each integration point. The value of the damage factor is accumulated and compared to the theoretical limit of unity or to a user input quantity. When the limit is reached, the clad is assumed to fail at that location and, consequently, the internal and external pressures are equalized for the remaining time of the analysis. Also inside oxidation begins as was described in the previous section.

It is important to mention that the theoretical value for  $D$  of unity gives best estimate measure of cladding failure. However, pre-selected values of  $D < 1$  or  $D > 1$  may be used by the user to bound the data from below or from above, respectively. Needless to say that an appropriate value, different from unity, to use for a particular application requires experimental verification.

#### 5.4.2 Low Temperature PCI Failure Model (SCC)

Cladding failures incurred under normal operating conditions are generally PCI-induced, and the failure mechanism is intergranular stress corrosion cracking. The problem surfaced in the early seventies in some of the BWR and CANDU power plants, and not many years after it was recognized as a generic thermal reactor problem. After a significant amount of analytical and experimental research several possible remedies emerged, the earliest of which was to impose certain operational restrictions on nuclear power plants, which was followed by the development of a PCI-immune-barrier fuel design. The physical problem can be described as follows. Under long service the fuel pellets sustain a complex history of cracking, relocation and crack healing which could lead to hard fuel-clad contact at low power levels (well below the average rod power) at one or more local points in the fuel rod. If the contact power is sufficiently low, such that a relatively high power increase is experienced at the region of contact, the resulting hoop stress can be high enough to cause stress corrosion cracking failure. The process that leads to this type of failure is highly random and the prediction of the number of failed rods in the reactor core as a whole is a statistical problem. However, deterministic modeling of this mechanism is useful in evaluating worst-case conditions and in interpreting test results or specific field occurrences. The model used to calculate clad failure in FALCON is based on the cumulative damage concept already discussed. Data for unirradiated zircaloy tubes containing iodine gas and pressurized internally [54] are used to quantify the model parameter. Considering the previous cumulative damage index:

$$D = \int_0^{t_n} \frac{dt}{t_f(\sigma, B, T)} \quad (\text{eq. 5-63})$$

where  $D$  is the amount of damage at  $t_n$ , and  $t_f$  is the failure time at stress  $\sigma$ , temperature  $T$ , and burnup  $B$ ;  $t_f$  has been evaluated from pressurized tube data:

$$t_f = \bar{t} e^{[(1.015 \sigma_y + 1.74 \sigma_{ref} - 2.775 \sigma) \times 10^{-2}]} \quad (\text{eq. 5-64})$$

where

$$\bar{t} = 5 \left( 1.13 \times 10^{-4} B - 0.13 \right)^{-0.75} e^{(30(1 - 611/T))}$$

and

$$\sigma_{ref} = \begin{cases} 336.476(B - 5000)^{-0.07262} & \text{for Zr2} \\ 310.275(B - 5000)^{-0.04400} & \text{for Zr4} \end{cases}$$

$\sigma_y$ : Yield stress (MPa)

$B$ : Burnup (MWd/MTU)

$T$ : Temperature (K)

$\sigma$ : Calculated hoop stress (MPa)

A threshold stress,  $\sigma_{ref}$ , and a minimum burnup (>5000 MWd/MTU) are used as criteria to activate the model. Both values must be exceeded before the SCC process is initiated. Equation 5-63 is the low temperature (normal operations) equivalent of eq. 5-62. FALCON uses eq. 5-63 during the steady state power history, then switches to eq. 5-62 after initiation of the transient. However, damage factors calculated from both of these equations are not additive, and the code calculates and prints out the applicable factor for each integration point in the clad elements.

### 5.4.3 Pellet-Cladding Mechanical Interaction (PCMI) Failure Model

For fast power ramp transients or postulated accidents, the cladding may crack by mechanical fracture, depending on the extent of cladding embrittlement from the fast neutron fluence, outer surface corrosion, and temperature. Mechanical fracture occurs in the cladding at the point when the combined stress and strain conditions caused by PCMI forces arising from pellet expansion exceed the mechanical capacity of the cladding. This failure mode differs from failure induced by stress corrosion cracking since cladding crack formation is controlled by the condition of the cladding and not by chemical assistance from fission product reactions at the inner cladding surface. Cladding from high burnup fuel rods are more susceptible to failure by mechanical fracture because of a reduction in cladding ductility by the combined effects of fast neutron damage and zirconium hydride formation. Mechanical fracture by PCMI occurs at cladding temperatures less than 450°C. Failure by high temperature ballooning and rupture or oxidation-induced embrittlement is still possible in high burnup fuel, provided the cladding survives the PCMI loads developed during the heating process.

The failure model for cladding mechanical fracture induced by PCMI assumes that cladding failure occurs at the instant that the combined stress and strain conditions exceed the capacity of



the cladding to withstand these conditions. This approach is consistent with the formulation of static failure theories (or strength theories) found in mechanics of materials textbooks. In general, the static failure theories development since the late 1700's [55, 56] can be grouped into five different categories, including:

- Maximum-Normal-Stress Theory (Rankine 1802-1872)
- Maximum-Shear-Stress Theory (Coulomb 1736-1806)
- Maximum-Normal-Strain Theory (Saint Venant 1797-1886)
- Maximum-Strain-Energy Theory (Baltrami 1885)
- Maximum-Distortion-Energy Theory (von Mises-Hencky 1913-1925)

Primarily, these theories have been formulated to establish the conditions of material failure as defined by yielding, for biaxial and triaxial stress states. Each of these failure theories relates the results from uniaxial tension tests to a multiaxial stress state through the development of a yield surface that depends on the stress state. In FALCON, a modified maximum-shear-stress theory (Mohr-Coulomb) is used to represent fracture of  $\text{UO}_2$  material under biaxial tension and compression states (see Appendix C). Conversely, the maximum-distortion-energy theory (von Mises-Hencky) is used in FALCON to represent the yield surface for cladding under biaxial and triaxial stress states (see Appendix C).

Possible candidates to develop the PCMI failure model for FALCON include any one of the above listed static failure theories. The primary requirement is to extend them from defining the conditions for yielding to the conditions for fracture. Such approaches are complex and are beyond the scope of this manual. For the plastic regime, methods have been developed to expand and translate the yield surfaces for these different static failure theories, including isotropic and kinematic hardening laws. FALCON uses kinematic hardening to expand and translate the von-Mises yield surface for irradiated Zircaloy.

The maximum-strain-energy theory was selected as the basis for the PCMI failure model in FALCON. This model is best suited for the analysis of irradiated Zircaloy cladding, which can exhibit either ductile failure, brittle failure or a mixed mode failure, depending on the conditions of the material. A failure model based on strain energy is consistent with the von Mises-Hencky plasticity/yield surface approach used in FALCON for Zircaloy cladding.

For the PCMI failure model, the cladding strain energy density is calculated by FALCON and is compared to a limit (critical) value derived from the results of mechanical property tests on irradiated Zircaloy cladding material. The model assumes that mechanical fracture occurs once the calculated strain energy density exceeds the critical value (Critical Strain Energy Density – CSED). As shown above, other parameters could be used to define cladding failure; e.g., the maximum-normal-strain theory would use a simple strain to failure approach. Such a strain to failure model would compare the maximum cladding strain calculated by FALCON with a critical strain value obtained from mechanical property tests, i.e. uniform elongation or total elongation. This strain limit could be a function of temperature, hydrogen content, strain rate, etc.. Unfortunately, there are two main weaknesses with using a strain to failure approach for the cladding. First, strain to failure data depends strongly on the type of mechanical property tests used to obtain the strain data. Such tests do not generally simulate the strain and stress-state the

cladding experiences under PCMI loading conditions. Second, the strain to failure is not path independent, and it depends on the rate of loading and the multi-axial condition of the imposed stresses.

The strain energy concept is important to the understanding of the behavior of materials under both static and dynamic loading [57, 58, 59]. In mechanics, energy is defined as the capacity to do work, where work is the product of force and the distance in the direction the force moves [55]. As an example of this concept, the illustration in Figure 5-6a shows a bar of uniform cross section subjected to an applied axial load  $P$  at the lower end and held at the upper end by a rigid support.

The work ( $W$ ) done in elongating the bar an amount  $\delta_2$  is given by

$$W = \int_0^{\delta_2} P(\delta) d\delta \quad (\text{eq. 5-65})$$

which represents the area under the load-deflection curve shown in Figure 5-6b. Clapeyron's theorem states that the work done on the bar must equal the change in energy of the material [55]. Since this energy changes involves a strained configuration of the material, the change in energy is termed strain energy,  $U'$ .

Relating the axial load and deflection to axial stress and strain, eq. 5-65 can be expressed as

$$W = U' = AL \int_0^{\epsilon_2} \sigma(\epsilon) d\epsilon \quad (\text{eq. 5-66})$$

where  $A$  is the cross-sectional area and  $L$  is the length of the bar. The product of  $AL$  in eq. 5-66 represents the volume of the bar. Dividing by  $AL$  yields the strain energy per unit volume ( $U$ ) given by

$$U = \int_0^{\epsilon_2} \sigma(\epsilon) d\epsilon \quad (\text{eq. 5-67})$$

Equation 5-67 represents the area under the stress-strain curve as shown in Figure 5-6c and is sometimes referred to as the strain energy intensity or the strain energy density. Strain energy density or SED will be used herein in reference to eq. 5-67.

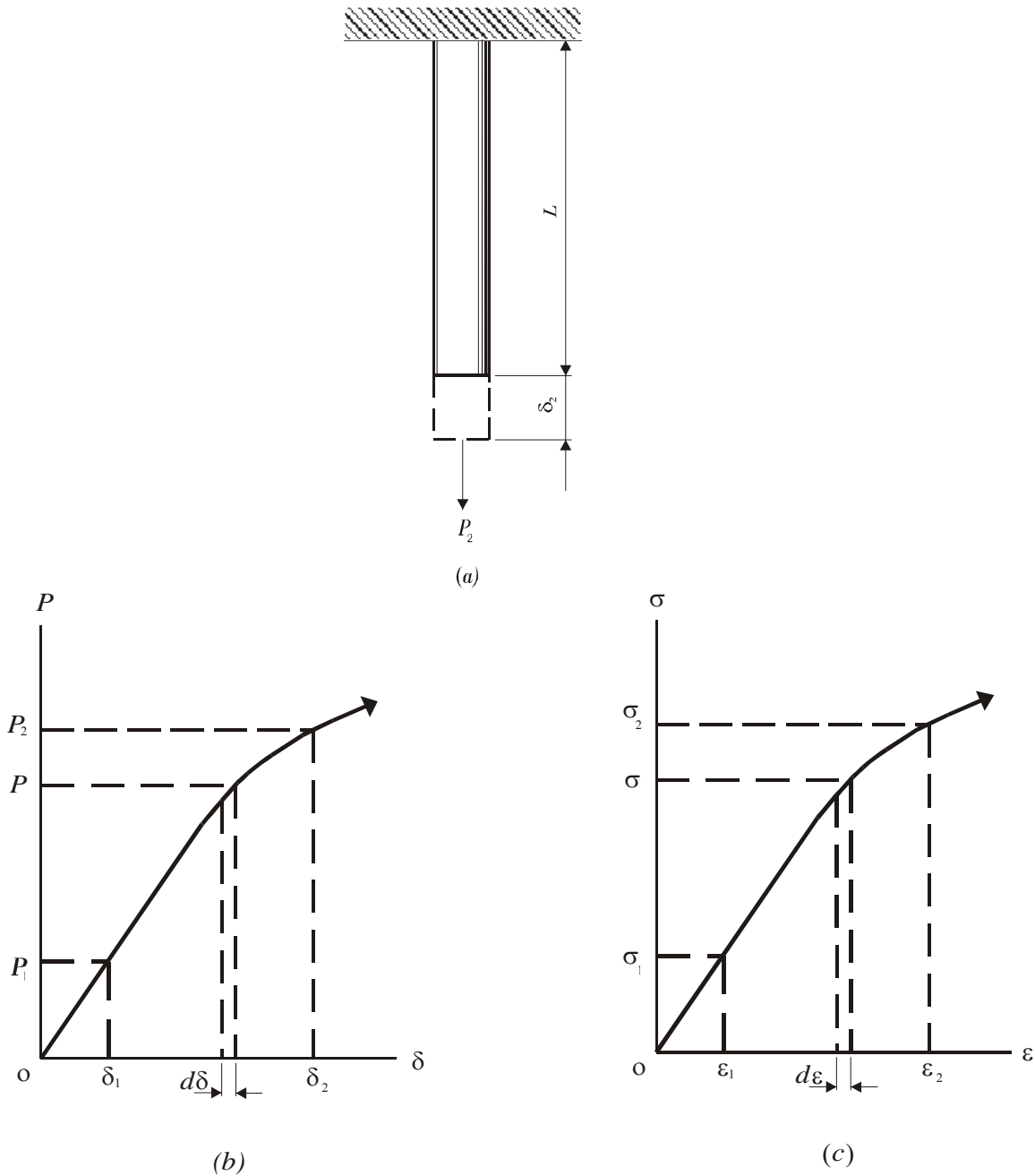


**Figure 5-6**  
**Schematic Diagram of Strain Energy, Force Deflection and Stress-Strain Relationship**

Evaluating eq. 5-67 from zero strain to the elastic limit (or the proportional limit), produces a property known as the modulus of resilience [55, 58]. This modulus is an index of the material's ability to store or absorb strain energy without inelastic deformation. Similarly, the area under the entire stress-strain curve from zero strain to the rupture strain gives the property known as the modulus of toughness and denotes the strain energy density necessary to rupture the material [55, 58]. For a material that obeys Hooke's law, eq. 5-61 can be shown to reduce to

$$U^e = \frac{\sigma^2}{2E} \quad (\text{eq. 5-68})$$

for stresses within the elastic regime. In eq. 5-68,  $E$  is Young's modulus for the material. The expression in eq. 5-68 represents the elastic strain energy density at a given elastic stress of  $\sigma$ .

Up to this point, the strain energy expression has been discussed from the vantage point of a uniaxial loading condition. Since energy is a positive scalar quantity, it is possible to sum arithmetically the energies from all different stresses coming from biaxial or triaxial loading conditions. The total strain energy density for a multiaxial state of stress can be represented as

$$U = \int_0^{\epsilon'_x} \sigma_x(\epsilon_x) d\epsilon_x + \int_0^{\epsilon'_y} \sigma_y(\epsilon_y) d\epsilon_y + \int_0^{\epsilon'_z} \sigma_z(\epsilon_z) d\epsilon_z \quad (\text{eq. 5-69})$$

where the indices represent the stress and strain coordinate directions. The integration shown in eq. 5-69 is from zero to the strain of interest,  $\epsilon'$ , in each of the different coordinate directions. For conditions where  $\epsilon'$  exceeds the elastic limit ( $\epsilon^{el}$ ),  $\epsilon'$  can be represented as

$$\epsilon' = \epsilon^{el} + \epsilon^p \quad (\text{eq. 5-70})$$

Using eq. 5-70, it is possible to rearrange eq. 5-69 into elastic and plastic terms

$$U = \int_0^{\epsilon^{el}} \sigma_x(\epsilon_x) d\epsilon_x + \int_{\epsilon^{el}}^{\epsilon^{el} + \epsilon^p} \sigma_x(\epsilon_x) d\epsilon_x + \dots \quad (\text{eq. 5-71})$$

where the first term in eq. 5-71 is the elastic strain energy density ( $U^e$ ) and the second term is the plastic strain energy density ( $U^p$ ). The total strain energy density can then be written as

$$U = U^e + U^p \quad (\text{eq. 5-72})$$

where

$$U^e = \int_0^{\epsilon^{el}} \sigma_x(\epsilon_x) d\epsilon_x + \int_0^{\epsilon^{el}} \sigma_y(\epsilon_y) d\epsilon_y + \int_0^{\epsilon^{el}} \sigma_z(\epsilon_z) d\epsilon_z \quad (\text{eq. 5-73})$$

and

$$U^p = \int_{\epsilon^{el}}^{\epsilon^{el} + \epsilon^p} \sigma_x(\epsilon_x) d\epsilon_x + \int_{\epsilon^{el}}^{\epsilon^{el} + \epsilon^p} \sigma_y(\epsilon_y) d\epsilon_y + \int_{\epsilon^{el}}^{\epsilon^{el} + \epsilon^p} \sigma_z(\epsilon_z) d\epsilon_z \quad (\text{eq. 5-74})$$

For strains within the elastic regime, the contribution from the plastic component is zero and eq. 5-73 can be simplified to yield the total elastic strain energy density as

$$U^e = \frac{\sigma_x \varepsilon_x}{2} + \frac{\sigma_y \varepsilon_y}{2} + \frac{\sigma_z \varepsilon_z}{2} \quad (\text{eq. 5-75})$$

Furthermore, eq. 5-75 can be expressed in terms of stress only using the generalized Hooke's law for isotropic materials. Assuming that  $\sigma_x, \sigma_y, \sigma_z$  are principal stresses, eq. 5-75 can be rewritten as

$$U^e = \frac{1}{2E} \left[ \sigma_x^2 + \sigma_y^2 + \sigma_z^2 - 2\nu(\sigma_x \sigma_y + \sigma_y \sigma_z + \sigma_z \sigma_x) \right] \quad (\text{eq. 5-76})$$

where  $E$  is Young's modulus, and  $\nu$  is Poisson's ratio

Because of the complex nature of the stress-strain relationship in the plastic regime, it is common to reformulate eq. 5-74 into a differential form. The incremental change in the plastic strain energy density ( $dU^p$ ) is given by

$$dU^p = \sigma_x d\varepsilon_x^p + \sigma_y d\varepsilon_y^p + \sigma_z d\varepsilon_z^p \quad (\text{eq. 5-77})$$

where  $d\varepsilon_i^p$  is the plastic strain increment in the three principal directions. The plastic strain energy density is given by integrating eq. 5-77 over the range of plastic strain increments which yields

$$U^p = \int_0^{\varepsilon_x^p} \sigma_x d\varepsilon_x^p + \int_0^{\varepsilon_y^p} \sigma_y d\varepsilon_y^p + \int_0^{\varepsilon_z^p} \sigma_z d\varepsilon_z^p \quad (\text{eq. 5-78})$$

The total strain energy density can then be obtained by the addition of equations 5-76 and 5-78. This methodology has been used to develop an analytical expression to compare the FALCON calculations under idealized stress and strain conditions.

The approach used in FALCON to calculate the strain energy density differs slightly from the approach described using equations 5-76 and 5-78. Because the general formulation in FALCON is based on an incremental strain approach, the method to calculate the strain energy density uses the differential form of eq. 5-69. The incremental change in strain energy density ( $dU$ ) is given by

$$dU = \sigma_x d\varepsilon_x + \sigma_y d\varepsilon_y + \sigma_z d\varepsilon_z \quad (\text{eq. 5-79})$$

The form of eq. 5-79 is analogous to that shown in eq. 5-77, except that it is a general formulation that applies equally to elastic or plastic strains. The expression in eq. 5-79 can be rewritten in cylindrical coordinates for a fuel rod as

$$\Delta U_{i+1} = \frac{1}{2} \sum_{j=r,\theta,z} (\sigma_i^j + \sigma_{i+1}^j) \cdot \Delta \varepsilon_{i+1}^j \quad (\text{eq. 5-80})$$

and

$$U_{i+1} = U_i + \Delta U_{i+1} \quad (\text{eq. 5-81})$$

where

$U_i$ : Strain energy density at time  $t$

$U_{i+1}$ : Strain energy density at time  $t+\Delta t$

$\Delta U_{i+1}$ : Change in strain energy density at time  $t+\Delta t$

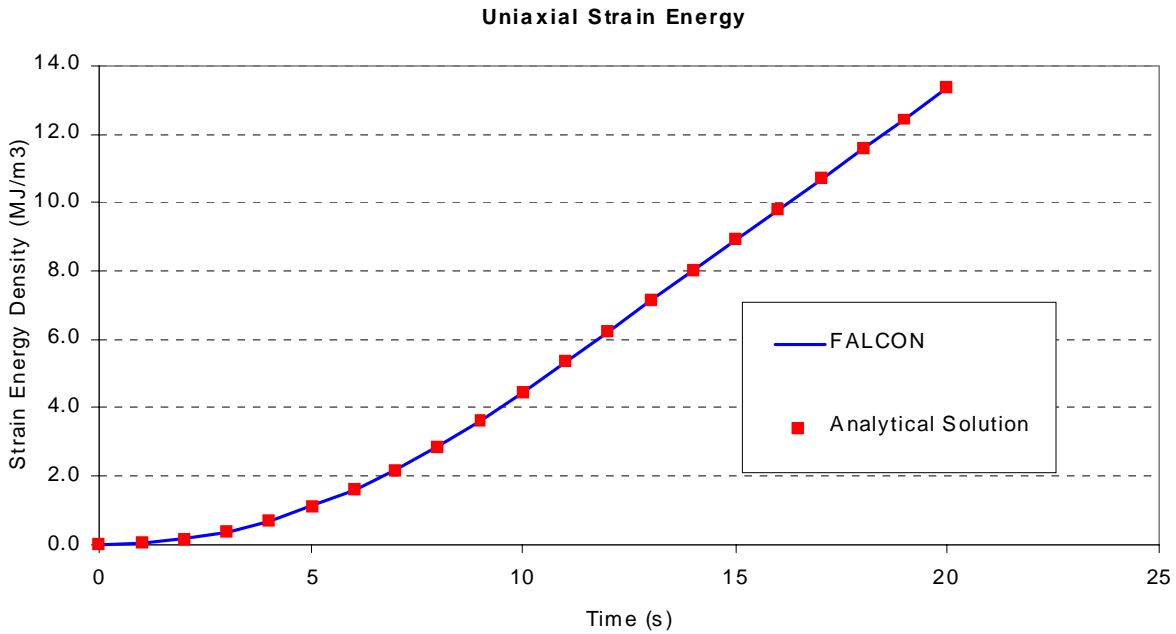
$\sigma_{i+1}^j$ : The  $j$ -component stress at time  $t+\Delta t$

$\sigma_i^j$ : The  $j$ -component stress at time  $t$

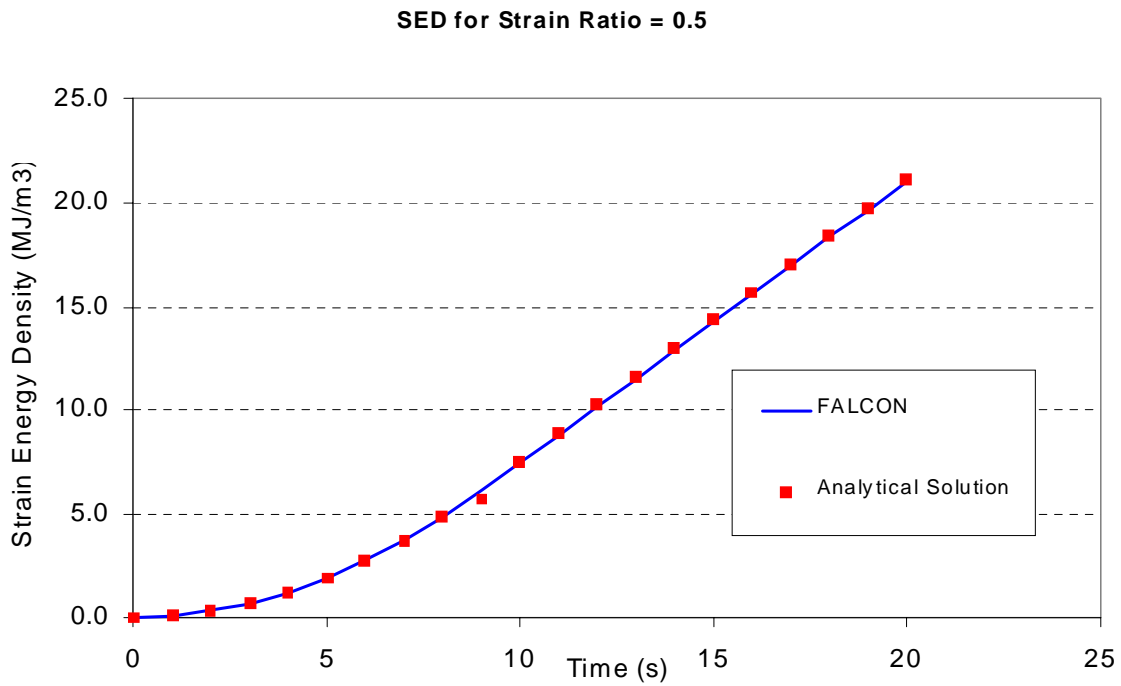
$\Delta \epsilon_{i+1}^j$ : The  $j$ -component strain increment at time  $t+\Delta t$

Figures 5-7 through 5-9 compares the results of the FALCON calculation using equations 5-83 and 5-81 and an analytical approach using equations 5-76 and 5-77 for three different stress ratios (uniaxial, 0.5, and 1.0). The results shown in Figures 5-7 through 5-9 are for a plane stress problem in the Cartesian coordinate system. The material constitutive law was elastic-perfect plastic with a yield stress of 900 MPa and a Young's modulus of  $9 \times 10^8$  MPa. Excellent agreement is demonstrated between the incremental approach used in FALCON and the analytical solution given by equations 5-76 and 5-78.

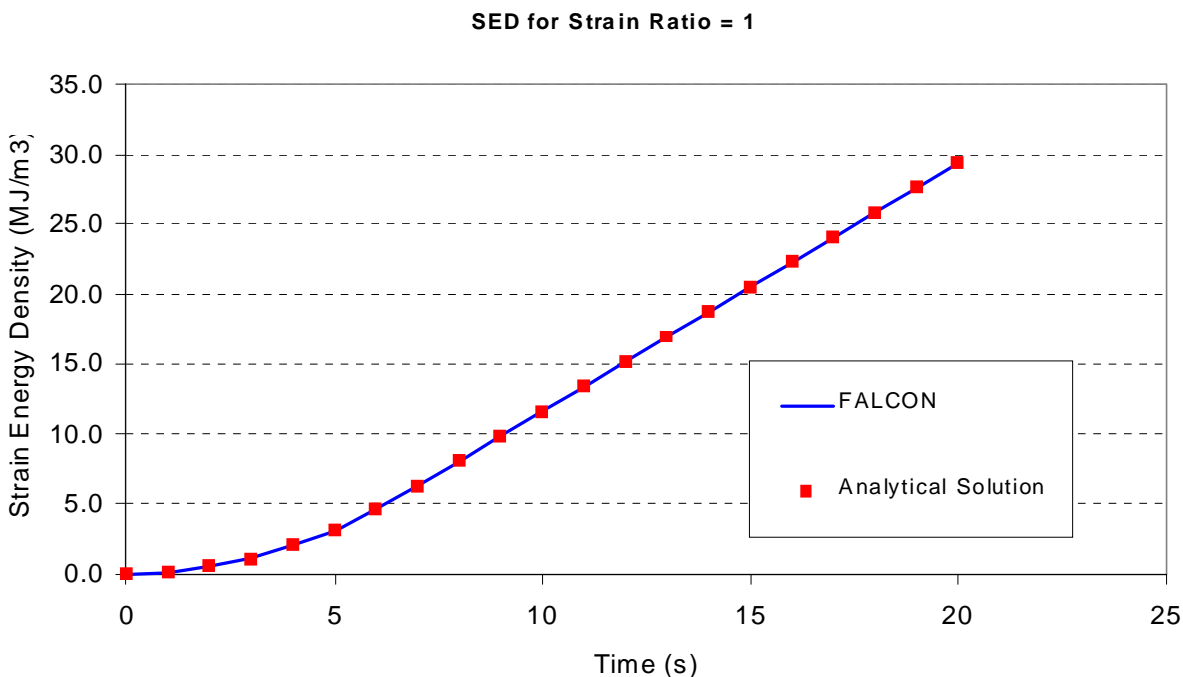
Using this approach, cladding failure is assumed to occur when the strain energy density calculated by FALCON using equations 5-80 and 5-81 exceeds a critical strain energy density (CSED) value obtained from material property tests. The influence of material conditions, such as temperature, fast fluence, hydrogen content, and zirconium hydride distributions, on the cladding failure response is obtained through the mechanical property data used to develop the CSED. At this time, no specific CSED model is included in FALCON. The user is required to provide the CSED model as a function of the key material variables such as temperature, fast fluence, hydrogen content, and zirconium hydride distribution. An example of a CSED developmental approach for Zircaloy cladding is included in Reference 60.



**Figure 5-7**  
Strain Energy Density as a Function of Strain for Uniaxial Loading



**Figure 5-8**  
Strain Energy Density as a Function of Strain for Biaxial Strain Ratio of 0.5 ( $\sigma_1/\sigma_2 = 0.5$ )

**Figure 5-9**

**Strain Energy Density as a Function of Strain for Equi-Biaxial Loading ( $\sigma_1/\sigma_2 = 1$ )**

## 5.5 Fission Gas Release

The process of fission gas production in light water reactor fuel and their subsequent release to the various voids in the fuel rods depends on the irradiation and power histories of the fuel, and the transient power changes. The released fission gases degrade the thermal conductivity of the fill gas and increase the fuel rod internal pressure, thus affecting both the thermal and mechanical responses. Steady state fission gas release calculations in FALCON are based on the ANS-5.4 model [61] the Forsberg-Massih model [62] or the ESCORE model [4]. The MATPRO FGASRL model is also included for completeness [1]. However, this model is not recommended and was not included in the code validation. During power transients, the EPRI/CE model [63] is used to calculate the release of gas from grain boundaries based on out-of-pile thermal anneal tests.

For non-zero burnup transient analysis, options are available to specify the fission gas molar concentration distributions (moles/cm<sup>3</sup>) within the fuel grains and on the fuel grain boundaries as functions of axial and radial position. In addition, the percent release is input and is used to determine the fuel-cladding gap fission gas molar concentrations. This option is made available in the code to allow for initialization from fuel performance codes other than FALCON. The values specified on the input are obtained from steady state fuel performance calculations of the power history by such programs as ENIGMA[64] or FRAPCON [14]. This procedure establishes the fission gas conditions for further steady state or transient calculations with FALCON. The input process only works as an initialization procedure for the EPRI/CE (transient) gas release model.



The production of fission gas moles is calculated in FALCON at each integration point within the finite element grid. The formula used in FALCON to calculate the production of fission gas moles is as follows:

$$\Delta C_{pr} = \frac{\beta_f Y_{FG}}{A_p A_v} \cdot P_L \cdot V_i \cdot \Delta t \quad (\text{eq. 5-82})$$

where

- $\Delta C_{pr}$ : Change in fission gas moles during the time step
- $Y_{FG}$ : Fractional yield of fission gas atoms per fission (0.3017)
- $A_p$ : Cross sectional area of the pellet
- $A_v$ : Avogadro's Number ( $6.23 \times 10^{23}$  atoms/mole)
- $P_L$ : Local power at an integration point
- $V_i$ : Integration point volume
- $\Delta t$ : Time increment
- $\beta_f$ : Conversion factor from watts to fission/sec and is calculated assuming 200 MeV/fission

The ratio of  $\beta_f/A_p$  can be input by the user for situations where the relationship between the fission density and power differ from that described above.

The fission gas release is calculated in FALCON at each integration point using the release models summarized below. The total xenon and krypton release is calculated by summing the fission gas release for all the integration points and multiplying by the individual mole fraction for the two gases. The mole fraction for xenon release is 0.847 and for krypton release is 0.153, yielding a Xe/Kr ratio of 5.54 in FALCON.

The verification and validation of FALCON for fission gas release calculations focused on the Forsberg-Massih and ESCORE models [65]. These models are recommended for best estimate fission gas release analyses under steady state fuel performance. Power ramp calculations have been performed using a combination of the Forsberg-Massih model for the base irradiation fission gas release and the EPRI/CE for the power burnup. Reasonable agreement has been found in this case, see Reference [65].

The following provides a summary of the ANS-5.4 model, the Forsberg-Massih model, the ESCORE, and the EPRI/CE model. Further details on the MATPRO FGASRL model can be found in Reference [1].

### 5.5.1 ANS-5.4 Model and ANS-5.4 Modified Model

The ANS-5.4 model utilizes what might be the simplest phenomenological model, namely, the Booth diffusion-type model, to predict the fission gas release. The Booth model, which

Material and Physical Models

describes only the diffusion of fission product atoms in a sphere of fuel material is a simplification of the physical process and contains only the mechanism of mass flow regardless of the complicated nature of the release mechanisms. This model fits empirically the various selected stable fission gas release data to characterize the effective diffusion parameter which is assumed to be temperature and burnup dependent. A complete derivation of gas release formulation used in FALCON can be found in Reference 61. The following is a summary of the key expressions used in the program.

The total cumulative release of stable fission gas isotopes during the time (t) is calculated from eq. 69 of Ref. 61 with  $\lambda = 0$  as

$$R(t) = 6 \int_0^t \beta(u) du \sum_{m=1}^{\infty} \frac{1 - \exp[-m^2 \pi^2 (\tau(t) - \tau(u))]}{m^2 \pi^2} \quad (\text{eq. 5-83})$$

where

R: Total fission gas release during time t (mol)

$\tau(t)$ :  $\int_0^t D'(u) du$

$D'$ :  $D/a^2$ , modified diffusion coefficient (1/sec)

D: Diffusion coefficient ( $\text{cm}^2/\text{sec}$ )

a: Radius of the sphere (cm)

The modified diffusion coefficient,  $D'$ , was assumed to be a function of temperature and burnup in the following form:

$$D' = (D_0/a^2) e^{-Q/R_g T} \times 100^{B_u/B_u} \quad (\text{eq. 5-84})$$

where

$R_g$ : Gas constant (cal/mol-K)

Q: Activation energy (cal/mol)

$D_0/a^2$ : Empirical constant (1/sec)

$B_u$ : Empirical constant (MWd/T)

Fitting to the low and high burnup data sets and meeting the low temperature requirement resulted in the following parameters:

$$Q = 2,000 \text{ cal/mol}$$

$$D_0/a^2 = 0.61 \text{ 1/sec}$$

$$B_u = 28,000 \text{ MWd/T}$$

The numerical implementation of the ANS-5.4 model in its present form requires prohibitive computer storage for large size problems. The formulation of the Booth diffusion-type model

was formatted and expanded into numerical recurrence forms which include diffusion variables that depend on temperature and burnup histories. This requires the recalculation and storage of these variables for all prior time steps and at each integration point. As a result, very large computer memory is needed to solve problems of practical size and time steps. It was necessary, therefore, to modify the numerical structure of the model to reduce the computer storage requirements. This modification is described in Appendix D.

### 5.5.2 Forsberg – Massih Model

Similar to the ANS 5.4 model, the Forsberg-Massih model is based on spherical diffusion of fission gas atoms within a fuel grain. However, it incorporates a two-stage fission gas release approach, and in contrast to previous models, utilizes time dependent boundary conditions to determine grain boundary gas accumulation, resolution, saturation, and release parameters [62]. Release from the grain boundaries is controlled using a grain boundary saturation criterion. The Forsberg-Massih model has been incorporated into FALCON as a best-estimate fission gas release model for the steady state analysis of fuel performance. A version of this model has also been incorporated into the FRAPCON-3 code [14]. The following provides a very brief summary of the general basis of the Forsberg-Massih model into FALCON and specific modifications made to the model following calibration against the Vitanza threshold [66]. A detailed description of the numerical approach used in the Forsberg-Massih model can be found in Reference 62.

The time rate of change of the fission gas concentration as a function of radial position can be written as;

$$\frac{\partial C}{\partial t}(r, t) = D(t)\Delta_r C(r, t) + \beta(t) \quad (\text{eq. 5-85})$$

where

$C(r, t)$ : Concentration of gas atoms in the grain

$D(t)$ : Gas atom diffusion coefficient

$\beta(t)$ : Generation rate of gas atoms (assumed to be uniform throughout the grain)

$t$ : Time

$r$ : Radial position within a grain

$\Delta_r$ : Spherical Laplacian operator  $\left( \frac{\partial}{\partial r^2} + \frac{2}{r} \frac{\partial}{\partial r} \right)$

Eq. 5-85 is solved subject to the following initial and boundary conditions,

$$C(r, 0) = 0 \quad (\text{eq. 5-86})$$

$$C(a, t) = \frac{b(t)\lambda N(t)}{2D(t)} \quad (\text{eq. 5-87})$$

where,

a: Grain radius

b: Resolution rate of gas atoms from intergranular bubbles ( $1.84 \times 10^{-6}/s$ )

$\lambda$ : Resolution layer depth from the grain boundary ( $1 \times 10^{-8}$  m)

$N(t)$ : Number of gas particles per unit area of grain boundary (surface gas concentration)

The time dependent grain boundary concentration accounts for gas resolution from grain boundary bubbles back to the grain.

Forsberg and Massih developed a solution to eq. 5-85 and the boundary condition given by eq. 5-87 using an approximation to the integration kernel. This approximation uses a three term exponential expansion series to determine the gas atom flux from the grain. Details of this solution can be found in Reference 62.

The results of solving eq. 5-84 is the grain boundary concentration ( $G_\beta$ ) as a function of time. Release of fission gas to the fuel rod free volume occurs once the grain boundary concentration reaches a saturation density given by

$$N_s = \frac{4r\omega(\theta)V_c}{3K_B T} \left( \frac{2\gamma}{r} + P_{\text{ext}} \right) \quad ((\text{eq. 5-88}))$$

where

$\gamma$ : Surface tension of the grain boundary bubble

r: Grain boundary bubble radius

$K_B$ : Boltzman constant

T: Temperature

$\omega(\theta)$ : Non-spherical bubble shape factor =  $\left(1 - 1.5 \cos(\theta) + 0.5 \cos^3(\theta)\right) / \sin^2 \theta$

$P_{\text{ext}}$ : External hydrostatic pressure

$V_c$ : Fractional coverage of the grain boundary at saturation.

Fission gas release is calculated to occur in the Forsberg-Massih model when the grain boundary concentration equals or exceeds the saturation concentration given by;

$$G_s = \frac{3}{2a} N_s \quad (\text{eq. 5-89})$$

When  $G_B \geq G_s$ , a fraction of the grain boundary gas is assumed released to the fuel rod void volume. This fraction can vary between zero and one.

The Forsberg-Massih model has been implemented into FALCON with the grain boundary gas resolution capability activated. To ensure numerical stability and that the mass balance ( $G_G + G_B + G_r = 0$ ) is maintained at all times, the ratio of  $b/\beta$  is enforced to be a constant with time. This is accomplished by calculating the time average production rate ( $\beta$ ) for the entire power history for the analysis and computing the ratio  $b/\beta$  for use in the Forsberg -Massih model.

The Forsberg -Massih model was calibrated to reproduce the Vitanza threshold by adjusting the parameters used to calculate the grain boundary saturation density ( $N_s$ ) given in eq. 5-87 [66]. In calculating  $N_s$ , the fuel hydrostatic pressure from PCMI is used. The remaining parameters are summarized in Table 5-6. The values shown in Table 5-6 are those recommended in the original Forsberg-Massih paper, except the fractional coverage of the grain boundary at saturation. This value was increased. In addition to the parameters shown in Table 5-6,  $N_s$  is multiplied by a factor of 6.5 in the FALCON implementation. Finally, the fraction of grain boundary gas released once saturation occurs was set to unity for the calibration of the model.

**Table 5-6**  
**Model Parameters Used to Calculate Grain Boundary Saturation Density in Forsberg-Massih Model**

Parameter	Value
$\gamma$	0.6 J/m <sup>2</sup>
$r$	0.5 $\mu$ m
$K_B$	$1.38 \times 10^{-23}$
$\omega(\theta)$	0.2873 ( $\theta=50^\circ$ )
$V_c$	0.85

The results of the calibration are shown in Figure 5-10.

Figure 5-10 illustrates the performance of the calibrated Forsberg - Massih model as compared to the Vitanza threshold for 1% release as a function of temperature and burnup as implemented in FALCON.

The diffusion coefficient used in the Forsberg-Massih model is that published by White and Tucker [67] and is given by;

$$D = 1.09 \times 10^{-17} \exp\left(-\frac{6614}{T}\right) \text{ for } T > 1650\text{K} \quad (\text{eq. 5-90})$$

$$D = 2.14 \times 10^{-13} \exp\left(-\frac{22884}{T}\right) \text{ for } 1381 < T < 1650\text{K}$$

$$D = 1.51 \times 10^{-17} \exp\left(-\frac{9508}{T}\right) \text{ for } T < 1381\text{K}$$

Furthermore, the lowest temperature used in FALCON to calculate the diffusion coefficient is 700K to minimize numerical instability problems in the Forsberg-Massih model at low temperature.

During benchmark testing and verification and validation, the Forsberg-Massih model was designated as the default steady state fission gas release model. The model performed fairly well over a wide range of rod designs and operating conditions, however two trends were noted: 1) the model tends to under predict BWR rods, and 2) response to late ramp or bump tests indicated a consistent trend to under predict release during the hold periods after the ramps. Evaluation of the response of the model to bump tests indicated that it was due to a combination of factors including the calculated grain boundary inventory, saturation concentration, and grain boundary gas resolution. Under high temperature conditions ( $>1600^{\circ}\text{C}$ ) additional release mechanisms such as diffusion of gas bubbles or sweeping of intragranular gas bubbles through grain growth may further enhance diffusional release Reference [68]. No satisfactory solution was found using the Forsberg - Massih model alone that adequately addressed the entire range of potential operational conditions required. However, coupling the Forsberg - Massih model to the EPRI/CE transient fission gas release model (applied only during the ramp portion of the power history) did appear to provide a reasonable response to the rapid release measured during bump tests. An example of the fission gas release response of FALCON using this method is shown in Figure 5-11 below.

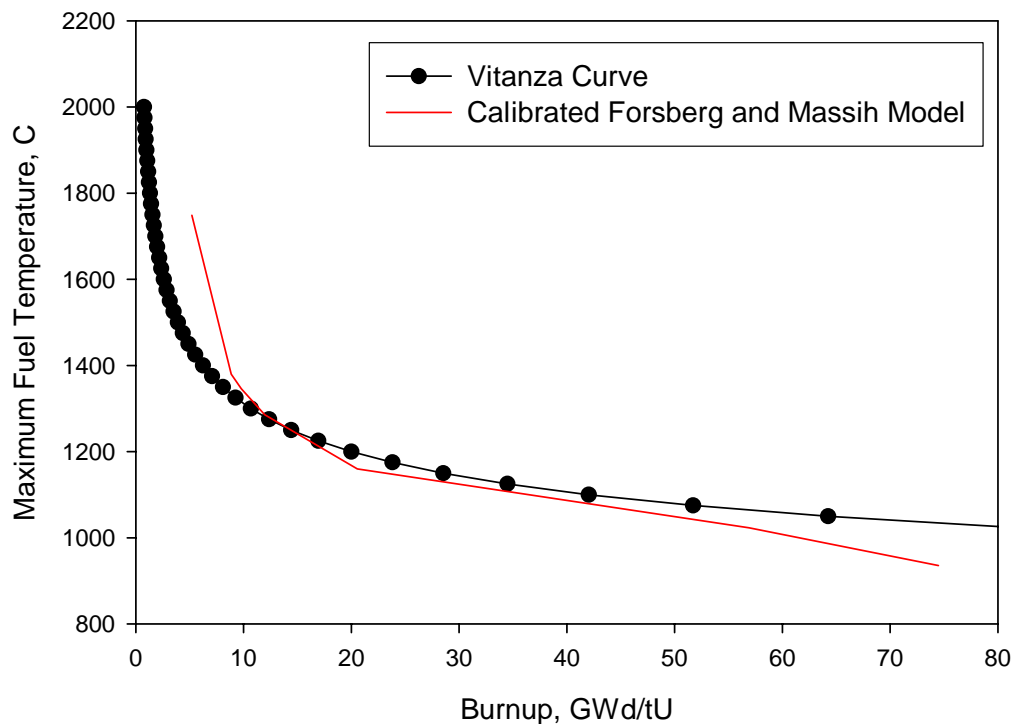


**Figure 5-10**  
**Comparison of the Forsberg - Massih Fission Gas Release Model to the Vitanza Threshold**

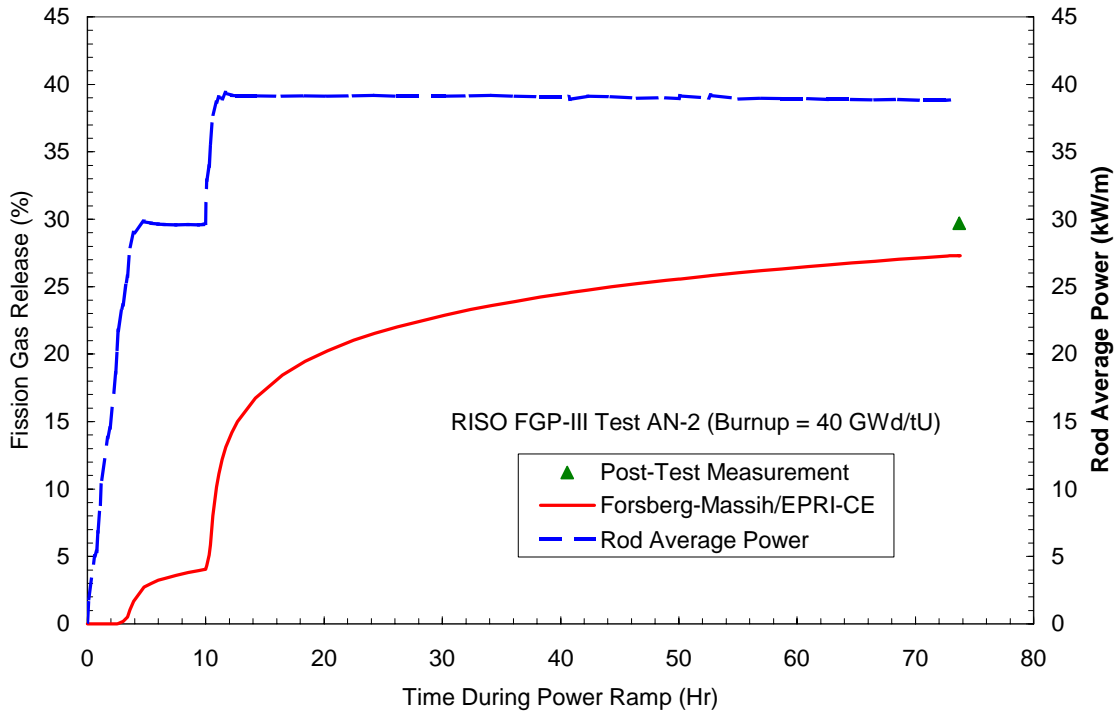


**Figure 5-11**  
**Fission Gas Release for RISO III AN-2 Calculated by FALCON using the Forsberg-Massih/EPRI-CE models. Experimental data shown for comparison**

### 5.5.3 Athermal Fission Gas Release Model

Athermal fission gas release takes place by recoil and knockout of fission gas atoms by energetic fission fragments. Only fission gas atoms located within a short distance ( $\cong 10\mu\text{m}$ ) from a free surface can be released by these mechanisms [69]. However, the formation of the high burnup microstructure (HBS) at the pellet rim has the potential to enhance the athermal FGR above the local burnup of 60~70 GWd/MTU. The typical features of the HBS include a subdivision of the grain and an increase in porosity. Both effects contribute to an increase of the specific surface. Based on these experimental observations, an athermal release model is incorporated in FALCON for use with the ESCORE and Forsberg-Massih thermal fission gas release models. This model is purely empirical and locally applied, which means that for radial integration points located within the re-structured rim zone, a certain fraction of the fission gas production is directly vented to the rod free volume. Neglecting the recoil contribution, the athermal FGR fraction is of the form  $C_1(S/V)\beta$ , where  $C_1$  is a model parameter,  $S/V$  is the specific surface of the fuel and  $\beta$  is burnup [70]. Contributions from fuel open porosity and from the HBS at the pellet periphery are included in the specific surface calculation:

$$S/V = (S/V)_0 + C_2 P_{\text{Open}} + (S/V)_{\text{Rim}} \quad (\text{eq. 5-91})$$

## Material and Physical Models

Where,  $(S/V)_0$  is the intrinsic specific surface,  $C_2 = 50000 \text{ cm}^{-1}$  is a model parameter,  $P_{\text{open}}$  is the open porosity (fraction), and  $(S/V)_{\text{rim}}$  is the additional specific surface that develops in the rim region HBS. Inside the rim, the specific surface takes the form:

$$(S/V)_{\text{rim}} = C_3(r - r_s + w), \quad 0 < (S/V)_{\text{rim}} < (S/V)_0 \quad (\text{eq. 5-92})$$

Where,  $r$  is the radial distance to the pellet center in mm,  $r_s$  is the pellet radius in mm,  $w$  is the width of the rim in mm, and  $C_3 = 75000 \text{ cm}^{-1} \text{ mm}^{-1}$  is a model parameter. Experimental data from Electricite de France (EDF) pressurized water reactors are shown in the Figure 5-12 were used to adjust the model parameters [70]. There are clearly two distinct regions, low and high burnup. At low burnup, the HBS has not formed and the release of gas from thermal diffusion has not yet occurred. As a result, fission gas release is proportional to burnup and the coefficient  $C_1$  is adjusted to fit the data. At high burnup, additional fission gas can be released from either a thermal effect or a the formation of the HBS, or both. In the model used in FALCON, the increase in  $S/V$  due to HBS formation causes an acceleration of athermal release at higher burnup.

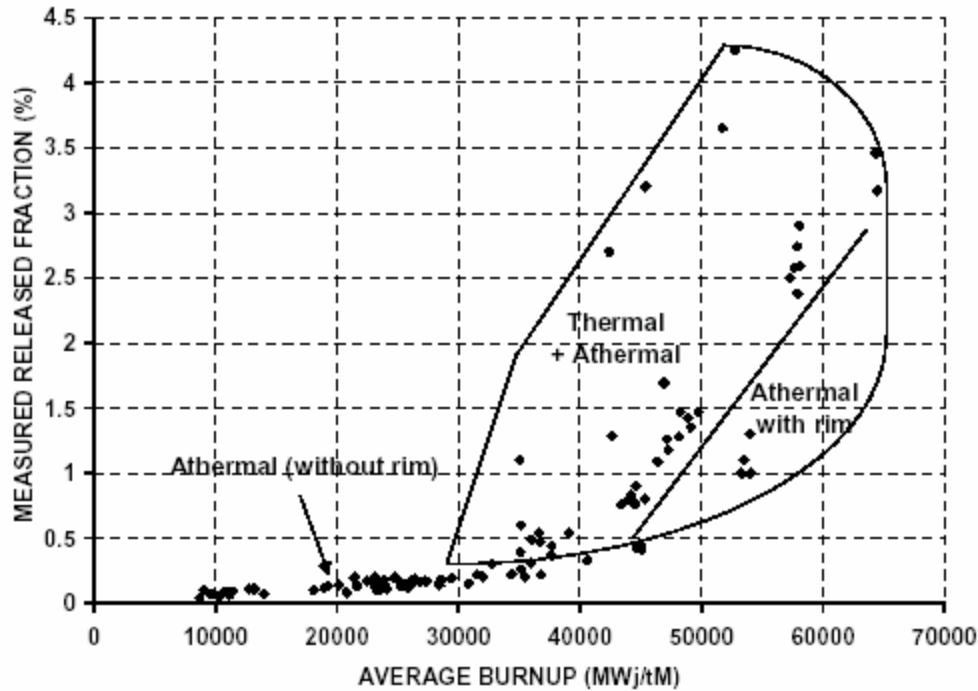


**Figure 5-12**  
Gas release fractions from FRAMATOME fuels irradiated in EDF reactors [70]



#### **5.5.4 ESCORE Fission Gas Release Model**

The ESCORE fission gas release model calculates the amount of fission gas that is released from the fuel matrix and retained within the grain and grain boundary regions of the fuel matrix. The model considers both direct gas release mechanisms and indirect gas release mechanisms. A detailed description of the ESCORE model and the coefficient calibration is contained in Reference 4. The following is a brief overview of the model structure as incorporated into FALCON.

The ESCORE model includes two direct gas release mechanisms: athermal release by high energy knockout/recoil and release by grain boundary sweeping during grain growth. In the FALCON implementation, the athermal release term in the original ESCORE model has been replaced by the more detailed model described in Section 5.5.3. Gas release by grain boundary sweeping is calculated based on grain growth during high temperature operation. During the grain boundary sweeping process, some fission gas is promptly released from grain boundaries to open void volumes such as crack or pellet surfaces.

Equiaxed grain growth is calculated in the ESCORE model using the MATPRO-11 Rev. 0 fuel restructuring model with recalibrated coefficients. Once the change in grain size is determined, the amount of volume swept by the grain boundary is used to calculate the amount of fission gas released directly by this process. Direct release by grain boundary sweeping occurs at temperatures in excess of 1200°C. An incubation period for release by grain boundary sweeping is included in the ESCORE model. The incubation period is completed by ~20 GWd/MTU.

The ESCORE model considers the indirect release process of time dependent, thermal diffusion of fission gas using a two stage model similar to the Forsberg -Massih approach. The first step in the ESCORE model is the thermal diffusion of fission gas atoms within the fuel grain to the grain boundary. The second stage is the migration of fission gas from the grain boundaries to open void volumes within the fuel stock, such as open porosity, cracks and fuel pellet surfaces. In the ESCORE fission gas release model, gas atom diffusion during each time step is calculated using time-constant equations that employ closed-form solutions. Time constants are used for each stage that dependent on temperature and grain size. In addition, the grain boundary time constant is burnup dependent, reflecting grain boundary saturation effects at higher burnup. The model uses incubation effects at burnups less than 20 GWd/MTU to inhibit gas release at these burnup levels.

#### **5.5.5 EPRI/CE Transient Model**

Fuel temperatures may rise above steady state values during transients. These higher fuel temperatures may cause additional fission gas release. The steady state gas release models above describe a smooth continuous process and although they include transient release data as part of their correlation base, they are not capable of predicting short time transient events. In order to model discontinuous or burst releases (i.e. abrupt releases observed during sudden temperature changes) in a quantitative manner the EPRI/CE model [63], which explicitly considers temperature and time dependence, is used. This model is based on data from transient direct-electrical-heating tests at Argonne National Laboratory (ANL) [71].

The temperature and time dependence of the gas release in this model is given in the following functional form:

$$F = 1 - \exp(-m t^n) \quad (\text{eq. 5-93})$$

where

- F: Fraction of the pre-transient gas inventory that is released during the time t (sec), relative to the beginning of the transient
- m: Temperature dependent variable
- n: Constant

This model is applied such that fission gases are released only if the fuel temperature increases above the operational steady state temperature and if the temperature is above 1000 °C. This is accomplished by storing the prior steady state fuel temperatures at the initiation of the transient. The fuel temperatures during the transient are then compared to the saved values, and the transient fission gas release process is not started until the fuel temperatures during the transient exceed the saved values and 1000 °C.

The best expression found for m and the best fit value for n are:

$$m = 2.22 \times 10^{-7} (T - 1000)^2$$

$$n = 0.25$$

## 5.6 Radial Power Distribution

The variation with burnup of the radial power profile across the pellet in a thermal reactor fuel rod is a complicated function both of rod design parameters, such as geometry and initial enrichment, and of the reactor operating conditions. General purpose fuel performance codes require a model of the radial power profile not only to calculate a satisfactory start of the life rating profile, but also to modify its shape as burnup proceeds. This means that the buildup of plutonium in a thin layer near the pellet surface and the consequential effects on the center temperature and the rate of crack closure are taken into account in order that the temperature distribution within the fuel may be determined accurately.

The calculation of the radial power distribution across the pellet is performed in FALCON using either the RADAR-G or the TUBRNP model. In addition, the radial power profile may be input by the user, which overrides the internal models. The following gives a brief overview of the RADAR-G and TUBRNP models. Detailed descriptions of the models can be found in Appendix E and References 72-75

### 5.6.1 BNFL -- RADAR-G Model

The RADAR-G model [72] described here (Rating Depression Analysis Routine incorporating Gadolinia) was developed by BNFL (British Nuclear Fuels Limited) specifically as a means of

calculating the radial power profile in a fuel rod of any type thermal reactor for use within a general purpose fuel performance code. RADAR-G was developed to represent the influence of gadolinia used as a burnable poison on the radial power profile. The routine is equivalent to the original RADAR routine in the absence of gadolinium [73].

The presence of gadolinia in the fuel pellet results in a rapidly varying neutron spectrum across the pellet as low energy neutrons are absorbed at the pellet periphery. As the gadolinium isotopes 155 and 157 are depleted, the low energy neutrons are able to penetrate further into the pellet. This behavior causes an irradiation dependence for the effective cross-sections of the gadolinium, uranium, and plutonium.

The gadolinium isotopes only influence the thermal fissions in the pellet, and the fast fissions which account for about 8% of the total power in a fuel assembly are not affected. As the gadolinium isotopes 155 and 157 are depleted, the ratio of fast-to-thermal fissions decreases. However, the total power produced by fast fissions remains unchanged throughout burnup in the presence of gadolinium. The RADAR-G model must therefore treat the fast fissions separately, requiring an additional input value which is time dependent. The relative power rating of the gadolinia fuel rod to the assembly rating is necessary to account for the fast fissions. This procedure is contrary to the treatment of fast fissions in the RADAR model. However, the methods produce comparable results when no gadolinium is present.

The self-shielding effects of the gadolinium isotopes influence both the fission and absorption cross-sections of the fissionable isotopes in addition to the gadolinium and results in cross-sections that are radius and irradiation dependent. The evaluation of the self-shielding effects in the presence of gadolinium requires multi-group neutron transport calculations within the fuel pellet. The neutron transport method is not possible in routine fuel performance calculations. Therefore, the self-shielding effects are incorporated in RADAR-G through empirical relationships used to determine effective thermal cross-sections and effective thermal fluxes. The relationships yield the cross-sections at a given radius as a function of the number densities of the gadolinium isotopes integrated from the pellet outer radius. An empirical multiplier is also applied to the inverse diffusion length to account for transport effects. The model's equations and their numerical representations are described in detail in Appendix E.

### **5.6.2 TUBRNP Model**

The TUBRNP model (TRANSURANUS burnup model) was developed by Lassmann, et al. as an extension of the RADAR model for high burnup applications [12, 74, 75]. The approach used in the TUBRNP model employs single neutron group, spectrum-averaged cross-section to calculate the production or loss of selected isotopes. This approach is the same as that used in the RADAR model, however, additional plutonium isotopes are considered in the TUBRNP model. Furthermore, Lassman, et al, refined the empirical radial shape function used for the resonance absorption process using plutonium isotope measurements from fuel rods with burnup levels ranging between 23 and 63 GWd/MTU. Comparison of the plutonium concentrations calculated by the TUBRNP model and post-irradiation EPMA measurements show good argument.

The TUBRNP model is applicable to  $\text{UO}_2$ ,  $\text{UO}_2\text{Gd}_2\text{O}_3$  and MOX fuel types irradiated in LWR or heavy water moderated reactors (HWR). TUBRNP uses a single set of common cross-sections for both PWR and BWR reactors. A separate set is used for HWR conditions. The TUBRNP model has been incorporated in several fuel performance codes, including FRAPCON-3 [14]. A detailed description of the model approach is provided in Appendix E.

## 5.7 Burnup Calculation

The fuel rod burnup distribution is used in FALCON to calculate the fuel pellet properties, the swelling and densification rates, and the formation of the high burnup structure. The axial and radial burnup distributions are also output by FALCON for comparison to other core analysis codes or measured data. The method used by FALCON to calculate the pellet average burnup and the local burnup distribution across the pellet is described below.

The change in pellet average burnup for a time step  $\Delta t$  is calculated in FALCON by:

$$\Delta \text{Bu}(z) = \frac{[P_{t+\Delta t}(z) + P_t(z)] \cdot \Delta t}{2 \cdot M_L \cdot f_u \cdot 10^3} \quad (\text{eq. 5-94})$$

where

$\Delta \text{Bu}(z)$  : Change in pellet average burnup at axial location  $z$

$P_{t+\Delta t}(z)$  : Current step linear power level at axial location  $z$

$P_t(z)$  : Previous step linear power level at axial location  $z$

$\Delta t$ : Time step

$M_L$ : Linear mass of  $\text{UO}_2$  at axial position  $z$

$f_u$ : Conversion factor between  $\text{UO}_2$  and uranium metal (0.8815)

The linear mass at axial position  $z$  is given by;

$$M_L = (1 - f_{\text{Gd}}) \cdot (1 - f_p) \cdot \rho_{\text{th}} \cdot \left( A_p - \frac{V_o}{L} \right) \quad (\text{eq. 5-95})$$

where

$f_{\text{Gd}}$ : Fractional enrichment of gadolinium

$f_p$ : Fractional as-manufactured porosity

$A_p$ : Cross-sectional area of the pellet based on as-manufactured dimensions

$V_o$ : Void volume associated with pellet dish ends, chamfers, and central hole

$L$ : Axial length of the segment containing the void volume

The fuel material theoretical density,  $\rho_{th}$ , is a function of gadolinium content and is given by [76];

$$\rho_{th} = \rho_{UO_2} - 4610 \cdot f_{Gd} \quad (\text{eq. 5-96})$$

where

$\rho_{UO_2}$  is the theoretical density of  $UO_2$  (Default = 10,980 kg/m<sup>3</sup>)

The  $UO_2$  theoretical density can be changed via input for fuel material that may differ from the default value used in FALCON.

The pellet average burnup is given by;

$$Bu_{t+\Delta t}(z) = \Delta Bu(z) + Bu_t(z) \quad (\text{eq. 5-97})$$

Furthermore, the radial burnup profile at axial position  $z$  is given by

$$Bu_{t+\Delta t}(r, z) = \Delta Bu(z) \cdot f_r(r, z) + Bu_t(r, z) \quad (\text{eq. 5-98})$$

where

$r$ : Radial position

$f_r(r, z)$ : Radial power distribution factor calculated from the RADAR-G or TUBRNP model at radial position  $r$  and axial position  $z$ .

To obtain an accurate calculation of the burnup accumulation based on the power history input to FALCON, the proper definition of the theoretical density, pellet dimensions and void volumes is required. Care should be taken in defining these parameters in FALCON.

## 5.8 References

1. Hagrman, D.L., "MATPRO - Version 11: A Handbook of Materials Properties for Use in the Analysis of Light Water Reactor Fuel Rod Behavior," NUREG/CR-0497 TREE-1280, February 1979.
2. SCDAP/RELAP5/MOD2 Code Manual, Volume 4: MATPRO – A Library of Materials Properties for Light-Water-Reactor Accident Analysis, EG&G Idaho, NUREG/CR-5273, February, 1990.
3. Yagnik, S. K., "Thermal Conductivity Recovery Phenomenon in Irradiated  $\text{UO}_2$  and (U, Gd)  $\text{U}_2$ ," Proceedings of the American Nuclear Society International Topical Meeting on LWR Fuel Performance, Park City, Utah, April 2000.
4. Kramman, M.A., Freeburn, H. R., Eds., *ESCORE--the EPRI Steady-State Core Reload Evaluator Code: General Description*, EPRI NP-5100, Electric Power Research Institute, Palo Alto, California, February 1987.
5. Christensen, J.A., Allio, R.J., Baincheria, A., "Melting Point of Irradiated Uranium Dioxide," WCAP-6065, 1965.
6. Philipponneau, Y., "Etude sur la Température a Fusion du Combustible Oxyde et sur son Evolution avec la taux de Combustion," Note Technique LPCA n°27.
7. Yamanouchi, S., et al. "Melting Temperature of Irradiated  $\text{UO}_2$  and  $\text{UO}_2$ -2wt% $\text{Gd}_2\text{O}_3$  Fuel Pellets up to Burnup of about 30 GWd/MTU," *Journal of Nuclear Science and Technology*, Volume: 25 No. 6, June 1988, pp. 528-533.
8. Komatsu, J., Tachibana, T., Konashi, K., "The Melting Temperature of Irradiated Oxide Fuel," *Journal of Nuclear Materials*, Volume: 154, 1988, pp. 38-44.
9. Krankota, J.L., Craig, C.N., "The Melting Point of Plutonia-Urania Mixed Oxide Fuel Irradiated to High Burnup," GEAP-13515, 1969.
10. Philipponneau, Y., "Catalogue Européen des Propriétés de l'oxyde mixte (U,Pu) $\text{O}_2$ ," Chapite II, Note Technique LPCA n°02.
11. Wiesenack, W., "Assessment of  $\text{UO}_2$  Conductivity Degradation Based on In-Pile Temperature Data," *Proceedings of the ANS International Topical Meeting on LWR Fuel Performance*, Portland, Oregon, March 2-6, 1997, p.507.
12. Lassman, K., Schubert, A., van de Laar, J., Vennix, C.W.H.M., "Recent Developments of the TRANSURANUS code with emphasis on high burnup phenomena," Nuclear Fuel behavior modeling at high burnup and its experimental support, Proceedings of a Technical Committee meeting in Windermere, United Kingdom, 19-23 June 2000.
13. Nakamura, J., "Thermal Diffusivity of High Burn-up  $\text{UO}_2$  Pellet Irradiated at HBWR," *Proceedings of OECD/NEA Seminar on Thermal Performance of High Burnup LWR Fuel*, Cadarache, France, March, 1998, p. 43.
14. Berna, G. A., "FRAPCON-3: A Computer Code for the Calculation of Steady State, Thermal-Mechanical Behavior of Oxide Fuel Rods for High Burnup," Pacific Northwest National Laboratory, NUREG/CR-6534, PNNL-11513, December 1997.

15. Turnbull, J. A., "An Empirical Model of  $\text{UO}_2$  Thermal conductivity Based on Laser Flash Measurements of Thermal Diffusivity," EPRI, Palo Alto, CA, 1998, TR-111347.
16. Baron, D. "Fuel Thermal Conductivity: A Review of the Modeling Available for  $\text{UO}_2$ , (U-Gd) $\text{O}_2$ , and MOX Fuel," *Proceedings of OECD/NEA Seminar on the Thermal Performance of High Burnup LWR Fuel*, Cadarache, France, March 1998, p. 99.
17. Freeburn, H. R., Ozer, O., Yang, R., "The Effect of Burnup on  $\text{UO}_2$  Thermal Conductivity - NRC Review of the ESCORE Model," *Enlarged Halden Programme Group Meeting on Fuels and Materials Performance and Computerized Man-Machine Communication*, Bolkesjo, Norway, June 9-14, 1991.
18. Ohira, K., Itagaki, N., "Thermal Conductivity Measurements of High Burnup  $\text{UO}_2$  Pellet and Benchmark Calculation of Fuel Centerline Temperature," *Proceedings of ANS International Topical Meeting on LWR Fuel Performance*, Portland, Oregon, March 2-6, 1997, p.541.
19. Lucuta, P. G., Matzke, H., Hastings, I.J., "A pragmatic approach to modeling thermal conductivity of irradiated  $\text{UO}_2$  fuel review and recommendations," *Journal of Nuclear Materials*, 232, 1996, pg. 166-180.
20. Watson, R. H., "Properties of the Urania-Gadolinia System (Part 2)," EPRI Report, NP-5861-LD.
21. Fukushima, S., et. al., "The Effect of Gadolinium Content on the Thermal Conductivity of Near-Stoichiometric (U,Gd) $\text{O}_2$  Solid Solutions," *Journal of Nuclear Materials*, 105, 1982, pg. 201-210.
22. Newman, L.W., Thornton, T. A., and Wrona, B.J., "Thermal and Physical Properties of Urania-Gadolinia Fuel," Babcock & Wilcox, DOE/ET/34212-43, BAW-1759, May 1984
23. Lippens, M, and Merters, L., "High Burnup  $\text{UO}_2$  and (U, Gd) $\text{O}_2$  Specimens: Thermal Diffusivity Measurements and Post-Irradiation Characterization," EPRI Report, TR-106501, December 1996.
24. Amaya M., et al., "Thermal conductivities of irradiated  $\text{UO}_2$  and (U, Gd) $\text{O}_2$  pellets," *Journal of Nuclear Materials*, 300, 2002, pg. 57-64.
25. Alvarez, M. T., Hirai, M., Wiesenack, W., "Analysis of the Thermal Behavior of Gd-Bearing Fuel in IFA-515.10," OECD Halden Reactor Project, HWR-470, April 1996.
26. S. Bremier, R. Manzel, and C.T. Walker, "Fission Gas Release and Fuel Swelling at Burn-Ups Higher than 50 MWd/kgU," *Proceedings of the International Seminar on Fission Gas Behaviour in Water Reactor Fuels*, Cadarache, France, 26-29 September, 2000.
27. Turnbull, T. A., Personal Communications, March 2001
28. P. Blanpain, X. Thibault, J-P. Pages, "Recent Results from the In-Reactor MOX Fuel Performance in France and Improvement Program," *Proceedings of the International Topical Meeting on Light Water Reactor Fuel Performance*, Portland Oregon, March 2-6, 1997.
29. K. Une, K. Nogita, Y. Suzawa, K. Hayashi, K. Ito and Y. Etoh, "Effects of Grain Size and PCI Restraint on the Rim Structure Formation of  $\text{UO}_2$  Fuels," *Light Water Fuel Performance Meeting*, Park City, Utah, April 2000.
30. F. Anselin, "The Role of Fission Products in the Swelling of Irradiated  $\text{UO}_2$  and (U,Pu) $\text{O}_2$  Fuel" GEAP-5583 (January 1969)

31. "Scientific Issues in Fuel Behavior," OECD/NEA Nuclear Science Committee Task Force Report, January 1995
32. R. M. Berman, A. H. Meieran and P. W. Patterson, "Irradiation Behavior of Zircaloy Clad Fuel Rods Containing Dished-end  $\text{UO}_2$  Pellets (LWB-LSBR Development Program)", WAPD-TM-629, Bettis Atomic Power Laboratory, Westinghouse Electric Corporation, July 1967.
33. Dutt, D.S., Baker, R.B. and Chastain, S.A., "Modeling of the Fuel Cladding Postirradiation Gap in Mixed-Oxide Fuel Pins," West-Hanford, *Trans. Amer. Nucl. Soc.* 17, 1973.
34. Lassmann, K., Walker, C. T., Laar, J., Lindstrom, F., "Modeling the High Burnup  $\text{UO}_2$  Structure in LWR Fuel" *Journal of Nuclear Materials* 226 (1995), pp. 1-8.
35. Manzel, R. and Coquerelle, M., "Fission Gas Release and Pellet Structure at Extended Burnup", Proceedings of the ANS Topical Meeting on Light Water Reactor Fuel Performance, Portland, Oregon, March 2-6, 1997, pp 463-470.
36. *In-Pile Determination of Thermal Conductivity of Oxide Layer on LWR Cladding: Part 1: Irradiation Period July-October 1995*, EPRI Report, TR-107718-P1, January 1997.
37. Gorscak, D. A., and Pfennigwerth, P.L., "Analysis of Cladding Deformation over Plenum Axial Gaps in Zircaloy Clad Fuel Rods," WAPD-TM-1339, December 1982.
38. Franklin, D. G., "Zircaloy-4 Cladding Deformation During Power Reactor Irradiation" *Zirconium in the Nuclear Industry; Fifth Conference ASTM STP 754*, D. G. Franklin, Ed., American Society for Testing and Materials, 1982, pp. 235-267.
39. Hobson, D. O., Thoms, K. R., Dodd, C. V., and van der Kaa, Th., "Effects of Temperature and Pressure on the In-Reactor Creepdown of Zircaloy Fuel Cladding," *Zirconium in the Nuclear Industry; Fifth Conference, ASTM STP 754*, D. G. Franklin, Ed., American Society for Testing and Materials, 1982, pp. 173-192.
40. Gilbon, D., Soniak, A., Doriot, S., and Mardon, J. P., "Irradiation Creep and Growth Behavior and Microstructural Evolution of Advanced Zr-Base Alloys," *Zirconium in the Nuclear Industry: Twelfth International Symposium, ASTM STP 1345*, G. P. Sabol and G. D. Moan, Eds, American Society for Testing and Materials, West Conshohocken, PA, 2000, pp. 51-73.
41. Limbäck, M. and Andersson, T., "A Model for Analysis of the Effect of Final Annealing on the In-and-Out-of-Reactor Creep Behavior of Zircaloy Cladding," *Zirconium in the Nuclear Industry: Eleventh International Symposium, ASTM STP 1295*, E. R. Bradeley and G. P. Sabol, Eds, American Society for Testing and Materials, 1996, pp. 448-468.
42. Matsuo, Y., "Thermal Creep of Zircaloy-4 Cladding under Internal Pressure," *Journal of Nuclear Science and Technology*, Vol. 24, No. 2, February 1987, pp. 111-119.
43. Hoppe, N. E., "Engineering Model for Zircaloy Creep and Growth," Proceedings, ANS-ENS International Topical Meeting in LWR Fuel Performance, Avignon, France 21-24 April 1991, pp. 201-209.
44. Gilmore, P.M., Klepfer, H. H., Sorensen, J. M., "EPRI PWR Fuel Cladding Corrosion (PFCC) Model Volume 1: Theory and User's Manual," EPRI Report, TR-105387-V1, December 1995.



45. Cathcart, J.V. "Quarterly Progress Report on the Zirconium Metal-Water Oxidation Kinetics Program" Sponsored by the NRC Division of Reactor Safety Research for April - June 1976, ORNL/NUREG/TM-41, August 1976.
46. Baker, L. and Just, L.C., "Studies of Metal-Water Reactions at High Temperatures - III. Experimental and Theoretical Studies of the Zirconium-Water Reaction," ANL-6548, May 1962.
47. Leistikow, S., Schanz, G., and vBerg, H., "Kinetik Und Morphologic der isothermen Dampf-Oxidation von Zircaloy-4 bei 700-1300°C," Kernforschungszentrum Karlsruhe, KFK 2587, March 1978.
48. Urbanic V. F., and Heidrick, "High-Temperature Oxidation of Zircaloy-2 and Zircaloy-4 in Steam," *Journal of Nuclear Materials*, 75, 1978, pg. 251-261.
49. Rashid, Y.R., Nerman, H., "Application of SAFE-2D Program to the Analysis of Fuel-Rod Ramp Tests," *Transactions of American Nuclear Society 1976 Winter Meeting*, Washington, D. C., November 1976, pp. 170-171.
50. Bocek, M., "Creep Rupture at Non-Steady Stress and Temperature Loading Conditions," Institut fur Material- und Festkorperforschung Projekt Nukleare Sicherheit, KfK-2699.
51. Cheung, T. and Rosinger, H.E., "A Failure Criterion for Thin-Walled Zircaloy Fuel Cladding under LOCA Conditions," *6th International Conference on Structural Mechanics in Reactor Technology*, Paris, France, August 1981.
52. Erbacher, F.J., Neitzel, H.J. and Wiehr, K., "Studies and Zircaloy Fuel Clad Ballooning in a LOCA, Results of Burst Tests with Indirectly Heated Fuel Rod Simulators," *STP 681 Proceedings of the ASTM 4th International Conference on Zirconium in the Nuclear Industry*, June 1978.
53. Rashid, Y.R., "Transient Failure of Zircaloy Cladding: State-of-the-Art Study and Model Development," EPRI NP-4976, December 1986.
54. Roberts, J.T.A., et al., "A Stress Corrosion Cracking Model for Pellet-Cladding Interaction Failures in Light-Water Reactor Fuel Rods," *STP 681 Proceedings of the ASTM 4th International Conference on Zirconium in the Nuclear Industry*, June 1978.
55. Higdon, A. Ohlsen, E., Stiles, W., Weese, J., Riley, W., *Mechanics of Materials*, John Wiley & Sons, New York, 3<sup>rd</sup> Edition, 1976.
56. Juvinall, R., *Engineering Considerations of Stress, Strain, and Strength*, McGraw-Hill, New York, 1<sup>st</sup> Edition, 1967.
57. Timoshenko, S., Goodier, J.N., *Theory of Elasticity*, McGraw-Hill, New York, 2<sup>nd</sup> Edition, 1951.
58. Popov, E.P., *Mechanics of Materials*, "Prentice-Hall, Inc., New York, 1<sup>st</sup> Edition, 1952.
59. Hoffman, O., Sachs, G., *Introduction to the Theory of Plasticity for Engineers*, McGraw-Hill, New York, 1<sup>st</sup> Edition, 1953.
60. Rashid, Y.R., Montgomery, R.O., Lyon, W.L., Yang, R., "A Cladding Failure Model for Fuel Rods Subjected to Operational and Accident Transients," *Nuclear Fuel Behavior Modeling at High Burnup and Its Experimental Support, IAEA Prodeedings of Technical Committee Meeting*, Windermere, U.K., June 2000, p. 187.

61. Turner, S.E., et al., "Background and Derivation of ANS-5.4 Standard Fission Product Release Model," NUREG/CR-2507, January 1982.
62. Forsberg, K., and Massih, A. R., "Diffusion Theory of Fission Gas Migration in Irradiated Nuclear Fuel  $\text{UO}_2$ ," Journal of Nuclear Materials, 135, 1985 pg. 140-148.
63. Ritterbusch, S.E., et al., "Factors Affecting Post-DNB Operation for Light Water Reactors, Volume 1," EPRI NP-1999, RP 1382-1, August 1981.
64. Gates, G.A., et. al., "Thermal Performance Modeling with the ENIGMA Code," Proceedings of the OECD/NEA Seminar on Thermal Performance of High Burnup LWR Fuel, Cadarache, France, March 1998.
65. Lyon W., Jahingir, N., and Montgomery, R., "Fuel Analysis and Licensing Code: FALCON MOD01, Volume 3, Verification and Validation," EPRI, Palo Alto, CA, December 2004, 1011308.
66. Vitanza, C., Kolstad, E., and Graziani, U., "Fission Gas Release from  $\text{UO}_2$  Pellet Fuel at High Burnup," Proceedings of the American Nuclear Society Topical Meeting on Light Water Reactor Fuel Performance, Portland Oregon, May 1979.
67. White, R. J. and Tucker, M. O., "A New Fission-Gas Release Model," Journal of Nuclear Materials, 118, 1983, pg. 1-38.
68. L.O. Jernkvist, A.R. Massih, J. In de Betou, "Evaluation of Fission Product Gas Release and the Impact of Fuel Microstructure at High Burnup" Halden Program Group Meeting, September 8-13, 2002, Storefjell, Gol, Norway.
69. Olander, D. R., "Fundamental Aspects of Nuclear Reactor Fuel Elements," TID-26711-PI, Technical Information Center Energy Research and Development Administration, 1976.
70. L.C. Bernard, J. L. Jacoud, and P. Vesco, "An Efficient Model for the Analysis of Fission Gas Release." Journal of Nuclear materials 302 (2002) 125-134
71. Gehl, S.M., et al., "Fission Gas Release from Irradiated PWR Fuel During Simulated PCM-Type Accidents," Progress Report, NUREG/CR-0088, ANL-77-80, May 1978.
72. Thomas, G.M., Hesketh, K.W., "RADAR-G - A Routine for Calculating Radial Power Profiles in Thermal Reactor Fuel," BNFL, EPRI Contract 18362, November 1986.
73. Palmer, I.D., et al., "A Model for Predicting the Radial Power Profile in a Fuel Pin," IAEA Specialists Meeting on Water Reactor Fuel Element Performance Computer Modeling, Preston, March 14-19, 1982.
74. Lassman, K., et al., "The radial distribution of plutonium in high burnup  $\text{UO}_2$  fuels," Journal of Nuclear Materials, 208, 1994, pg. 223-231.
75. Lassman, K., Walker, C. T., van de Laar, J., "Extension of the TRANSURANUS burnup model to heavy water reactor conditions," Journal of Nuclear Materials, 255, 1998, 222-233.
76. Newman, L.W., "Development and Demonstration of an Advanced Extended-Burnup Fuel Assembly Design Incorporating Urania-Gadolinia, First Semi-Annual Progress Report, March-September 1981, "DOE/ET/34212-34, BAW-1681-1, February 1982.

# 6

## NUMERICAL SOLUTION PROCEDURE

---

### 6.1 General

FALCON solves a complex set of coupled thermal-mechanical heat conduction and equilibrium equations. This coupling occurs because the thermal solution depends on both the temperature and deformations of the fuel and clad, especially as they affect the gap thickness which affects the gap conductances. The fuel and clad thermal solution affects and is affected by the (optional) coolant channel enthalpy solution. The mechanical solution is strongly dependent on the thermal solution in that fuel thermal expansion and fission gas release are determined by the temperature, and the fuel and clad mechanical properties are strong functions of temperature.

### 6.2 Iteration Procedure Between Thermal and Mechanical Analysis

An important consideration in fuel rod modeling is the procedure used to provide proper interaction between the thermal analysis and the mechanical analysis during a time step. The complex interdependence of the two solutions requires adequate coupling to insure solution accuracy. A staggered thermal-mechanical solution strategy is implemented in FALCON that links the thermal and mechanical results during a time step solution. Convergence and improved accuracy is achieved by this method.

The staggered solution strategy loops around the thermal and the mechanical solutions in each thermal-mechanical iteration as follows. At time,  $t+\Delta t$ , the time step is initiated by conducting a thermal analysis using the current conditions for the coolant and power. The mechanical results from the previous time step,  $t$ , are used to establish the gap conditions required in the gap conductance calculation. Within the thermal analysis, a Picard iterative solution for steady state conditions or a direct solution for transient conditions is used to solve for the temperatures throughout the fuel rod. Next, the mechanical analysis is conducted using a Newton-Raphson iterative solution using the thermal results just calculated to define the temperature dependent material properties, the thermal forces and expansion strains. The mechanical solution produces a new deformation state which may change the fuel-clad gap status, thus affecting the gap conductance. This completes the first thermal-mechanical iteration in the step. At a minimum, a second iteration is conducted using the new deformation state and the new temperatures. The new thermal results are then used in a second mechanical analysis. User options are available to control and increase the number of iterations, if necessary.

The MOD-1 release of FALCON includes substantial enhancements and improvements to the iteration procedures. In the next release, it should be possible to fully test for convergence and eliminate the need for users to deal with these numerical issues.

The final thermal solution is used to compute the fission gas release increment for time  $t+\Delta t$ . The fission gas release results are then used in the next step for both the thermal and mechanical solutions.

### 6.3 Thermal Analysis

A large body of literature [1, 2] is available on possible time integration schemes for equations of the heat conduction type. Both implicit and explicit methods have been used successfully. In order to efficiently apply typical explicit integration schemes to the heat conduction equation, the capacity matrix  $\tilde{M}$  defined in eq. 3-12 is replaced with an "equivalent" matrix  $\tilde{M}_D$  which has non-zero coefficients only on the diagonal. This lumping procedure, which expedites the inversion of  $\tilde{M}$  as required in explicit schemes, has been widely studied for use with lower order finite element approximations, e.g., bilinear approximations for the dependent variable. In FALCON, a higher order finite element approximation was chosen (biquadratic), and rather than perform an exhaustive study of lumping procedures for such an element, an implicit integration method was used. Implicit methods have the added advantage of unconditional numerical stability thus allowing the use of larger time increments. However, implicit integration produces zero-energy spatial variations in the temperature field when time steps too short to allow conduction are used. This can be eliminated by switching to explicit integration when small time steps are needed.

The numerical integration procedure implemented in FALCON is a central difference method which is related to the c Crank-Nicholson scheme. The derivation of the algorithm is given elsewhere [2, 3]. Based on eq. 3-19, the integration procedure is

$$\left\{ \frac{2}{\Delta t} \tilde{M}(\tilde{T}^a) + \tilde{K}^*(\tilde{T}^a) \right\} \tilde{T}^a = \tilde{F}^*(\tilde{T}^a) + \frac{2}{\Delta t} \tilde{M}^*(\tilde{T}^a) \tilde{T}^n \quad (\text{eq. 6-1})$$

where\*

$$\tilde{T}^a = \frac{\tilde{T}^{n+1} + \tilde{T}^n}{2}, \quad (\text{eq. 6-2})$$

and superscript n indicates the time step number and  $\Delta t$  the time step size ( $\Delta t = t^{n+1} - t^n$ ).

---

\* Superscripts on nodal vectors such as  $\tilde{T}^{n,i}$  denotes Step number ( $n=1,2,\dots$ ) and Iteration number ( $i=1,2,\dots$ ) with steps always identified using the superscript "n", iterations always identified using the superscript "i", and "a" is always used for average.  $\tilde{T}^{n,i}$  means the nodal point temperature at step "n" and iteraton "i".  $\tilde{T}^n$  means the converged or final temperature at Step "n".

### 6.3.1 Steady State Solution

In eq. 6-1, if  $\Delta t \rightarrow \infty$ , then the steady state form of the heat conduction equation is recovered. For this condition, the basic matrix equation reduces to

$$\underset{\sim}{K}^* \left( \underset{\sim}{T} \right) \underset{\sim}{T}^{n+1} = \underset{\sim}{F}^* \left( \underset{\sim}{T} \right) \quad (\text{eq. 6-3})$$

Considering first the case where  $\underset{\sim}{K}^*$  and  $\underset{\sim}{F}^*$  are not functions of  $\underset{\sim}{T}$ , eq. 6-3 reduces to a linear matrix equation which may be solved directly. When eq. 6-3 retains its nonlinear form, an iterative technique is required. FALCON uses a Picard iteration (successive substitution) method which is expressed by

$$\underset{\sim}{K}^* \left( \underset{\sim}{T}^{n+1,i} \right) \bullet \underset{\sim}{T}^{n+1,i+1} = \underset{\sim}{F}^* \left( \underset{\sim}{T}^{n+1,i} \right) \quad (\text{eq. 6-4})$$

where superscript i indicates the iteration level within the time step n. The algorithm in eq. 6-4 is equivalent to solving a time dependent problem using eq. 6-1 with  $\Delta t \rightarrow \infty$ . As can be seen from eq. 6-4, the steady state solution is not governed by the size of the time step but rather by the power increment. Experience has shown that a power increment in the range of 2-3 kW/m provides sufficient accuracy for the thermal as well as the deformation solutions.

The algorithm in eq. 6-1 is identical to a standard Crank-Nicholson method except that the solution is not extended to the end of the time interval. This method (termed an averaged Crank-Nicholson) can be shown to be unconditionally stable for linear problems. For nonlinear problems, predictor-corrector methods [2] can be used in conjunction with eq. 6-1 to improve the temperature estimates for evaluation of the temperature dependent terms. In actual implementation of eq. 6-1, note that if  $\Delta t$  is kept constant and the problem is linear with time independent boundary conditions, then the left-hand side of eq. 6-1 needs to be triangularized only once. This is not the case in FALCON since the problem is highly nonlinear and the time step size, which is also influenced by the deformation solution, varies from step to step. This requires that the governing equations be reformulated at every time step.

## 6.4 Deformation (Mechanical) Analysis

The derivations presented in Section 4 produce a set of equations that relate the incremental displacements (two components at each node in the grid), to the incremental nodal forces. The net incremental nodal force vector is the sum of external and internal forces, thermal forces, inelastic internal forces, and fuel-clad interaction forces. Designating the incremental nodal force vector by  $\Delta \underset{\sim}{F}$ , then

$$\Delta \underset{\sim}{F} = \Delta \underset{\sim}{F}_P + \Delta \underset{\sim}{F}_I \quad (\text{eq. 6-5})$$

where

$$\Delta \tilde{F}_I = \Delta \tilde{F}_T + \Delta \tilde{F}_C + \Delta \tilde{F}_R \quad (\text{eq. 6-6})$$

In the above

$\Delta \tilde{F}_P$ : External force vector due to surface pressures;

$\Delta \tilde{F}_I$ : Internal force vector due to internal stresses;

$\Delta \tilde{F}_T$ : Thermal force vector;

$\Delta \tilde{F}_C$ : Inelastic force vector due to material nonlinearity (creep and plasticity); and

$\Delta \tilde{F}_R$ : Interaction force vector due to changes in fuel-clad gap status.

The governing equations can then be expressed as:

$$\tilde{K} \Delta \tilde{v} = \Delta \tilde{F} \quad (\text{eq. 6-7})$$

where  $\Delta \tilde{v}$  is the incremental nodal displacement vector and  $\tilde{K}$  is the tangent stiffness matrix which consists of three parts as follows:

$$\tilde{K} = \tilde{K}_U + \tilde{K}_\sigma + \tilde{K}_P \quad (\text{eq. 6-8})$$

where

$\tilde{K}_U$ : Updated Lagrangian tangent stiffness matrix referenced to the current (deformed) configuration which counts for material nonlinearities and the displacements.

$\tilde{K}_\sigma$ : Initial stress stiffness matrix.

$\tilde{K}_P$ : Load stiffness matrix resulting from pressure applied on the deformed surface or, in general, deformation-following loads.

The step-by-step solution of eq. 6-7 requires that

$$\Delta \tilde{F}^{(n)} = \tilde{K}^{(n)} \Delta \tilde{v}^{(n)} \quad (\text{eq. 6-9})$$

where  $n$  is the current time step or the time step for which the new solution is sought. Equation 6-9 presumes that the structure is in equilibrium at the end of the preceding time step; i.e., the internal stresses are in exact equilibrium with the external loads and no residual unbalanced

forces exist. Such an ideal case, however, would exist only if the system is linear and if the computations are done in infinite precision. Neither condition exists here; hence, it becomes necessary to restore equilibrium by calculating the residual vector and adding it to eq. 6-9. Let  $\tilde{F}_{\sigma}^{(n)}$  be the nodal force vector which results from converting the element stresses  $\tilde{\sigma}^{(n)}$  to equivalent nodal forces in the current configuration, then the residual vector is

$$\tilde{R}^{(n+1)} = \tilde{F}_P^{(n)} - \tilde{F}_{\sigma}^{(n)} \quad (\text{eq. 6-10})$$

where

$\tilde{R}^{(n+1)}$ : Residual (out of equilibrium) force vector for time step n+1.

$\tilde{F}_P^{(n)}$ : Total external load vector (due to surface pressure in this case) at time step n.

Clearly,  $\tilde{R}^{(n+1)}$  approaches the null vector as equilibrium is satisfied. Adding the residual load vector to  $\Delta \tilde{F}^{(n+1)}$  and making use of eq. 6-5 gives

$$\tilde{F}_P^{(n+1)} - \tilde{F}_{\sigma}^{(n)} + \Delta \tilde{F}_I^{(n+1)} = \tilde{K}^{(n+1)} \Delta \tilde{v}^{(n+1)} \quad (\text{eq. 6-11})$$

The solution of eq. 6-11 gives rise to a new set of stresses which are referenced to the beginning-of-step configuration. Also, since the stiffness matrix  $\tilde{K}$  and internal force vector  $\Delta \tilde{F}_I$  are functions of the stresses and displacements, iteration is required to satisfy not only the new equilibrium balance but also the material properties data. Consider the  $i^{\text{th}}$  iteration in the step  $\Delta t = t^{(n+1)} - t^{(n)}$ , then eq. 6-11 can be written as

$${}^{(i)}\tilde{F}_P^{(n+1)} - {}^{(0)}\tilde{F}_{\sigma}^{(n)} + {}^{(i)}\Delta \tilde{F}_I^{(n+1)} = {}^{(i-1)}\tilde{K}^{(n+1)} {}^{(i)}\Delta \tilde{v}^{(n+1)} \quad (\text{eq. 6-12})$$

where the left-position superscript (i) refers to the  $i^{\text{th}}$  iteration in the step and the (0) left superscript on  $\tilde{F}_{\sigma}^{(n)}$  refers to beginning-of-step conditions, i.e.,  ${}^{(0)}\tilde{F}_{\sigma}^{(n)}$  is based on  $\tilde{\sigma}^{(n)}$  rather than  $\tilde{\sigma}^{(i-1)}$ . At the end of the step, one usually carries out a Newton iteration in which a small correction on the displacement due to the residual load vector is calculated as follows:

$${}^{(i+1)}\tilde{F}_P^{(n+1)} - {}^{(i)}\tilde{F}_{\sigma}^{(n+1)} = {}^{(i)}\tilde{K}^{(n+1)} {}^{(i+1)}\delta \tilde{v}^{(n+1)} \quad (\text{eq. 6-13})$$

Numerical Solution Procedure

The final displacement increment is the sum of  $^{(i)}\Delta_{\tilde{v}}^{(n+1)}$  and  $^{(i+1)}\delta_{\tilde{v}}^{(n+1)}$ . Equilibrium balance demands that

$$\lim_{i \rightarrow \infty} \left| ^{(i+1)}F_{\tilde{P}}^{(n+1)} - ^{(i)}F_{\tilde{\sigma}^{(i)}}^{(n+1)} \right| \rightarrow e_f \quad (\text{eq. 6-14})$$

where  $e_f$  is an arbitrarily small number.

In the above,  $^{(i)}K_{\tilde{\sigma}}^{(n+1)}$  is based on the most recent displacements and beginning-of-step stress state, i.e.,

$$^{(i)}K_{\tilde{\sigma}}^{(n+1)} = ^{(0)}K_{\tilde{\sigma}}^{(n+1)} + ^{(i)}K_{\tilde{u}}^{(n+1)} + ^{(i)}K_{\tilde{p}}^{(n+1)} \quad (\text{eq. 6-15})$$

Convergence is achieved if eq. 6-14 is satisfied or alternatively if the displacement correction satisfies

$$\lim_{i \rightarrow \infty} \left| ^{(i+1)}\Delta_{\tilde{v}}^{(n+1)} - ^{(i)}\Delta_{\tilde{v}}^{(n+1)} \right| \rightarrow e_v \quad (\text{eq. 6-16})$$

where  $e_v$  is arbitrarily small.



## 6.5 Time-Step Selection Criteria

The selection of an appropriate time step size is governed by stability and accuracy requirements for both the deformation and thermal solutions. Because of the very complex interaction of the many material and geometric nonlinearities that exist in fuel rod analysis, it is almost impossible to devise a fool-proof method for selecting an economical time step size while simultaneously satisfying solution accuracy. Users experienced in analysis of this type are usually very adept at selecting workable time step sizes that suit the particular problem being solved. It is more convenient, however, to rely on a form of automatic selection of the time step size.

### 6.5.1 Thermal Solution Criteria

During the steady state part of the thermal solution, two criteria are used to limit the time step size. For steady state power ramps,  $\Delta t$  is chosen to give a maximum power change (positive or negative) of 3 kW/m, i.e.,

$$\max_{z_j} \left| \dot{Q}^{(n+1)} - \dot{Q}^{(n)} \right| \leq 3 \quad , \quad j = 1, \dots \quad (\text{eq. 6-17})$$

The inequality is evaluated at all axial positions  $z_j$  at which the axial power profile is specified. The maximum power change per step can be defined by the user. For steady state constant power hold times, a maximum time step size is required to provide for an accurate solution. The default value is 200 hours, and a user option is available to redefine this criterion.

For transients, two criteria are used to determine a  $\Delta t$  for stability, maximum flow rate change ( $\Delta \dot{m}$ ), and maximum coolant pressure change ( $\Delta p$ ). The percent change is limited to 2% at the inlet by default; however, user input options are available to allow for modification of these criteria. The selection process is represented by

$$\max_{\text{inlet}} \left| \frac{r^{(n+1)} - r^{(n)}}{r^{(n+1)}} \right| \leq 0.02 \quad (\text{eq. 6-18})$$

where  $r$  represents the response parameters  $\dot{m}$  and  $p$ , respectively. These criteria are only activated for analysis using the coolant enthalpy model.

A stability time step criterion of the type normally used for explicit solutions is not required in FALCON. The implicit solution method used for the transient solution is unconditionally stable. The thermal time step selection criterion as specified above has been established to provide satisfactory accuracy of the results based on the coolant channel/fuel rod interface.

### 6.5.2 Deformation Solution Criteria

Criteria for time-step selection in the deformation solution are more complex due to the many variables that influence the accuracy of the solution. The most important of these variables are the thermal expansion and creep rates of the fuel and the cladding. Taking this as the primary measure, one can derive an expression for the upper bound on the size of the time step that ensures a well-behaved solution.

Let the calculated strain rate in the element be  $\dot{\epsilon}_c$ , and the material data strain rate that corresponds to the calculated stresses, temperature, etc., be  $\dot{\epsilon}_m$ . Then the condition that

$$\dot{\epsilon}_c^{(j)} \leq \dot{\epsilon}_m^{(j)} \quad j = 1, \dots, J \quad (\text{eq. 6-19})$$

This equation ensures compatibility between the structural response and material data. In this equation,  $J$  is equal to the total number of integration points in the grid including fuel and clad elements. Large differences between  $\dot{\epsilon}_c$  and  $\dot{\epsilon}_m$  indicate inaccurate or unstable solution. This occurs when  $\Delta t$  becomes large. Using this fact we can require that

$$\Delta t_{\text{mechanical}}^{(n+1)} \leq \max_j \left| \frac{\Delta \epsilon_c}{\dot{\epsilon}_m^{(j)}} \right|^{(n)} \quad j = 1, \dots, J \quad (\text{eq. 6-20})$$

The quantity  $\Delta \epsilon_c$  is the maximum strain increment that can be calculated without incurring instability or accuracy deterioration.  $\Delta \epsilon_c$  is assigned on the basis of experience. In small strain analysis  $\Delta \epsilon_c$  is usually limited to a fraction (less than 50%) of the elastic strain [4]. In large strain transient analysis, however,  $\Delta \epsilon_c$  can be as high as 0.2% strain. This value of 0.2% is used for both the fuel and cladding. Equation 6-21 is implemented in FALCON with a user override input value that limits  $\Delta t$  from below.

Equation 6-20 is applied to both fuel and clad elements. However, the fuel governs the  $\Delta t$  selection during steady state where the clad temperature, consequently the clad strain rate, is much smaller than their fuel counterparts. The cladding behavior, on the other hand, controls the time step selection during transients.

In summary, the FALCON code provides an automatic time stepping procedure which selects the minimum of the following:

1. An equivalent power step of 3 kW/m (see eq. 6-17)
2. Maximum constant power  $\Delta t = 200$  hours
3.  $\Delta t_{\text{coolant}}$  from eq. 6-18
4.  $\Delta t_{\text{mechanical}}$  from eq. 6-20
5. User specified  $\Delta t$
6. Satisfying the inflection points of all input forcing functions

As guidance to the user's choice of Criteria 5 above, the following table is provided.

**Table 6-1**  
**Guidelines for Time Step Size Selection**

Type of Problem	Time Step
Steady State/Fuel Performance Analysis	Time step size required to give 3 kW/m per step. During constant power, time step size may vary geometrically; e.g., 0.5, 1, 2, 4, 10, 20, 50, 100, 200, 500, 1000 ... hrs.
Power-Coolant-Mismatch (slow coolant mass flux decrease at constant power)	Time step size required to give 2%-3% reduction in mass flux per step. Activate automatic time stepping option with minimum step size to give 2% decrease in mass flux per step.
Power Excursion due to Reactivity Insertion	During the power spike use a time step size equal to 5%-10% of the time period of the spike. Also use automatic time stepping with 0.0025 sec. minimum step size. Restart the problem at the end of the power spike with automatic time stepping and minimum step sizes of 0.05, 0.1, 0.5 and 1.0 sec., respectively, for 2-sec. duration, 3-sec. duration and 10-sec. duration, and the remainder of the transient, respectively.
Loss of Coolant Blowdown Event (rapid changes in power, coolant pressure and mass flux)	Time step size required to give about 2% change in the coolant pressure and/or mass flux. Combine automatic time stepping with minimum step size equivalent to 2% of the blowdown period. Use multiple restarts and use code recommendations for changing the minimum step size in each restart run.
Oscillatory Power	Time step size required to give 3 kW/m per step.
Other Events	Interpolate between the above criteria, depending upon the severity of the event.

## 6.6 References

1. Wood, W. L. and Lewis, R. W., "A Comparison of Time Marching Schemes for the Transient Heat Conduction Equation," *Int. J. Num. Meth. Engng.*, Volume 9, 1975, pp. 679-689.
2. Nickell, R. E., "Applications of the Finite Element Method in Solid Mechanics, Fluid Mechanics and Heat Transfer, Developments in Mechanics, Volume 8," *Proc. 14th Midwestern Mech. Conf.*, Norman, Oklahoma, 1975, pp. 599-626.
3. Wilson, E. L. and Nickell, R. E., "Application of the Finite Element Method to Heat Conduction Analysis," *Nuclear Engineering and Design*, Volume 4, 1966, pp. 276-286.
4. Rashid, Y. R., "Computational Techniques in Incremental Methods in Mechanics," *Proceedings of the Conference on Computational Methods in Nuclear Engineering*, CONF-750413, Charleston, South Carolina, April 1975.



# A

## APPENDIX A: FINITE ELEMENT SPATIAL EQUATIONS

---

There are three types of elements available in FALCON: two-dimensional quadrilateral continuum elements, triangular continuum elements, and one-dimensional gap/contact elements. There is a complete family of linear to quadratic isoparametric quadrilaterals and triangles available as shown in Figures A-1 and A-2, respectively. For the quadrilateral, there are elements with 0, 1, 2, 3, and 4 quadratic sides; for the triangular, there are elements with 0, 1, 2, and 3 quadratic sides. A total of sixteen quadrilateral and eight triangular elements are possible.

The triangular and variable node quadrilateral elements are included in this section for completeness. These elements have been used for special interest problems only and have not been verified for fuel rod analysis. These elements are not recommended for licensing analysis unless independent verification is conducted for these elements. The only elements recommended for fuel rod licensing analysis are the linear (4-node) and quadratic (8-node and 9-node) quadrilateral elements and the linear (2-node) gap/contact element.

### A.1 Element Shape Functions and Basic Equations

All points within an element are identified by their natural coordinates ( $\tilde{L}$ ) using the shape functions and nodal point coordinates

$$X(\tilde{L}) = \sum_{n=1}^N \phi_n(\tilde{L}) X_n$$

for plane geometries (eq. A-1)

$$Y(\tilde{L}) = \sum_{n=1}^N \phi_n(\tilde{L}) Y_n$$

$$R(\tilde{L}) = \sum_{n=1}^N \phi_n(\tilde{L}) R_n$$

for axisymmetric geometries (eq. A-2)

$$Z(\tilde{L}) = \sum_{n=1}^N \phi_n(\tilde{L}) Z_n$$

## Appendix A: Finite Element Spatial Equations

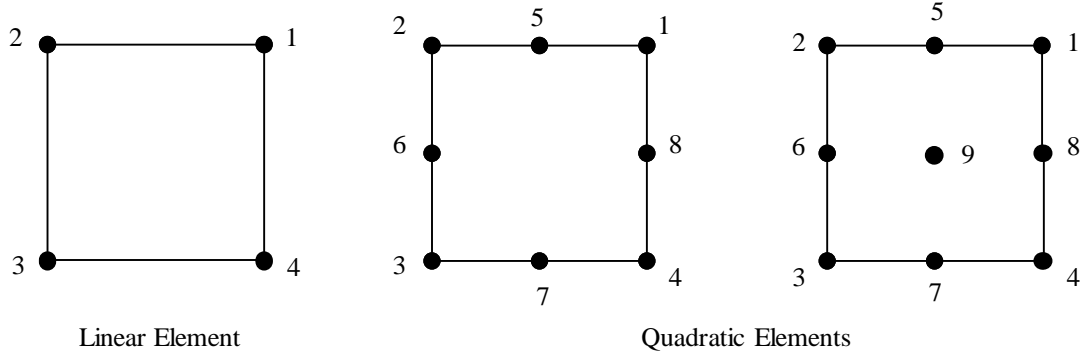


**Figure A-1**  
**Linear-Quadratic Quadrilateral Elements**

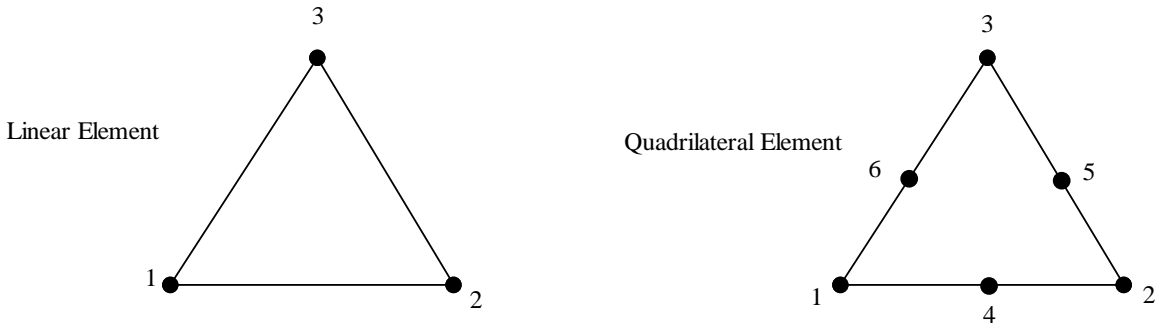


**Figure A-2**  
**Linear-Quadratic Triangular Elements**

In the above,  $X$  and  $Y$  or  $R$  and  $Z$  represent the material coordinates of a point in two-dimensional planar or axisymmetric geometries, respectively,  $\phi_n$  is then the  $n^{\text{th}}$  shape function, and  $X_n, Y_n$  or  $R_n, Z_n$  are the coordinates of the  $n^{\text{th}}$  nodal point. The total number of nodal points in the element is  $N$ , for quadratic quadrilaterals,  $N=8$  or  $9$ , and for quadratic triangles,  $N=6$ . As shown in Figures A-1 and A-2, the nodes are numbered counterclockwise starting at any corner node and numbering all corner nodes first, then all possible midside nodes are numbered.

The choice of the "natural" coordinates for the elements is a critical step in the development of the finite element methodology. As illustrated in Figure A-3, the natural coordinates for quadrilateral elements are the so-called "parametric" coordinates  $\xi$  and  $\eta$ , i.e.,  $L_1 = \xi$  and  $L_2 = \eta$ . These coordinates are defined such that  $-1 \leq \xi, \eta \leq 1$  and the extreme values represent the edges or sides of the element:

- $\xi = -1$  is the node 4-1 side
- $\xi = +1$  is the node 2-3 side
- $\eta = -1$  is the node 1-2 side
- $\eta = +1$  is the node 3-4 side

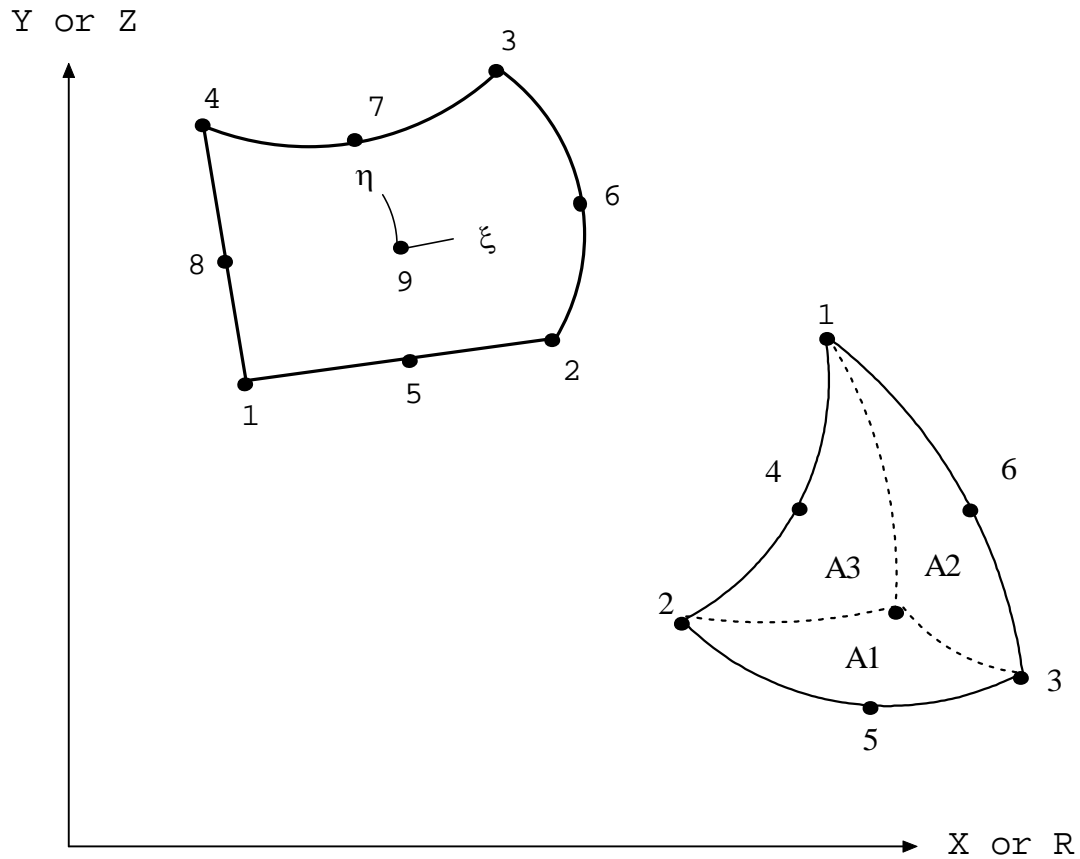


**Figure A-3**  
**Symbolic Natural Coordinates for Quadrilateral and Triangular Elements**

The following is a list of the values of the parametric coordinates at all eight possible nodes in a quadrilateral element:

	<u>Node (n)</u>	$\xi_n$	$\eta_n$
Corner Nodes:	1	-1	-1
	2	+1	-1
	3	+1	+1
	4	-1	+1
Midside Nodes:	5	0	-1
	6	+1	0
	7	0	+1
	8	-1	0

The "natural" coordinates for a triangular element are the "area" coordinates. As illustrated in Figure A-3,

Appendix A: Finite Element Spatial Equations

$$L_i = A_i / A \quad \text{for plane geometries}$$

where

$$A = A_1 + A_2 + A_3$$

The area associated with the  $i^{\text{th}}$  node is the area bounded by the side of the triangle opposite the  $i^{\text{th}}$  node and the curves drawn from the corner nodes of the opposite side. There are, of course, only two independent natural coordinates because of the constraint  $L_1 + L_2 + L_3 = 1$ . The  $L_i$  area coordinates vary from 0 at all points on the opposite side to +1 at the  $i^{\text{th}}$  node. The following is a list of the values of the area coordinates at all six possible nodes in a triangular element.

	<u>Node</u>	<u><math>L_1</math></u>	<u><math>L_2</math></u>	<u><math>L_3</math></u>
Corner Nodes:	1	1	0	0
	2	0	1	0
	3	0	0	1
Midside Nodes:	4	$\frac{1}{2}$	$\frac{1}{2}$	0
	5	0	$\frac{1}{2}$	$\frac{1}{2}$
	6	$\frac{1}{2}$	0	$\frac{1}{2}$



## A.2 Quadrilateral Shape Functions

The linear shape functions for a quadrilateral element are:

$$QH_i = (1 + \xi \xi_i)(1 + \eta \eta_i)/4 \quad \text{for } 1 \leq i \leq 4$$

The quadratic shape functions for an 8-node quadrilateral are:

$$QQ_i = (\xi \xi_i + \eta \eta_i - 1)QH_i \quad \text{for } 1 \leq i \leq 4$$

$$QQ_i = (1 - \xi^2)(1 + \eta \eta_i)/2 \quad \text{for } i = 5, 7$$

and

$$QQ_i = (1 - \eta^2)(1 + \xi \xi_i)/2 \quad \text{for } i = 6, 8$$

The quadratic shape functions for a 9-node quadrilateral are:

$$Q9_9 = (1 - \xi^2)(1 - \eta^2)$$

$$Q9_i = QQ_i + \frac{1}{4}Q9_9 \quad \text{for } 1 \leq i \leq 4$$

$$Q9_i = QQ_i - \frac{1}{2}Q9_9 \quad \text{for } 5 \leq i \leq 8$$

## A.3 Triangular Shape Functions (For Research Purposes Only)

The linear shape functions for a triangular element are:

$$TH_i = L_i \quad \text{for } 1 \leq i \leq 3$$

The quadratic shape functions are:

$$TQ_i = L_i(2L_i - 1) \quad \text{for } 1 \leq i \leq 3$$

and

$$TQ_i = 4L_j L_k \quad \text{for } 4 \leq i \leq 6$$

where  $j = i - 3$ ,  $1 \leq k \leq 3$ ,  $k \neq i - 3$ , and  $k \neq j$ .

## A.4 Shape Function Derivatives/Jacobian

The development of finite element stiffness and conductivity matrices for solid continuum elements requires the evaluation of the first derivatives of the shape functions. Since the shape functions have been expressed in terms of the natural coordinates,  $\tilde{L} = L_1, L_2$  (equations A-1 and A-2), this requires the development of the Jacobian matrix. For simplicity the derivation will be done in plane geometry. Using the chain rule

$$\frac{\partial}{\partial L_1} = \frac{\partial}{\partial X} \frac{\partial X}{\partial L_1} + \frac{\partial}{\partial Y} \frac{\partial Y}{\partial L_1}$$

$$\frac{\partial}{\partial L_2} = \frac{\partial}{\partial X} \frac{\partial X}{\partial L_2} + \frac{\partial}{\partial Y} \frac{\partial Y}{\partial L_2}$$

or in matrix form

$$\begin{bmatrix} \frac{\partial}{\partial L_1} \\ \frac{\partial}{\partial L_2} \end{bmatrix} = [J] \begin{bmatrix} \frac{\partial}{\partial X} \\ \frac{\partial}{\partial Y} \end{bmatrix}$$

where

$$[J] = \begin{bmatrix} \frac{\partial X}{\partial L_1} & \frac{\partial Y}{\partial L_1} \\ \frac{\partial X}{\partial L_2} & \frac{\partial Y}{\partial L_2} \end{bmatrix}$$

The coefficients in the Jacobian matrix are easily evaluated from the shape functions

$$\frac{\partial X}{\partial L_i} = \sum_{n=1}^N \frac{\partial \phi_n}{\partial L_i} (\tilde{L}) X_n$$

$$\frac{\partial Y}{\partial L_i} = \sum_{n=1}^N \frac{\partial \phi_n}{\partial L_i} (\tilde{L}) Y_n$$

The inverse relationships are

$$\frac{\partial}{\partial X} = \frac{\partial}{\partial L_1} \frac{\partial L_1}{\partial X} + \frac{\partial}{\partial L_2} \frac{\partial L_2}{\partial X}$$

$$\frac{\partial}{\partial Y} = \frac{\partial}{\partial L_1} \frac{\partial L_1}{\partial Y} + \frac{\partial}{\partial L_2} \frac{\partial L_2}{\partial Y}$$

or

$$\begin{bmatrix} \frac{\partial}{\partial X} \\ \frac{\partial}{\partial Y} \end{bmatrix} = [J^{-1}] \begin{bmatrix} \frac{\partial}{\partial L_1} \\ \frac{\partial}{\partial L_2} \end{bmatrix}$$

Thus,

$$\partial L_1 / \partial X = (\partial Y / \partial L_2) / J$$

$$\partial L_2 / \partial X = -(\partial Y / \partial L_1) / J$$

$$\partial L_1 / \partial Y = -(\partial X / \partial L_2) / J$$

$$\partial L_2 / \partial Y = (\partial X / \partial L_1) / J$$

where

$$J = (\partial X / \partial L_1)(\partial Y / \partial L_2) - (\partial Y / \partial L_1)(\partial X / \partial L_2)$$

## A.5 Isoparametric Interpolation

All of the continuum (solid) element types in the FALCON code are isoparametric elements; that is, the nodal point unknowns (temperature and displacements) are interpolated using the same shape functions as were used to interpolate the coordinates. Thus

$$T(\tilde{L}, t) = \sum_{n=1}^N \phi_n(\tilde{L}) \theta_n(t) = \tilde{\phi}^T(\tilde{L}) \tilde{\theta}(t)$$

and

$$U_i(\tilde{L}, t) = \sum_{n=1}^N \phi_n(\tilde{L}) v_i^n(t) = \tilde{\phi}^T(\tilde{L}) \tilde{v}_i(t)$$

where  $T$  and  $U_i$  are the temperature and displacement fields, respectively, and  $\tilde{\theta}$  and  $\tilde{v}$  are vectors of nodal point temperatures and displacements for a particular element.

Gradients of the interpolated variables are computed using the chain rule and Jacobian matrix; e.g.,

$$\partial T / \partial X_i = \tilde{\phi}_{,i}^T \tilde{T} = \tilde{T}^T \tilde{\phi}_{,i}$$

Appendix A: Finite Element Spatial Equations

where

$$\phi_{,i} = \frac{\partial \phi}{\partial L_1} \frac{\partial L_1}{\partial X_i} + \frac{\partial \phi}{\partial L_2} \frac{\partial L_2}{\partial X_i}$$

thus

$$\partial \phi / \partial X = (\partial \phi / \partial L_1 (\partial Y / \partial L_2) - \partial \phi / \partial L_2 (\partial Y / \partial L_1)) / J$$

Recall

$$\underline{X} = \underline{\phi}^T \underline{X}$$

$$\underline{Y} = \underline{\phi}^T \underline{Y}$$

thus

$$\partial \phi / \partial X = (\partial \phi / \partial L_1 (\partial \phi^T / \partial L_2) \underline{Y} - \partial \phi / \partial L_2 (\partial \phi^T / \partial L_1) \underline{Y}) / J$$

Denote

$$\phi_i \phi_j^T = (\partial \phi / \partial L_i) (\partial \phi^T / \partial L_j)$$

Note that commas are not used because the differentiation is not with respect to the Cartesian coordinates. Thus,

$$\partial T / \partial X = \underline{T}^T (\phi_1 \phi_2^T \underline{Y} - \phi_2 \phi_1^T \underline{Y}) / J$$

In the above, note that the shape function product matrices are independent of the nodal coordinates.

# B

## APPENDIX B: COOLANT ENTHALPY MODEL

The coolant channel model is based on a homogeneous closed channel flow model with thermal equilibrium between the vapor and liquid phases. These assumptions do not provide for energy or momentum transfer to other channels in the rod bundle. The continuity equation and the energy equation are used to solve for the enthalpy and velocity distributions along the channel. A total pressure drop for the channel can be input that is assumed to vary linearly along the rod. The coolant channel is subdivided into control volumes, as shown in Figure B-1, each of which coincides with a clad element. The input inlet conditions for the mass flow rate, fluid temperature or enthalpy, and pressure are used to initialize the model at the lower plenum. For each control volume, the inlet conditions at the lower interface ( $z_i$ ) are used to solve for the exit conditions at the upper interface ( $z_{i+1}$ ). As will be shown, average control volume parameters ( $\rho_k$ ,  $V_k$ ,  $u_k$ ) are also used in the energy equation.

The following presents the derivations required to produce the steady state and time dependent solutions to the continuity and energy equations that provide the basis for the coolant model in FALCON. A one-dimensional approach in the axial direction is used; therefore, all components in the lateral directions ( $x$ ,  $y$ ) can be set to zero. A complete explanation of the consequences and limitations resulting from the assumptions used to develop the coolant flow model are presented in Section 3.

### B.1 Steady State Flow Conditions

The steady state conservation of mass and energy equations in the axial direction ( $z$ ) can be written as follows.

Continuity Equation:

$$\frac{\partial}{\partial Z} (\rho V) = 0 \quad (\text{eq. B-1})$$

Energy Equation:

$$\frac{\partial}{\partial Z} \left[ \rho V \left( u + \frac{1}{2} V^2 + gz \right) \right] + \frac{\partial}{\partial Z} (pV) = Q \quad (\text{eq. B-2})$$

where  $\rho$  is density,  $V$  is velocity,  $u$  is the coolant specific energy,  $p$  is the pressure,  $Q$  is the heat energy, and  $g$  is the gravitational acceleration. The assumption of homogeneous equilibrium flow (i.e.,  $V_g = V_\ell = V$ ) requires that only one system of equations be used to determine the

## Appendix B: Coolant Enthalpy Model

enthalpy at each control volume. Integrating the continuity equation over the length of the control volume yields:

$$(\rho V)_{i+1} = (\rho V)_i \quad (\text{eq. B-3})$$

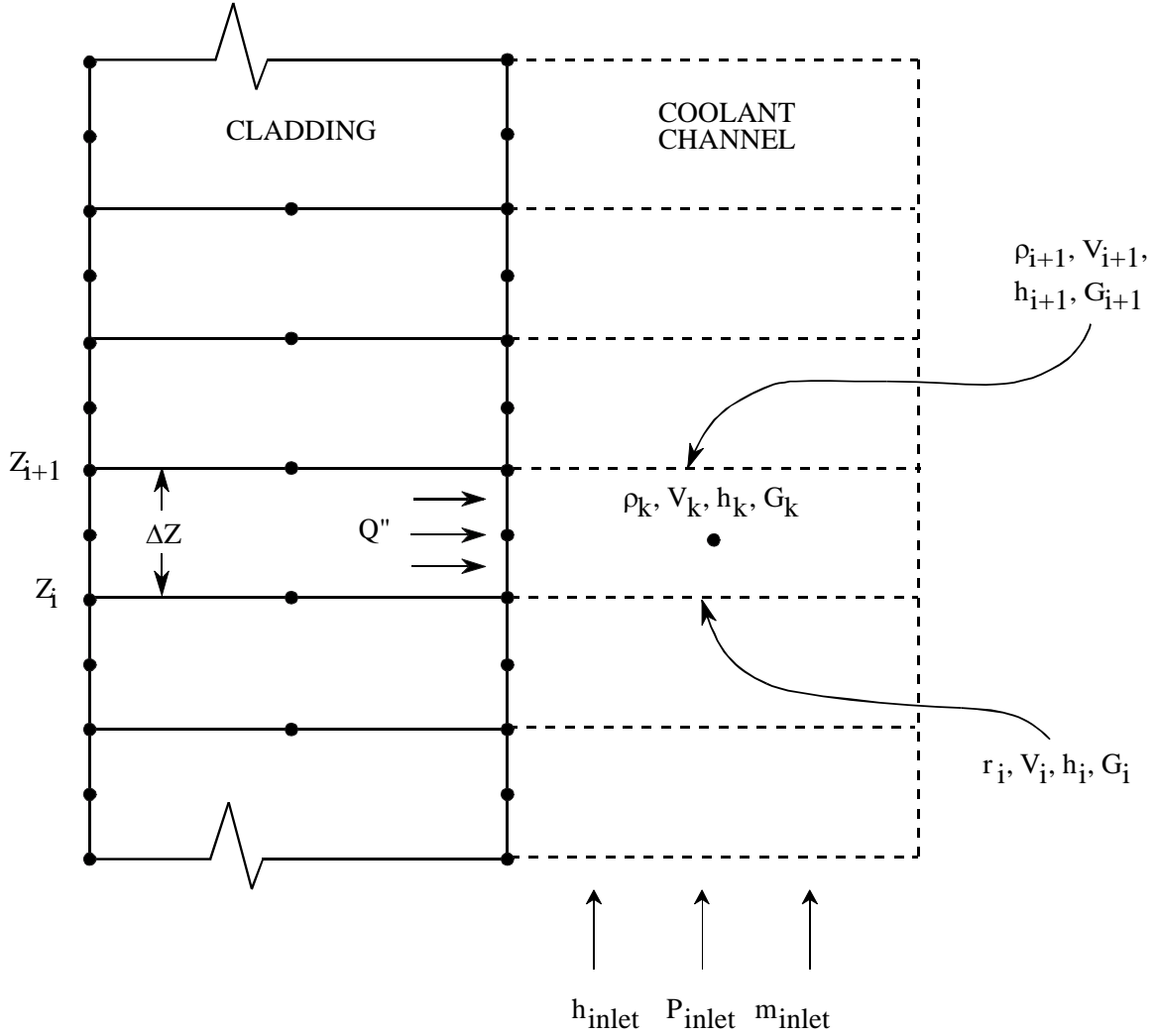


**Figure B-1**  
**Coolant Channel Nodalization**

The integral of the energy equation produces:

$$\rho V_{i+1} \left( u + \frac{1}{2} V^2 + gz \right)_{i+1} - \rho V_i \left( u + \frac{1}{2} V^2 + gz \right)_i + (pV)_{i+1} - (pV)_i = Q_k \Delta z \quad (\text{eq. B-4})$$

where  $Q_k$  is the average heat added in the control volume. Utilizing the continuity equation and combining like terms, the energy equation can be rewritten as:

$$\rho V(u_{i+1} - u_i) + \frac{1}{2} \rho V(V_{i+1}^2 - V_i^2) + \rho V g \Delta z + \rho V \left( \frac{p_{i+1}}{\rho_{i+1}} - \frac{p_i}{\rho_i} \right) = Q_k \Delta z \quad (\text{eq. B-5})$$

The mass flow rate,  $G$ , is defined as:

$$G_i = \rho_i V_i A_i \quad (\text{eq. B-6})$$

where  $A_i$  is the flow area at interface  $i$ . Currently, FALCON does not consider the change in flow area with axial position. Therefore,  $G_i$  is the same for each control volume for steady state conditions and will be represented as  $G$ . Dividing by  $\rho V$  and using the relationship between specific internal energy and enthalpy:

$$h_i = u_i + p_i v_i \quad (\text{eq. B-7})$$

where  $v_i$  is the specific volume. The energy equation can be simplified to:

$$h_{i+1} = h_i - \frac{1}{2} (V_{i+1}^2 - V_i^2) - g \Delta z + \frac{Q_k \Delta z A}{G} \quad (\text{eq. B-8})$$

Equation B-8 is used to determine the enthalpy at the exit of the control volume. Once  $h_{i+1}$  is calculated, the density ( $\rho_{i+1}$ ) is determined from the water properties. The flow velocity ( $V_{i+1}$ ) is calculated from:

$$V_{i+1} = \frac{G_{i+1}}{\rho_{i+1} A} \quad (\text{eq. B-9})$$

An iterative procedure is used at each control volume until the flow velocity  $V_{i+1}$  is within 1% of the previous iteration, i.e.,

$$V_{i+1}^{(j+1)} - V_{i+1}^{(j)} < 0.01 V_{i+1}^{(j)} \quad (\text{eq. B-10})$$

where the superscript  $j$  represents the iteration index.

## B.2 Transient Flow Conditions

The time dependent continuity and energy equations can be written in differential form as:

$$\frac{\partial \rho}{\partial t} + \frac{\partial}{\partial z} (\rho V) = 0 \quad (\text{eq. B-11})$$

and

Appendix B: Coolant Enthalpy Model

$$\frac{\partial}{\partial t} \left[ \rho \left( u + \frac{1}{2} V^2 \right) \right] + \frac{\partial}{\partial z} \left[ \rho V \left( u + \frac{1}{2} V^2 + g z \right) \right] = \frac{\partial}{\partial z} (\rho V) + Q \quad (\text{eq. B-12})$$

respectively, where the terms have been previously defined. First, the continuity equation, eq. B-11, will be solved to provide a solution for flow velocity  $V_{i+1}^{t+\Delta t}$  for the current step. In integral form, eq. B-11 can be written as:

$$\int_i^{i+1} \int_t^{t+\Delta t} \frac{\partial \rho}{\partial t} dt dz + \int_t^{t+\Delta t} \int_i^{i+1} \frac{\partial}{\partial z} (\rho V) dt dz = 0 \quad (\text{eq. B-13})$$

The time integral in the first term reduces to

$$\int_t^{t+\Delta t} \frac{\partial \rho}{\partial t} dt = \rho^{t+\Delta t} - \rho^t \quad (\text{eq. B-14})$$

Using eq. B-14, the first term in eq. B-13 becomes

$$\int_i^{i+1} (\rho^{t+\Delta t} - \rho^t) dz = \Delta z \left[ (\rho^{t+\Delta t} - \rho^t)_{i+1} f_1 + (\rho^{t+\Delta t} - \rho^t)_i (1 - f_1) \right] \quad (\text{eq. B-15})$$

Using the same approach, the second term in eq. B-13 can be written as

$$\begin{aligned} & \int_t^{t+\Delta t} \int_i^{i+1} \frac{\partial}{\partial z} (\rho V) dt dz \\ &= \Delta t \left[ (\rho_{i+1} V_{i+1} - \rho_i V_i)^{t+\Delta t} f_2 - (\rho_{i+1} V_{i+1} - \rho_i V_i)^t (1 - f_2) \right] \end{aligned} \quad (\text{eq. B-16})$$

Using a Crank-Nicholson method for the spatial integration and a fully implicit method for the temporal integration results in

$$f_1 = \frac{1}{2}$$

$$f_2 = 1$$

Therefore, eq. B-13 can be written as

$$\frac{\Delta z}{2} = \left[ \rho_{i+1}^{t+\Delta t} + \rho_i^{t+\Delta t} - \rho_{i+1}^t - \rho_i^t \right] + \Delta t \left( \rho_{i+1}^{t+\Delta t} V_{i+1}^{t+\Delta t} - \rho_i^{t+\Delta t} V_i^{t+\Delta t} \right) = 0 \quad (\text{eq. B-17})$$

Rearranging eq. B-17, the flow velocity at the control volume exit for the current time step is given by



$$V_{i+1}^{t+\Delta t} = \left[ \rho_i^{t+\Delta t} V_i^{t+\Delta t} - \frac{\Delta z}{2\Delta t} \left( \rho_{i+1}^{t+\Delta t} + \rho_i^{t+\Delta t} - \rho_{i+1}^t - \rho_i^t \right) \right] / \rho_{i+1}^{t+\Delta t} \quad (\text{eq. B-18})$$

The form of eq. B-18 used in FALCON substitutes the term  $\rho_i^{t+\Delta t} V_i^{t+\Delta t}$  with  $\rho_i^t V_i^t$  which represents an approximation to eq. B-18. This approach was used to provide faster convergence. The amount of error introduced is minimal for the conditions under which FALCON is applied.

The integral of the energy equation, eq. B-12, can be written as

$$\begin{aligned} & \int_i^{i+1} \int_t^{t+\Delta t} \frac{\partial U}{\partial t} dt dz + \int_t^{t+\Delta t} \int_i^{i+1} \frac{\partial E}{\partial z} dz dt \\ &= \int_t^{t+\Delta t} \int_i^{i+1} (\rho V) dz dt + \int_t^{t+\Delta t} \int_i^{i+1} Q dz dt \end{aligned} \quad (\text{eq. B-19})$$

where

$$U = \rho \left( u + \frac{1}{2} V^2 \right) \quad (\text{eq. B-20})$$

and

$$E = \rho V \left( u + \frac{1}{2} V^2 + g z \right) \quad (\text{eq. B-21})$$

Conducting the first integration for each term produces

$$\int_t^{t+\Delta t} \frac{\partial U}{\partial t} dt = U^{t+\Delta t} - U^t \quad (\text{eq. B-22})$$

$$\int_i^{i+1} \frac{\partial E}{\partial z} dz = E_{i+1} - E_i \quad (\text{eq. B-23})$$

$$\int_i^{i+1} \frac{\partial}{\partial z} (\rho V) dz = (\rho V)_{i+1} - (\rho V)_i \quad (\text{eq. B-24})$$

$$\int_i^{i+1} Q dz = \left[ f_3 Q_{i+1} + (1 - f_3) Q_i \right] \Delta z = Q_k \Delta z \quad \text{for } f_3 = \frac{1}{2} \quad (\text{eq. B-25})$$

Conducting the second integration and, as in the previous derivation, using a fully implicit algorithm in the temporal integration and a Crank-Nicholson in the spatial dimension results in

Appendix B: Coolant Enthalpy Model

$$\int_i^{i+1} (U_k^{t+\Delta t} - U_k^t) dz = \Delta z [U_k^{t+\Delta t} - U_k^t] \quad (\text{eq. B-26})$$

$$\int_t^{t+\Delta t} (E_{i+1} - E_i) dt = \Delta t [E_{i+1}^{t+\Delta t} - E_i^{t+\Delta t}] \quad (\text{eq. B-27})$$

$$\int_t^{t+\Delta t} ((\rho V)_{i+1} - (\rho V)_i) dt = \Delta t [(\rho V)_{i+1}^{t+\Delta t} - (\rho V)_i^{t+\Delta t}] \quad (\text{eq. B-28})$$

and finally

$$\int_t^{t+\Delta t} Q_k \Delta z dt = \Delta t \Delta z Q_k^{t+\Delta t} \quad (\text{eq. B-29})$$

Recalling that  $U_k^{t+\Delta t}$  can be rewritten as

$$U_k^{t+\Delta t} = \rho_k^{t+\Delta t} \left( u_k^{t+\Delta t} + \frac{1}{2} (V_k^{t+\Delta t})^2 \right) \quad (\text{eq. B-30})$$

and

$$U_k^{t+\Delta t} = \frac{1}{2} (u_{i+1}^{t+\Delta t} + u_i^{t+\Delta t}) \quad (\text{eq. B-31})$$

$U_k^{t+\Delta t}$  becomes

$$U_k^{t+\Delta t} = \frac{1}{2} \rho_k^{t+\Delta t} (u_{i+1}^{t+\Delta t} + u_i^{t+\Delta t}) + \frac{1}{2} \rho_k^{t+\Delta t} (V_k^{t+\Delta t})^2 \quad (\text{eq. B-32})$$

The second term in eq. B-26 can be written as

$$U_k^t = \rho_k^{t+\Delta t} u_k^t + \frac{1}{2} \rho_k^{t+\Delta t} (V_k^t)^2 \quad (\text{eq. B-33})$$

by assuming that  $\rho_k^t = \rho_k^{t+\Delta t}$  for small time steps. Concentrating on the second term in the energy equation, eq. B-27, can be reduced to

$$E_{i+1}^{t+\Delta t} = \rho_k^{t+\Delta t} V_k^{t+\Delta t} \left( u_{i+1}^{t+\Delta t} + \frac{1}{2} (V_{i+1}^{t+\Delta t})^2 + g z_{i+1}^{t+\Delta t} \right) \quad (\text{eq. B-34})$$

$$E_i^{t+\Delta t} = \rho_k^{t+\Delta t} V_k^{t+\Delta t} \left( u_i^{t+\Delta t} + \frac{1}{2} \left( V_i^{t+\Delta t} \right)^2 + g z_i^{t+\Delta t} \right) \quad (\text{eq. B-35})$$

where the following assumptions are made

$$\rho_{i+1}^{t+\Delta t} V_{i+1}^{t+\Delta t} = \rho_k^{t+\Delta t} V_k^{t+\Delta t} \quad (\text{eq. B-36})$$

$$\rho_i^{t+\Delta t} V_i^{t+\Delta t} = \rho_k^{t+\Delta t} V_k^{t+\Delta t} \quad (\text{eq. B-37})$$

and

$$\rho_k^{t+\Delta t} = \frac{1}{2} \left( \rho_{i+1}^{t+\Delta t} + \rho_i^{t+\Delta t} \right) \quad (\text{eq. B-38})$$

$$V_k^{t+\Delta t} = \frac{1}{2} \left( V_{i+1}^{t+\Delta t} + V_i^{t+\Delta t} \right) \quad (\text{eq. B-39})$$

Consolidating the like terms, the energy equation becomes

$$\begin{aligned} & \Delta z \left[ \frac{1}{2} \rho_k \left( u_{i+1}^{t+\Delta t} + u_i^{t+\Delta t} \right) + \frac{1}{2} \rho_k^{t+\Delta t} \left( V_{i+1}^{t+\Delta t} \right)^2 - \rho_k^{t+\Delta t} u_k^t + \frac{1}{2} \rho_k^{t+\Delta t} \left( V_k^t \right)^2 \right] \\ & + \Delta t \left[ \rho_k^{t+\Delta t} V_k^{t+\Delta t} u_{i+1}^{t+\Delta t} - \rho_k^{t+\Delta t} V_k^{t+\Delta t} u_i^{t+\Delta t} \right] \\ & + \frac{\Delta t}{2} \rho_k^{t+\Delta t} V_k^{t+\Delta t} \left[ \left( V_{i+1}^{t+\Delta t} \right)^2 - \left( V_i^{t+\Delta t} \right)^2 - g \Delta z \Delta t \right] \\ & = Q_k^{t+\Delta t} \Delta t \Delta z - \Delta t \left[ (\rho V)_{i+1}^{t+\Delta t} - (\rho V)_i^{t+\Delta t} \right] \end{aligned} \quad (\text{eq. B-40})$$

Rearranging and solving for the internal energy  $u_{i+1}^{t+\Delta t}$ , the result is

$$\begin{aligned} u_{i+1}^{t+\Delta t} &= \left\{ Q_k^{t+\Delta t} \Delta t - g \Delta t - u_i^{t+\Delta t} \rho_k^{t+\Delta t} \left[ \frac{1}{2} - V_k^{t+\Delta t} \frac{\Delta t}{\Delta z} \right] \right. \\ &+ \rho_k^{t+\Delta t} u_k^t - \frac{1}{2} \rho_k^{t+\Delta t} \left[ \left( V_k^{t+\Delta t} \right)^2 - \left( V_k^t \right)^2 \right] \\ &- \frac{\Delta t}{2 \Delta z} \rho_k^{t+\Delta t} V_k^{t+\Delta t} \left[ \left( V_{i+1}^{t+\Delta t} \right)^2 - \left( V_i^{t+\Delta t} \right)^2 \right] \\ &\left. - \frac{\Delta t}{\Delta z} \left[ (\rho V)_{i+1}^{t+\Delta t} - (\rho V)_i^{t+\Delta t} \right] \right\} / \rho_k^{t+\Delta t} \left[ \frac{1}{2} + V_k^{t+\Delta t} \frac{\Delta t}{\Delta z} \right] \end{aligned} \quad (\text{eq. B-41})$$

## Appendix B: Coolant Enthalpy Model

Equation B-41 expresses the internal energy at the exit of the control volume for the current step in terms of the average control volume values for  $\rho$  and  $V$ . The method for calculating the coolant conditions at time  $t+\Delta t$  and axial position  $i+1$  is as follows:

1. Use eq. B-41 to determine the internal energy  $u_{i+1}^{t+\Delta t}$ , assuming  $V_{i+1}^{t+\Delta t} = V_i^{t+\Delta t}$  and  $\rho_{i+1}^{t+\Delta t} = \rho_i^{t+\Delta t}$ .
2. Use relationship between specific internal energy and enthalpy (eq. B-7).

$$h_{i+1}^{t+\Delta t} = u_{i+1}^{t+\Delta t} + p_{i+1}^{t+\Delta t} / \rho_{i+1}^{t+\Delta t}$$

3. Determine the density,  $\rho_{i+1}^{t+\Delta t}$ , from the enthalpy using the water properties at  $p_{i+1}^{t+\Delta t}$ .
4. Calculate the flow velocity,  $V_{i+1}^{t+\Delta t}$ , using eq. B-18 (continuity equation) and the new value for density,  $\rho_{i+1}^{t+\Delta t}$ .
5. Repeat steps 1 through 4 using the previous iteration results for  $V_{i+1}^{t+\Delta t}$  and  $\rho_{i+1}^{t+\Delta t}$  until the convergence criteria are satisfied, namely,

$$(j+1)V_{i+1}^{t+\Delta t} - (j)V_{i+1}^{t+\Delta t} = 0.01 (j)V_{i+1}^{t+\Delta t}$$

and

$$(j+1)\rho_{i+1}^{t+\Delta t} - (j)\rho_{i+1}^{t+\Delta t} = 0.01 (j)\rho_{i+1}^{t+\Delta t}$$

where  $j$  and  $j+1$  represent the previous and current iteration results, respectively.

The iteration method for the coolant channel model consists of a sub-stepping approach in which the time step  $\Delta t$  is subdivided into several sub-steps using the formula

$$\Delta t_{\text{sub}} = \frac{2\Delta z}{V_k^t} \quad (\text{eq. B-42})$$

with a maximum of five sub-steps per time step. For each sub-step, the previous iteration method is carried out at each control volume along the coolant channel. The approach produces a coolant enthalpy model which is conditionally stable and numerically efficient.

### B.3 Heat Transfer Coefficient and Critical Heat Flux Correlations

This appendix describes the heat transfer, critical heat flux and critical power ratio correlations included in FALCON. The coolant enthalpy rise model in FALCON can treat either water (liquid and vapor) or sodium (liquid). The entire single and two-phase heat transfer regimes are considered for flowing water conditions. However, only single-phase heat transfer is considered for liquid sodium conditions. The sodium convective heat transfer correlation is from Lyon [1]. The correlations for water used are consistent with the heat transfer correlation packages employed in the RETRAN and VIPRE codes [2, 3]. However, these correlations are applied using the coolant channel model described above. As a consequence of the assumptions and limitations inherent to the FALCON coolant model, the application of some correlations may result in errors in the predicted heat transfer regime or heat transfer coefficients. It is recommended that the user judiciously select the correlations which are appropriate for the anticipated channel conditions for the application. For licensing applications, the use of these correlations should be restricted to pre-DNB conditions. The symbols and dimensions used in Appendix B are defined in Table B-1. The ranges of applicability of the data are given in Tables B-2 and B-3 for the heat transfer correlations and Table B-4 for the critical heat flux correlations.

**Table B-1**  
**Symbol Definitions for Appendix B**

$C_p$	Specific heat at constant pressure (Btu/lbm-°F)
$C_{pg}$	Specific heat of vapor phase (Btu/lbm-°F)
$C_{pl}$	Specific heat of liquid phase (Btu/lbm-°F)
$D_{he}$	Heated equivalent diameter (ft)
$D_{hy}$	Hydraulic diameter (ft)
$F_{APk}$	Axial power profile factor for critical heat flux correlation at elevation station k
$F_{cw}$	Cold wall factor
$G$	Mass flux (lbm/ft <sup>2</sup> -hr)
$G'$	$G/10^6$ (Mlbm/ft <sup>2</sup> -hr)
$h$	Heat transfer coefficient (Btu/ft <sup>2</sup> -hr-°F)
$h_4$	Heat transfer coefficient based on Modified Condie-Bengston Correlation (Btu/ft <sup>2</sup> -hr-°F)
$h_5$	Heat transfer coefficient based on stable film boiling with the $T_w = T_{CHF}$ (Btu/ft <sup>2</sup> -hr-°F)
$h_{45}$	Heat transfer coefficient for transition from Mode 4 to Mode 5 (Btu/ft <sup>2</sup> -hr-°F)
$h_{fg}$	Heat of vaporization (Btu/lbm)
$h_l$	Enthalpy of liquid phase (Btu/lbm)
$h_{ls}$	Enthalpy of saturated liquid phase (Btu/lbm)
$\Delta h_{in} = h_{ls} - h_l$	Subcooled enthalpy at inlet (Btu/lbm)

Appendix B: Coolant Enthalpy Model

**Table B-1 (continued)**  
**Symbol Definitions for Appendix B**

$k_g$	Thermal conductivity of vapor phase (Btu/ft-hr-°F)
$k_l$	Thermal conductivity of liquid phase (Btu/ft-hr-°F)
$L$	Coolant channel length (ft)
$p$	Pressure (psia)
$p_r$	Critical pressure ratio
$Q$	Heat flux (Btu/ft <sup>2</sup> -hr)
$Q_{CHF}$	Critical heat flux (Btu/ft <sup>2</sup> -hr)
$Q_{FB}$	Film boiling heat flux at $T_{w_{CHF}}$ (Btu/ft <sup>2</sup> -hr)
$q_i$	Surface heat flux at axial node $i$ (Btu/ft <sup>2</sup> -hr)
$Q_{min}$	Minimum heat flux (Btu/ft <sup>2</sup> -hr)
$Q_w$	Wall heat flux (Btu/ft <sup>2</sup> -hr)
$T_{ref}$	Bulk temperature of coolant (°F)
$T_{sat}$	Saturation temperature of coolant (°F)
$T_w$	Wall temperature at critical heat flux (°F)
$\Delta T_{min} = T_w - T_{sat}$	Wall super heat at minimum heat flux (°F)
$\Delta T_w = T_w - T_{sat}$	Wall super heat (°F)
$z_i$	Elevation of axial node $i$ from the inlet (ft)
Void fraction	
$\mu_g$	Viscosity of vapor phase (lbm/ft-hr)
$\mu_l$	Viscosity of liquid phase (lbm/ft-hr)
$\mu_w$	Viscosity of liquid phase at wall temperature (lbm/ft-hr)
$\rho_{gs}$	Density of saturated vapor (lbm/ft <sup>3</sup> )
$\rho_{ls}$	Density of saturated liquid (lbm/ft <sup>3</sup> )
$\chi$	Quality
$\chi_{in}$	Quality at inlet

**Table B-2**  
**Data Ranges for Pre-CHF Heat Transfer Correlations**

	<b>Thom</b>	<b>Jens-Lottes</b>	<b>Schrock-Grossman</b>
Fluid	Water	Water	Water
Flow Direction	Up	Up	Up
Channel Geometry	Tube, Annulus	Tubes	Tube
Diameter (in.)	0.5, 0.710, 0.900	0.143 - 0.226	60,000 - 1,450,000
Length (ft)	5, 1	N/A	1.3 - 3.3
Pressure (psia)	750 - 2000	100 - 2500	42 - 505
Mass Flux, G/10 <sup>5</sup> (lbm/hr-ft <sup>2</sup> )	7.7 - 28	0.08 - 77.4	1.76 - 32.8
Heat Flux (Btu/hr- ft <sup>2</sup> )	Up to 0.5 x 10 <sup>6</sup>	Up to 4 x 10 <sup>6</sup>	60,000 - 1,450,000
Inlet Temperature (°F)	36 - 180	239 - 644	N/A
Exit Quality	N/A	N/A	0 - 0.57

**Table B-3**  
**Data Ranges for Post-CHF Heat Transfer Correlations**

	<b>McDonough</b>	<b>Groenveld</b>	<b>Dougall-Rohsenow</b>
Fluid	Water	Water	Water
Flow Direction	Up	Up	Up
Channel Geometry	Tube	Tube, Annulus	Tube
Diameter (in.)	0.152	0.06 - 1.0	0.108, 0.408
Length (ft)	1	N/A	1.25
Pressure (psia)	800, 1200, 2000	500 - 3100	17 - 24
Mass Flux, G/10 <sup>5</sup> (lbm/hr-ft <sup>2</sup> )	2 - 14	2 - 30	3.32 - 8.18
Heat Flux (Btu/hr- ft <sup>2</sup> )	N/A	Up to 0.7 x 10 <sup>6</sup>	1.4 x 10 <sup>4</sup> - 4.2 x 10 <sup>4</sup>
Wall Temperature (°F)	T <sub>w</sub> < 1030	N/A	N/A
Exit Quality	N/A	0.1 - 0.9	Up to 0.5

## Appendix B: Coolant Enthalpy Model

**Table B-4**  
**Data Ranges for Critical Heat Flux Correlations**

	<b>Barnett</b>	<b>Modified Barnett</b>
Fluid	Water	Water
Flow Direction	Up	Up
Channel Geometry	Annulus	Tube
Equivalent Wetted Diameter (in.)	0.0106 - 0.0729	N/A
Rod Diameter (in.)	N/A	0.395 - 0.543
Length (ft)	2 - 5	2.7 - 14.6
Pressure (psia)	1000 - 1300	150 - 725
Mass Flux, $G/10^5$ (lbm/hr-ft <sup>2</sup> )	1.7 - 62	0.3 - 17
Inlet Subcooling (Btu/lbm)	0 - 412	6 - 373

	<b>Babcock &amp; Wilcox</b>	<b>EPRI-Columbia</b>
Fluid	Water	Water
Flow Direction	Up	Up
Channel Geometry	Rod Bundles	Rod Bundles
Heated Equivalent Diameter (in.)	0.2 - 0.5	PWR, BWR, Typical
Length (ft)	6	2.5 - 14
Pressure (psia)	2000 - 2400	200 - 2450
Mass Flux, $G/10^5$ (lbm/hr-ft <sup>2</sup> )	7.5 - 40	2 - 45
Quality (Equilibrium)	-0.03 - 0.2	-0.25 - 0.75

	<b>Westinghouse</b>	<b>Combustion Engrg.</b>
Fluid	Water	Water
Flow Direction	Up	Up
Channel Geometry	Rod Bundles	Rod Bundles
Wetted Equivalent Diameter (in.)	0.2 - 0.7	0.36 - 0.55
Length (ft)	0.8 - 12	7 - 12.5
Pressure (psia)	1000 - 2300	1785 - 2415
Mass Flux, $G/10^5$ (lbm/hr-ft <sup>2</sup> )	10 - 50	8.7 - 32
Quality (Equilibrium)	-0.15 - 0.15	-0.16 - 0.2



## B.4 Sodium Heat Transfer Correlation

### Mode 1 - Forced Convection to Liquid (Lyon) [1]

$$h = \frac{k_\ell}{D_{hy}} \left( 7 + 0.025 P_e^{0.8} \right) \quad (\text{eq. B-43})$$

$$P_e = \max \left( \frac{G C_p D_{hy}}{k_\ell}, 200 \right)$$

## B.5 Water Heat Transfer Correlations

### Mode 1 - Forced Convection to Liquid (Sieder-Tate) [4]

$$h = \frac{k_1}{D_{hy}} (0.023) \left( \frac{G D_{hy}}{\mu_1} \right)^{0.8} \left( \frac{C_{p1} \mu_1}{k_1} \right)^{0.33} \left( \frac{\mu_1}{\mu_w} \right)^{0.14} \quad (\text{eq. B-44})$$

### Mode 2 - Fully Developed Surface Boiling [5, 6]

$$h = Q_w / (T_2 - T_{ref}) \quad (\text{eq. B-45})$$

where

$$T_2 = T_{sat} + a_1 \left[ e^{-p/a_2} \right] Q_w^{1/a_3} \quad (\text{eq. B-46})$$

Thom	Jenn-Lottes
$a_1 = 0.072$	$a_1 = 1.9$
$a_2 = 1260$	$a_2 = 900$
$a_3 = 2$	$a_3 = 4$

### Mode 3 - Forced Convection Vaporization (Schrock-Grossman) [7, 8]

$$h = (2.5)(0.023) \frac{k_1}{D_{hy}} \left( \frac{C_{p1}}{k_1} \right)^{0.4} \cdot \left( \frac{G D_{hy} (1-\chi)}{\mu_1} \right)^{0.8} \left( \left( \frac{\chi}{1-\chi} \right)^{0.9} \left( \frac{\rho_1}{\rho_g} \right)^{0.5} \left( \frac{\mu_g}{\mu_1} \right)^{0.1} \right)^{0.75} \quad (\text{eq. B-47})$$

### Mode 4A - Forced Convection Transition Boiling (Modified Condie-Bengston) [9]

$$h = c_1 e^{-\sqrt{T_w - T_{sat}}/2} \quad (\text{eq. B-48})$$

Appendix B: Coolant Enthalpy Model

where

$$c_1 = e^{\left[ \ln(Q_{CHF} - Q_{FB}) + 0.5 \sqrt{T_{CHF} - T_{sat}} - \ln(T_{CHF} - T_{sat}) \right]}$$

The transition from forced convection transition boiling to stable film boiling is determined using the surface heat fluxes based on the two different heat transfer coefficients. The method is as follows:

$$Q_4 = h_4(T_w - T_{sat}) \quad 30,000 \leq Q_4 \leq Q_{CHF}$$

$$Q_5 = h_5(T_w - T_{ref})$$

$$Q_{45} = Q_4 + Q_5$$

$$\text{and for } Q_4 > Q_5 \quad Q_{45} \leq Q_{CHF}$$

$$h_{45} = Q_{45} / (T_w - T_{ref})$$

Mode 4B - Forced Convection Transition Boiling (McDonough, Milich, King) [10]

$$h = \frac{Q_{CHF} - C(p)(T_w - T_{ref})}{T_w - T_{ref}} \quad (\text{eq. B-49})$$

where

$$\begin{aligned} p > 1200 \quad , \quad C(p) &= 1180.8 - 201.6 \left( \frac{p - 1200}{800} \right) \\ p \leq 1200 \quad , \quad C(p) &= 1180.8 + 320.4 \left( \frac{1200 - p}{400} \right) \end{aligned} \quad (\text{eq. B-50})$$

Mode 5A - Forced Convection Stable Film Boiling (Groeneveld) [11]

$$h = a \frac{k_g}{D_{hy}} \left[ \frac{GD_{hy}}{\mu_g} \left( \chi + \frac{\rho_{gs}}{\rho_{ls}} (1 - \chi) \right) \right]^b \left( \frac{C_{pg} \mu_g}{k_g} \right)^c Y^d \quad (\text{eq. B-51})$$

where

$$Y = 1.0 - 0.1(1 - \chi)^{0.4} \left( \frac{\rho_{ls}}{\rho_{gs}} - 1 \right) \quad \text{or} \quad Y = 0.1 \quad (\text{eq. B-52})$$

whichever is larger. Vapor properties of the Prandtl number  $C_{pg}\mu_g/k_g$  are evaluated at the film temperature:

$$T = 1/2(T_w + T_{ref}) \quad (\text{eq. B-53})$$

	Groeneveld eq. 5.9 Cluster Geometry	Groeneveld eq. 5.7 Annular Geometry
A	0.00327	0.052
B	0.901	0.688
C	1.32	1.26
D	-1.5	-1.06

Mode 5B - Forced Convection Stable Film Boiling (Dougall-Rohsenow) [12]

$$h = 0.023 \frac{k_g}{D_{hy}} \left[ \frac{GD_{hy}}{\mu_g} \left( \chi + (1 - \chi) \frac{\rho_{gs}}{\rho_{ls}} \right) \right]^{0.8} \left( \frac{C_{pg} \mu_g}{k_g} \right)^{0.4} \quad (\text{eq. B-54})$$

where the vapor properties of the Prandtl number are evaluated at the saturation temperature.

Mode 6 - Pool Transition Boiling (Berenson) [13]

$$h = Q/(T_w - T_{sat}) \quad (\text{eq. B-55})$$

where

$$Q = 20,000 \left( \frac{\Delta T_{min}}{T_w - T_{sat}} \right)^{\frac{1.504}{\ln(\Delta T_{min}/20)}} , \quad Q \leq 90,000 \text{ Btu/ft}^2\text{-hr} \quad (\text{eq. B-56})$$

$$\Delta T_{min} = (20,000/F(p))^{4/3} \quad (\text{eq. B-57})$$

with F(p) the same function as in Mode 7.

Appendix B: Coolant Enthalpy Model

Mode 7 - Pool Stable Film Boiling (Berenson) [14]

$$Q = F(p) (T_w - T_{sat})^{3/4}$$

$$h = Q / (T_w - T_{ref})^{1/4}$$

(eq. B-58)

where  $F(p)$  is linearly interpolated from [15]:

p	F(p) (Btu/ft <sup>2</sup> -hr-°F <sup>0.75</sup> )
15	128
100	236
500	412
1000	510
1500	615
2000	705

Mode 8 - Forced Convection to Superheated Vapor (Dittus-Boelter) [16]

$$h = \frac{k_g}{D_{hy}} (0.023) \left( \frac{GD_{hy}}{\mu_g} \right)^{0.8} \left( \frac{C_{pg} \mu_g}{k_g} \right)^{0.4}$$

(eq. B-59)

## B.6 Critical Heat Flux Correlations

Correlation 1 - Modified Barnett [17]

$$Q_{CHF} = \left( \frac{A + B \Delta h_{in}}{C + L} \right) 10^6$$

(eq. B-60)

where

$$A = 73.71 D_{he}^{0.052} (G')^{0.663} \left( 1.0 - 0.315 e^{-11.34 D_{hy} G'} \right) 888.6 / h_{fg}$$

$$B = 0.104 D_{he}^{1.445} (G')^{0.691}$$

$$C = 45.55 D_{hy}^{0.0817} (G')^{0.5866}$$

(eq. B-61)

Correlation 2 - Barnett [18]

$$Q_{CHF} = \left( \frac{A + B \Delta h_{in}}{C + L} \right) 10^6 \quad (\text{eq. B-62})$$

where

$$\begin{aligned} A &= 67.45 D_{he}^{0.68} (G')^{0.192} \left( 1.0 - 0.744 e^{-6.512 D_{hy} G'} \right) \\ B &= 0.2587 D_{he}^{1.261} (G')^{0.817} \\ C &= 185 D_{hy}^{1.415} (G')^{0.212} \end{aligned} \quad (\text{eq. B-63})$$

Correlation 3 - B&W-2 (Babcock & Wilcox Company) [19]

$$Q_{CHF} = \frac{1.15509 - 0.40703 D_{he}}{(12.71)(3.054 G')^A} \left[ (0.3702 E8)(0.59137 G')^B - 0.15208 \chi_{hfg} G \right] / F_{APk} \quad (\text{eq. B-64})$$

where

$$\begin{aligned} A &= 0.71186 + (2.0729 \times 10^{-4}) (p - 2000) \\ B &= 0.8304 + (6.8479 \times 10^{-4}) (p - 2000) \end{aligned} \quad (\text{eq. B-65})$$

$F_{APk}$ : Axial power profile factor for the B&W-2 correlation at elevation station k.

The axial power profile factor is calculated by the equation [20]

$$\begin{aligned} F_{APk} &= 1.01 \left\{ S_1 + \sum_{i=2}^k \left[ \{q_i - (dq/dZ)_i\} \exp(C_1(Z_i - Z_k)) \right. \right. \\ &\quad \left. \left. - \{q_i - (dq/dZ)_i\} \exp(C_1(Z_{i-1} - Z_k)) \right] \right\} / C_2 q_k \end{aligned} \quad (\text{eq. B-66})$$

where

$$\begin{aligned} (dq/dZ)_i &= (q_i - q_{i-1}) / C_1 (Z_i - Z_{i-1}) \\ C_1 &= 2.988 (1 - \chi)^{7.82} / (G')^{0.457} \quad [C_1 \text{ has been converted to ft}^{-1}] \\ C_2 &= [1 - \exp(-C_1 Z_k)] \\ S_1 &= q_1 [\exp(C_1(Z_1 - Z_k)) - \exp(-C_1 Z_k)] \end{aligned} \quad (\text{eq. B-67})$$

Appendix B: Coolant Enthalpy Model

Correlation 4 - B&W-2 (EPRI-Columbia) [21]

$$\frac{Q_{CHF}}{10^6} = \frac{F_a p_1 p_r^{p_2} G^{(p_5 + p_7 p_r)} - \chi_{in}}{F_c F_{APk} p_3 p_r^{p_4} G^{(p_6 + p_8 p_r)} + \left( \frac{\chi - \chi_{in}}{Q_w} \right)} \quad (\text{eq. B-68})$$

where

$$\begin{aligned} p_1 &= 0.5328 \\ p_2 &= 0.1212 \\ p_3 &= 1.6151 \\ p_4 &= 1.4066 \\ p_5 &= -0.3040 \\ p_6 &= 0.4843 \\ p_7 &= -0.3285 \\ p_8 &= -2.0749 \end{aligned} \quad (\text{eq. B-69})$$

where the cold wall factors are defined by

$$\begin{aligned} F_a &= G^{0.1} \\ F_c &= 1.183 G^{0.1} \\ F_a &= F_c = 1 \quad \text{for no cold wall} \end{aligned}$$

$F_{APk}$  is the non-uniform axial heat flux distribution parameter for station k.

$$F_{APk} = 1 + \frac{(Y - 1)}{(1 - G)}$$

where

$$Y = \frac{\sum_{j=2}^k q_j (z_{j+1} - z_j)}{q_j z_j}$$

Correlation 5 - CE-1 (Combustion Engineering) [22]

$$\frac{Q_{CHF}}{10^6} = \frac{b_1(d/d_m)^{b_2} \left[ (b_3 + b_4 P)(G')^{(b_5 + b_6 P)} - (G')(\chi)(h_{fg}) \right]}{F_{APk} G'^{(b_7 P + b_8 G')}} \quad (\text{eq. B-70})$$

where

$$\begin{aligned} b_1 &= 2.8922 \times 10^{-3} \\ b_2 &= -0.50749 \\ b_3 &= 405.32 \\ b_4 &= -9.9290 \times 10^{-2} \\ b_5 &= -0.67757 \\ b_6 &= 6.8235 \times 10^{-4} \\ b_7 &= 3.1240 \times 10^4 \\ b_8 &= -8.3245 \times 10^2 \end{aligned} \quad (\text{eq. B-71})$$

The axial power profile factor,  $F_{APk}$ , is calculated by the same equation as is shown for the B&W-2 correlation, except that  $C_1$  is redefined as follows [23]:

$$C_1 = 1.8(1 - \chi)^{4.31} / [(G')^{0.478}] \quad (\text{eq. B-72})$$

Correlation 6 - W-3, W3-S, W3-R, W3-L (Westinghouse Company) [23]

$$\begin{aligned} Q_{CHF} &= 1 \times 10^6 \left[ 2.022 - 4.302 \times 10^{-4} P + (0.1722 - 9.84 \times 10^{-5} P) \right. \\ &\quad \left. \exp \left( (18.177 - 4.129 \times 10^{-3} P) \chi \right) [1.157 - 0.869 \chi] \right. \\ &\quad \left. [(0.1484 + \chi(-1.596 + 0.1729 \text{ABS}(\chi))) G' + 1.037] \right. \\ &\quad \left. [0.8258 + 7.94 \times 10^{-4} \Delta h_{in}] [0.2664 + 0.8357 \exp(-3.151 D_{he})] \right] \\ &\quad F_{CW} F_{GRID} / F_{APk} \end{aligned} \quad (\text{eq. B-73})$$

where

$F_{APk}$ : Axial power profile factor at elevation station k, the same as for the CE-1 correlation

Appendix B: Coolant Enthalpy Model

The cold wall factor is calculated by the equation

$$F_{CW} = 1 - \left(1 - D_{hy}/D_{he}\right) \left[ 13.76 - 1.372 \exp(1.78\chi) - 4.732(G')^{-0.0535} - 0.0619(P/1000)^{0.14} - 8.509 D_{he}^{0.107} \right] \quad (\text{eq. B-74})$$

The grid factor is taken on different forms according to whether the grid type is the simple (or S) grid, the mixing vane (or R) grid, or another mixing vane grid called L-type. The S grid factor [23] is given by

$$F_{GRID(S)} = 1.0 + 0.03 G' (TDC/0.019)^{0.35} \quad (\text{eq. B-75})$$

where TDC is the turbulent crossflow mixing parameter. The L-grid or R-grid factor [24], identical except for a leading coefficient  $F_g$ , is given by

$$F_{GRID(RL)} = F_g \left\{ (1.445 - 0.0371 L_H) (P/225.896)^{0.5} \left[ e^{(x_e + 0.2)^2} - 0.73 \right] + K_S G' (TDC/0.019)^{0.35} \right\} \quad (\text{eq. B-76})$$

where

$L_H$ : Heated length (ft)

$K_S$ : Grid spacing factor (an empirical constant dependent on the distance between grids - usually proprietary for a given design)

TDC: Empirical turbulent cross flow mixing parameter

$x_e$ : Equilibrium quality

$F_g$ : Grid-type modifier; 1.0 for R-grids, and 0.986 for L-grids

Correlation 7 - GE (General Electric Company) [25]

$$Q_{CHF} = 10^6 (0.8 - \chi) \quad \text{for} \quad G \geq 0.5 \times 10^6 \text{ lb}_m / \text{ft}^2 - \text{hr} \quad (\text{eq. B-77})$$

$$Q_{CHF} = 10^6 (0.84 - \chi) \quad \text{for} \quad G \leq 0.5 \times 10^6 \text{ lb}_m / \text{ft}^2 - \text{hr} \quad (\text{eq. B-78})$$



## B.7 Critical Power Ratio Correlations

### Correlation 1 - Hensch-Levy Limit Equations [26, 27]

This correlation defines conservative limit lines for the minimum CHF ratio (MCHFR) in BWR bundles. The equations calculate a limiting critical heat flux for the bundle as a function of mass flux, equilibrium quality and empirical constants. There is also a pressure correction for conditions at pressures above or below 1000 psia. At 1000 psia,

$$\frac{Q_{CHF}}{10^6} = 1.0 \quad (\text{eq. B-79})$$

for

$$\bar{x}_e \leq 0.273 - 0.212 \tanh^2(3\bar{G}/10^6)$$

$$\frac{Q_{CHF}}{10^6} = 1.9 - 3.3 \bar{x}_e - 0.7 \tanh^2(3\bar{G}/10^6) \quad (\text{eq. B-80})$$

for

$$\begin{aligned} (0.273 - 0.212 \tanh^2(3\bar{G}/10^6)) &\leq \bar{x}_e \\ &\leq (0.5 - 0.269 \tanh^2(3\bar{G}/10^6) + 0.0346 \tanh^2(2\bar{G}/10^6)) \end{aligned}$$

$$\frac{Q_{CHF}}{10^6} = 0.6 - 0.7 \bar{x}_e - 0.09 \tanh^2(2\bar{G}/10^6) \quad (\text{eq. B-81})$$

for

$$\bar{x}_e > (0.5 - 0.269 \tanh^2(3\bar{G}/10^6) + 0.0346 \tanh^2(2\bar{G}/10^6))$$

where

$\bar{G}$ : Bundle-average mass velocity (lbm/hr-ft<sup>2</sup>)

$\bar{x}_e$ : Bundle-average equilibrium quality ( $0 < x_e < 1.0$ )

The pressure correction is

$$F_p = [1.1 - 0.1((p - 600)/400)^{1.25}] \quad (\text{eq. B-82})$$

$$Q_{CHF} = Q_{CHF}|_{1000 \text{ psia}} F_p \quad (\text{eq. B-83})$$

Appendix B: Coolant Enthalpy Model

The data, which were used as a basis for this correlation, spanned the ranges described below:

Mass flux, $G10^6$ (lbm/ft <sup>2</sup> -hr)	10.2 to 1.6
Hydraulic diameter (in.)	0.324 to 0.485
Pressure (psia)	600 to 1450
Rod-to-wall spacing (in.)	above 0.6

Correlation 2 - Hench-Gillis Quality Correlation [28]

This correlation is a critical quality/boiling length equation. It was derived starting from an equation of the form of the CISE-II correlation and is based on publicly available boiling transition data from BWR-type geometries [3].

$$x_c = \frac{AZ}{B+Z} (2 - J) + F_p \quad (\text{eq. B-84})$$

where

$$\begin{aligned} A &= 0.50(G')^{-0.43} \\ B &= 165 + 115(G')^{2.3} \\ Z &= \frac{\text{boiling heat transfer area}}{\text{bundle flow area}} = \frac{\pi D_r n L_B}{A_f} \end{aligned} \quad (\text{eq. B-85})$$

with

- $D_r$ : Rod diameter
- $n$ : Number of active rods in the bundle
- $L_B$ : Boiling length

The pressure correction factor is

$$F_p = 0.006 - 0.0157 \left( \frac{P-800}{1000} \right) - 0.0714 \left( \frac{P-800}{1000} \right)^2 \quad (\text{eq. B-86})$$

The J-factor accounts for local peaking in the bundle and is defined as follows (see Figure B-2):

$$J = J_1 - \frac{0.19}{G'} (J_1 - 1)^2 \text{ for corner rods} \quad (\text{eq. B-87})$$

$$J = J_1 - \frac{0.19}{G'} (J_1 - 1)^2 - \left( \frac{0.70}{G' + 0.25} - 0.05 \right) \text{ for side rods} \quad (\text{eq. B-88})$$

$$J = J_1 - \frac{0.19}{G'} (J_1 - 1)^2 - \left( \frac{0.14}{G' + 0.25} - 0.10 \right) \text{ for central rods} \quad (\text{eq. B-89})$$

$J_1$  is a weighted factor depending on the relative power factors,  $f_n$ , of the rods surrounding a given rod. Rods are weighted differently if they are in the same row (column) as a rod, or diagonally adjacent. The  $J_1$  factors are calculated as follows (see Figure B-2):

$$J_1 = \frac{1}{16} \left[ 12.5 f_p + 1.5 \sum_{i=1}^2 f_i + 0.5 f_j \right] \quad \text{for corner rods} \quad (\text{eq. B-90})$$

$$- \frac{n D_p (2D_s + D_r - D_p)}{64 A} \left[ 4 f_p + \sum_{i=1}^2 f_i \right]$$

$$J_1 = \frac{1}{16} \left[ 11.0 f_p + 1.5 \sum_{i=1}^2 f_i + f_k + 0.5 \sum_{j=1}^2 f_j \right] \quad \text{for side rods} \quad (\text{eq. B-91})$$

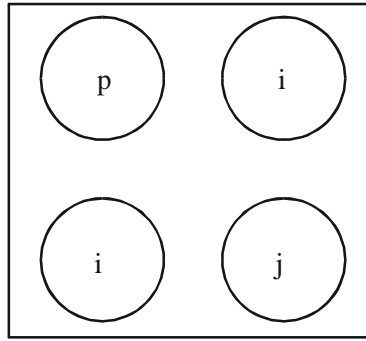
$$- \frac{n D_p (2D_s + D_r - D_p)}{64 A} \left[ 2 f_p + \sum_{i=1}^2 f_i \right]$$

$$J_1 = \frac{1}{4} \left[ 2.5 f_p + 0.25 \sum_{i=1}^4 f_i + 0.125 \sum_{j=1}^4 f_j \right] \text{ for central rods} \quad (\text{eq. B-92})$$

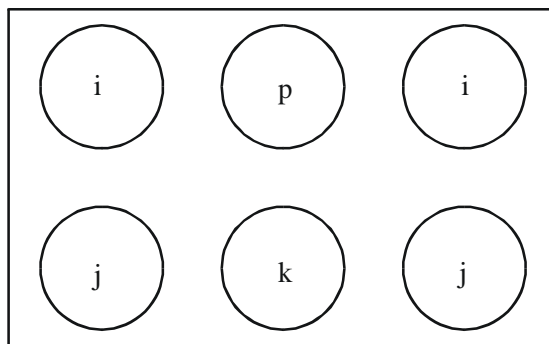
where

- $f_p$ : Radial power factor for a given rod
- $f_i$ : Radial power factor of rod adjacent to rod p in the same row or column (not including the rod adjacent to rod p in the same column, if p is a side rod)
- $f_j$ : Radial power factor of rod adjacent to rod p on a diagonal line in the matrix
- $f_k$ : Radial power factor of rod adjacent to rod p in the same column when p is a side rod (the weighted summation of rod power factors for corner and central rods do not define a k-rod)
- n: Number of rods and water tubes in the fuel bundle
- $D_p$ : Rod pitch
- $D_s$ : Rod -to-wall gap
- A: Total flow area in the bundle
- $D_r$ : Fuel pin diameter

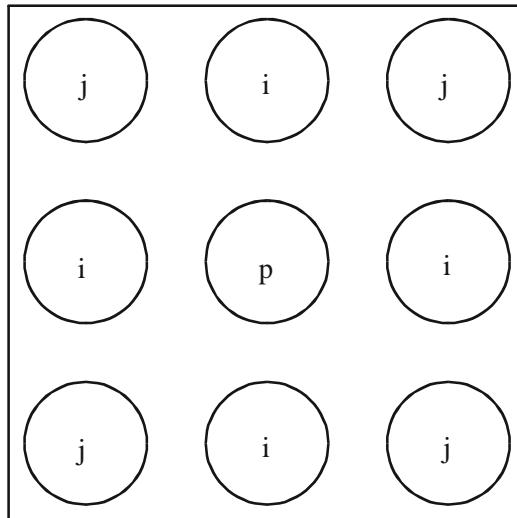
Appendix B: Coolant Enthalpy Model



CORNER ROD (a)



SIDE ROD (b)



INTERIOR ROD (c)

**Figure B-2**  
**Adjacent Rod Weighting Patterns for Hench-Gillis J Factor**

## B.8 References

1. Lyon, R.M., "Liquid Metal Heat-Transfer Coefficients," *Chem. Eng. Prog.* 47, 75, 1951.
2. "RETRAN - A Program for One-Dimensional Transient Thermal-Hydraulic Analysis of Complex Fluid Flow Systems," Volume 1, EPRI CCM-5, December 1978.
3. Stewart C.W., et al., "VIPRE-01, A Thermal-Hydraulic Analysis Code for Reactor Cores: Volume 1, Mathematical Modeling," EPRI NP-2511, August 1982.
4. Sieder, E.N. and Tate, G.E., "Heat Transfer and Pressure Drop of Liquids in Tubes," Ind. Eng. Chemistry, Vol. 28, No. 12, 1936, pp. 1429-1435.
5. Thom, J.R.S. Walker, W.M., Fallon, T.A. and Reising, G.F.S., "Boiling in Subcooled Water During Flow-Up Heated Tubes or Annuli," Paper No. 7, Symposium on Boiling Heat Transfer in Steam Generating Units and Heat Exchangers, by Inst. of Mech. Engrs., London, September 15-16, 1965.
6. Jens, W.H. and Lottes, P.A., "Analysis of Heat Transfer Burnout, Pressure Drop and Density Data for High Pressure Water," ANL-4627, May 1951.
7. Schrock, V.E. and Grossman, L.M., "Forced Convection Vaporization Project," TID-14632, 1959.
8. Schrock, V.E. and Grossman, L.M., "Local Heat Transfer Coefficients and Pressure Drop in Forced Convection Boiling," University of California Institute of Engineering Research Report Series, 73308-UCX 2159, No. 1, September 30, 1957.
9. RELAP/MOD7 Blowdown Code, Version 2, Code Development and Analysis Program Report, Idaho National Engineering Laboratory, CDAP-TR-78-036, August 1978.
10. McDonough, J.B., Milich, W. and King, E.C., "Partial Film Boiling with Water at 2000 psig in a Round Vertical Tube," MSA Research Corp., Technical Report 62 (NP-6976), 1958.
11. Groenveld, D.C., "Post-Dryout Heat Transfer at Reactor Operating Condition," AECL-4513, June 1973.
12. Dougall, R.L. and Rohsenow, W.M., "Film-Boiling on the Inside of Vertical Tubes with Upward Flow of the Fluid at Low Qualities," MIT-TR-9079-26, 1973.
13. Berenson, P.J., "Transition Boiling Heat Transfer from a Horizontal Surface," MIT Technical Report No. 17, 1960.
14. Berenson, P.J., "Film-Boiling Heat Transfer from a Horizontal Surface," Journal Heat Transfer, 83, 1961, pp. 351-358.
15. Hocesvar, C.J. and Wineinger, T.W., "THETA1-B, A Computer Code for Nuclear Reactor Core Thermal Analysis," IN-1445, 1971.
16. Dittus, F.W. and Boelter, L.M.K., "Heat Transfer in Automobile Radiators of the Tubular Type," University of California Publications in Engineering, 2, 1930, pp. 443-461.
17. Hughes, E.D., "A Correlation of Rod Bundle Critical Heat Flux for Water in the Pressure Range 150 to 725 psia," IN-1412, 1970.
18. Barnett, P.G., "A Correlation of Burnout Data for Uniformly Heated Annuli and Its Use for Predicting Burnout in Uniformly Heated Rod Bundles," AEEW-R 463, 1966.

*Appendix B: Coolant Enthalpy Model*

19. Gellerstedt, J.S., et al., "Two-Phase Flow and Heat Transfer in Rod Bundles," ASME, Los Angeles, 1969, pp. 63-71.
20. Wilson, R.H., et al., "Two-Phase Flow and Heat Transfer in Rod Bundles," ASME, Los Angeles, 1969, pp. 56-62.
21. "Parametric Study of CHF Data, Vol. 2: A Generalized Subchannel CHF Correlation for PWR and BWR Fuel Assemblies," Electric Power Research Institute, Report No. EPRI-NP-2609, prepared by Heat Transfer Research Facility, Dept. of Chemical Engineering, Columbia University, March 1982.
22. "CE Critical Heat Flux: Critical Heat Flux Correlation for CE Fuel Assemblies with Standard Spacer Grids - Part 1, Uniform Axial Power Distribution," CENPD-162-P-A, Supplement 1-A, February 1977. (Note: This document contains only the CHF correlation developed by CE. The data base has not been released and is still considered proprietary.)
23. Tong, L.S., "Boiling Crisis and Critical Heat Flux," U.S. AEC, 1972.
24. "Application of Modified Spacer Factor to L-Grid Typical and Cold Wall Cell DNB," WCAP-80-30-A, January 1975.
25. Slifer, B.C. and Hensch, J.E., "Loss-of-Coolant Accident and Emergency Core Cooling Models for General Electric Boiling Water Reactors," NED0-10329, April 1971.
26. Healzer, J.M., Hensch, J.E., Janssen, E. and Levy, S., "Design for Critical Heat Flux Condition in Boiling Water Reactors," APED-5286, 1966.
27. Lahey, R.T. and Moody, F.J., "The Thermal-Hydraulics of a Boiling Water Nuclear Water Reactor," American Nuclear Society, 1977.
28. Hensch, J.E. and Gillis, J.C., "Correlation of Critical Heat Flux Data for Application to Boiling Water Reactor Conditions," EPRI NP-1898, Project 1751-1, June 1981.

# C

## APPENDIX C: FIELD AND EQUILIBRIUM EQUATIONS

---

The field variables are the displacements  $U_i$ , the strain  $\epsilon_{ij}$  and the stresses  $\sigma_{ij}$ . The equilibrium variables are the nodal displacements and the nodal forces. The field variables are inter-related through two systems of equations: the strain-displacement relations and the stress-strain relations. The equilibrium variables are inter-related through the boundary conditions and the stiffness matrix, which is the matrix of coefficients of the governing equations of the overall finite element system. These are derived from the field equation and the virtual work variational procedure. In the following derivations, the usual summation convention is adopted, where repeated indices implies summation.

### C.1 Strain Displacement Relations

The following notation is adopted for the two-dimensional problem of plane and axisymmetric geometry presented in Section 4.

- $X_i$ : Original coordinates (referred to the initial configuration) of a material point
- $x_i$ : Deformed coordinates
- $U_i$ : Displacements relative to original coordinates
- $dU_i$ : Increments of displacement (within a time step)
- $\delta U_i$ : Virtual displacements

Then

$$\begin{aligned} x_i &= X_i + U_i \\ \delta x_i &= \delta U_i \quad i = 1, 2 \\ dx_i &= dU_i \end{aligned} \quad (\text{eq. C-1})$$

Variables are represented in terms of their nodal values and shape functions as:

Appendix C: Field And Equilibrium Equations

$$\begin{aligned}
 x_i &= \sum_{n=1}^N \phi_n x_i^n \\
 U_i &= \sum_{n=1}^N \phi_n v_i^n \\
 \delta U_i &= \sum_{n=1}^N \phi_n \delta v_i^n \\
 dU_i &= \sum_{n=1}^N \phi_n dv_i^n, \quad i = 1, 2
 \end{aligned}
 \tag{eq. C-2}$$

In the above,  $n$  ranges over the number of nodes in the element  $N$ , which is 8 for quadratic quadrilaterals and 6 for triangles, as described in Appendix A;  $x_i^n$  is the  $i^{\text{th}}$  coordinate of node  $n$ ;  $v_i^n$  is the  $i^{\text{th}}$  displacement component of node  $n$ ; and similarly for the virtual displacement  $\delta v_i^n$  and displacement increment  $dv_i^n$ . The shape functions are continuous functions of the natural (parametric) coordinates within the element. In matrix form the equations in eq. C-2 are written as

$$\begin{aligned}
 x_i &= \tilde{\phi}^T \tilde{x}_i \\
 U_i &= \tilde{\phi}^T \tilde{v}_i \\
 \delta U_i &= \tilde{\phi}^T \delta \tilde{v}_i \\
 dU_i &= \tilde{\phi}^T d\tilde{v}_i
 \end{aligned}
 \tag{eq. C-3}$$

It is necessary to distinguish between the quantity  $x_i$  which is the  $i^{\text{th}}$  component of the deformed coordinate as continuous functions of  $\xi$  and  $\eta$  over the element and  $\tilde{x}_i$  which is a vector consisting of the nodal values of the deformed coordinates. The same is true for the other variables in eq. C-3. The physical components of strain are:

$$\begin{aligned}
 \varepsilon_{ij} &= \frac{1}{2} \left[ \frac{\partial X_k}{\partial X_i} \frac{\partial X_k}{\partial X_j} - \delta_{ij} \right] - \theta_{ij} \quad (i, j = 1, 2) \\
 \varepsilon_{33} = \varepsilon_{\theta\theta} &= \frac{1}{2} \left[ (r/R)^2 - 1 \right] - \theta_{33}, \quad \varepsilon_{r\theta} = \varepsilon_{z\theta} = 0
 \end{aligned}
 \tag{eq. C-4}$$

where  $\theta_{ij}$  are the free expansion strains caused by the combined effects of temperature, swelling and densification, and  $\delta_{ij}$  is the Kronecker delta. In matrix form,



$$\underset{\sim}{\varepsilon} = \begin{bmatrix} \varepsilon_{11} \\ \varepsilon_{22} \\ \varepsilon_{33} \\ 2\varepsilon_{12} \end{bmatrix} = \begin{bmatrix} \frac{1}{2} \left[ (\partial x_1 / \partial X_1)^2 + (\partial x_2 / \partial X_1)^2 - 1 \right] - \theta_{11} \\ \frac{1}{2} \left[ (\partial x_1 / \partial X_2)^2 + (\partial x_2 / \partial X_2)^2 - 1 \right] - \theta_{22} \\ \frac{1}{2} \left[ (r/R)^2 - 1 \right] - \theta_{33} \\ (\partial x_1 / \partial X_1 \partial x_1 / \partial X_2 + \partial x_2 / \partial X_1 \partial x_2 / \partial X_2) - 2\theta_{12} \end{bmatrix} \quad (\text{eq. C-5})$$

where

$$r = \underset{\sim}{\phi}^T \underset{\sim}{x}_i$$

$$R = \underset{\sim}{\phi}^T \underset{\sim}{X}_i$$

$$\partial x_i / \partial X_j = \underset{\sim}{\phi}_{,j}^T \underset{\sim}{x}_i$$

with

$$\underset{\sim}{\phi}_{,j} = \partial \underset{\sim}{\phi} / \partial X_j$$

With the view towards formulating the incremental problem, the variation in the strains is given by

$$\begin{aligned} \delta \varepsilon_{ij} &= \frac{1}{2} \left[ \partial \delta x_k / \partial X_i \partial x_k / \partial X_j + \partial \delta x_k / \partial X_j \partial x_k / \partial X_i \right] \quad (i = 1, 2) \\ &= \frac{1}{2} \left[ \delta \underset{\sim}{v}_k^T \underset{\sim}{\phi}_{,i} \partial x_k / \partial X_j + \delta \underset{\sim}{v}_k^T \underset{\sim}{\phi}_{,j} \partial x_k / \partial X_i \right] \\ \delta \varepsilon_{33} &= [r/R \delta r/R] \\ &= r/R^2 \delta \underset{\sim}{v}_1^T \underset{\sim}{\phi} \end{aligned} \quad (\text{eq. C-6})$$

Therefore

$$\delta_{\tilde{\varepsilon}} = \begin{bmatrix} \delta\varepsilon_{11} \\ \delta\varepsilon_{22} \\ \delta\varepsilon_{33} \\ 2\delta\varepsilon_{12} \end{bmatrix} = \begin{bmatrix} \left( \delta \tilde{v}_1^T \partial x_1 / \partial X_1 + \delta \tilde{v}_2^T \partial x_2 / \partial X_1 \right) \tilde{\phi}_{,1} \\ \left( \delta \tilde{v}_1^T \partial x_1 / \partial X_2 + \delta \tilde{v}_2^T \partial x_2 / \partial X_2 \right) \tilde{\phi}_{,2} \\ \delta \tilde{v}_1^T \tilde{\phi} / R^2 \\ \delta \tilde{v}_1^T \left( \tilde{\phi}_{,1} \partial x_1 / \partial X_2 + \tilde{\phi}_{,2} \partial x_1 / \partial X_1 \right) \\ + \delta \tilde{v}_2^T \left( \tilde{\phi}_{,1} \partial x_2 / \partial X_2 + \tilde{\phi}_{,2} \partial x_2 / \partial X_1 \right) \end{bmatrix} \quad (\text{eq. C-7})$$

or

$$\delta_{\tilde{\varepsilon}} = \tilde{\beta} \begin{bmatrix} \delta \tilde{v}_1 \\ \delta \tilde{v}_2 \end{bmatrix} = \tilde{\beta} \delta \tilde{v} \quad (\text{eq. C-8})$$

where

$$\tilde{\beta} = \begin{bmatrix} \tilde{\phi}_{,1}^T \partial x_1 / \partial X_1 & \tilde{\phi}_{,1}^T \partial x_2 / \partial X_1 \\ \tilde{\phi}_{,2}^T \partial x_1 / \partial X_2 & \tilde{\phi}_{,2}^T \partial x_2 / \partial X_2 \\ \tilde{\phi}^T / R^2 & 0 \\ \left( \tilde{\phi}_{,1}^T \partial x_1 / \partial X_2 + \tilde{\phi}_{,2}^T \partial x_1 / \partial X_1 \right) & \left( \tilde{\phi}_{,1}^T \partial x_2 / \partial X_2 + \tilde{\phi}_{,2}^T \partial x_2 / \partial X_1 \right) \end{bmatrix} \quad (\text{eq. C-9})$$

## C.2 Stress-Strain Relations

The stress-strain relations in large-strain theory are formulated in terms of the Jaumann rate of the Cauchy stress, namely,

$$\overset{\nabla}{\tilde{\sigma}} = H \underset{\approx}{\tilde{\varepsilon}} \quad (\text{eq. C-10})$$

and the Jaumann rate is given by

$$\overset{\nabla}{\tilde{\sigma}} = \underset{\approx}{\dot{\tilde{\sigma}}} - \underset{\approx}{\Omega}^T \underset{\approx}{\tilde{\sigma}} - \underset{\approx}{\tilde{\sigma}} \underset{\approx}{\Omega} \quad (\text{eq. C-11})$$

where, in the above,  $\underline{\sigma}$  is the Cauchy (true) stress,  $\underline{\Omega}$  is the antisymmetric part of the velocity gradient,  $\underline{\dot{\epsilon}}$  is the strain rate vector and  $\underline{H}$  is the constitutive material matrix. The derivation of this matrix, in the following paragraphs, is first given in a general form which is then specialized for each material.

### C.2.1 General Relations

Consider a material element where it is assumed that the strain rate tensor  $\dot{\epsilon}_{ij}$  be expressed as the sum of four components: elastic, time-independent plastic, creep, and free expansion; namely

$$\dot{\epsilon}_{ij} = \dot{\epsilon}_{ij}^e + \dot{\epsilon}_{ij}^p + \dot{\epsilon}_{ij}^c + \dot{\epsilon}_{ij}^f \quad (\text{eq. C-12})$$

Note the free expansion term is due to the combined effects of temperature and irradiation induced swelling and densification. In incremental form, eq. C-12 can be expressed as

$$d\epsilon_{ij} = d\epsilon_{ij}^e + d\epsilon_{ij}^p + d\epsilon_{ij}^c + d\epsilon_{ij}^f \quad (\text{eq. C-13})$$

The elastic strains are related to the incremental stress by

$$d\epsilon_{ij}^e = d(C_{ijkl} \sigma_{kl}) = C_{ijkl} d\sigma_{kl} + dC_{ijkl} \sigma_{kl} \quad (\text{eq. C-14})$$

or by the inverse relation

$$d\sigma_{ij} = d(D_{ijkl} \epsilon_{kl}^e) = D_{ijkl} d\epsilon_{kl}^e + dD_{ijkl} \epsilon_{kl}^e \quad (\text{eq. C-15})$$

Equations C-14 and C-15 admit the variation of the material tensors  $C_{ijkl}$  and  $D_{ijkl}$  with temperature and neutron flux. For isotropic material, they reduce to

$$C_{ijkl} = \frac{1-\nu}{E} \delta_{ik} \delta_{jl} - \frac{\nu}{E} \delta_{ij} \delta_{kl} \quad (\text{eq. C-16})$$

and

$$D_{ijkl} = \frac{E}{1-\nu} \delta_{ik} \delta_{jl} + \frac{\nu E}{(1+\nu)(1-2\nu)} \delta_{ij} \delta_{kl} \quad (\text{eq. C-17})$$

where E is Young's modulus and  $\nu$  is Poisson's ratio.

### C.2.2 Creep Relations

We direct our attention next to the creep strain rates  $\dot{\varepsilon}_{ij}^c(t)$ . The most common form of creep theories used in analysis is the equation of state theory based on the strain hardening rule, which is fashioned after plasticity theory.

Consider an isothermal single-step creep experiment in which the measured creep strain for stress  $\sigma$ , temperature  $T$  and fast neutron fluence  $q$  is expressed as follows:

$$\varepsilon^c(t) = J(\sigma, T, q, t) \sigma \quad (\text{eq. C-18})$$

where

$$q = q(t) = \int_0^t \phi(t') dt' \quad (\text{eq. C-19})$$

In the above,  $t$  is time and  $\phi(t)$  is the fast neutron flux. By the strain hardening rule, the time  $t$  in eq. C-18 is replaced by the accumulated creep strain such that the strain increment is given by

$$\Delta \varepsilon^c(t) = J'(\sigma, T, q, \varepsilon^c) \sigma \quad (\text{eq. C-20})$$

This equation is generalized to multiaxial relations by

$$\dot{\varepsilon}_{ij}^c = B_{ijkl} J' \sigma_{kl} \quad (\text{eq. C-21})$$

where  $J'$  stands for  $dt \partial J / \partial t$ . For isotropic creep behavior we have

$$B_{ijkl} = (0.5 + \nu_0) \delta_{ik} \delta_{jl} - (0.5 - \nu_0) \delta_{ij} \delta_{kl} \quad (\text{eq. C-22})$$

In this equation  $\nu_0$  is a material constant which governs the creep volume change generally exhibited by the fuel material. For the cladding,  $\nu_0$  is zero.

### C.2.3 Time-Independent Elastic-Plastic Relations

A general yield criterion can be expressed as

$$F(\sigma_{ij}, \varepsilon_{ij}^p, K) = 0 \quad (\text{eq. C-23})$$

where  $\sigma_{ij}$  and  $\varepsilon_{ij}^p$  are the stresses and plastic strains, respectively, and  $K$  is a material parameter.

The plastic strain increments must obey a flow rule of the form

$$d\varepsilon_{ij}^p = d\lambda \left( \partial F / \partial \sigma_{ij} \right) \quad (\text{eq. C-24})$$

where  $d\lambda$  is a positive scalar function which depends on the state of stress, strain, temperature, hardening, and neutron flux. Combining equations C-12, C-14, C-15, C-21 and C-24 the incremental stress-strain relations may be written as

$$d\sigma_{ij} = D_{ijkl} \left( d\varepsilon_{kl} - d\lambda \frac{\partial F}{\partial \sigma_{kl}} - dt B_{klmn} J' \sigma_{mn} - dC_{klmn} \sigma_{mn} - d\varepsilon_{kl}^f \right) \quad (\text{eq. C-25})$$

In the above equation, the scalar function  $d\lambda$  remains to be determined. The consistency condition which ensures that the stresses remain on the yield surface is given by

$$dF = \frac{\partial F}{\partial \sigma_{ij}} d\sigma_{ij} + \frac{\partial F}{\partial \varepsilon_{ij}^p} d\varepsilon_{ij}^p + \frac{\partial F}{\partial K} dK = 0 \quad (\text{eq. C-26})$$

This equation admits the dependence of the yield function on the temperature and neutron flux through the parameter  $K$ . Making use of equations C-24 through C-26, and after some manipulation, the final form of the incremental stress-strain law is found to be

$$d\sigma_{ij} = D_{ijkl} \left( d\varepsilon_{kl} - \eta \frac{\partial F}{\partial \sigma_{kl}} \Lambda_{mn} d\varepsilon_{mn}^* \right) - d\psi_{ij} \quad (\text{eq. C-27})$$

where

$$d\psi_{ij} = \eta D_{ijkl} \frac{\partial F}{\partial \sigma_{kl}} \frac{\partial F}{\partial K} dK \left/ \left( D_{mnpq} \frac{\partial F}{\partial \sigma_{mn}} \frac{\partial F}{\partial \sigma_{pq}} - \frac{\partial F}{\partial \varepsilon_{mn}^p} \frac{\partial F}{\partial \sigma_{mn}} \right) \right. \quad (\text{eq. C-28})$$

$$d\varepsilon_{kl}^* = d\varepsilon_{kl} - dt B_{klmn} J' \sigma_{mn} - dC_{klmn} \sigma_{pq} - d\varepsilon_{kl}^f \quad (\text{eq. C-29})$$

$$\Lambda_{kl} = D_{ijkl} \frac{\partial F}{\partial \sigma_{ij}} \left( D_{mnpq} \frac{\partial F}{\partial \sigma_{mn}} \frac{\partial F}{\partial \sigma_{pq}} - \frac{\partial F}{\partial \varepsilon_{mn}^p} \frac{\partial F}{\partial \sigma_{mn}} \right) \quad (\text{eq. C-30})$$

and

$$\begin{aligned} \eta &= 0 \quad \text{when} \quad F < 0 \\ \eta &= 1 \quad \text{when} \quad F = 0 \quad \text{and} \quad \frac{\partial F}{\partial \sigma_{ij}} d\sigma_{ij} + \frac{\partial F}{\partial K} dK \geq 0 \end{aligned} \quad (\text{eq. C-31})$$

Equation C-27 is too general, and to reduce it to a form which can be used in analysis the yield function  $F$  has to be defined. In doing so, we must also define the type of hardening the material exhibits during plastic flow. A combined Mohr-Coulomb and von Mises yield conditions [1]

Appendix C: Field And Equilibrium Equations

together with Prager's kinematic hardening rule [2] are adopted in the following derivations. The yield function  $F$  is given by

$$F = \frac{1}{2} J_2 + \beta I_1^2 - K^2 = 0 \quad (\text{eq. C-32})$$

where  $I_1$  and  $J_2$  are invariants of the stress tensor  $\sigma'_{ij}$  given by

$$\sigma'_{ij} = \sigma_{ij} - \alpha_{ij} \quad (\text{eq. C-33})$$

in which  $\sigma_{ij}$  are the stresses and  $\alpha_{ij}$  are the coordinates of the center of the translating yield surface. In eq. C-32,  $K$  is a material parameter which depends on the temperature and neutron flux. The stress invariants  $I_1$  and  $J_2$  are as follows:

$$I_1 = \sigma'_{ii} \quad (\text{eq. C-34})$$

$$J_2 = \frac{1}{2} S'_{ij} S'_{ij} \quad (\text{eq. C-35})$$

where

$$S'_{ij} = \sigma'_{ij} - \frac{1}{3} \sigma'_{kk} \delta_{ij} \quad (\text{eq. C-36})$$

$S'_{ij}$  are the deviatoric components of the tensor  $\sigma'_{ij}$ . The parameter  $\beta$  in eq. C-32 is a material constant which governs the plastic volume change of the material. The derivative of the yield criterion,  $F$ , with respect to  $\sigma_{ij}$  can be obtained by differentiating eq. C-32 using the definitions C-34 and C-35. The result is

$$\frac{\partial F}{\partial \sigma_{ij}} = S_{ij} + 2\beta I_1 \delta_{ij} \quad (\text{eq. C-37})$$

Substituting the results into C-24, making use of the fact that  $S_{ii} = 0$  and  $\delta_{ii} = 3$ , the time-independent plastic dilatation becomes

$$d\varepsilon_{ii}^p = 6\beta d\lambda I_1 \quad (\text{eq. C-38})$$

It is clear from eq. C-38 that, if the plastic volume change is zero as is the case for metals,  $\beta = 0$ . Hence the yield function (eq. C-32) reduces to the ordinary von Mises condition. However, for porous materials such as nuclear fuel,  $\beta \neq 0$ .

Remaining within the framework of the classical kinematic hardening rule, the yield surface is assumed to translate in the direction of the plastic strain increments, hence,

$$d\alpha_{ij} = C d\varepsilon_{ij}^p \quad (\text{eq. C-39})$$

where  $C$  is a material parameter and is equal to  $2/3 E'$ , where  $E'$  is the slope of the stress-plastic strain curve in simple tension. The parameter  $K$  is related to the uniaxial yield stress  $\sigma_y$  by

$$K = \sigma_y / \sqrt{3} \quad (\text{eq. C-40})$$

Substituting equations C-32 through C-40 gives

$$\Lambda_{kl} = D_{ijkl} (S'_{ij} + 2\beta I_1 \delta_{ij}) / Q \quad (\text{eq. C-41})$$

$$d\sigma_{ij} = D_{ijkl} \left\{ d\varepsilon_{kl}^* - \eta (S'_{kl} + 2\beta I_1 \delta_{kl}) \Lambda_{mn} d\varepsilon_{mn}^* \right\} - d\psi_{ij} \quad (\text{eq. C-42})$$

where

$$d\psi_{ij} = \eta D_{ijkl} (S'_{kl} + 2\beta I_1 \delta_{kl}) (-2K dK) / Q \quad (\text{eq. C-43})$$

$$Q = D_{mnpq} (S'_{mn} + 2\beta I_1 \delta_{mn}) (S'_{pq} + 2\beta I_1 \delta_{pq}) + \frac{2}{3} E' (S'_{mn} + 2\beta I_1 \delta_{mn}) (S'_{mn} + 2\beta I_1 \delta_{mn}) \quad (\text{eq. C-44})$$

The yield surface translations  $\alpha_{ij}$  are given by

$$d\alpha_{ij} = \sigma'_{ij} \left( \frac{\partial F}{\partial \sigma_{mn}} d\sigma_{mn} + \frac{\partial F}{\partial K} dK \right) \sigma'_{kl} \frac{\partial F}{\partial \sigma_{kl}} \quad (\text{eq. C-45})$$

or

$$d\alpha_{ij} = \sigma'_{ij} \{ (S'_{mn} + 2\beta I_1 \delta_{mn}) d\sigma_{mn} - 2K dK \} / \{ \sigma'_{kl} (S'_{kl} + 2\beta I_1 \delta_{kl}) \} \quad (\text{eq. C-46})$$

#### C.2.4 Incremental Stress-Strain Relations

In the following derivations of the incremental stress-strain relations, the backward-Euler algorithm is used, and to do this conveniently, matrix notation is adopted in place of the indicial notation. We first examine the creep contribution to eq. C-42. If  $\overset{\nabla}{\underset{\sim}{\sigma}}_n$  is defined to be the

Jaumann rate vector whose elements are  $\overset{\nabla}{\underset{\sim}{\sigma}}_{ij}(t_n)$  at the  $n^{\text{th}}$  time instant and  $\underset{\sim}{B}$  is the matrix of

$B_{ijkl}$ , then the time difference form of eq. C-21 is

Appendix C: Field And Equilibrium Equations

$$\Delta \tilde{\varepsilon}_n^c = \underset{\approx}{B} \underset{\approx}{J}'_n \left( \Delta t_n \overset{\nabla}{\tilde{\sigma}}_n + \tilde{\sigma}_{n-1} \right) \quad (\text{eq. C-47})$$

where  $\Delta \tilde{\varepsilon}_n^c$  is the increment of the creep strain vector at  $t_n$  and  $J'_n$  denotes  $\Delta J(\sigma, T, q, \varepsilon)$  evaluated at  $t = t_n$ .

Defining the Jaumann increment of Cauchy stress as

$$\Delta \overset{\nabla}{\tilde{\sigma}}_n = \overset{\nabla}{\tilde{\sigma}}_n dt_n \quad (\text{eq. C-48})$$

the final form of the incremental stress-strain matrix equation is

$$\begin{aligned} \Delta \overset{\nabla}{\tilde{\sigma}}_n = \underset{\approx}{H} \left\{ \Delta \tilde{\varepsilon}_n - \Delta \tilde{\varepsilon}_n^f - \left( \underset{\approx}{J}'_n \underset{\approx}{B} + \Delta \underset{\approx}{C} \right) \tilde{\sigma}_{n-1} \right\} \\ + 2 \eta \frac{\underset{\approx}{K} \underset{\approx}{A} \underset{\approx}{K}}{\underset{\approx}{Q}} \left( \underset{\approx}{I} + \underset{\approx}{J}'_n \underset{\approx}{M} \underset{\approx}{C} \right)^{-1} \left( \underset{\approx}{S}'_n + 2 \beta \underset{\approx}{I}_{ln} \underset{\approx}{\delta} \right) \end{aligned} \quad (\text{eq. C-49})$$

in which

$$\underset{\approx}{M} = \left[ \underset{\approx}{I} + \underset{\approx}{D} \left( \underset{\approx}{J}'_n \underset{\approx}{B} + \Delta \underset{\approx}{C} \right) \right]^{-1} \underset{\approx}{D} \quad (\text{eq. C-50})$$

$$\underset{\approx}{H} = \underset{\approx}{M} - (\eta/Q) \underset{\approx}{M} \left( \underset{\approx}{S}'_n + 2 \beta \underset{\approx}{I}_{ln} \underset{\approx}{\delta} \right) \left( \underset{\approx}{S}'_n + 2 \beta \underset{\approx}{I}_{ln} \underset{\approx}{\delta} \right)^T \underset{\approx}{M} \quad (\text{eq. C-51})$$

$$\underset{\approx}{Q} = \left( \underset{\approx}{S}'_n + 2 \beta \underset{\approx}{I}_{ln} \underset{\approx}{\delta} \right)^T \underset{\approx}{M} \left( \underset{\approx}{S}'_n + 2 \beta \underset{\approx}{I}_{ln} \underset{\approx}{\delta} \right) + \frac{2}{3} E' \left( \underset{\approx}{S}'_n + 2 \beta \underset{\approx}{I}_{ln} \underset{\approx}{\delta} \right)^T \left( \underset{\approx}{S}'_n + 2 \beta \underset{\approx}{I}_{ln} \underset{\approx}{\delta} \right) \quad (\text{eq. C-52})$$

where  $\Delta \tilde{\varepsilon}_n^c$  is the incremental strain vector,  $\Delta \overset{\nabla}{\tilde{\sigma}}_n$  is the Jaumann incremental stress vector,  $\Delta \tilde{\varepsilon}_n^f$  is the free expansion incremental strain vector,  $\underset{\approx}{S}'$  is the deviatoric stress vector,  $\underset{\approx}{\delta}$  is the Kronecker delta in vector form,  $\underset{\approx}{D}$  is the elasticity matrix,  $\underset{\approx}{I}$  is the identity matrix, and  $\Delta \underset{\approx}{C}$  is the change in  $\underset{\approx}{C}$  due to a change in temperature and/or fluence. The other symbols have been defined in previous relations.



Equation C-49 is the matrix equation used in the derivations of finite element stiffness and force matrices, as will be discussed later in this appendix.

### C.2.5 Radial Return Correction

Because of the highly nonlinear material response, the computations can be very sensitive to the size of the time step. Therefore, special measures, such as the use of small time steps for example, have to be taken to prevent the breakdown of the solution. While reducing the step size may be necessary to ensure solution accuracy, it is not sufficient by itself and may be computationally impractical. The numerical behavior of the solution is governed primarily by the degree to which the computed stresses deviate from the yield function, eq. C-32, and the consistency condition, eq. C-26. In order to ensure that these two conditions are satisfied incrementally, it is necessary to apply a correction factor to the computed stresses. This correction factor is referred to in computational mechanics as the radial return. The name is descriptive of the procedure, which simply returns the computed stresses to the yield surface radially along the yield surface normal. This is accomplished by the following equation:

$$\left( \tilde{\sigma}_n \right)_{\text{corrected}} = \tilde{\sigma}_n \left[ \left( \frac{1}{2} \tilde{S}'_n{}^T \tilde{S}'_n + \beta I_{In}^2 \right) / K_n^2 \right]^{1/2} \quad (\text{eq. C-53})$$

where the quantities on the right-hand side of this equation are those computed at the end of the step.

### C.2.6 Incremental Stress-Strain Relations for Clad Material

Some of the general relations presented in the preceding subsection are not required for the clad material, which leads to significant simplifications of the incremental stress-strain relations. In particular, the clad material is assumed to be initially isotropic and exhibits only elastic dilatational response. This requires that  $\nu_0 = 0$ ,  $\beta = 0$ .

Introducing these conditions and simplifying the results yields

$$\Delta \tilde{\sigma}_n^{\nabla} = \tilde{H} \left\{ \Delta \tilde{\varepsilon}_n - \Delta \tilde{\varepsilon}_n^f - \left( \tilde{J}'_n \tilde{S}'_n + \Delta \tilde{C} \tilde{\sigma}_{n-1} \right) \right\} + \frac{2\eta K \Delta K}{Q} \tilde{M} \tilde{S}'_n \quad (\text{eq. C-54})$$

$\tilde{H}$  now becomes

$$\tilde{H} = \tilde{M} - \eta \tilde{M} \tilde{S}'_n \tilde{S}'_n{}^T \tilde{M} / \left( \tilde{S}'_n{}^T \tilde{M} \tilde{S}'_n + \frac{2}{3} E' \tilde{S}'_n{}^T \tilde{S}'_n \right) \quad (\text{eq. C-55})$$

### C.2.7 Incremental Stress-Strain Relations for Fuel Material

Because of the small strain response of the fuel material, the infinitesimal strain theory is used in the derivation of the stress-strain relations for the fuel. This means that the Jaumann rate  $\overset{\nabla}{\sigma}$  is replaced by the stress rate  $\dot{\sigma}$ . Unlike the clad, the fuel material exhibits inelastic volume change or hot pressing; thus the hot pressing parameters  $\upsilon_0$  and  $\beta$  which appear in equations C-22 and C-23 respectively are non-zero.

#### C.2.7.1 Hot Pressing Parameters

The creep and plasticity hot pressing parameters  $\upsilon_0$  and  $\beta$  respectively were determined using mathematical models of an idealized porous material described in [3]. Using Reference [3] analysis, the plasticity hot pressing parameter is given by

$$\beta = \left[ Y(\rho_0)/Y_s / \left( 2\sqrt{3} \ln(0.74/(1-\rho_0)) \right) \right]^2 \quad (\text{eq. C-56})$$

where

$\rho_0$ : Initial (as-manufactured) fractional density of the fuel

$Y(\rho_0)$ : Initial yield strength of the fuel

$Y_s$ : Yield strength of solid (100% dense)  $\text{UO}_2$

Except for  $Y_s$ , the parameters in eq. C-56 are known for a typical fuel design. Because it is virtually impossible to determine  $Y_s$  experimentally, and porosity dependent yield strength data is not available for extrapolation to zero porosity, it would be necessary to estimate  $Y_s$  in order to make use of the above expression for  $\beta$ . However, it is possible to avoid this process by allowing  $Y(\rho_0)$  to approach  $Y_s$  as  $\rho_0$  approaches unity and then calculate an asymptotic value for  $\beta$ . Using this procedure  $\beta$  can be calculated as follows:

$$\beta = \lim_{\rho_0 \rightarrow 1} \left[ 1 / \left( 2\sqrt{3} \ln(0.74/(1-\rho_0)) \right) \right]^2 \doteq 0.005 \quad (\text{eq. C-57})$$

This value of  $\beta$  was found to give best results with respect to observed behavior of fuel-clad mechanical interaction.

Using the same theoretical analysis of porous media, described in Reference [3], an expression for the creep hot pressing parameter  $\upsilon_0$  was obtained as follows:

$$\upsilon_0 = \left[ \frac{1}{4} \left( \frac{3}{2} \right) / \left( (0.74/(1-\rho))^{1/n} - 1 \right) \right]^n \quad (\text{eq. C-58})$$

where  $n$  is the exponent in a power creep law of the form  $\dot{\epsilon} = \dot{A} \sigma^n$ , and  $\rho$  is the current density (fraction of theoretical). As can be seen, eq. C-58 depends only on known parameters, namely  $\rho$  and  $n$ , provided that  $\text{UO}_2$  creep can be expressed as a power law, which is the case for thermal creep where  $n$  varies from unity at low stresses to 4.5 at high stresses based on the MATPRO material properties package [4] which is used in FALCON. For irradiation creep, however, the exponent is unity. Thus, in order to account for both creep effects throughout the expected stress range, an average value of  $n = 3$  was used in eq. C-58. The fractional density  $\rho$  is history dependent and is taken to be the smeared density. Equation C-58 with  $n = 3$  is used in FALCON with a cutoff value of zero as  $\rho$  approaches unity, at which point the fuel becomes incompressible.

### C.2.7.2 Pellet Cracking

The major point of departure of the fuel behavior from the cladding behavior is that it cracks in brittle modes under relatively low power. This cracking, which is an inherent behavior of solid fuel pellets, plays an important role in the fuel relocation and fuel-clad mechanical interaction mechanisms.

A typical representation of the tensile response of the material is displayed in Figure C-1 which shows an initially linear behavior up to a peak point followed by a strain softening regime.

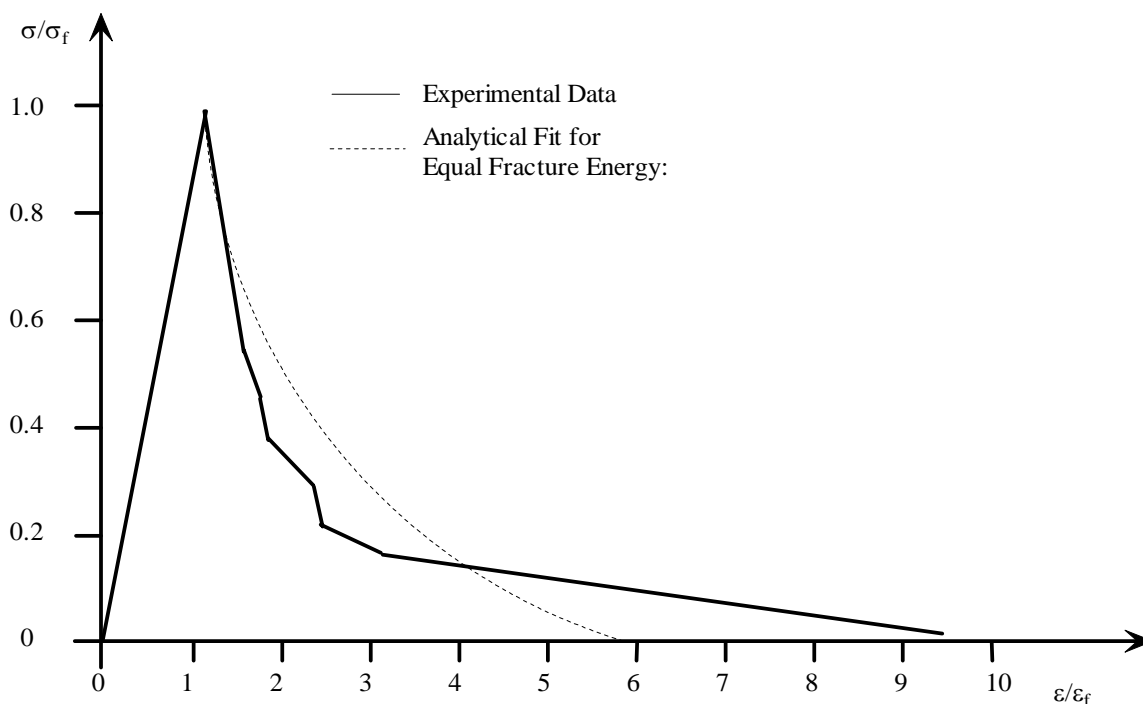


**Figure C-1**  
**Normalized Tension Response Curve for Ceramic Materials**

## Appendix C: Field And Equilibrium Equations

The peak point on this figure is the crack initiation point; however, the crack is not fully formed until the end of the strain softening regime, which can extend to a strain that is five or ten times larger than the fracture strain. The modeling of this post-peak response of the material is very important to the behavior of the fuel pellet, particularly under cyclic power histories where pellet expansion and contraction, which influences the gap conductance and consequently the thermal response, are greatly affected by that regime. Experimental stress-strain data in tension for fuel pellets is totally lacking. However, Figure C-1 was constructed using the observed response of ceramic materials which generally exhibit the strain softening response shown in the figure. By knowing the fracture stress or strain and the elastic modulus and making an assumption on the extent of the strain softening regime, a normalized form of the stress-strain curve can be constructed as shown in Figure C-1. It should be noted, however, that the model is not very sensitive to the shape of the strain softening curve.

Using the analytical fit in Figure C-1, the normalized stress is expressed as

$$\frac{\sigma}{\sigma_f} = A + B e^{-C\varepsilon/\varepsilon_f} \quad (\text{eq. C-59})$$

where  $\varepsilon_f$  and  $\sigma_f$  are the fracture strain and stress respectively and A, B and C are functions of the ratio  $\varepsilon_0/\varepsilon_f$ , where  $\varepsilon_0$  is the crack opening strain when the crack is assumed to be fully formed. For strains greater than  $\varepsilon_0$ , the material is not allowed to support any tensile stress normal to the crack plane. In the strain softening range between the peak point  $\varepsilon = \varepsilon_f$  and  $\varepsilon = \varepsilon_0$ , the material loses its stiffness and sheds the tensile stress gradually. This behavior, however, is valid only for previously uncracked material, but once the crack becomes fully formed, the material loses its tensile stiffness capacity in the normal direction to the crack regardless of the magnitude of the tensile strain. However, under strain reversals during power cycling, the crack is allowed to close and develop compressive stiffness even under residual tensile strain. This compressive stiffness recovery occurs gradually, from a very small residual value until the strain across the crack plane reaches  $\varepsilon_0$ , then gradually increasing to full value when the calculated crack strain becomes negative. This stiffness history is derived below using a non-dimensional crack history parameter  $e(t)$ , as will be discussed below. Equation C-59 can be written as follows for  $\varepsilon > \varepsilon_f$ .

$$\frac{\sigma}{\sigma_f} = \frac{\sigma}{\varepsilon} \frac{\varepsilon}{\varepsilon_f} \frac{\varepsilon_f}{\sigma_f} = A + B e^{-C\varepsilon/\varepsilon_f} \quad (\text{eq. C-60})$$

recognizing that  $\sigma/\varepsilon = E$  and  $\sigma_f/\varepsilon_f = E_0$ , where E is the post peak (cracking) modulus and  $E_0$  is the initial (elastic) modulus, and introducing the definition of  $e(t)$ , eq. C-60 becomes

$$e(t) = E/E_0 = (\varepsilon_f/\varepsilon) \left( A + B e^{-C\varepsilon/\varepsilon_f} \right) \quad (\text{eq. C-61})$$

From eq. C-61,  $e(t)$  takes on the values of unity and zero respectively for the conditions  $\varepsilon \leq \varepsilon_f$  and  $\varepsilon \geq \varepsilon_0$ . In the range  $\varepsilon_f < \varepsilon < \varepsilon_0$ ,  $e(t)$  will have a value between unity and zero according to eq. C-61. In this sense,  $e(t)$  can be regarded as the memory function of the crack. This expression for  $e(t)$  will be used to modify the constitutive relations for the fuel pellet.

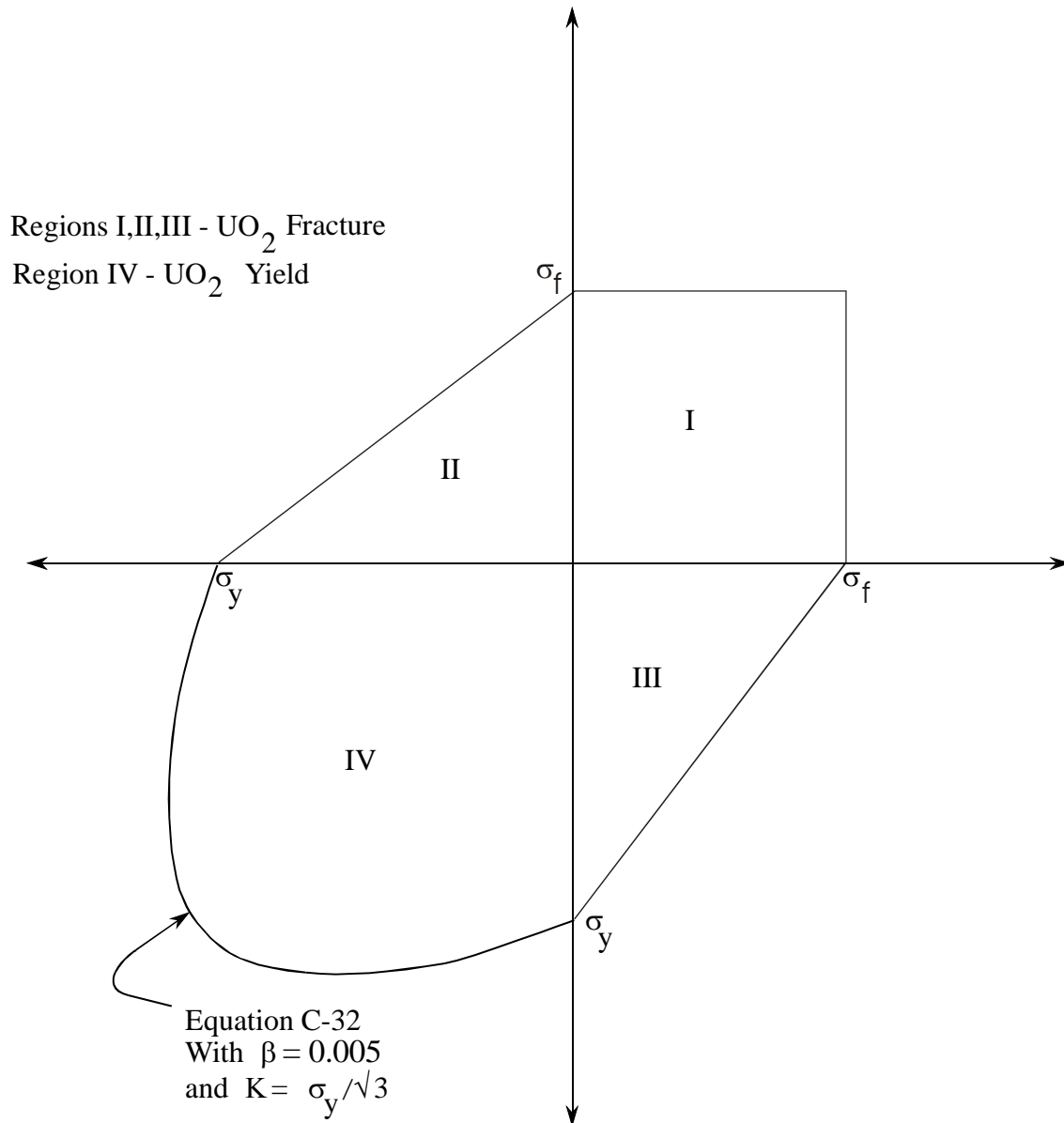


**Figure C-2**  
 **$\text{UO}_2$  Failure/Yield Surface**

The preceding discussion dealt with the uniaxial response in tension. To generalize this one-dimensional response to two- and three-dimensional stress states, the crack is assumed to initiate at a point when the calculated principal strain reaches the material fracture strain as a temperature-dependent material property. The crack surface is the perpendicular plane to the principal direction. A failure/yield surface for the fuel under general two-dimensional stress states is shown in Figure C-2. Stress states in the compression-compression quadrant of Figure C-2 are characterized as elasto-plastic regimes where the material responds elastically until the stress state reaches the yield surface where the material will deform plastically. The plasticity of the fuel material is governed by the yield function given in eq. C-32. For stress states in the positive-positive or positive-negative quadrants of the failure surface, the material responds elastically until the stress state reaches the failure surface where the material will fail in the

Appendix C: Field And Equilibrium Equations

cracking mode; the tangent to the failure surface determines the orientation of the crack surface. A smeared-cracking model is used in which the crack is viewed as a mechanism that changes the material behavior from isotropic to orthotropic, where the material stiffness normal to the crack surface drops to zero while full stiffness parallel to the crack is maintained. Consider a strain state  $\bar{\varepsilon}_n$ , expressed in the principal coordinate system, then the transformation of the coordinate strains  $\varepsilon_n$  to  $\bar{\varepsilon}_n$  is

$$\bar{\varepsilon}_n = \mathbf{P} \varepsilon_n \quad (\text{eq. C-62})$$

where  $\mathbf{P}$  is function of the direction cosines of the principal direction unit vectors.

Transforming the incremental quantities  $\Delta \varepsilon_n$  and  $\Delta \sigma_n$  to the principal axes gives:

$$\Delta \bar{\varepsilon}_n = \mathbf{P} \Delta \varepsilon_n \quad (\text{eq. C-63})$$

$$\Delta \bar{\sigma}_n = \left( \mathbf{P}^{-1} \right)^T \Delta \sigma_n \quad (\text{eq. C-64})$$

The transformed vectors  $\Delta \bar{\varepsilon}_n$  and  $\Delta \bar{\sigma}_n$  and the untransformed vectors  $\Delta \varepsilon_n$  and  $\Delta \sigma_n$  must satisfy the inner product relation

$$\Delta \varepsilon_n^T \Delta \sigma_n = \Delta \bar{\varepsilon}_n^T \Delta \bar{\sigma}_n \quad (\text{eq. C-65})$$

Rewriting eq. C-49 in short form

$$\Delta \sigma_n = \mathbf{H} \Delta \varepsilon_n - \mathbf{R}_n \quad (\text{eq. C-66})$$

where  $\mathbf{R}_n$  is an internal stress vector which contains the rest of the terms in eq. C-49.

Transforming eq. C-66 to the principal coordinate system yields

$$\Delta \bar{\sigma}_n = \bar{\mathbf{H}} \Delta \bar{\varepsilon}_n - \left( \mathbf{P}^{-1} \right)^T \mathbf{R}_n \quad (\text{eq. C-67})$$

where

$$\bar{\mathbf{H}}_{\approx} = \left( \mathbf{P}_{\approx}^{-1} \right)^T \mathbf{H}_{\approx} \mathbf{P}_{\approx}^{-1} \quad (\text{eq. C-68})$$

Now the memory function  $e(t)$  introduced in eq. C-61 can be generalized to describe the history of a crack in a principal plane, i.e.,  $e_i(t)$  describes the history of the crack whose normal is in the  $i^{\text{th}}$  principal direction, namely,

$$e_i(t) = (\varepsilon_f / \varepsilon_i) \left( A + B e^{-C\varepsilon / \varepsilon_f} \right), \quad i = 1, 2, 3 \quad (\text{eq. C-69})$$

Applying eq. C-69 to C-67 leads to the following incremental stress-strain equation expressed in the principal coordinate system:

$$\Delta \bar{\boldsymbol{\sigma}}_n = \mathbf{E}_{\approx}^T \bar{\mathbf{H}}_{\approx} \mathbf{E}_{\approx} \Delta \bar{\boldsymbol{\varepsilon}}_n - \left( \mathbf{P}_{\approx}^{-1} \right)^T \mathbf{R}_n + \left( \mathbf{I}_{\approx} - \mathbf{E}_{\approx} \right) \left[ \left( \mathbf{P}_{\approx}^{-1} \right)^T \mathbf{R}_n - \bar{\boldsymbol{\sigma}}_{n-1} \right] \quad (\text{eq. C-70})$$

where  $\mathbf{E}_{\approx}$  is a diagonal matrix whose diagonal elements are functions of the three possible crack histories  $e_i(t)$ ,  $i = 1, 2, 3$ , defined by eq. C-69. Specifically for the axisymmetric two-dimensional case,

$$\mathbf{E}_{\approx} = \begin{bmatrix} e_1 & 0 & 0 & 0 \\ 0 & e_2 & 0 & 0 \\ 0 & 0 & e_3 & 0 \\ 0 & 0 & 0 & e_1 e_3 \end{bmatrix} \quad (\text{eq. C-71})$$

In plane stress  $\mathbf{E}_{\approx}$  defines two possible orthogonal cracks. In an axisymmetric stress state,

however, a third crack surface can develop along a radius, which implies the existence of an infinite number of such cracks. Figure C-3 shows the three possible crack types that can develop in the fuel. In the present development the cracks can follow independent histories, including crack closing and possible healing if the fuel temperature rises above the sintering temperature. Finally, eq. C-70 is transformed back to the original coordinate system with the result

$$\Delta \boldsymbol{\sigma}_n = \mathbf{Z}_{\approx}^T \mathbf{H}_{\approx} \mathbf{Z}_{\approx} \Delta \boldsymbol{\varepsilon}_n - \mathbf{Z}_{\approx}^T \mathbf{R}_n - \left( \mathbf{I}_{\approx} - \mathbf{Z}_{\approx}^T \right) \boldsymbol{\sigma}_{n-1} \quad (\text{eq. C-72})$$

where

$$\mathbf{Z}_{\approx} = \mathbf{P}_{\approx}^{-1} \mathbf{E}_{\approx} \mathbf{P}_{\approx} \quad (\text{eq. C-73})$$

$$\tilde{R}_n = \tilde{H} \left[ \Delta \tilde{\varepsilon}_n^f + \left( J'_n \tilde{B} + \Delta \tilde{C} \right) \tilde{\varsigma}_{n-1} \right] + 2 \eta \frac{K \Delta K}{Q} \left( 1 + J'_n \tilde{M} \tilde{C} \right)^{-1} \left[ \tilde{S}'_n + 2 \beta + J_1 \tilde{\delta} \right] \quad (\text{eq. C-74})$$

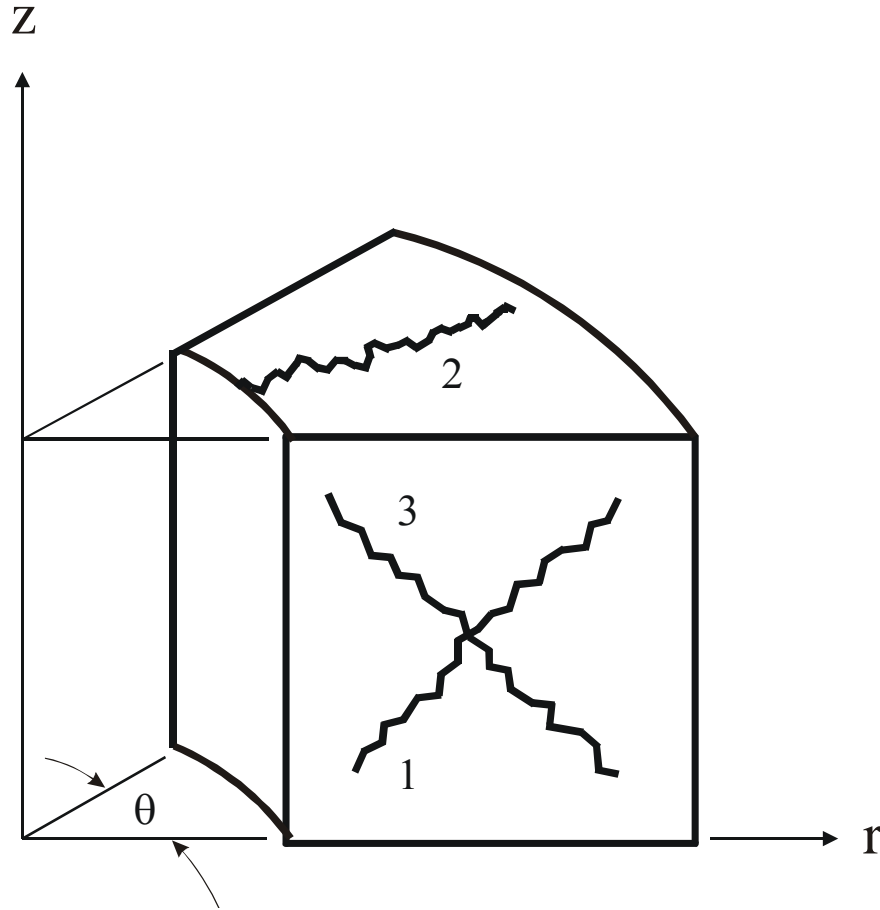


**Figure C-3**  
**Fuel Cracking Pattern**

Implementation of the cracking model described above in FALCON is quite involved because of the transient nature of fuel deformations, particularly under power cycling where crack opening and closing can follow a complex history. It should be emphasized that the three possible crack types can follow their individual histories, and the memory of each crack is retained through the function  $e_i(t)$ .

The material data required for these equations is derived from MATPRO-11 [4]. These include the fuel and clad elastic constants, the low temperature yield strength and creep compliance for both the fuel and clad, and the high temperature strain rate-stress relations for the clad.



### C.3 Equilibrium Equations

Equilibrium equations are derived for the finite element system using the variational technique and the principle of virtual work. In the updated Lagrangian framework, the principle of virtual work can be written as

$$\int_v \underline{\underline{\sigma}} : \delta \underline{\underline{D}} \, dv = \int_v \underline{\underline{f}} \delta \underline{\underline{u}} \, dv + \int_s \underline{\underline{t}} \delta \underline{\underline{u}} \, ds \quad (\text{eq. C-75})$$

where  $v$  and  $s$  are the current volume and surface of the body,  $\underline{\underline{\sigma}}$  is the Cauchy stress,  $\underline{\underline{u}}$  is the velocity,  $\underline{\underline{D}}$  is the symmetric part of the velocity gradient, and  $\underline{\underline{t}}$  is the surface traction. The ":" is used to represent a double dot product of two tensors. When all quantities are written as functions of a reference configuration  $V^0$  with surface  $S^0$  the same principle becomes

$$\int_{V^0} \underline{\underline{T}} : \delta \underline{\underline{\dot{F}}} \, dV^0 = \int_{V^0} \underline{\underline{f}}^0 \delta \underline{\underline{u}} \, dV^0 + \int_{S^0} \underline{\underline{t}}^0 \delta \underline{\underline{u}} \, dS^0 \quad (\text{eq. C-76})$$

in which  $\underline{\underline{T}}$  is the first Piola Kirchoff stress and  $\underline{\underline{F}}$  is the deformation gradient. The rate (or incremental) form of the left hand side of eq. C-76 is

$$\frac{d}{dt} \int_{V^0} \underline{\underline{T}} : \delta \underline{\underline{\dot{F}}} \, dV^0 = \int_{V^0} \underline{\underline{\dot{T}}} : \delta \underline{\underline{\dot{F}}} \, dV^0 \quad (\text{eq. C-77})$$

because  $\frac{d}{dt} \delta \underline{\underline{\dot{F}}}$  can be chosen as zero. If we choose to write eq. C-76 using, instead of  $\underline{\underline{T}}$  and  $\underline{\underline{\dot{F}}}$ ,

the conjugate pair  $S$  (second Piola Kirchoff stress) and  $\frac{d}{dt} \delta \underline{\underline{\dot{E}}}$  (rate of Green strain) and interpret the reference configuration as the original configuration of the body then we have the usual "Total Lagrangian" formulation. In this case there is an additional term in eq. C-75 since  $\frac{d}{dt} \delta \underline{\underline{\dot{E}}} \neq 0$ .

The rate  $\underline{\underline{\dot{T}}}$  can be expressed in terms of the Cauchy stress  $\underline{\underline{\sigma}}$  and the Kirchoff stress  $\underline{\underline{\tau}}$  as

$$\underline{\underline{\dot{T}}} = \underline{\underline{F}}^{-1} \left( \frac{\nabla}{\underline{\underline{\tau}}} + \underline{\underline{\sigma}} \underline{\underline{\Omega}}^T - \underline{\underline{D}} \underline{\underline{\tau}} \right) \quad (\text{eq. C-78})$$

Appendix C: Field And Equilibrium Equations

where  $\overset{\nabla}{\underset{\sim}{\tau}}$  is the Jaumann rate

$$\left( \overset{\nabla}{\underset{\sim}{\tau}} = \underset{\sim}{\dot{\tau}} - \underset{\sim}{\Omega}^T \underset{\sim}{\tau} - \underset{\sim}{\tau} \underset{\sim}{\Omega} \right) , \quad \underset{\sim}{\tau} = J \underset{\sim}{\sigma} \quad (\text{eq. C-79})$$

and

$$J \text{ is the determinant of the deformation gradient } \underset{\sim}{F}. \quad (\text{eq. C-80})$$

Now we choose the reference configuration to be the configuration at the beginning of a time increment. This is the distinguishing feature of the Updated Lagrangian Formulation. This choice gives us the following simplifications:

$$\underset{\sim}{F} = \underset{\sim}{I}$$

$$\underset{\sim}{\dot{F}} = \underset{\sim}{L} \underset{\sim}{F} \text{ so that } \delta \underset{\sim}{F} = \delta \underset{\sim}{L}$$

$$J = 1 \text{ so that } \underset{\sim}{\tau} = \underset{\sim}{\sigma}$$

in which  $\underset{\sim}{L}$  is the velocity gradient with symmetric and antisymmetric parts  $\underset{\sim}{D}$  and  $\underset{\sim}{\Omega}$ . Now the integrand in eq. C-77 becomes

$$\underset{\sim}{\dot{T}} : \delta \underset{\sim}{\dot{F}} = \left( \overset{\nabla}{\underset{\sim}{\tau}} + \underset{\sim}{\sigma} \underset{\sim}{\Omega}^T - \underset{\sim}{D} \underset{\sim}{\sigma} \right) : \delta \underset{\sim}{L} \quad (\text{eq. C-81})$$

and, finally, the increment of internal virtual work is

$$\int_{V^0} \left[ \overset{\nabla}{\underset{\sim}{\tau}} : \delta \underset{\sim}{D} - \underset{\sim}{\sigma} : \delta \left( \underset{\sim}{D} \underset{\sim}{D} - \frac{1}{2} \underset{\sim}{L}^T \underset{\sim}{L} \right) \right] dV^0 \quad (\text{eq. C-82})$$

The constitutive assumption is that the Jaumann rate of Cauchy stress  $\overset{\nabla}{\underset{\sim}{\sigma}}$  is proportional to the strain rate  $\underset{\sim}{D}$ . Thus

$$\overset{\nabla}{\underset{\sim}{\sigma}} = \underset{\sim}{H} \underset{\sim}{D} \text{ or } \overset{\nabla}{\underset{\sim}{\tau}} = J \underset{\sim}{H} \underset{\sim}{D} \quad (\text{eq. C-83})$$

where the constitutive matrix  $\underline{\underline{H}}$  was derived in the previous section.

The two terms in eq. C-82 give us the two parts of the tangent stiffness matrix when finite element shape functions are introduced. In terms of the shape function and nodal point variables we expand the virtual displacements and increments of displacement as

$$\begin{aligned}\delta \underline{\underline{u}} &= \underline{\underline{\phi}}^T \delta \underline{\underline{v}} \\ \Delta \underline{\underline{u}} &= \underline{\underline{\phi}}^T \Delta \underline{\underline{v}}\end{aligned}\tag{eq. C-84}$$

Then the terms in eq. C-82 are written as

$$\int_{V^0} \underline{\underline{\tau}} : \delta \underline{\underline{D}} \, dV^0 = \delta \underline{\underline{v}}^T \underline{\underline{K}} \Delta \underline{\underline{v}}\tag{eq. C-85}$$

$$\int_{V^0} \underline{\underline{\sigma}} : \delta \left( \frac{1}{2} \underline{\underline{L}}^T \underline{\underline{L}} - \underline{\underline{D}} \underline{\underline{D}} \right) dV^0 = \delta \underline{\underline{v}}^T \underline{\underline{K}}_{\sigma} \Delta \underline{\underline{v}}\tag{eq. C-86}$$

where  $\underline{\underline{K}}$  is the conventional stiffness matrix and  $\underline{\underline{K}}_{\sigma}$  is the initial stress stiffness matrix. The details of the derivation of these matrices in a form suitable for coding is given next. The conventional stiffness matrix  $\underline{\underline{K}}$  has the same form as for small strain formulations, namely that derived from

$$\underline{\underline{K}} = \delta \underline{\underline{D}} \underline{\underline{H}} \underline{\underline{D}}\tag{eq. C-87}$$

In the coding scheme employed in FALCON, the stiffness matrix is calculated by partitions

$$\underline{\underline{K}} = \begin{bmatrix} \underline{\underline{K}}^{11} & \underline{\underline{K}}^{12} \\ \underline{\underline{K}}^{21} & \underline{\underline{K}}^{22} \end{bmatrix}\tag{eq. C-88}$$

Each submatrix is the linear combination of outer product of shape function gradients. Let

$$\underline{\underline{\phi}}_0 = \frac{1}{r} \underline{\underline{\phi}} \quad , \quad \underline{\underline{\phi}}_1 = \frac{\partial \underline{\underline{\phi}}}{\partial r} \quad , \quad \underline{\underline{\phi}}_2 = \frac{\partial \underline{\underline{\phi}}}{\partial z}\tag{eq. C-89}$$

then the submatrices have the form

Appendix C: Field And Equilibrium Equations

$$\begin{aligned}
 \mathbf{K}_{\approx}^{11} &= \phi_0^T \left( \mathbf{H}_{22} \phi_0 + \mathbf{H}_{21} \phi_1 + \mathbf{H}_{24} \phi_2 \right) + \phi_1^T \left( \mathbf{H}_{12} \phi_0 + \mathbf{H}_{11} \phi_1 + \mathbf{H}_{14} \phi_2 \right) \\
 &\quad + \phi_2^T \left( \mathbf{H}_{42} \phi_0 + \mathbf{H}_{41} \phi_1 + \mathbf{H}_{44} \phi_2 \right) \\
 \mathbf{K}_{\approx}^{21} &= \phi_1^T \left( \mathbf{H}_{42} \phi_0 + \mathbf{H}_{41} \phi_1 + \mathbf{H}_{44} \phi_2 \right) + \phi_2^T \left( \mathbf{H}_{32} \phi_0 + \mathbf{H}_{31} \phi_1 + \mathbf{H}_{34} \phi_2 \right) \\
 \mathbf{K}_{\approx}^{22} &= \phi_1^T \left( \mathbf{H}_{44} \phi_1 + \mathbf{H}_{43} \phi_2 \right) + \phi_2^T \left( \mathbf{H}_{34} \phi_1 + \mathbf{H}_{33} \phi_2 \right)
 \end{aligned} \tag{eq. C-90}$$

The initial stress stiffness matrix  $\mathbf{K}_{\approx \sigma}$  is obtained by expanding  $\sigma: \delta \left( -\mathbf{D} \mathbf{D} + \frac{1}{2} \mathbf{L}^T \mathbf{L} \right)$ .

Arranging the results in the same form as given above yields

$$\begin{aligned}
 \mathbf{K}_{\approx \sigma}^{11} &= \phi_0^T \left( -\sigma_{33} \phi_0 \right) + \phi_1^T \left( -\sigma_{11} \phi_1 \right) + \phi_2^T \left( \frac{1}{2} \sigma_{22} - \frac{1}{2} \sigma_{11} \right) \phi_2 \\
 \mathbf{K}_{\approx \sigma}^{21} &= \phi_1^T \left( -\sigma_{12} \phi_1 \right) + \phi_1^T \left( \frac{1}{2} \sigma_{11} - \frac{1}{2} \sigma_{22} \right) \phi_2 + \phi_2^T \left( -\sigma_{12} \right) \phi_2 \\
 \mathbf{K}_{\approx \sigma}^{22} &= \phi_1^T \left( \frac{1}{2} \sigma_{11} - \frac{1}{2} \sigma_{22} \right) \phi_1 + \phi_2^T \left( -\sigma_{22} \right) \phi_2
 \end{aligned} \tag{eq. C-91}$$

In the coding of the element stiffness matrix in FALCON, the following notation is used:

$$\mathbf{K}_{\approx}^{ij} = \sum_{m=0}^2 \sum_{n=0}^2 \mathbf{H}_{mnij} \left( \phi_m^T \right) \left( \phi_n \right) \tag{eq. C-92}$$

The individual element matrices are merged into the total element system by an algebraic sum of the element matrices. The final system of equations is positive definite which is solved by Gaussian elimination. Because of the highly nonlinear character (the system is linearized within the time step) of these equations, they are iterated upon and are reformulated every time step and at every iteration. This procedure is described in Section 6.

## **C.4 References**

1. Drucker, D. C. and Prager, W., "Soil Mechanics and Plastic Analysis or Limit Design," Quarterly of Applied Mathematics 10, 1952, pp. 157-165.
2. Prager, W., "The Theory of Plasticity: A Survey of Recent Achievements," Proc. Inst. Mech. Eng. 169, 1955, p. 41.
3. Rashid, Y. R., Tang, H. T., Johansson, E. B., "Mathematical Treatment of Hot Pressing of Reactor Fuel," Nuclear Engineering and Design, Vol. 29, No. 1, November 1974.
4. Hagrman, D. L., "MATPRO - Version 11: A Handbook of Materials Properties for Use in the Analysis of Light Water Reactor Fuel Rod Behavior," NUREG/CR-0497 TREE-1280, February 1979.



# D

## APPENDIX D: NUMERICAL SCHEME FOR ANS-5.4 (MODIFIED) MODEL

The total cumulative release of stable fission gas during the time  $t$  is calculated as

$$R(t) = \int_0^t \beta(u) du - 6 \int_0^t \sum_{m=1}^{\infty} \frac{\exp[-m^2 \pi^2 z(u)]}{m^2 \pi^2} \beta(u) du = B(t) - A(t) \quad (\text{eq. D-1})$$

where

$R(t)$ : Total fission gas release during time  $t$  (mol)

$B(t)$ : Total fission gas produced

$A(t)$ : Total fission gas trapped within the fuel grain during time  $t$

$$z(u) = \tau(t) - \tau(u) \int_0^t D'(v) dv - \int_0^u D'(v) dv, \quad 0 \leq z \leq \tau(t)$$

Since the infinite series in the function  $A(t)$  converges uniformly, it may be integrated termwise and can be determined using a finite number of terms for a given accuracy.

Thus,

$$\begin{aligned} A(t) &= 6 \int_0^t \sum_{m=1}^M \frac{\exp(m^2 \pi^2 [\tau(u) - \tau(t)])}{m^2 \pi^2} \beta(u) du \\ &= 6 \sum_{m=1}^M \int_0^t \frac{\exp(m^2 \pi^2 [\tau(u) - \tau(t)])}{m^2 \pi^2} \beta(u) du \end{aligned} \quad (\text{eq. D-2})$$

This equation requires large computer storage for practical size problems. However, it is possible to simplify the history integral in eq. D-2 by evaluating it approximately from a recursion type formula, as is done in the following derivations. As a result, a much smaller storage in computer memory is needed to solve problems with a large number of elements and time steps.

Let

$$A(t_N) = 6 \sum_{m=1}^M H(m, N) \quad (\text{eq. D-3})$$

Appendix D: Numerical Scheme for ANS-5.4 (Modified) Model

where

$$H(m, N-1) = \sum_{m=1}^{N-1} \int_{t_0}^{t_{N-1}} \frac{\exp(m^2 \pi^2 [\tau(u) - \tau(t_{N-1})])}{m^2 \pi^2} \beta(u) du \quad (\text{eq. D-4})$$

Note the presence of  $\tau(t_{N-1})$ , then

$$H(m, N) = \exp[-m^2 \pi^2 \Delta\tau(t_N)] H(m, N-1) + \Delta H(m, N) \quad (\text{eq. D-5})$$

where

$$\Delta\tau(t_N) = \tau(t_N) - \tau(t_{N-1})$$

and

$$\Delta H(m, N) = \tilde{\beta}(N) \int_{t_{N-1}}^{t_N} \frac{\exp(m^2 \pi^2 [\tau(u) - \tau(t_N)])}{m^2 \pi^2} du \quad (\text{eq. D-6})$$

where

$$\tilde{\beta}(N) = \beta\left(\frac{t_N + t_{N-1}}{2}\right)$$

but

$$\tau(t_N) = \int_0^{t_N} D'(u) = \tau(t_{N-1}) + \int_{t_{N-1}}^{t_N} D'(u) du \quad (\text{eq. D-7})$$

Let

$$\tilde{D}' = D'\left(\frac{t_N + t_{N-1}}{2}\right) \text{ and } \Delta t_N = t_N - t_{N-1}$$

then

$$\tau(t_N) = \tau(t_{N-1}) + \tilde{D}' \Delta t_N$$

and

$$\Delta H(m, N) = \tilde{\beta}(N) \frac{[1 - \exp(-\lambda_m)]}{\lambda_m} \quad (\text{eq. D-8})$$



where

$$\lambda_m = m^2 \pi^2 \tilde{D}' \Delta t_N$$

Comparisons have been made of both numerical forms by using a one-dimensional fuel pin model problem to test the convergence and accuracy of the ANS-5.4 (Modified) form as compared to the original ANS-5.4 form. Calculations of total fraction gas release vs accumulated burnup are given in Figure D-1. The results indicate that the series in D-1 is fast convergent and the error introduced by using a small number of terms is small (4.5% for  $M = 3$  compared to 0.2% for  $M = 20$ ). Currently  $M = 8$ , giving an error less than 1%, is used in FALCON.

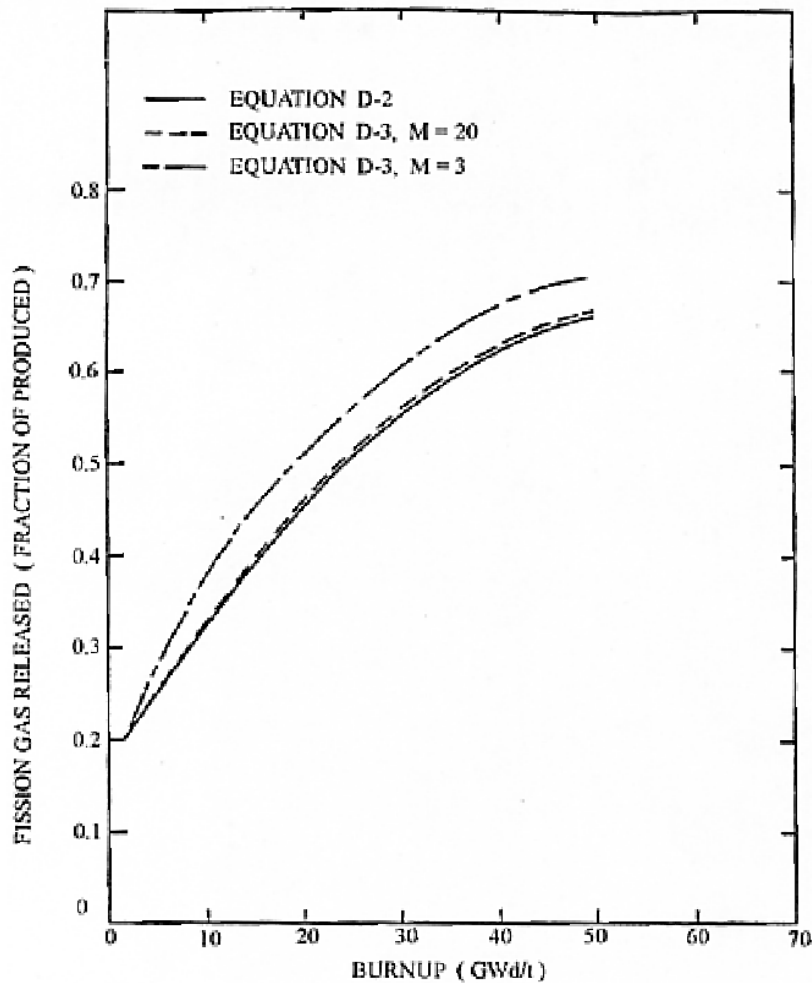


**Figure D-1**  
**Gas Release Predictions for Two Numerical Forms of the ANS-5.4 Model**



# E

## APPENDIX E: RADIAL POWER AND BURNUP DISTRIBUTION

---

The capture of resonance energy neutrons by  $^{238}\text{U}$  results in the production of plutonium isotopes in an LWR fuel pellet. The large value of the capture cross-section for  $^{238}\text{U}$  at resonance energies results in a preferential buildup of plutonium at the pellet surface. Experimental data on the plutonium distribution in an irradiated fuel pellet shows that the plutonium near the pellet outer edge is two to three times the centerline concentration. The result is a non-uniform fissile atom distribution across the pellet with the peak occurring at the pellet edge. Since the volumetric heat generation at any point within a fuel-pellet is proportional to the fissile atom concentration, the power generation is also non-uniform across the pellet. At low burnup, little plutonium buildup has occurred by  $^{238}\text{U}$  resonance energy neutron capture, and the power distribution is only slightly non-uniform. Edge-peaked power and burnup distributions begin to develop as burnup progresses. For high burnup fuel, the pellet edge region can have a normalized power factor above 3 and a local burnup more than two times the pellet average, depending on the initial  $^{235}\text{U}$  enrichment, pellet dimensions and neutron flux energy spectrum.

A fuel behavior code, such as FALCON, must consider the influence of a non-uniform power and burnup distribution on the fuel rod thermal, mechanical, and behavioral response during steady state and transient conditions. Several models have been developed to address the influence of burnup on the radial power and burnup distributions [1, 2, 3, 4]. Some of these models have also included the impact of burnable absorbers,  $^{155}\text{Gd}$  and  $^{158}\text{Gd}$  used to control fuel rod reactivity.

FALCON includes two models to calculate the radial power and burnup distributions as a function of pellet average burnup. The RADAR-G model was developed by BNFL and includes the treatment of  $\text{UO}_2$  and  $\text{UO}_2\text{-Gd}_2\text{O}_3$  fuel material in a PWR or BWR application [1, 2]. The TUBRNP model developed by Lassmann is also available. This model includes treatment for  $\text{UO}_2$ , MOX, and  $\text{UO}_2\text{-Gd}_2\text{O}_3$  material for PWR, BWR, and HWR conditions [4, 7, 8].

FALCON also allows for manual input of the radial power distribution via input. For this option, the radial power distribution is assumed constant throughout the analysis.

### E.1 RADAR-G Model

The RADAR-G model divides the fuel pellet into a number of concentric annuli for each of which it solves for the concentrations of uranium, plutonium, and gadolinium [1]. Contrary to the original RADAR model, the inverse diffusion length varies with radial position in the RADAR-G model due to the self-shielding of the absorption cross-section [2]. The diffusion equation for the thermal flux is solved using a finite difference method. The resulting thermal

Appendix E: Radial Power and Burnup Distribution

flux profile is multiplied by the concentration cross-sections and profiles of uranium and plutonium to give a radial rating profile which is normalized to unity.

The presence of gadolinia burnable poison requires that small burnup steps be used due to the rapid depletion of the gadolinium isotopes 155 and 157. In each annulus, the burnup of  $U^{235}$  during a burnup step is governed independently and incrementally by the equation

$$\Delta W_u = -W_u h_{235}(r) \Delta B_t \quad (\text{eq. E-1})$$

where

$W_u$ : Concentration of  $U^{235}$

$\Delta W_u$ : Variation of  $W_u$  during a time increment

$\Delta B_t$ : Variation of pellet burnup due to thermal fissions during a time increment (MWd/T) at position  $r$

and  $h_{235}$  is defined as

$$h_{235}(r) = \sigma_{235}(r) \phi / R \quad (\text{eq. E-2})$$

where

$\sigma_{235}$ : Absorption cross-section for  $U^{235}$  (barns)

$\phi$ : Relative thermal flux

and  $R$  is the relative specific rating which is given by

$$R = \frac{\phi N_{\text{mol}}}{e_0} (\sigma_{f235}(r) W_u + \sigma_{f239}(r) W_p) E \quad (\text{eq. E-3})$$

where

$N_{\text{mol}}$ : Molecular number density ( $1/\text{cm}^3$ )

$e_0$ : Theoretical density of  $\text{UO}_2$  ( $\text{g}/\text{cm}^3$ )

$\sigma_{f235}$ : Fission cross-section for  $U^{235}$  (barns)

$\sigma_{f239}$ : Fission cross-section for  $\text{Pu}^{239}$  (barns)

$E$ : Energy liberated per fission (joule)

The equations governing the plutonium concentration are more complicated than for uranium because, in addition to burnout, two production mechanisms relevant to  $U^{238}$  beta decay and  $U^{238}$  absorption spectrum resonance, respectively, are also considered. Allowing for burnout, the plutonium concentration is then given by

$$\Delta W_p = -W_p h_{239}(r) \Delta B_t + \Delta W_{p_{dec}} + \Delta W_{p_{res}} \quad (\text{eq. E-4})$$

where

$W_p$ : Concentration of  $\text{Pu}^{239}$

$\Delta W_p$ : Variation of  $W_p$  during a time increment

$\Delta W_{p_{dec}}$ : Production of  $W_p$  due to  $\text{U}^{238}$  beta decay during a time increment

$\Delta W_{p_{res}}$ : Production of  $W_p$  due to  $\text{U}^{238}$  absorption spectrum resonance during a time increment

and  $h_{239}$  is defined as

$$h_{239} = \sigma_{239}(r) \phi / R \quad (\text{eq. E-5})$$

where

$\sigma_{239}$ : Absorption cross-section for  $\text{Pu}^{239}$  (barns)

First, thermal neutrons are captured by  $\text{U}^{238}$  nuclei which subsequently decay via two short half-life beta decays to  $\text{Pu}^{239}$ , whose production rate is proportional to the thermal flux and the  $\text{U}^{238}$  thermal capture cross-section and is calculated as

$$\Delta W_{p_{dec}} = \frac{\sigma_{238}}{\sigma_{239}(r)} h_{239}(r) \Delta B_t \quad (\text{eq. E-6})$$

where

$\sigma_{238}$ : Thermal capture cross-section for  $\text{U}^{238}$  (barns)

Second, the  $\text{U}^{238}$  absorption spectrum contains large resonant peaks in the epithermal energy region, giving rise to enhanced plutonium production near the surface of the fuel pellet. For a given burnup step, the total amount produced across the whole pellet is given by

$$\Delta W_{p_{tot}} = (1 - p) F_L \Delta B_{ass} \nu \frac{86400 \times 238}{E \times 6.02 \times 10^{23}} \quad (\text{eq. E-7})$$

where

$W_{p_{tot}}$ : Total amount of plutonium production across the whole fuel pellet due to  $\text{U}^{238}$  resonance during a time increment

$p$ : Resonance escape probability

$F_L$ : Fast leakage factor

$\nu$ : Average number of fast neutrons liberated per fission

Appendix E: Radial Power and Burnup Distribution

$\Delta B_{\text{ass}}$ : Assembly burnup due to total fissions

The RADAR-G model distributes this plutonium among the various fuel annuli according to a very steep inverse exponential function

$$\Delta W_{\text{p}_{\text{res}}} = 1 + 3 \exp(-9.7 \sqrt{r_2 - r}) \quad (\text{eq. E-8})$$

and subject to the normalization condition

$$\sum (\Delta W_{\text{p}_{\text{res}}} \cdot V) = \Delta W_{\text{p}_{\text{tot}}} \quad (\text{eq. E-9})$$

where

$r$ : Mean radius of an annulus (cm)

$r_2$ : Pellet outer radius (cm)

$V$ : Volume of an annulus (cm<sup>3</sup>)

Two isotopes of gadolinium are of importance to the absorber performance of gadolinia fuel rods. Gd-155 and Gd-157 are the dominant isotopes in gadolinia for neutron absorption. Therefore, RADAR-G contains the necessary equations to account for both Gd-155 and Gd-157. The governing equations for the depletion of Gd-155 and Gd-157 are:

$$\begin{aligned} \frac{dW_{155}(r)}{dt} &= -\sigma_{155}(r) \phi(r) W_{155}(r) \\ \frac{dW_{157}(r)}{dt} &= -\sigma_{157}(r) \phi(r) W_{157}(r) \end{aligned} \quad (\text{eq. E-10})$$

where

$W_{155}, W_{157}$ : Weight fractions of Gd-155 and Gd-157

$\sigma_{155}, \sigma_{157}$ : Self-shielded thermal absorption cross-sections

$\phi$ : Relative thermal flux

The depletion of Gd-155 and Gd-157 occurs rapidly as compared to the  $U_{235}$  and  $Pu_{238}$  absorptions. As a result, finite difference representation of the Gd-155 and Gd-157 depletion equations will not adequately model the gadolinia irradiation response. The full solution of the depletion equations were used in RADAR-G to compensate for this effect. For Gd-155, the equation is:

$$W_{155}(t + \Delta t) = W_{155}(t) \exp(-h_{155}(r) \Delta B_t) \quad (\text{eq. E-11})$$

where

$W_{155}$ : Concentration of Gd<sup>155</sup>

$\Delta t$ : Time interval

and  $h_{155}$  is defined as

$$h_{155} = \sigma_{155}(r) \phi / R$$

The equation is the same for  $Gd^{157}$  with  $\sigma_{155}$  replaced with  $\sigma_{157}$ .

The RADAR-G model has thus calculated concentration profiles for the two fissionable atoms and the gadolinium isotopes. By using these concentrations together with simple diffusion theory, the thermal neutron inverse diffusion length for each annulus is determined according to

$$\alpha = 3/(\lambda_{tr} \lambda_{abs})^{1/2} \quad (\text{eq. E-12})$$

where

$\alpha$ : Thermal neutron inverse diffusion length (1/cm)

$\lambda_{tr}$ : Transport mean free path (cm)

$\lambda_{abs}$ : Absorption mean free path (cm)

For large atomic weights,  $\lambda_{tr}$  is well approximated by

$$\frac{1}{\lambda_{tr}} = N_{mol} (\bar{\sigma}_s)_{heavy} + 2 N_{mol} (\bar{\sigma}_s)_{oxygen} \quad (\text{eq. E-13})$$

where

$(\bar{\sigma}_s)_{heavy}$ : Scattering cross section for uranium and plutonium (barns)

$(\bar{\sigma}_s)_{oxygen}$ : Scattering cross section for oxygen (barns)

Likewise,  $\lambda_{abs}$  is the reciprocal of the macroscopic absorption cross section

$$\begin{aligned} \frac{1}{\lambda_{abs}} = & 2.1 N_{mol} (\bar{\sigma}_{235} W_u + \bar{\sigma}_{239} W_p + \bar{\sigma}_{238} (1 - W_u - W_p)) \\ & + \text{MULT} (\sigma_a^{155} W_{155} + \sigma_{157} W_{157}) \end{aligned} \quad (\text{eq. E-14})$$

where

MULT: An empirical factor which varies with initial gadolinium content to account for the poor approximation of diffusion theory in a highly absorbing pellet

Combining equations E-12, E-13, and E-14 gives

Appendix E: Radial Power and Burnup Distribution

$$\alpha = (17.6 W_u + 26.6 W_p + 0.069 + \text{MULT}(\sigma_{155} W_{155} + \sigma_{157} W_{157}))^{1/2} \quad (\text{eq. E-15})$$

In the case of an unpoisoned pellet, or a gadolinia pellet where the  $\text{Gd}^{155}$  and  $\text{Gd}^{157}$  isotopes are depleted, eq. E-15 is identical to that used in the original RADAR routine.

The solution to the neutron flux diffusion equation is calculated using a simple finite difference method. Each annuli of the RADAR-G mesh is subdivided into four fine mesh intervals to minimize computational errors. This method differs from that used by the original RADAR model due to the spatial dependence of  $\alpha$ . The fine mesh flux solutions are used to determine the flux at the midpoint of the coarse mesh. The boundary conditions are:

$$\phi \Big|_{r=r_0} = 1; \quad \frac{d\phi}{dr} \Big|_{r=r_0} = 0 \quad (\text{eq. E-16})$$

where  $r_0$  is the radius of the central void for a hollow pellet or set equal to 0 for a solid pellet.

The finite difference representation at the innermost annulus is

$$\phi_1 = \phi_0 \left[ I_0(\alpha_1 r) + \frac{I_1(\alpha_1 r_0)}{K_1(\alpha_1 r_0)} K_0(\alpha_1 r) \right] \quad (\text{eq. E-17})$$

where

- $\phi_0$ : Flux in first mesh interval
- $\phi_1$ : Flux in second interval corresponding to a radius  $r$
- $\alpha_1$ : Inverse diffusion length for the first mesh
- $I_0$ : Modified Bessel function of the first kind of order 0
- $I_1$ : Modified Bessel function of the first kind of order 1
- $K_0$ : Modified Bessel function of the second kind of order 0
- $K_1$ : Modified Bessel function of the second kind of order 1
- $r_0$ : Inner fuel radius (cm)

This method is used at each mesh interval to compute the flux throughout the pellet. This method implicitly accommodates both hollow and duplex pellets.

The final radial power rating profile is then represented by the thermal flux profile and the above calculated uranium and plutonium concentration profiles which are further weighted by their own fission cross-section.

$$R = \phi(\bar{\sigma}_{f_{235}}(r) W_u + \bar{\sigma}_{f_{239}}(r) W_p) N_{\text{mol}} \quad (\text{eq. E-18})$$



where R is the radial rating factor which is again normalized to unity for the whole pellet.

Empirical relationships are required to account for the self-shielding effects on the cross-sections as a result of gadolinium absorption. The equations used in RADAR-G are a function of the integrated number density of  $Gd^{155}$  and  $Gd^{157}$  from the outside of the pellet. The equations expressed in terms of the fitting parameters are:

$$\sigma_{155}(r) = \sigma_{155}^{\circ} (1 - \beta_1) \{ \beta_2 \exp(-\gamma_1 I(r)) + (1 - \beta_2) \exp(-\gamma_2 I(r)) \} + \beta_1 \sigma_{155}^{\circ} \quad (\text{eq. E-19})$$

with

$$I(r) = \int_0^r (W_{155}(r) + 4.3 W_{155}(r)) r \, dr \quad (\text{eq. E-20})$$

and

$$\sigma_{157}(r) = 4.3 \sigma_{155}(r)$$

where

$$\sigma_{155}^{\circ}, \beta_1,$$

$\beta_2, \gamma_1, \gamma_2$ : Fitting parameters

$r_2$ : Outer pellet radius (cm)

The assumption is made in RADAR-G that the  $Gd^{157}$  absorption cross-section is 4.3 times larger than the  $Gd^{155}$  cross-section.

The absorption and fission cross-sections for  $U^{235}$  and  $Pu^{239}$  are also influenced by the self-shielding effects of gadolinium. The empirical equation for the relationship of the  $U^{235}$  and gadolinium content is

$$\sigma_{235}(r) = \sigma_{235}^{\circ} (1 - \beta_3) \exp(-\gamma_3 I(r)) + \beta_3 \sigma_{235}^{\circ} \quad (\text{eq. E-21})$$

where

$\beta_3, \gamma_3$ : Fitting parameters

$\sigma_{235}^{\circ}$ : Constant absorption cross-section for  $U^{235}$

The additional cross-sections are given by

$$\begin{aligned} \sigma_{f235}(r) &= \sigma_{235}(r) \times \sigma_{f235}^{\circ} / \sigma_{235}^{\circ} \\ \sigma_{239}(r) &= \sigma_{235}(r) \times \sigma_{239}^{\circ} / \sigma_{235}^{\circ} \\ \sigma_{f239}(r) &= \sigma_{235}(r) \times \sigma_{f239}^{\circ} / \sigma_{235}^{\circ} \end{aligned} \quad (\text{eq. E-22})$$

Appendix E: Radial Power and Burnup Distribution

The fitting parameters used in equations E-19, E-20 and E-21 were determined by using the WIMS-E code [3]. WIMS-E was used to conduct a multigroup transport calculation at zero burnup to determine the radial variation of the gadolinium and  $U^{235}$  effective cross-sections as functions of initial gadolinium concentration. As a result, the fitting parameters are functions of initial gadolinium content and the pellet outer radius. Some spectral dependence was also found necessitating a different set of parameters for PWR and BWR pellets. The fitting parameters for a PWR fuel rod are:

$$\begin{aligned}
 \beta_1 &= 0.039 / (r_2 \times G^{0.67}) \\
 \beta_2 &= 0.032 + 0.043 G \\
 \beta_3 &= 0.61 - 0.009 G - 0.1(r_2 - 0.412) \\
 \gamma_1 &= 10200 / (r_2 \times G^{0.90}) \\
 \gamma_2 &= (3550 - 275 G) \times 0.17 / r_2^2 \\
 \gamma_3 &= 2500 / (r_2 \times G^{0.50})
 \end{aligned}
 \tag{eq. E-23}$$

where

- G: Initial gadolinia concentration (wt %)  
 $r_2$ : Pellet outer radius (cm)

The corresponding equations for a BWR fuel rod are:

$$\begin{aligned}
 \beta_1 &= (0.05 - 0.005 G) \times 0.574 / r_2 \\
 \beta_2 &= 0.5 \\
 \beta_3 &= 0.478 - 0.015 G - 0.1(r_2 - 0.574) \\
 \gamma_1 &= (340 - 265 G) / r_2 \\
 \gamma_2 &= (790 - 66 G) / r_2^2 \\
 \gamma_3 &= (1800 - 187 G) / r_2
 \end{aligned}
 \tag{eq. E-24}$$

In the case of duplex fuel designs, G is taken to be the initial gadolinia concentration in the outer region of the pellet.

The empirical parameters  $\sigma_{155}^\circ$  and MULT were determined by comparing radial power profiles from WIMS-E and RADAR-G.  $\sigma_{155}^\circ$  determines the rate at which the  $Gd^{155}$  and  $Gd^{157}$  isotopes burn out. MULT affects the thermal flux depression in the pellet. Both of these parameters were

found to be independent of irradiation and geometry and depend only on the initial gadolinia concentration. The relationships are:

$$\begin{aligned}\sigma_{235}^{\circ} &= \begin{cases} 9640(1.707 - 0.078 G) \\ 9640(0.900 - 0.050 G) \end{cases} \begin{matrix} PWR \\ BWR \end{matrix} \\ MULT &= \begin{cases} 3.53 \\ 0.44 + 0.22 G \end{cases} \begin{matrix} PWR \\ BWR \end{matrix}\end{aligned}\quad (\text{eq. E-25})$$

Typical values for the physical parameters input to the RADAR-G model are listed as follows:

$$\begin{aligned}\bar{\sigma}_{235} &= 547 \text{ barns} \\ \bar{\sigma}_{238} &= 2.14 \text{ barns} \\ \bar{\sigma}_{239} &= 822 \text{ barns} \\ \bar{\sigma}_{f235} &= 455 \text{ barns} \\ \bar{\sigma}_{f239} &= 584 \text{ barns} \\ (\bar{\sigma}_s)_{\text{heavy}} &= 10 \text{ barns} \\ (\bar{\sigma}_s)_{\text{oxygen}} &= 4 \text{ barns} \\ E &= 200 \text{ MeV} \\ K_1 &: \text{ Modified Bessel function of the second kind of order 1} \\ e_0 &= 10.96 \text{ g/cm}^3 \\ N_{\text{mol}} &= 2.445 \times 10^{22} \text{ 1/m}^3 \\ \nu &= 2.44 \text{ 1/fission}\end{aligned}$$

The range of application for the RADAR-G model in the presence of gadolinia absorbers is as follows:

PWR: 2 to 10 w/o gadolinia

BWR: 2 to 6 w/o gadolinia

## E.2 TRANSURANUS Burnup Model (TUBRNP)

Lassman, et al., have developed the TUBRNP model to calculate the radial power density distribution and the radial burnup distribution for LWR fuel rods [4]. The TUBRNP model represents an extension of the RADAR model developed by Palmer [2]. An important disadvantage of the RADAR-G model is that it only considers the formation of  $^{239}\text{Pu}$  by  $^{238}\text{U}$  decay and neutron resonance absorption. Experience has shown that considering only  $^{239}\text{Pu}$  formation underestimates the role of plutonium on the power and burnup distribution above pellet average burnups of 40 GWd/MTU [4]. At these burnup levels, the  $^{239}\text{Pu}$  isotope accounts for less than 60% of the total plutonium concentration.

The approach used in TUBRNP is based on the concept of one neutron group, spectrum-average cross-sections, similar to isotopic concentration codes such as ORIGEN and KORIGEN [5, 6]. Using this approach, the average concentrations in the fuel are given by:

$$\frac{d\bar{N}_{235}}{dt} = -\sigma_{a,235} \bar{N}_{235} \phi \quad (\text{eq. E-26a})$$

$$\frac{d\bar{N}_{238}}{dt} = -\sigma_{a,238} \bar{N}_{238} \phi \quad (\text{eq. E-26b})$$

$$\frac{d\bar{N}_j}{dt} = -\sigma_{a,j} \bar{N}_j \phi + \sigma_{c,j-1} N_{j-1} \phi \quad (\text{eq. E-26c})$$

where  $\bar{N}$  is the number of atoms per unit volume,  $\sigma_a$  is the absorption cross-section,  $\sigma_c$  is the capture cross-section,  $\phi$  is the neutron flux, and  $j$  represents the isotopes  $^{239}\text{Pu}$ ,  $^{240}\text{Pu}$ ,  $^{241}\text{Pu}$ ,  $^{242}\text{Pu}$ . By relating the increment in fluence  $\phi\Delta t$  to a burnup increment  $\Delta bu$ , it is possible to rewrite eq. E-26 as

$$\frac{d\bar{N}_{235}}{d\text{Bu}} = -\sigma_{a,235} \bar{N}_{235} A \quad (\text{eq. E-27a})$$

$$\frac{d\bar{N}_{238}}{d\text{Bu}} = -\sigma_{a,238} \bar{N}_{238} A \quad (\text{eq. E-27b})$$

$$\frac{d\bar{N}_j}{d\text{Bu}} = -\sigma_{a,j} \bar{N}_j A + \sigma_{c,j-1} N_{j-1} A \quad (\text{eq. E-27c})$$

where

$$A = 0.8815 \frac{\rho_{\text{fuel}}}{\alpha \sum_k \sigma_{f,k} \bar{N}_k}$$

$$\alpha = 3.8 \times 10^{-6}$$

The quantity  $\sum_k \sigma_{f,k} \bar{N}_k$  represents the number of fissions per unit volume per unit time. In the development of eq. E-28, it is assumed that the fuel is  $\text{UO}_2$  and that the burnup is given in MWd per ton of heavy metal (MWd/tU). The cross-sections used in eq. E-27 are considered the spectrum-average effective cross-sections valid for a specific reactor type. A summary of the cross-sections used in TUBRNP are shown in Table E-1.

**Table E-1**  
**Spectrum Average Cross-Sections Used in TUBRNP (in Barns)**

Light Water Reactor (BWR and PWR)								
	$^{235}\text{U}$	$^{238}\text{U}$	$^{239}\text{Pu}$	$^{240}\text{Pu}$	$^{241}\text{Pu}$	$^{242}\text{Pu}$	$^{155}\text{Gd}$	$^{157}\text{Gd}$
Fission	41.95	0	105	0.584	120	0.458	-	-
Capture	9.7	0.78	58.6	100	50	80	490	1267
Absorption (Thermal)	359.68	1.56	1207.5	193.5	1095.2	11.11	19800	85000

Heavy Water Reactor								
	$^{242}\text{U}$	$^{242}\text{Pu}$	$^{239}\text{Pu}$	$^{240}\text{Pu}$	$^{241}\text{Pu}$	$^{242}\text{Pu}$	Gd	Gd
Fission	107.95	0	239.18	0.304	296.95	0.191	-	-
Capture	22.3	1.16	125.36	127.26	122.41	91.3	1471	3800
Absorption (Thermal)	395.59	1.7	1095.7	202.2	1113.7	11.98	23924	102477

Equations E-26 and E-27 are formulated as an average balance in the fuel. The local concentrations can be obtained using the following:

$$\frac{d N_{235}(r)}{d bu} = -\sigma_{a,235} N_{235}(r) A \quad (\text{eq. E-28a})$$

$$\frac{d N_{238}(r)}{d bu} = -\sigma_{a,238} \bar{N}_{238} f(r) A \quad (\text{eq. E-28b})$$

$$\frac{d N_{239}(r)}{d bu} = -\sigma_{a,239} N_{239}(r) A + \sigma_{c,238} \bar{N}_{238} f(r) A \quad (\text{eq. E-28c})$$

$$\frac{d N_j(r)}{d bu} = -\sigma_{a,j} N_j(r) A + \sigma_{c,j-1} N_{j-1}(r) A \quad (\text{eq. E-28d})$$

Appendix E: Radial Power and Burnup Distribution

where for eq. E-28d,  $j$  represents the isotopes  $^{240}\text{Pu}$ ,  $^{241}\text{Pu}$ , and  $^{242}\text{Pu}$ . For the isotope  $^{238}\text{U}$ ,  $N(r)$  is written as  $\bar{N}_{238}$ , where  $f(r)$  is a radial shape function which is normalized to a volume-average value of unity, i.e.,

$$\frac{\int_{A_p} f(r) dA}{\int_{A_r} dA} = 1 \quad (\text{eq. E-29})$$

where  $A_p$  is the area of the fuel pellet. The shape function  $f(r)$  accounts for the spatial variation of  $^{238}\text{U}$  neutron absorption. The form of the distribution function  $f(r)$  is given by

$$f(r) = 1 + p_1 \exp(-p_2(r_0 - r)^{p_3}) \quad (\text{eq. E-30})$$

where  $p_1$ ,  $p_2$ , and  $p_3$  are model constants,  $r_0$  is the pellet outer radius and  $r$  is the location of interest in the pellet. The distribution function can be considered to consist of two terms: a constant production term for  $^{239}\text{Pu}$  by thermal neutron capture, and a highly nonlinear term for the production of  $^{239}\text{Pu}$  by resonance absorption. The model parameters have been developed by an extensive comparison with measurements of radial plutonium distribution. The distribution function shown in eq. E-30 represents an improvement over the function used in the RADAR-G model (eq. E-8).

TUBRNP solves for the neutron flux distribution  $\phi(r)$  within the fuel pellet using a one-neutron group one-dimensional diffusion theory applied to a cylindrical geometry. The resulting solution of the one-dimensional neutron flux diffusion equation is:

$$\phi(r) = C_1 I_0(\kappa r) \text{ for a solid pellet} \quad (\text{eq. E-31})$$

$$\phi(r) = C_1 \left( I_0(\kappa r) + \left[ \frac{I_1(\kappa r_0)}{K_1(\kappa r_0)} \right] K_0(\kappa r) \right) \text{ for a hollow pellet} \quad (\text{eq. E-32})$$

where

$I$  and  $K$ : Modified Bessel functions

$C$ : An integration constant

$\kappa$ : The inverse diffusion length given by

$$\kappa = \sqrt{\frac{\epsilon_{a,tot}}{D}} \quad (\text{eq. E-33})$$

where

$$\varepsilon_{a,tot} = \sum_i \sigma_{a,i} \bar{N}_i$$

$$D = \frac{1}{3 \sigma_s} \bar{N}_{tot}$$

$\bar{N}_{tot}$ : Pellet average atom concentration of all U and Pu isotopes

$\bar{N}_i$ : Pellet average atom concentration for each U or Pu isotope  $i$

Once the neutron flux distribution given by equations E-31 and E-32 is obtained, TUBRNP calculates the power density distribution,  $q'''(r)$  using the following

$$q'''(r) = C_2 \sum_i \sigma_{f,i} N_i(r) \phi(r) \quad (\text{eq. E-34})$$

where

$C_2$ : Conversion factor

$N_i(r)$ : Concentration distribution for isotope  $i$

$\sigma_{f,i}$ : Fission cross-section for isotope  $i$

The equations described above are solved incrementally at each time step or burnup increment. First, the power density distribution is obtained from which the radial burnup profile is calculated. Finally, the U and Pu isotopic concentrations are derived from the coupled differential equations. The radial nodalization scheme used in TUBRNP is specified by the user and is independent of the finite element grid used for the thermal and mechanical solutions.

In addition to the LWR  $\text{UO}_2$  fuel application described above, the TUBRNP model used in FALCON also includes capabilities to calculate the radial power and burnup distributions for heavy water moderated reactors (HWRs) and for gadolinia-doped fuel pellets [7, 8]. The HWR and gadolinia capabilities are extensions to the LWR version of the TUBRNP model. The basic approach is the same for these applications except for changes addressing the difference in the neutron flux energy spectrum. For the HWR model, the one-neutron group, spectrum-averaged cross-sections for neutron absorption and capture were developed based on the Halden HWR neutron spectrum. In the Halden reactor, the thermal flux is higher and the fast flux is lower than in a typical LWR [7]. Using the OECD/NEA JEF2.2 cross-section libraries, the spectrum average cross-sections shown in Table E-1 were obtained for TUBRNP. Further, the distribution function shown in eq. E-30 is modified to consider the lower neutron capture in the epithermal energy spectrum, i.e.,

$$p_1^{\text{HWR}} = 0.64 p_1^{\text{LWR}} \quad (\text{eq. E-35})$$

The TUBRNP model for HWR applications has been validated using the radial distribution of Pu and Nd concentrations obtained from electron probe microanalysis (EPMA) on fuel pellets

Appendix E: Radial Power and Burnup Distribution

irradiated in the DR3 and Halden heavy water reactors. The specimen burnup values ranged from 20 to 70 GWd/MTU [7]. Excellent agreement is observed between the TUBRNP model and the EPMA measurements.

As discussed in the RADAR-G section, the primary isotopes of concern for  $\text{UO}_2$  with gadolinia additives are  $^{155}\text{Gd}$  and  $^{157}\text{Gd}$  because of the high neutron absorption cross-sections for these two isotopes. The approach used to describe the neutron absorption of  $^{155}\text{Gd}$  and  $^{157}\text{Gd}$  is the same as for the U and Pu isotopes, i.e.,

$$\frac{d N_{155}}{d bu} = -\sigma_{a,155} N_{155}(r) A \quad (\text{eq. E-36})$$

where  $N_{155}(r)$  is the local concentration and  $\sigma_{a,155}$  is the spectrum averaged absorption cross-section for  $^{155}\text{Gd}$ . The same equation is written for  $^{157}\text{Gd}$ .

The high neutron absorption cross-sections of  $^{155}\text{Gd}$  and  $^{157}\text{Gd}$  at thermal neutron energies ( $<1$  eV) result in a significant spatial self-shielding across the pellet and a local shift of the neutron spectrum for the thermal flux. These effects complicate the approach used to define the effective absorption cross-section that is used in the TUBRNP methods. Whereas for non-gadolinia fuel, the inverse diffusion length ( $\kappa$ ) is a pellet average value; this parameter is considered to vary across the pellet for gadolinia fuel. The resulting one-group neutron diffusion equation is written as:

$$\nabla^2 \phi - \kappa(r) \phi = 0 \quad (\text{eq. E-37})$$

In TUBRNP, eq. E-37 is solved using a numerical approach as opposed to the exact solution given in equations E-31 and E-32 for non-gadolinia fuel.

The spatial variation of the inverse diffusion length ( $\kappa$ ) was determined using measurements for the average  $^{155}\text{Gd}$  and  $^{157}\text{Gd}$  concentrations as a function of burnup developed by Fuje, et al., [9]. Further, comparison of the radial  $^{155}\text{Gd}$  and  $^{157}\text{Gd}$  distributions calculated by TUBRNP with measurements and integral neutron transport codes show good agreement [8], verifying the predictive capabilities of the model.

For more information on the TUBRNP model, please refer to References 4, 7, and 8 by Lassman, et al.



### E.3 References

1. Thomas, G. M. and Hesketh, K. W., "RADAR-G - A Routine for Calculating Radial Power Profiles in Thermal Reactor Fuel," BNFL, EPRI Contract 18362, November 1986.
2. Palmer, I. D., et al., "A Model for Predicting the Radial Power Profile in a Fuel Pin," IAEA Specialists Meeting on Water Reactor Fuel Element Performance Computer Modeling, Preston, March 14-19, 1982.
3. Askew, J. R. and Roth, M. J., "WIMS-E - A Scheme for Neutronics Calculations," AEEW-R1315, January 1982.
4. Lassmann, K., O'Carroll, C., van de Laar, J., Walter, C.T., "The Radial Distribution of Plutonium in High Burnup  $\text{UO}_2$  Fuel," *J. Nuc. Mat.* 208, 1994, pp. 223-231.
5. Bell, M.J., "ORIGEN: The ORNG Isotope Generation and Depletion Code," ORNL Report, ORNL-4628, 1973.
6. Fisher, U., Wiese, H.W., Kernforschungszentrum Karlsruhe Report, KfK-3014, 1983.
7. Lassmann, K., Walter, C.T., van de Laar, J., "Extension of the TRANSURANUS Burnup Model to Heavy Water Reactor Conditions," *J. Nuc. Mat.* 255, 1998, pp. 222-233.
8. Lassmann, K., Schubert, A., van de Laar, J., Vennix, C., "Recent Development of the TRANSURANUS Code with Emphasis on High Burnup Phenomena," Proceedings of a Technical Committee Meeting on Nuclear Fuel Behavior Modeling at High Burnup and Its Experimental Support, Windermere, U.K., IAEA-TECDOC-1233, June 2000.
9. Fuje, A., et al., "Benchmark Experiments on Poisoned Fuel Rods with High Concentration Gadolinia in BWR-Type Assembly," Topical Meeting on Advances in Fuel Management, American Nuclear Society, Pinehurst, North Carolina, March 1986.



# F

## APPENDIX F: EQUATION OF STATE

---

The coolant enthalpy model consists of four unknowns: velocity,  $V$ ; enthalpy,  $h$ ; density,  $\rho$ ; and temperature,  $T$ . The continuity and energy equations provide solutions for  $V$  and  $h$ . Two additional equations are required to determine  $\rho$  and  $T$ . These equations are obtained from the fundamental fluid properties and are called the equations of state. The equations of state used in FALCON are:

$$\rho = \rho(p, h) \quad (\text{eq. F-1})$$

$$T = T(p, h) \quad (\text{eq. F-2})$$

where the independent variables are pressure and enthalpy. Equations F-1 and F-2 provide the closure relationships necessary for the coolant enthalpy model.

FALCON considers two different coolant media as part of the coolant enthalpy model. For standard LWR applications, water is the primary coolant. For special experiments, FALCON includes a sodium option. The properties for each of these coolant types is provided below.

### F.1 Water Properties

FALCON uses the EPRI water properties functions from RETRAN-02 [1]. FALCON utilizes explicit approximating expressions for: (1) temperature and specific volume as functions of pressure and specific enthalpy, (2) saturated liquid enthalpy and saturated vapor enthalpy as functions of pressure, (3) thermal conductivity and dynamic viscosity as functions of temperature and density, and (4) specific heat capacity as functions of pressure and specific enthalpy. The expressions for temperature, specific volume, and specific heat capacity are valid in the range of pressures from 0.1 to 6000 psia and specific enthalpies from approximately 200 to 1750 Btu/lbm. The functions should not be used outside this range. The average errors in the expressions for temperature and specific volume are approximately 0.15% and 0.4%, respectively. The expressions for the saturated liquid and vapor specific enthalpies are valid in the range from 0.1 psia to the critical pressure (3208.2 psia). The saturation values are generally within 0.04% of the 1967 ASME values, but the errors approach 1% in the vicinity of the critical point.

#### ***F.1.1 Saturated Liquid and Saturated Vapor Enthalpies as Functions of Pressure***

The specific enthalpy of saturated liquid,  $h_f$ , or saturated vapor,  $h_g$ , may be expressed solely as a function of pressure,  $p$ . The relationships may be adequately approximated throughout the range

Appendix F: Equation of State

of pressures from 0.1 psia to the critical pressure of 3208.2 psia ( $p_{\text{CRIT}}$ ) by the following functions:

$$h_f = \begin{cases} \sum_{i=0}^8 CF1_i (\ln(p))^i & \text{if } 0.1 \text{ psia} \leq p \leq 950 \text{ psia} & \text{(eq. F - 3)} \\ \sum_{i=0}^8 CF2_i (\ln(p))^i & \text{if } 850 \text{ psia} \leq p \leq 2550 \text{ psia} & \text{(eq. F - 4)} \\ \sum_{i=0}^8 CF3_i ((p_{\text{CRIT}} - p)^{0.41})^i & \text{if } 2350 \text{ psia} \leq p \leq p_{\text{CRIT}} & \text{(eq. F - 5)} \end{cases}$$

and

$$h_g = \begin{cases} \sum_{i=0}^{11} CG1_i (\ln(p))^i & \text{if } 0.1 \text{ psia} \leq p \leq 1500 \text{ psia} & \text{(eq. F - 6)} \\ \sum_{i=0}^8 CG2_i (\ln(p))^i & \text{if } 1100 \text{ psia} \leq p \leq 2650 \text{ psia} & \text{(eq. F - 7)} \\ \sum_{i=0}^6 CG3_i ((p_{\text{CRIT}} - p)^{0.41})^i & \text{if } 2550 \text{ psia} \leq p \leq p_{\text{CRIT}} & \text{(eq. F - 8)} \end{cases}$$

The constant coefficients,  $CFn_i$  and  $CGn_i$ , in equations F-3 through F-8 are listed in Table F-1. The resulting specific enthalpy is in units of Btu/lbm. Note that the subintervals overlap. Within each region, either of the two corresponding expressions yields a good approximation. In FALCON, the transitions for  $h_f$  are 950 psia for equations F-3 to F-4, 2550 psia for equations F-4 to F-5, 1100 psia for equations F-6 to F-7, and 2650 psia for equations F-7 to F-8.

**Table F-1**  
**Constants for Saturated Liquid and Vapor Enthalpies as Functions of Pressure**

i	CF1 <sub>i</sub>	CF2 <sub>i</sub>	CF3 <sub>i</sub>
0	0.6970887859 x 10 <sup>-2</sup>	0.8408618802 x 10 <sup>6</sup>	0.9060030436 x 10 <sup>3</sup>
1	0.3337529994 x 10 <sup>2</sup>	0.3637413208 x 10 <sup>6</sup>	-0.1426813520 x 10 <sup>2</sup>
2	0.2318240735 x 10 <sup>1</sup>	-0.4634506669 x 10 <sup>6</sup>	0.1522233257 x 10 <sup>1</sup>
3	0.1840599513	0.1130306339 x 10 <sup>6</sup>	-0.6973992961
4	-0.5245502284 x 10 <sup>-2</sup>	-0.4350217298 x 10 <sup>3</sup>	0.1743091663
5	0.2878007027 x 10 <sup>-2</sup>	-0.3898988188 x 10 <sup>4</sup>	-0.2319717696 x 10 <sup>-1</sup>
6	0.1753652324 x 10 <sup>-2</sup>	0.6697399434 x 10 <sup>3</sup>	0.1694019149 x 10 <sup>-2</sup>
7	-0.4334859620 x 10 <sup>-3</sup>	-0.4730726377 x 10 <sup>2</sup>	-0.6454771710 x 10 <sup>-4</sup>
8	0.3325699282 x 10 <sup>-4</sup>	0.1265125057 x 10 <sup>1</sup>	0.1003003098 x 10 <sup>-5</sup>

i	CG1 <sub>i</sub>	CG2 <sub>i</sub>	CG3 <sub>i</sub>
0	0.1105836875 x 10 <sup>4</sup>	-0.2234264997 x 10 <sup>7</sup>	0.9059978254 x 10 <sup>3</sup>
1	0.1436943768 x 10 <sup>2</sup>	0.1231247634 x 10 <sup>7</sup>	0.5561957539 x 10 <sup>1</sup>
2	0.8018288621	-0.1978847871 x 10 <sup>6</sup>	0.3434189609 x 10 <sup>1</sup>
3	0.1617232913 x 10 <sup>-1</sup>	0.1859988044 x 10 <sup>2</sup>	-0.6406390628
4	-0.1501147505 x 10 <sup>-2</sup>	-0.2765701318 x 10 <sup>1</sup>	0.5918579484 x 10 <sup>-1</sup>
5	0.0000000000	0.1036033878 x 10 <sup>4</sup>	-0.2725378570 x 10 <sup>-2</sup>
6	0.0000000000	-0.2143423131 x 10 <sup>3</sup>	0.5006336938 x 10 <sup>-4</sup>
7	0.0000000000	0.1690507762 x 10 <sup>2</sup>	
8	0.0000000000	-0.4864322134	
9	-0.1237675562 x 10 <sup>-4</sup>		
10	0.3004773304 x 10 <sup>-5</sup>		
11	-0.2062390734 x 10 <sup>-6</sup>		

### F.1.2 Liquid and Vapor Temperature as Functions of Enthalpy and Pressure

The temperature of water is approximated by the following function of pressure and enthalpy:

$$T_\ell = \begin{cases} \sum_{i=0}^{i=1} \sum_{j=0}^{j=3} CT1_{i,j} p^i h^j & \text{if } p < p_{\text{CRIT}} \text{ and } h \leq h_f(p) \\ & \text{(Liquid Region)} \end{cases} \quad (\text{eq.F-9})$$

$$T_\ell = \begin{cases} \sum_{i=0}^{i=4} \sum_{j=0}^{j=4} CT2_{i,j} p^i h^j & \text{if } p \geq p_{\text{CRIT}} \text{ and } h \leq h_f(p_{\text{CRIT}}) \\ & \text{(Critical Region)} \end{cases} \quad (\text{eq.F-10})$$

$$T_v = \begin{cases} \sum_{i=0}^{i=4} \sum_{j=0}^{j=4} CT3_{i,j} p^i h^j & \text{if } p < p_{\text{CRIT}} \text{ and } h \geq h_g(p) \\ & \text{(Vapor Region)} \end{cases} \quad (\text{eq.F-11})$$

$$T_v = \begin{cases} \sum_{i=0}^{i=4} \sum_{j=0}^{j=4} CT4_{i,j} p^i h^j & \text{if } p \geq p_{\text{CRIT}} \text{ and } h > h_g(p_{\text{CRIT}}) \\ & \text{(Critical Region)} \end{cases} \quad (\text{eq.F-12})$$

The constant coefficients,  $CTn_{i,j}$ , in equations F-9 through F-12 are listed in Table F-2. The resulting water temperature is in units of degrees Fahrenheit. The sub-domain division boundary values,  $p_{\text{CRIT}}$  and  $h(p_{\text{CRIT}})$ , are 3208.2 psia and 906 Btu/lbm, respectively.

Appendix F: Equation of State

The two-phase region is bounded by the saturation curve. This region is described by the criteria that  $0.1 \text{ psia} \leq p < p_{\text{CRIT}}$  and  $h_f(p) < h < h_g(p)$ . Temperature is constant along lines of constant pressure across this region. Thus, within the two-phase region,

$$T_f = \sum_{i=0}^{i=1} \sum_{j=0}^{j=3} CT1_{i,j} p^i [h_f(p)]^j \quad (\text{Two-Phase Region}) \quad (\text{eq. F-13})$$

**Table F-2**  
**Constants for Temperature as a Function of Pressure and Enthalpy**

CT1 <sub>i,j</sub>					
i/j	0	1	2	3	
0	.3276275552x10 <sup>2</sup>	.9763617000	.1857226027x10 <sup>-3</sup>	-.4682674330x10 <sup>-6</sup>	
1	.3360880214x10 <sup>-2</sup>	-.5595281760x10 <sup>-4</sup>	.1618595991x10 <sup>-6</sup>	-.1180204381x10 <sup>-9</sup>	

CT2 <sub>i,j</sub>					
i/j	0	1	2	3	4
0	.6390801208x10 <sup>3</sup>	-.3055217235x10 <sup>1</sup>	.8713231868x10 <sup>-2</sup>	-.6269403683x10 <sup>-5</sup>	-.9844700000x10 <sup>-17</sup>
1	-.4302857237	.2673303442x10 <sup>-2</sup>	-.5198380474x10 <sup>-5</sup>	.3037825558x10 <sup>-8</sup>	.3309704045x10 <sup>-12</sup>
2	.1174524584x10 <sup>-3</sup>	-.6839200986x10 <sup>-6</sup>	.1168011772x10 <sup>-8</sup>	-.4260074181x10 <sup>-12</sup>	-.2732087163x10 <sup>-15</sup>
3	-.1473977290x10 <sup>-7</sup>	.8018858166x10 <sup>-10</sup>	-.1164901355x10 <sup>-12</sup>	.4559400289x10 <sup>-17</sup>	.5825511142x10 <sup>-19</sup>
4	.7104327342x10 <sup>-7</sup>	-.3649500626x10 <sup>-14</sup>	.4457387575x10 <sup>-17</sup>	.1678398723x10 <sup>-20</sup>	-.3756804091x10 <sup>-23</sup>

CT3 <sub>i,j</sub>					
i/j	0	1	2	3	4
0	-.1179100862x10 <sup>5</sup>	.2829274345x10 <sup>2</sup>	-.2678181564x10 <sup>-1</sup>	.1218742752x10 <sup>-4</sup>	-.2092033147x10 <sup>-8</sup>
1	.1256160907x10 <sup>3</sup>	-.3333448850	.3326901268x10 <sup>-3</sup>	-.1477890326x10 <sup>-6</sup>	.2463258371x10 <sup>-10</sup>
2	-.1083713369	.2928177730x10 <sup>-3</sup>	-.2972436458x10 <sup>-6</sup>	.1342639113x10 <sup>-9</sup>	-.2275585718x10 <sup>-13</sup>
3	.3278071846x10 <sup>-4</sup>	-.8970959364x10 <sup>-7</sup>	.9246248312x10 <sup>-10</sup>	-.4249155515x10 <sup>-13</sup>	.7338316751x10 <sup>-17</sup>
4	-.3425564927x10 <sup>-8</sup>	.9527692453x10 <sup>-11</sup>	-.1001409043x10 <sup>-13</sup>	.4703914404x10 <sup>-17</sup>	-.8315044742x10 <sup>-21</sup>

CT4 <sub>i,j</sub>					
i/j	0	1	2	3	4
0	.3795256853x10 <sup>4</sup>	-.6347031007x10 <sup>1</sup>	.2867228326x10 <sup>-2</sup>	.5953599813x10 <sup>-8</sup>	.4798207438x10 <sup>-10</sup>
1	-.3910086240x10 <sup>1</sup>	.1222747819x10 <sup>-1</sup>	-.1404664699x10 <sup>-4</sup>	.7505679464x10 <sup>-8</sup>	-.1608693653x10 <sup>-11</sup>
2	.3410500159x10 <sup>-4</sup>	.7010900113x10 <sup>-9</sup>	-.1030201866x10 <sup>-9</sup>	.5731099333x10 <sup>-14</sup>	.3720795449x10 <sup>-16</sup>
3	.1527377542x10 <sup>-6</sup>	-.5356866315x10 <sup>-9</sup>	.6823225984x10 <sup>-12</sup>	-.3668096142x10 <sup>-15</sup>	.6946004624x10 <sup>-19</sup>
4	-.1437179752x10 <sup>-10</sup>	.5006731336x10 <sup>-13</sup>	-.6365519546x10 <sup>-16</sup>	.3473711350x10 <sup>-19</sup>	-.6842306083x10 <sup>-23</sup>

### F.1.3 Specific Volume of Liquid and Vapor as Functions of Enthalpy and Pressure

The specific volume,  $v$ , of water is approximated by the following function of pressure and enthalpy:

$$v_\ell = \exp\left(\sum_{i=0}^2 \sum_{j=0}^4 CN1_{i,j} p^i h^j\right) \begin{cases} \text{if } p < p_{\text{CRIT}} \text{ and } h \leq h_f(p) & \text{or} \\ \text{if } p \geq p_{\text{CRIT}} \text{ and } h < 1000 \text{ Btu/lbm} & \text{(Liquid Region)} \end{cases} \quad (\text{eq. F-14})$$

$$v_v = \sum_{i=-1}^2 \sum_{j=0}^2 CN2_{i,j} p^i h^j \begin{cases} \text{if } p < p_{\text{CRIT}} \text{ and } h \geq h_g(p) & \text{or} \\ \text{if } p \geq p_{\text{CRIT}} \text{ and } h > 1000 \text{ Btu/lbm} & \text{(Vapor Region)} \end{cases} \quad (\text{eq. F-15})$$

The constant coefficients,  $CNn_{i,j}$ , in equations F-14 and F-15 are listed in Table F-3. The resulting specific volume,  $v$ , is in units of  $\text{ft}^3/\text{lbm}$ . The critical pressure division value is 3208.2 psia and the saturation enthalpy boundary functions,  $h_f$  and  $h_g$ .

The two-phase region under the "dome" of the saturation curve requires the quality,  $x$ , which is defined under thermal equilibrium conditions as

$$x = \frac{h - h_f(p)}{h_g(p) - h_f(p)} \quad (\text{eq. F-16})$$

When the quality is greater than zero, the specific volume of the two-phase mixture is expressed by

$$v = N_\ell(p, h_\ell) + [N_g(p) - N_\ell(p, h_\ell)] \quad (\text{eq. F-17})$$

where

$$N_\ell(p, h_\ell) \equiv \exp\left(\sum_{i=0}^2 \sum_{j=0}^4 CN1_{i,j} p^i h_\ell^j\right) \quad (\text{eq. F-18})$$

and

$$N_g(p) \equiv \sum_{i=-1}^2 \sum_{j=0}^2 CN2_{i,j} p^i [h_g(p)]^j \quad (\text{eq. F-19})$$

Appendix F: Equation of State

**Table F-3**  
**Constants for Specific Volume as a Function of Pressure and Enthalpy**

CN1 <sub>ij</sub>					
i/j	0	1	2	3	4
0	-.4117961750x10 <sup>1</sup>	-.3811294543x10 <sup>-3</sup>	.4308265942x10 <sup>-5</sup>	-.9160120130x10 <sup>-8</sup>	.8017924673x10 <sup>-11</sup>
1	-.4816067020x10 <sup>-5</sup>	.7744786733x10 <sup>-7</sup>	-.6988467605x10 <sup>-9</sup>	.1916720525x10 <sup>-11</sup>	-.1760288590x10 <sup>-14</sup>
2	-.1820625039x10 <sup>-8</sup>	.1440785930x10 <sup>-10</sup>	-.2082170753x10 <sup>-13</sup>	-.3603625114x10 <sup>-16</sup>	.7407124321x10 <sup>-19</sup>

CN2 <sub>ij</sub>					
i/j	0	1	2		
-1	-.1403086182x10 <sup>4</sup>	.1802594763x10 <sup>1</sup>	-.2097279215x10 <sup>-3</sup>		
0	.3817195017	-.5394444747x10 <sup>-3</sup>	.1855203702x10 <sup>-6</sup>		
1	-.6449501159x10 <sup>-4</sup>	.8437637660x10 <sup>-7</sup>	-.2713755001x10 <sup>-10</sup>		
2	.7823817858x10 <sup>-8</sup>	-.1053834646x10 <sup>-10</sup>	.3629590764x10 <sup>-14</sup>		

#### F.1.4 Thermal Conductivity as a Function of Temperature and Density

The thermal conductivity of water,  $k$ , may be correlated to its temperature,  $T$ , and density,  $\rho$ . The correlation utilized was formulated under the auspices of the International Association for the Properties of Steam, as reported by Kestin [2]. For completeness, this correlation is described below in SI units:

$$k = \lambda_0 + \bar{\lambda} + \Delta\lambda \quad (\text{eq. F-20})$$

where

$$\lambda_0 = \left(\frac{T}{T^*}\right)^{1/2} \sum_{i=0}^3 a_i \left(\frac{T}{T^*}\right)^i \quad (\text{eq. F-21})$$

$$\bar{\lambda} \equiv b_0 + b_1 \left(\frac{\rho}{\rho^*}\right) + b_2 \exp \left[ B_1 \left(\frac{\rho}{\rho^*} - B_2\right)^2 \right] \quad (\text{eq. F-22})$$

$$\begin{aligned} \Delta\lambda \equiv & \left[ d_1 \left(\frac{T^*}{T}\right)^{10} - d_2 \right] \left(\frac{\rho}{\rho^*}\right)^{1.8} + \exp \left\{ C_1 \left[ 1 - \left(\frac{\rho}{\rho^*}\right)^{2.8} \right] \right\} \\ & + d_3 S \left(\frac{\rho}{\rho^*}\right)^Q \exp \left\{ \frac{Q}{R} \left[ 1 - \left(\frac{\rho}{\rho^*}\right)^R \right] \right\} + d_4 \exp \left[ C_2 \left(\frac{T}{T^*}\right)^{1.5} + C_3 \left(\frac{\rho}{\rho^*}\right)^5 \right] \end{aligned} \quad (\text{eq. F-23})$$



and

$$Q \equiv 2.0 + C_5 (\Delta T^*)^{-6} \quad (\text{eq. F-24})$$

$$R \equiv Q + 1.0 \quad (\text{eq. F-25})$$

$$S = \begin{cases} (\Delta T^*)^{-1} & \text{for } T/T^* \geq 1.0 \\ C_6 (\Delta T^*)^{-0.6} & \text{for } T/T^* < 1.0 \end{cases} \quad (\text{eq. F-26})$$

$$\Delta T^* = \left| \frac{T}{T^*} - 1.0 \right| + C_4 \quad (\text{eq. F-27})$$

The constants in these expressions are as follows:

$T^* = 647.3 \text{ K}$	$\rho^* = 317.7 \text{ kg/m}^3$
$a_0 = 1.02811 \times 10^{-2} \text{ W/}^\circ\text{K-m}$	$d_1 = 7.01309 \times 10^{-2} \text{ W/}^\circ\text{K-m}$
$a_1 = 2.99621 \times 10^{-2} \text{ W/}^\circ\text{K-m}$	$d_2 = 1.18520 \times 10^{-2} \text{ W/}^\circ\text{K-m}$
$a_2 = 1.56146 \times 10^{-2} \text{ W/}^\circ\text{K-m}$	$d_3 = 1.69937 \times 10^{-3} \text{ W/}^\circ\text{K-m}$
$a_3 = -4.22464 \times 10^{-3} \text{ W/}^\circ\text{K-m}$	$d_4 = 1.02000 \text{ W/}^\circ\text{K-m}$
$b_0 = -3.97070 \times 10^{-1} \text{ W/}^\circ\text{K-m}$	$C_1 = 6.42857 \times 10^{-1}$
$b_1 = 4.00302 \times 10^{-1} \text{ W/}^\circ\text{K-m}$	$C_2 = -4.11717$
$b_2 = 1.06000 \text{ W/}^\circ\text{K-m}$	$C_3 = -6.17937$
$B_1 = -1.71587 \times 10^{-1}$	$C_4 = 3.08976 \times 10^{-3}$
$B_2 = 2.39219$	$C_5 = 8.22994 \times 10^{-2}$
	$C_6 = 1.00932 \times 10^1$

With these coefficients, the thermal conductivity given by eq. F-20 has units of (W/K-m).

### F.1.5 Dynamic Viscosity as a Function of Temperature and Density

The dynamic viscosity of water,  $\mu$ , may be correlated to its temperature,  $T$ , and density,  $\rho$ . As in the case of thermal conductivity, a correlation [3] is utilized that was formulated under the auspices of the International Association for the Properties of Steam. This correlation in SI units is as follows:

$$\mu = \mu_0 \exp \left[ \frac{\rho}{\rho^*} \sum_{i=0}^5 \sum_{j=0}^4 b_{ij} \left( \frac{T}{T^*} - 1 \right)^i \left( \frac{\rho}{\rho^*} - 1 \right)^j \right] \quad (\text{eq. F-28})$$

where

$$\mu_0 \equiv 10^{-6} \left( \frac{T}{T^*} \right)^{1/2} \left[ \sum_{k=0}^3 a_k \left( \frac{T}{T^*} \right)^k \right]^{-1} \quad (\text{eq. F-29})$$

The constants appearing in these expressions have the numerical values given below and in Table F-4 for the  $b_{ij}$ .

$$T^* = 647.27 \text{ K}$$

$$\rho^* = 317.763 \text{ kg/m}^3$$

$$a_0 = 0.0181583$$

$$a_1 = 0.0177624$$

$$a_2 = 0.0105287$$

$$a_3 = -0.0036744$$

The dynamic viscosity computed from eq. F-28 has units of ( $\mu\text{Pa} \cdot \text{s}$ ).

**Table F-4**  
**Coefficients  $b_{ij}$  for Dynamic Viscosity**

j/i	0	1	2	3	4	5
0	0.5019380	0.1628880	-0.1303560	0.9079190	-0.5511190	0.1465430
1	0.2356220	0.7893930	0.6736650	1.2075520	0.0670665	-0.0843370
2	-0.2746370	-0.7435390	-0.9594560	-0.6873430	-0.4970890	0.1952860
3	0.1458310	0.2631290	0.3472470	0.2134860	0.1007540	-0.0329320
4	-0.0270448	-0.0253093	-0.0267758	-0.0822904	0.0602253	-0.0202595

## F.2 Sodium

The sodium thermophysical and transport properties used in FALCON were obtained from the Argonne National Laboratory properties database [4]. FALCON only considers the liquid phase of sodium below the boiling point. The thermophysical and transport properties considered by FALCON include heat capacity ( $c_p$ ), enthalpy ( $h$ ), density ( $\rho$ ), and thermal conductivity ( $k$ ). These properties are independent of pressure and only depend on the sodium temperature.

### F.2.1 Heat Capacity as Function of Temperature

$$c_p = 0.46272726 \times 10^{-6} T^2 - 0.58053783 \times 10^{-3} T + 1.436716 \quad (\text{eq. F-30})$$

where

$c_p$ : Heat capacity (J/g °C)

$T$ : Sodium temperature (°C)

### F.2.2 Enthalpy as Function of Temperature

$$h = \frac{0.46272726 \times 10^{-6} T^3}{3} - \frac{0.58053783 \times 10^{-3} T^2}{2} + 1.436716 T \quad (\text{eq. F-31})$$

where

$h$ : Mass enthalpy (J/g)

$T$ : Sodium temperature (°C)

### F.2.3 Density as Function of Temperature

$$\rho = (0.06035 \times 10^{-9} T_F^3 - 0.2872 \times 10^{-6} T_F^2 - 7.9 \times 10^{-3} T_F + 59.566) 0.016018 \times 10^3 \quad (\text{eq. F-32})$$

where

$\rho$ : Density (kg/m<sup>3</sup>)

$T_F$ : Sodium temperature (°F)

**F.2.4 Thermal Conductivity as Function of Temperature**

$$k = 1.1727457 \times 10^{-5} T^2 - 5.808759 \times 10^{-2} T + 92.951006 \quad (\text{eq. F-33})$$

where

k: Thermal conductivity (W/m °C)

T<sub>F</sub>: Sodium temperature (°C)

**F.3 References**

1. RETRAN-02 - A Program For Transient Thermal-Hydraulic Analysis of Complex Fluid Flow Systems, Vol. 1: Equations and Numerics, EPRI-NP-1850, Electric Power Research Institute, May 1981.
2. Kestin J., "Thermal Conductivity of Water and Steam," Mechanical Engineering, 100, No. 8, August 1978, pp. 46-48.
3. "New Values for the Viscosity of Water Substance," Mechanical Engineering, 98, No. 7, July 1976, p. 79.
4. Fink, J.K., Leibowitz, L., "Thermophysical Properties of Sodium," ANL-CEN-RSD-79-1, Argonne National Laboratory Report, 1979.





**WARNING:** This Document contains information classified under U.S. Export Control regulations as restricted from export outside the United States. You are under an obligation to ensure that you have a legal right to obtain access to this information and to ensure that you obtain an export license prior to any re-export of this information. Special restrictions apply to access by anyone that is not a United States citizen or a Permanent United States resident. For further information regarding your obligations, please see the information contained below in the section titled "Export Control Restrictions."

## Export Control Restrictions

Access to and use of EPRI Intellectual Property is granted with the specific understanding and requirement that responsibility for ensuring full compliance with all applicable U.S. and foreign export laws and regulations is being undertaken by you and your company. This includes an obligation to ensure that any individual receiving access hereunder who is not a U.S. citizen or permanent U.S. resident is permitted access under applicable U.S. and foreign export laws and regulations. In the event you are uncertain whether you or your company may lawfully obtain access to this EPRI Intellectual Property, you acknowledge that it is your obligation to consult with your company's legal counsel to determine whether this access is lawful. Although EPRI may make available on a case by case basis an informal assessment of the applicable U.S. export classification for specific EPRI Intellectual Property, you and your company acknowledge that this assessment is solely for informational purposes and not for reliance purposes. You and your company acknowledge that it is still the obligation of you and your company to make your own assessment of the applicable U.S. export classification and ensure compliance accordingly. You and your company understand and acknowledge your obligations to make a prompt report to EPRI and the appropriate authorities regarding any access to or use of EPRI Intellectual Property hereunder that may be in violation of applicable U.S. or foreign export laws or regulations.

## About EPRI

EPRI creates science and technology solutions for the global energy and energy services industry. U.S. electric utilities established the Electric Power Research Institute in 1973 as a nonprofit research consortium for the benefit of utility members, their customers, and society. Now known simply as EPRI, the company provides a wide range of innovative products and services to more than 1000 energy-related organizations in 40 countries. EPRI's multidisciplinary team of scientists and engineers draws on a worldwide network of technical and business expertise to help solve today's toughest energy and environmental problems.

EPRI. Electrify the World

## SINGLE USER LICENSE AGREEMENT

**THIS IS A LEGALLY BINDING AGREEMENT BETWEEN YOU AND THE ELECTRIC POWER RESEARCH INSTITUTE, INC. (EPRI). PLEASE READ IT CAREFULLY BEFORE REMOVING THE WRAPPING MATERIAL.**

BY OPENING THIS SEALED PACKAGE YOU ARE AGREEING TO THE TERMS OF THIS AGREEMENT. IF YOU DO NOT AGREE TO THE TERMS OF THIS AGREEMENT, PROMPTLY RETURN THE UNOPENED PACKAGE TO EPRI AND THE PURCHASE PRICE WILL BE REFUNDED.

### 1. GRANT OF LICENSE

EPRI grants you the nonexclusive and nontransferable right during the term of this agreement to use this package only for your own benefit and the benefit of your organization. This means that the following may use this package: (I) your company (at any site owned or operated by your company); (II) its subsidiaries or other related entities; and (III) a consultant to your company or related entities, if the consultant has entered into a contract agreeing not to disclose the package outside of its organization or to use the package for its own benefit or the benefit of any party other than your company.

This shrink-wrap license agreement is subordinate to the terms of the Master Utility License Agreement between most U.S. EPRI member utilities and EPRI. Any EPRI member utility that does not have a Master Utility License Agreement may get one on request.

### 2. COPYRIGHT

This package, including the information contained in it, is either licensed to EPRI or owned by EPRI and is protected by United States and international copyright laws. You may not, without the prior written permission of EPRI, reproduce, translate or modify this package, in any form, in whole or in part, or prepare any derivative work based on this package.

### 3. RESTRICTIONS

You may not rent, lease, license, disclose or give this package to any person or organization, or use the information contained in this package, for the benefit of any third party or for any purpose other than as specified above unless such use is with the prior written permission of EPRI. You agree to take all reasonable steps to prevent unauthorized disclosure or use of this package. Except as specified above, this agreement does not grant you any right to patents, copyrights, trade secrets, trade names, trademarks or any other intellectual property, rights or licenses in respect of this package.

### 4. TERM AND TERMINATION

This license and this agreement are effective until terminated. You may terminate them at any time by destroying this package. EPRI has the right to terminate the license and this agreement immediately if you fail to comply with any term or condition of this agreement. Upon any termination you may destroy this package, but all obligations of nondisclosure will remain in effect.

### 5. DISCLAIMER OF WARRANTIES AND LIMITATION OF LIABILITIES

NEITHER EPRI, ANY MEMBER OF EPRI, ANY COSPONSOR, NOR ANY PERSON OR ORGANIZATION ACTING ON BEHALF OF ANY OF THEM:

- (A) MAKES ANY WARRANTY OR REPRESENTATION WHATSOEVER, EXPRESS OR IMPLIED, (I) WITH RESPECT TO THE USE OF ANY INFORMATION, APPARATUS, METHOD, PROCESS OR SIMILAR ITEM DISCLOSED IN THIS PACKAGE, INCLUDING MERCHANTABILITY AND FITNESS FOR A PARTICULAR PURPOSE, OR (II) THAT SUCH USE DOES NOT INFRINGE ON OR INTERFERE WITH PRIVATELY OWNED RIGHTS, INCLUDING ANY PARTY'S INTELLECTUAL PROPERTY, OR (III) THAT THIS PACKAGE IS SUITABLE TO ANY PARTICULAR USER'S CIRCUMSTANCE; OR
- (B) ASSUMES RESPONSIBILITY FOR ANY DAMAGES OR OTHER LIABILITY WHATSOEVER (INCLUDING ANY CONSEQUENTIAL DAMAGES, EVEN IF EPRI OR ANY EPRI REPRESENTATIVE HAS BEEN ADVISED OF THE POSSIBILITY OF SUCH DAMAGES) RESULTING FROM YOUR SELECTION OR USE OF THIS PACKAGE OR ANY INFORMATION, APPARATUS, METHOD, PROCESS OR SIMILAR ITEM DISCLOSED IN THIS PACKAGE.

### 6. EXPORT

The laws and regulations of the United States restrict the export and re-export of any portion of this package, and you agree not to export or re-export this package or any related technical data in any form without the appropriate United States and foreign government approvals.

### 7. CHOICE OF LAW

This agreement will be governed by the laws of the State of California as applied to transactions taking place entirely in California between California residents.

### 8. INTEGRATION

You have read and understand this agreement, and acknowledge that it is the final, complete and exclusive agreement between you and EPRI concerning its subject matter, superseding any prior related understanding or agreement. No waiver, variation or different terms of this agreement will be enforceable against EPRI unless EPRI gives its prior written consent, signed by an officer of EPRI.

---

*Program:*

1011307

Nuclear Power

---

© 2004 Electric Power Research Institute (EPRI), Inc. All rights reserved. Electric Power Research Institute and EPRI are registered service marks of the Electric Power Research Institute, Inc. EPRI. ELECTRIFY THE WORLD is a service mark of the Electric Power Research Institute, Inc.

♻️ Printed on recycled paper in the United States of America